TECHNISCHE UNIVERSITÄT DRESDEN

Max-Planck-Institut
für Chemische Physik fester Stoffe

Magnetization Study of the Heavy-Fermion System $Yb(Rh_{1-x}Co_x)_2Si_2$ and of the Quantum Magnet $NiCl_2$-4SC$(NH_2)_2$

Luis Pedrero Ojeda

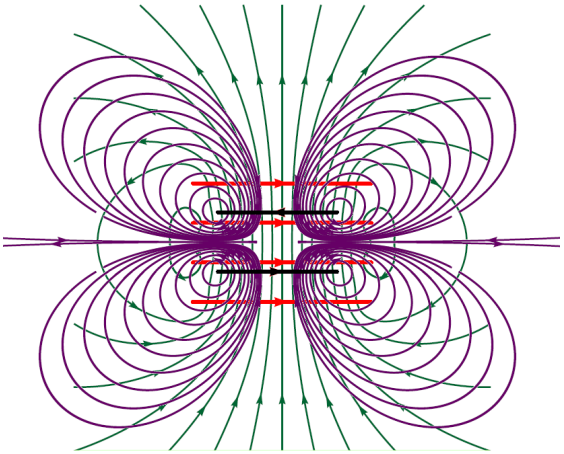

Max-Planck-Institut für Chemische Physik fester Stoffe

Fakultät Mathematik und Naturwissenschaften der Technischen Universität Dresden

The **cover picture** represents the lines of force that a specimen experiences in the Faraday magnetometer . The violet lines are produced for the gradient coils (coils in anti-Helmholtz configuration) and the green ones produced by the main magnetic coil which magnetized the sample under investigation.

Magnetization Study of the Heavy-Fermion System $Yb(Rh_{1-x}Co_x)_2Si_2$ and of the Quantum Magnet $NiCl_2$-4SC$(NH_2)_2$

DISSERTATION

zur Erlangung des akademischen Grades

Doctor rerum naturalium
(Dr. rer. nat.)

vorgelegt

der Fakultät Mathematik und Naturwissenschaften der Technischen Universität Dresden

von

M. Sc. Luis Pedrero Ojeda
geboren in Mexiko Stadt

Max-Planck-Institut
für Chemische Physik fester Stoffe

Gutachter:

Prof. Dr. Frank Steglich
Prof. Dr. Hans-Henning Klauß

Eingereicht am: 17.01.2013
Verteidigt am: 28.05.2013

Unidad en el saber...
pues un solo analfabeta no tiene que haber.

Martha Ojeda Mancera (1936 - 2010),
Mexikanisher Arzt,
soziale Kämpferin

Wer alle seine Ziele erreicht hat, hat sie wahrscheinlich zu niedrig gewählt.

Herbert von Karajan (1908 - 1989),
Dirigent

The test of all knowledge is experiment.

Richard Feynman (1918 - 1988),
Physicist

To my three favorites girls.

Ceci, Ana & Isabel

To the beloved memory of

Martha Ojeda Mancera & **Eduardo Pedrero Nieto**

two gentle souls and the two great lights in my life and in science.

Abstract

This thesis presents a comprehensive study of the magnetic properties and of quantum phase transitions (QPTs) of two different systems which have been investigated by means of low-temperature magnetization measurements. The systems are the heavy-fermion $Yb(Rh_{1-x}Co_x)_2Si_2$ (metallic) and the quantum magnet $NiCl_2$-$4SC(NH_2)_2$ (insulator). Although they are very different materials, they share two common properties: magnetism and QPTs. Magnetism originates in $Yb(Rh_{1-x}Co_x)_2Si_2$ from the trivalent state of the Yb^{3+} ions with effective spin $S = 1/2$. In $NiCl_2$-$4SC(NH_2)_2$, the magnetic Ni^{2+} ions have spin $S = 1$. These magnetic ions are located on a body-centered tetragonal lattice in both systems and, in this study, the QPTs are induced by an external magnetic field.

In $Yb(Rh_{1-x}Co_x)_2Si_2$ the evolution of magnetism from itinerant in slightly Co-doped $YbRh_2Si_2$ to local in $YbCo_2Si_2$ is examined analyzing the magnetic moment μ versus chemical pressure x phase diagram in high-quality single crystals, which indicates a continuous change of dominating energy scale from the Kondo to the RKKY one. The physics of the antiferromagnet $YbCo_2Si_2$ can be completely understood. On the other hand, the physics of pure and slightly Co-containing $YbRh_2Si_2$ is much more complex, due to the itinerant character of magnetism and the vicinity of the system to an unconventional quantum critical point (QCP). The field-induced AFM QCP in $Yb(Rh_{0.93}Co_{0.07})_2Si_2$ and in pure $YbRh_2Si_2$ under a pressure of 1.5 GPa is characterized by means of the magnetic Grüneisen ratio.

The final part of this thesis describes quantum criticality near the field-induced QCP in $NiCl_2$-$4SC(NH_2)_2$. These results will be compared to the theory of QPTs in Ising and XY antiferromagnets. Since the XY-AFM ordering can be described as BEC of magnons by mapping the spin-1 system into a gas of hardcore bosons, the temperature dependence of the magnetization for a BEC is analytically derived and compared to the results just below the critical field. The remarkable agreement between the BEC theory and experiments in this quantum magnet is one of the most prominent examples of the concept of universality.

Contents

1 Introduction

The central topic of this PhD work is the study of magnetic quantum phase transitions (QPT)s in condensed matter. Two systems were chosen to be investigated: The heavy-fermion (HF) system $Yb(Rh_{1-x}Co_x)_2Si_2$ and the quantum magnet $NiCl_2$-4SC$(NH_2)_2$. Although they are very different materials, i.e. $Yb(Rh_{1-x}Co_x)_2Si_2$ is a metal and $NiCl_2$-4SC$(NH_2)_2$ is an insulator, they share two common properties: magnetism and QPTs. Magnetism originates in $Yb(Rh_{1-x}Co_x)_2Si_2$ from the trivalent state of the Yb^{3+} ions with effective spin $S = 1/2$. In $NiCl_2$-4SC$(NH_2)_2$, the magnetic Ni^{2+} ions have spin $S = 1$. These magnetic ions are located on a body-centered tetragonal lattice in both systems and, in this study, the QPTs are induced by an external magnetic field.

Quantum phase transitions are phase transitions between two different ground states of matter, which take place at $T = 0$ and, therefore, are driven by quantum fluctuations. These transitions have been the focus of scientific interest during the last 30 years since their properties are different from the well-understood properties of classical thermal phase transitions, which are driven by thermal fluctuations [1]. More importantly, the associated quantum critical point (QCP), in case of a continuous QPT, is usually surrounded by a regime of quantum critical fluctuations where unconventional superconductivity or novel phases of matter may arise [2, 3, 4]. The discovery of new states of matter could open the way to future applications (e.g., high-T_c superconductor technology is already used for the creation of strong magnetic fields). This is why the understanding of the intrinsic properties of these materials is not just driven by fundamental curiosity, but it is necessary for pioneering new technologies.

Since QPTs can be induced by an external parameter like a magnetic field, pressure or chemical substitution, a large number of materials have been investigated with the objective to find universal behaviors [5]. In general, the properties of QPTs in magnetic insulators can well be described by the current theories, as will be reviewed in section 2.4 and demonstrated in chapter 5 for $NiCl_2$-4SC$(NH_2)_2$. QPTs in metals, on the other hand, are poorly understood. The regime around the QCP is characterized by non-Fermi liquid properties, i.e. the Fermi liquid theory, the standard theory of electronic interactions in metals, seems to break down at QCPs between a magnetically ordered (MO) state and a paramagnetic (PM) state. This has been verified not just in a few particular materials, but in all strongly correlated electron systems which show a QCP. It is therefore crucial to be able

to establish the presence of a QCP in a certain compound, as it was done, e.g., for $YbRh_2Si_2$ [6, 7] (see Sec. 4.1.1).

Another important matter is the "local" versus "itinerant" character of magnetism in metals. Similarly to their wave-particle duality nature, electrons in a metal can have dual character: Itinerant, if their wave function is mostly spatially delocalized or local, if their wave function is mostly localized. The conventional theory of QPTs in metals (the spin-density-wave (SDW) scenario) considers magnetism to be itinerant, in other words, the electrons that are providing the magnetic moments are delocalized and part of the Fermi surface as in the case of $3d$-electron systems (cf. Sec. 2.3.1). Apparently quite a number of heavy fermions compounds can be described by such theory, like $CeNi_2Ge_2$ [8] or $CeCu_2Si_2$ [9]. Yet, magnetism may be better described by a local approach, although electrons in metals are never completely localized [10], i.e. assuming that the magnetic electrons are not part of the Fermi surface, like for insulators. A typical example is $YbCo_2Si_2$, to which Secs. 4.1.2 and 4.5 are dedicated.

Magnetic QPTs are particularly well-studied in HF-systems. Here, the hybridization between the f-electrons with the (s, p, d) conduction electrons leads to the formation of a heavy composite quasiparticle band with d and f character, which dominates the thermodynamic and transport properties at low temperatures. This hybridization can be described by the Kondo interaction. The magnetic f-moment is progressively screened when $T < T_K$, the Kondo temperature, leaving a non-magnetic ground state. The magnetic coupling between neighboring f electrons can nevertheless be mediated by the so-called Ruderman-Kittel-Kasuya-Yosida (RKKY) interaction. This can produce both an antiferromagnetically or a ferromagnetically ordered state at $T = 0$, depending on the carrier concentration, band structure and the distance between the adjacent f moments, if the RKKY energy $k_B T_{RKKY}$ is larger than the Kondo energy $k_B T_K$. The interplay between these two energy scales defines the position of the QCP between the MO ground state and the PM one (see Sec. 2.2.4).

Some years ago, it has been shown that at the antiferromagnetic (AFM) QCP in $CeCu_{6-x}Au_x$ [11] the magnetic correlations have surprisingly local character. It has been found that at the pressure-induced QCP in $CeRhIn_5$ [12] and at the magnetic field-induced QCP in $YbRh_2Si_2$ [13], the Kondo effect breaks down, causing an abrupt change of the Fermi surface. None of these properties is predicted by the SDW scenario. Recently, new theories have been developed, which can model many of the newly observed features, and are known as local QCP scenario (cf. Sec. 2.3.2). None of these theories can so far completely describe the physics of QPTs in metals [14]. However, general scaling can provide precise predictions of the behavior of some thermodynamic quantities, like the Grüneisen ratio Γ [15]. If scaling applies, the temperature dependence of $\Gamma(T)$ at the QCP is independent

of the microscopical details of the material but follows a universal power law associated with the type of critical magnetic fluctuations and their dimensionality (cf. Sec. 2.3.4).

The objective of this work is to study MO-to-PM QPTs in the aforementioned two systems and to compare the results with the present theories in order to make a step forward to a more complete understanding. The physical quantity that has been chosen to be measured is the magnetization, from which we can derive the magnetic Grüneisen ratio. Since QPTs are per definition phase transitions at $T = 0$, we need measurements of the magnetization at very low temperatures. To do this, a Faraday magnetometer was built and adapted into a dilution refrigerator which achieves 0.05 K [16]. A special setup was developed to measure the magnetization with a high resolution (close to that of a SQUID) and in magnetic fields up to 12 T.

The outline of this work is as follows:

Chapter 2 contains the basic theoretical models, which will later be used for the data analysis. A brief overview of the Fermi-liquid theory, of quantum phase transitions and of the SDW and local QCP scenarios are presented. Finally, a general description of the theory of quantum magnets as well as their description in terms of Bose-Einstein condensation (BEC) of magnons are presented.

Chapter 3 introduces the principle of operation of a Faraday magnetometer, its setup and its application in a dilution refrigerator. Since the magnetization was also measured under hydrostatic pressure, a brief introduction to this technique is given.

Chapter 4 is the central chapter of this work. Seven high-quality single crystals of the series $Yb(Rh_{1-x}Co_x)_2Si_2$ are investigated. The evolution of magnetism from itinerant in slightly Co-doped $YbRh_2Si_2$ to local in $YbCo_2Si_2$ is examined analyzing the magnetic moment μ versus chemical pressure x phase diagram, which indicates a continuous change of dominating energy scale from the Kondo to the RKKY one. The findings show that the physics of the antiferromagnet $YbCo_2Si_2$ can be completely understood. On the other hand, the physics of pure and slightly Co-containing $YbRh_2Si_2$ is much more complex, due to the itinerant character of magnetism and the vicinity of the system to an unconventional QCP. The field-induced AFM QCP in $Yb(Rh_{0.93}Co_{0.07})_2Si_2$ and in pure $YbRh_2Si_2$ under a pressure of 1.5 GPa is studied by means of the magnetic Grüneisen ratio. This QCP is located in the itinerant part of the phase diagram and supposed to be described by the SDW scenario.

Chapter 5 describes the comprehensive study of quantum criticality near the field-induced QCP in $NiCl_2$-4SC$(NH_2)_2$ by means of magnetization measurements. These results will be compared to the theory of QPTs in Ising and XY antiferromagnets. Since the XY-AFM ordering can be described as BEC of magnons by

mapping the spin-1 system into a gas of hardcore bosons, the temperature dependence of the magnetization for a BEC is analytically derived and compared to the results just below the critical field. The remarkable agreement between the BEC theory and experiments in this quantum magnet is one of the most prominent example of the concept of universality.

2 Theoretical concepts

2.1 Ce- and Yb-based 4f-electron systems

During the last four decades, systems which contain elements with incompletely filled 4f-shells like Ce, Yb have assumed a central role in the field of strongly correlated electron systems. The main reason is that the non-magnetic electronic configurations Ce^{4+} ([Xe]$5d^2 6s^2$) and Yb^{2+} ([Xe]$4f^{14} 6s^2$) lie in energy very close to the magnetic configurations Ce^{3+} ([Xe]$4f^1 5d^1 6s^2$ with one 4f electron) and Yb^{3+} ([Xe]$4f^{13} 5d^1 6s^2$ with thirteen 4f electrons, i.e. one 4f hole), respectively. Since the magnetic Ce^{+3} is larger than the non-magnetic Ce^{4+}, a change of hydrostatic pressure or chemical substitution can induce dramatic valence change [17]. Specifically, a decrease of the unit-cell volume due to pressure or substitution of an element by a smaller one (chemical pressure) favors the non-magnetic Ce configuration. On the other hand, the magnetic Yb^{3+} ion is smaller than the non-magnetic Yb^{2+}, therefore, in Yb systems a decreasing of the unit-cell volume favors the magnetic ground state. This is schematically displayed in Fig. 2.1. The size of the f shells is small compared to the interatomic distances, implying that the f electrons do not participate in the chemical bonding and the f electron wave functions of neighboring atoms do not overlap. Therefore, the magnetic moments associated with the f electrons can be treated as localized. However, in intermetallic systems the f electrons can hybridize with the conduction electrons - typically 3d electrons - leaving a non-magnetic ground state (see Sec. 2.2.2). On the other side, the local magnetic moments of the f electrons can polarize the conduction electrons

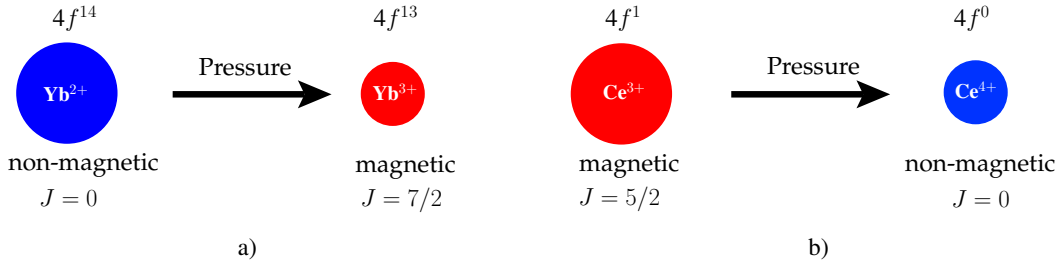

Figure 2.1 – Schematic pressure dependence of Ce and Yb ions in intermetallic compounds. The arrows indicate the direction of hydrostatic or chemical pressure. The red color indicates the magnetic atoms while the blue the non-magnetic ones. Here J is the total angular momentum of the f electron.

producing a magnetic coupling between neighboring f moments leaving a magnetically ordered ground state (see Sec. 2.2.3). Since both mechanisms depend in a different way on the hybridization strength J, a change of pressure strongly modifies J and therefore the ground state of f intermetallic compounds. The discovery of new many-body phase of matter (e.g. unconventional superconductivity) across the point of phase change between a magnetically ordered ground state and the non-magnetic one - the so-called quantum critical point (see Sec. 2.3) - has increased the interest of scientists in $4f$- and $5f$-based intermetallic compounds, in particular in the so-called heavy-fermion systems (see sec. 2.2). One of these, $Yb(Rh_{1-x}Co_x)_2Si_2$, is studied in this work (Chapter 4).

2.1.1 Crystalline electric field

The magnetic properties of rare-earth compounds commonly exhibit a strong anisotropy due to the effect of the crystalline electrical field (CEF) on the orbital part of the total angular momentum J. Basically, in $4f$-based systems the effect of the CEF on the magnetic atoms is much weaker than in $3d$-based materials. This is because the $4f$ shell is much better shielded by the outer shells than the $3d$ shell. The CEF interaction ($\approx 10\,\mathrm{meV}$) results to be smaller than the spin-orbit coupling ($\approx 100\,\mathrm{meV}$) and can be treated as a perturbation on each J-multiplet [18, 19]. In this case, the CEF Hamiltonian can be generally written as

$$H_{CF} = \sum_i \sum_l r_i^l \sum_{m=-l}^{+l} B_l^m Y_l^m(\theta_i, \phi_i) \tag{2.1}$$

where $Y_l^m(\theta_i, \phi_i)$ are the spherical harmonics and B_l^m are the CEF parameters which depends on the environment. Adding the Zeeman term, the global Hamiltonian becomes:

$$H = H_{CF} + gJ\mu_B B \tag{2.2}$$

where μ_B is the Bohr magneton and B the magnetic field.

In this work, systems with tetragonal crystal structure are investigated. In a tetragonal point symmetry the Hamiltonian can be simplified into

$$H_{CF} = B_2^0 O_2^0 + B_4^0 O_4^0 + B_4^4 O_4^4 + B_6^0 O_6^0 + B_6^4 O_6^4 \tag{2.3}$$

where B_m^n are the CEF parameters and O_m^n are the Stevens operators [20]. These dimensionless coefficients are tabulated and vary in sign and amplitude from one rare earth to another. The lowest term of the Hamiltonian are of order 2 and it is generally dominant. The six-fold multiplet of Ce^{3+} (with $J = 5/2$) and eight-fold multiplet of Yb^{3+} (with $J = 7/2$) are then split at least into 2-fold degenerate

energy levels (Kramers doublets). These can be represented in the case of Yb^{3+} in the basis of $|j_z>$ and their eigenfunctions as

$$\begin{aligned}
|\Gamma_{6,1}> &= \cos(\alpha)|\pm 1/2> + \sin(\alpha)|\mp 7/2> \\
|\Gamma_{6,2}> &= \sin(\alpha)|\pm 1/2> - \cos(\alpha)|\mp 7/2> \\
|\Gamma_{7,1}> &= \cos(\alpha')|\pm 3/2> - \sin(\alpha')|\mp 5/2> \\
|\Gamma_{7,2}> &= \sin(\alpha')|\pm 3/2> + \cos(\alpha')|\mp 5/2>
\end{aligned} \tag{2.4}$$

with $(\alpha)^2+(\alpha')^2 = 1$. The knowledge of the mixing parameters and the transition energies within the Hund's rule ground state fully describe the crystal-field scheme and determines all B_m^n parameters. The low-lying doublet is magnetic and represents the ground state of the system. Its entropy amounts to $Rln2$ where $R = 8.31$ J/Kmol is the molar gas constant. The magnetic field lifts the degeneracy of the doublets. At very low temperature the ground state doublet is splitted by the field into levels with different magnetic moments $\mu_{B\|c}$ and $\mu_{B\perp c}$ (where c is the crystallographic c-axis) according to the field orientation. The difference between the size of the magnetic moments is a measure of the magnetocrystalline anisotropy. Since the CEF splitting energy is usually small ($\approx 10\,\mathrm{meV}$), at room temperature the total effective moment of the J- multiplet

$$\mu_{\mathrm{eff}} = g\sqrt{J(J+1)}\mu_{\mathrm{B}}, \tag{2.5}$$

where g is the Landé factor, can be measured. For Ce^{3+} it is about $\mu_{\mathrm{eff}}^{Ce} = 3/7\sqrt{35} \approx 2.54\mu_{\mathrm{B}}$ and for Yb^{3+} it is $\mu_{\mathrm{eff}}^{Yb} = 12/\sqrt{7} \approx 4.54\mu_{\mathrm{B}}$. At high temperature, the magnetic susceptibility χ^{-1} follows a Curie-Weiss behavior

$$\chi^{-1} \propto \frac{\mu_{\mathrm{eff}}^2}{T - \theta_W} \tag{2.6}$$

with θ_W the Weiss temperature. The paramagnetic Weiss temperatures θ_W^{ab} and θ_W^c, along both principal crystallographic axes, can be expressed on the basis of molecular field theory [21] as a function of the first CEF parameter B_2^0 which is therefore a measure of the strength of the magnetocrystalline anisotropy:

$$B_2^0 = \left(\theta_W^{ab} - \theta_W^c\right) \frac{10k_B}{3(2J-1)(2J+3)}. \tag{2.7}$$

Information about the crystalline electric field splitting of the free-ion states can usually be derived from many spectroscopic methods. The principal experimental method used for such purpose is inelastic neutron scattering (INS), but optical methods, ESR and hyperfine methods like NMR and Mössbauer spectroscopy are also widely used. Recently, polarization dependent soft x-ray absorption spectroscopy (XAS) was shown to be a powerful tool for determining the crystal-field ground state for these class of materials [22]. The treatment outlined above is applied in Sec. 4.1.2 for the case of $YbCo_2Si_2$.

2.2 Heavy-fermion systems

The term "heavy fermion" (HF) is used to describe the low temperature electronic state of a new class of intermetallic compounds, based on lanthanide ($4f$-electrons) and actinide ($5f$-electrons) atoms, with an electronic density of states $N(E_F)$ at the Fermi level and at low temperatures as much as 1000 times larger than in normal metals. There are quite a large number of HF compounds based on Ce and Yb. The heavy electron state has its origin in the hybridization between the $4f/5f$ local moments and the usually-$3d$ conduction electrons, an effect that is known as Kondo effect (see Sec. 2.2.2). At high temperature a HF system behaves like a local magnet, showing Curie-Weiss behavior in the susceptibility, but below a characteristic temperature, the Kondo temperature, the conduction electrons start to compensate the f-moments, leaving a non-magnetic ground state at $T \to 0$. The increasing overlap of the electronic d and f states creates a new flat band at the Fermi level, separated by the so-called hybridization gap, which contains $d-f$ composite quasiparticles and results in an expansion of the Fermi surface volume [23, 24]. These quasiparticles have a heavy (effective) mass, reflected in the enhanced value of the Sommerfeld coefficient $\gamma_0 = C(T)/T|_{T\to 0}$ or the Pauli susceptibility χ_0, both proportional to $N(E_F)$. The ground state of a HF system can be well described by the Fermi liquid theory (see Sec. 2.2.1). The conduction-electrons-mediated interaction between the f-moments (the RKKY interaction, see Sec. 2.2.3) in a HF system can overcome the Kondo effect and yields a magnetically ordered ground state. Since the discovery of $CeAl_3$ (with a Sommerfeld coefficient $\gamma_0 = 1620\,\mathrm{mJ/mol\ K^2}$) [25], various types of ground states were observed in HF systems, such as superconducting, magnetic ordered or insulating state. The limit of the HF state was established in a somehow arbitrary way, with $\gamma_0 \leq 400\,\mathrm{mJ/mol\ K^2}$ [26] defined as lower limit.

2.2.1 Fermi liquid theory

The standard theory of metals is the Fermi-liquid (FL) theory. Its discovery goes back to the work of L. D. Landau in 1956. He introduced a phenomenological theory to describe the properties of a weak interacting fermion system at low temperatures [27]. Landau's basic idea is the one-to-one correspondence between the energy states of a system of non-interacting Fermi particles (Fermi gas), like electrons or ^{3}He atoms, and the states of the interacting particles (Fermi liquid). The particles of the Fermi liquid are known as quasiparticles, which are elementary excitations of the Fermi gas. A quasiparticle has the same charge and spin quantum numbers of the non-interacting fermion. The dynamical properties of this quasi-

particles, such as the effective mass m^*, are renormalized due to the interaction between the quasiparticles. In metals the effective mass is

$$\frac{m^*}{m_e} = 1 + \frac{F_1^s}{3} \tag{2.8}$$

where F_1^s is a non-dimensional Landau parameter and m_e is the bare electron mass. In simple metals, m^* is generically one order of magnitude larger than m_e, whereas in HF systems m^* can attain values as large as $10^3 m_e$. The thermodynamic and transport properties of a FL are related to m^* since the density of states at the Fermi energy $N(E_F) \propto m^*$. The temperature independent susceptibility has the form

$$\chi_0 = \chi^0_{Pauli} \frac{m^*}{m_e} \left(\frac{1}{1 + F_0^a} \right) \tag{2.9}$$

where F_0^a is the antisymmetric Landau parameter and χ^0_{Pauli} is the free electron Pauli susceptibility. The electronic specific heat is [28]

$$C(T) = \gamma_0 T + \delta T^3 \ln(T/T^*) + O(T^3) \tag{2.10}$$

where the Sommerfeld coefficient $\gamma_0 = C(T)/T|_{T \to 0}$ is

$$\gamma_0 = \frac{1}{3} \left(\frac{k_\mathrm{B}}{\hbar} \right)^2 k_\mathrm{F} m^* \tag{2.11}$$

where the term $\delta T^3 \ln(T/T^*)$ is large is systems close to a magnetic instability and T^* is a cutoff temperature. The electrical resistivity varies as

$$\rho(T) = \rho_0 + AT^2 \tag{2.12}$$

where ρ_0 is the residual resistivity and the prefactor A reflects the quasiparticles-quasiparticles scattering cross-section which results in $A \propto (m^*)^2 \propto \gamma_0^2 \propto N(E_F)^2$. Therefore, in HF systems, A takes values of four to six orders of magnitude larger than in a normal metal [29]. Experimentally, it was found that for the most HF compounds A is related to γ by the empirical Kadowaki-Woods relation: $A/\gamma_0^2 \approx 10^{-5} \mu\Omega\mathrm{cm(mol\ K/mJ)}^{-2}$ [30].

2.2.2 Kondo effect

The Kondo problem goes back to the experimental observation by de Haas *et al.* [31] of a resistivity minimum at low temperatures in Au diluted with Fe magnetic impurities. The resistivity minimum was successfully explained by Jun Kondo in 1964 [32]. Using perturbation theory he explained the upturn of the resistivity at low temperatures by considering the scattering of the conduction

electrons on a single magnetic ion embedded in a non-magnetic sea of conduction electrons. The theory gives a $-\ln T$ contribution to the resistivity which, added on the phononic T^5 contribution, yields a minimum at a certain temperature. This effect has come to be known as the Kondo effect. The single-impurity Kondo effect is observed in diluted alloys with a small amount of $3d$ or $4f$ impurities, in which the magnetic moments do not, directly or indirectly, interact due to the large distance between them. The theoretical estimations made by Kondo are valid only above a characteristic temperature, which is know as the Kondo temperature T_K. Below T_K, Kondo's prediction leads to an unphysical result, namely the resistance diverges as $T \to 0$. There are two theoretical models that are used to tackle this problem: the $s-d$ hamiltonian, where d represents either d or f orbitals, and the Anderson model [33, 23]. In the $s-d$ model, a magnetic impurity is described by a local spin S coupled by an exchange interaction constant J to the conduction electrons of the host metal. The low temperature behavior was solved by Wilson using renormalization-group technique [34]. Later on, Wiegmann and Andrei found the exact solution of the $s-d$ model with spin $S = 1/2$ using the Bethe ansatz [35, 36]. Within this framework, the exact solution at $T = 0$ consists in a non-magnetic spin-singlet state formed by an antiparallel coupling between the impurity spin and the conduction electron spins. The characteristic energy scale can be estimated to be

$$k_{\mathrm{B}} T_K \propto \frac{1}{N(E_F)} \exp\left(-\frac{1}{|J|\, N(E_F)}\right), \tag{2.13}$$

where k_{B} is the Boltzmann constant. Note that the Kondo temperature is not a phase transition temperature, but rather a characteristic crossover.

HF systems consist often of a periodical arrangement of magnetic ions on the crystal lattice and can not be described as magnetic impurities embedded in a non-magnetic sea of conduction electrons. As a consequence of the periodicity, Bloch plane waves forms and the resistivity drops to low values after having reached a maximum (cf. left panel of Fig. 2.2) at a characteristic temperature, the coherence temperature T_{coh}. These systems are known as Kondo-lattice (KL) systems. The hybridization between the f and d electrons below T_{coh} creates a sharp peak in $N(E_F)$ (Abrikosov-Suhl resonance) which has a width proportional to $k_{\mathrm{B}} T_{coh}$, hence $m^* \propto 1/T_{coh}$. In addition, when a hybridizing f-shell is embedded into a metallic host, it is necessary to consider the ground state f-spin degeneracy $N = 2j+1$. In this limit, the N-fold degenerate Coqblin-Schrieffer model [37] and the degenerate periodic Anderson model [38] have been developed and successfully applied to rare-earth systems. The general behavior of a Kondo-lattice system at low temperature is summarized in Fig. 2.2, which shows the resistivity $\rho(T)$, magnetic susceptibility $\chi(T)$ and specific heat $C(T)$. For $T > T_{coh}$ the Kondo effects is responsible for the logarithmically increase of $\rho(T)$ with decreasing T. At $T \approx T_{coh}$

coherence effects start to dominate and $\rho(T)$ drops steeply. A quadratic temperature dependence of $\rho(T)$ at the lowest temperatures is expected because of the FL ground state. Because of local moment ions, at high temperatures $\chi(T)$ follows a Curie-Weiss behavior and flattens to a constant value χ_0 at $T << T_{coh}$ which is the renormalized Pauli susceptibility. At low temperatures, below T_{coh}, the electronic specific heat coefficient $C(T)/T$ increases due to the formation of the resonance peak at the Fermi level and then becomes constant with $\gamma_0 = C(T)/T|_{T\to 0} \propto \chi_0$.

2.2.3 RKKY interaction

Because of the dense periodic distribution of magnetic ions in KL systems, the distance between the neighboring magnetic moments is small compared to the distance in diluted Kondo systems. Although the direct interactions between the $4f$ moments are negligible, they can interact via polarization of the conduction electrons. This indirect exchange interaction was first proposed by Ruderman and Kittel [39] and later considered by Kasuya and Yosida, and now it is generally know as the RKKY interaction. The indirect exchange interaction is defined as

$$J^2 N(E_F)\cos(2k_F r)/r^3. \tag{2.14}$$

It has to be noted that here J is the same exchange interaction constant as considered for the Kondo effect. This creates an oscillating interaction (depicted in the left panel of Fig. 2.3) where r is the distance from the local moment setting up the oscillations. The energy scale associated with this type of interaction is proportional to magnitude of the wavelength $\pi/k_F = \lambda_F/2$, which is also given by the Fermi wavelength k_F. Depending on the separation R between a pair of ions their magnetic coupling can be ferromagnetic (FM) or antiferromagnetic (AFM) (see right panel of Fig. 2.3).

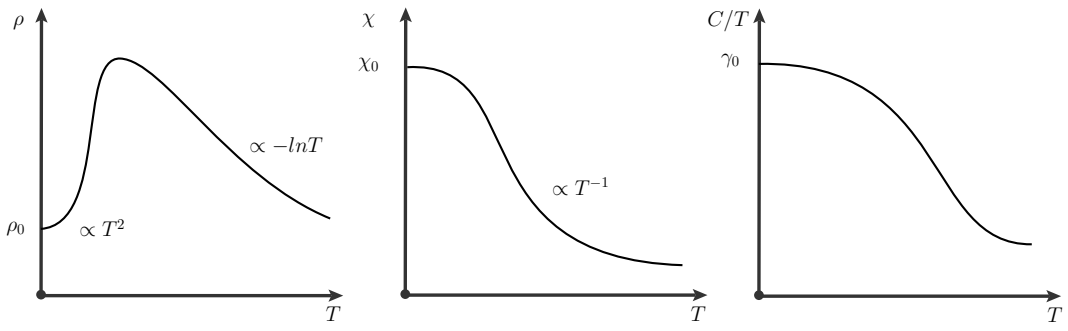

Figure 2.2 – Schematic behavior of a Kondo-lattice system at low temperature in resistivity $\rho(T)$, magnetic susceptibility $\chi(T)$ and specific heat $C(T)$.

The strength of the interaction can be expressed by the characteristic temperature

$$k_{\mathrm{B}}T_{RKKY} \propto J^2 N(E_F). \tag{2.15}$$

In Ce-based KL systems, the RKKY interaction usually promotes an AFM ground state with a Néel temperature T_N of the order of $J^2N(E_F)$, usually few Kelvins.

2.2.4 Doniach phase diagram

The competition between the Kondo screening (on-site) and the RKKY (inter-site) interactions governs the phase diagram of the Kondo lattice, since both energy scales $k_{\mathrm{B}}T_K$ and $k_{\mathrm{B}}T_{RKKY}$ depend on $|J|N(E_F)$ (cf. Eq. 2.13 and 2.15). This is schematically represented by the phase diagram in Fig. 2.4 for an AFM KL system, first proposed by S. Doniach [41]. When $|J|N(E_F)$ is small, than the $k_{\mathrm{B}}T_{RKKY}$ is the dominant energy scale and the magnetically ordered phase (MO) forms at enough low T, but when $|J|N(E_F)$ is large, $k_{\mathrm{B}}T_K$ dominates and the moments of the KL become fully screened, leaving a FL ground state. For intermediate values of $|J|N(E_F)$, where $T_K \approx T_{RKKY}$, a local maximum in the transition temperature T_m occurs and implies that there should be a critical value $J_cN(E_F)$ at which a quantum phase transition between the magnetically ordered phase and the paramagnetic one (PM) takes place. The point at $|J_c|N(E_F)$ is called quantum critical point (QCP). Except for the special case of some materials which are located exactly at the QCP, like $CeNi_2Ge_2$ [8], it is necessary to tune the system to the QCP using a non-thermal control parameter like pressure, chemical substitution or magnetic field. This phase diagram was found to describe the behavior of a large number of KL systems apart from the region close to the QCP where

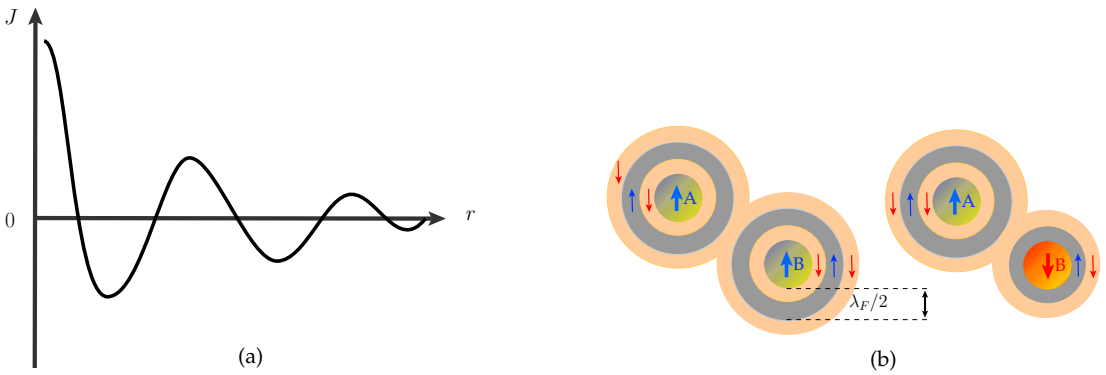

Figure 2.3 – a) Variation of the indirect exchange interaction constant J as a function of r, the distance between the magnetic atoms A and B. b) Depending on r, the magnetic coupling between the atoms can be ferromagnetic (left) or antiferromagnetic (right). Figure taken from Ref. [40].

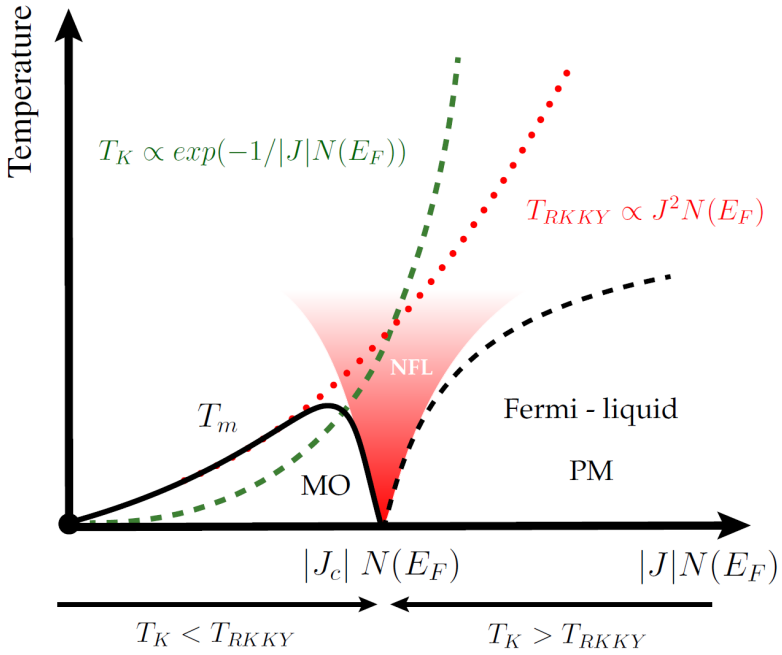

Figure 2.4 – Doniach diagram, illustrating the magnetically ordered regime at $T_K < T_{RKKY}$ and the HF non-magnetic regime at $T_K > T_{RKKY}$. At a critical concentration of the exchange interaction constant $|J_c|N(E_F)$, where $T_K \approx T_{RKKY}$, a quantum phase transition between the magnetically ordered phase (MO) and the paramagnetic one (PM) takes place. The point at $|J_c|N(E_F)$ is called quantum critical point (QCP). Experimentally, at the QCP non-Fermi-liquid (NFL) behavior is observed, caused by the magnetic quantum critical fluctuations.

pronounced deviations from the FL behavior were observed. Such deviations are a consequence of the magnetic quantum critical fluctuations present at the QCP, which break down the FL state, i.e. known as non-Fermi liquid (NFL) behavior. Experimentally, such a NFL behavior can manifest itself in, e.g., a logarithmic divergence of the specific heat coefficient or a linear temperature dependence of the resistivity [42]. Generically, in KL systems the FL ground state competes with the magnetically ordered state, but in presence of strong quantum effects or geometric frustration other ground states can also occur, like spin glass and spin liquid states [24].

2.3 Quantum phase transitions

When a system consists of more than one phase, a phase change is called phase transition (PT). It could be discontinuous, if the first derivative of the free energy $F(T, p, H)$, like the entropy, volume or magnetization, changes discontinuously

between the two phases or continuous if is the second or the third differential of F that changes abruptly. According to the Landau's theory of PTs [43], an order parameter can be defined to be zero outside one phase and finite inside the other, as schematically drawn in Fig. 2.5 (the red line is the transition boundary line). Hence, there is a spontaneous symmetry breaking at the PT between a disordered phase and an ordered one. A typical example is the PT from a paramagnetic state into a ferromagnetic one at the critical temperature T_C (in this case, the Curie temperature), where the order parameter is the magnetization. What is not

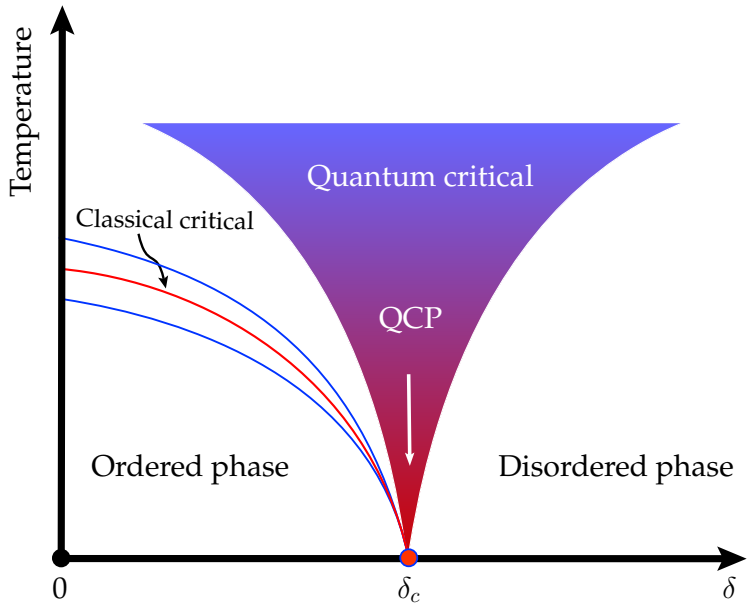

Figure 2.5 – Schematic phase diagram of a system with magnetic order at $T > 0$ that can be continuously suppressed to zero by a non-thermal control parameter δ (red line). The point where the transition temperature reaches zero is the quantum critical point (QCP). The blue lines delimit the region of strong classical/thermal critical fluctuations around the transition phase boundary line. The blue-red region indicates the quantum critical region which marks the crossover between a predominantly classical-to-quantum character of the fluctuations.

treated in this theory are correlations and fluctuations of the order parameter, which become very important near the transition temperature of continuous PTs (region delimited by the blue lines in Fig. 2.5). Here the dominant length scale which characterizes the fluctuations is the correlation length ξ which diverges at the critical point as $\xi \propto t^{-\nu}$ with $t = |T - T_C|/T_C$ and ν is the correlation length critical exponent. The order parameter fluctuates not only in space but also in time with $\xi_\tau \propto \xi^z \propto t^{-\nu z}$, where z is the dynamic critical exponent. Critical length and

time scales are the only characteristics of the system close to T_C. Therefore, the scaling is universal and depends only on the symmetry of the order parameter [44].

When the PT is induced at $T = 0$ by a non-thermal external parameter (represented in Fig. 2.5 by δ), like pressure or magnetic field, this is called quantum phase transition (QPT). A classical PT involves thermal fluctuations occurring at finite temperatures only. In the thermodynamic limit $T \to 0$, where the thermal energy scale is absent only fluctuations associated with the Heisenberg's uncertainty principle may be present. If the transition between the ordered phase and the disordered phase is continuous, those zero-point fluctuations drive the QPT which takes place at the quantum critical point (QCP), i.e. when $\delta = \delta_c$. Fluctuations can have predominantly thermal or quantum character near δ_c depending on whether their thermal energy $k_B T$ is larger or smaller than the quantum energy scale $\hbar\omega_c$. The interplay between classical and quantum fluctuations in the vicinity of a QCP is illustrated in the $T - \delta$ phase diagram of Fig. 2.5. At $\delta = 0$, classical fluctuations dominate in the vicinity of the finite phase boundary line, but this region becomes narrower with decreasing temperature and increasing δ. Quantum critical fluctuations have an effect in the quantum critical region above the QCP (blue-red region). Its boundaries are crossover lines and not phase transitions, being determined by the condition $k_B T \approx \hbar\omega_c \propto |\delta - \delta_c|^{\nu z}$. Here, the properties of a system are governed by thermal excitations of the quantum critical ground state. This can cause unusual physical properties at finite temperatures, such as unconventional power laws in thermodynamic quantities, i.e. NFL behavior, or in some cases can promote novel states of matter. Importantly, quantum ordered phases occurring at $T = 0\,\mathrm{K}$ survive to a finite temperature range. This makes empirical investigations of QPTs possible. A wide range of QPTs have been investigated, e.g in cuprate superconductors, which can be tuned from a Mott insulating state into a superconducting phase by a carrier doping [45, 46]. An increasing number of QPTs in HF systems, unconventional metals and insulating quantum magnets were discovered. For a comprehensive review about the state of the art of QPTs, see articles in Ref. [47]. Two main theoretical models have been developed to describe QPTs in HF systems, the "spin-density-wave" scenario and the "local quantum critical point" scenario.

2.3.1 Spin density wave scenario

The spin-density-wave (SDW) scenario, which is also known as the itinerant scenario [1, 48, 49], assumes the formation of the magnetic order in metals due to a SDW instability. The electrons which form the Fermi surface on the PM side of a QPT, namely the FL side in Fig. 2.4, retain their integrity when entering the magnetically ordered phase. Thermal and quantum fluctuations of the order parameter are considered. The traditional approach proposed by J. A. Hertz is

based on the Ginzburg-Landau-Wilson functional of the order parameter and its fluctuations, ϕ^4 theory, in $d_c^+ = d + z$ dimensions, where d is the spatial dimension [1, 5]. Meanwhile, different techniques have been used to calculate physical quantities at the SDW-QCP, like the renormalization group theory (J. A. Hertz [1] and A. J. Millis [48]), the self-consistent renormalization theory (T. Moriya [49]) and molecular field approach (G. G. Lonzarich [50]). The results are very similar in all theories since they only depend on the dimension d and the critical exponent z. The predictions for the temperature dependencies of the transport and thermodynamic properties are summarized in Tab. 2.1. The results for the uniform susceptibility are slightly different in every theory. We have included in Tab. 2.1 the predictions from Ref. [50]. Two important predictions of the SDW theory are the behavior of the phase boundary line close to δ_c

$$T_{N,C} \sim |\delta - \delta_c|^{\epsilon} \quad \text{with} \quad \epsilon = z/(d + z - 2) \tag{2.16}$$

and

$$m^* \propto |\delta - \delta_c|^{(d-z)/2} \tag{2.17}$$

showing how the effective mass of the quasiparticles diverges when approaching the QCP at the critical parameter δ_c [15]. A crucial aspect of the SDW scenario

	AFM ($z = 2$)		FM ($z = 3$)		FL
	$d = 2$	$d = 3$	$d = 2$	$d = 3$	
α/T	$1/T \log\log(1/T)$	$T^{-1/2}$	$1/T \log(1/T)$	$T^{-2/3}$	const.
C/T	$\log(1/T)$	$-\sqrt{T}$	$T^{-1/3}$	$\log(1/T)$	const.
Γ	$\frac{\log\log(1/T)}{T\log(1/T)}$	$-T^{-1}$	$T^{-2/3}\log(1/T)$	$(T^{2/3}\log(1/T))^{-1}$	const.
ρ	T	$T^{3/2}$	$T^{4/3}$	$T^{5/3}$	T^2
χ		$T^{-3/2}$	T^{-1}	$T^{-4/3}$	const.

Table 2.1 – Predictions of the SDW scenario at the QCP and of the FL theory for the thermal expansion coefficient $\alpha(T)$, specific heat $C(T)$ and thermal Grüneisen ratio $\Gamma(T)$ after Ref. [15], electrical resistivity after Ref. [49] and magnetic susceptibility $\chi(T)$ after Ref. [50]. Only the critical contributions are considered.

in HF systems is that the Kondo energy scale remains finite at the QCP [14], implying that the heavy quasiparticles survive near the QCP. Therefore, for such a transition one does not expect the Kondo energy scale to change significantly while the system is tuned through the QCP by varying the control parameter. A schematic phase diagram of this scenario is shown in Fig. 2.6 (right panel), where the characteristic energy scale T_0 represents the Kondo temperature [14].[1]

[1] For $T \gg T_0$ the Kondo lattice behaves as individual local moments, following the Curie-Weiss behavior.

There are indeed few HF compounds that can be well described by the SDW scenario, like $CeNi_2Ge_2$ [8] or $CeCu_2Si_2$ [9]. But in other HF systems, that have been strongly investigated in the proximity of a QCP, this theory fails. Prototypical examples of HF system which do not fit into the SDW scenario are $YbRh_2Si_2$ and $CeCu_{6-x}Au_x$ which both show evidence of an AFM-QCP. It has been shown that at the QCP in $CeCu_{6-x}Au_x$ with $x = 0.1$ the magnetic correlations have surprisingly local character and that the dynamical susceptibility $\chi''(\omega, \mathbf{q})$ shows ω/T scaling which is not expected in the SDW theory [11]. It has been also found that at the pressure-induced QCP in $CeRhIn_5$ [12] and at the magnetic field-induced QCP in $YbRh_2Si_2$ [13], the Kondo effect breaks down, causing an abrupt change of the Fermi surface. None of these properties is predicted by the SDW scenario. Recently, new theories have been developed, which can model many of the newly observed features, and are known as local QCP scenario.

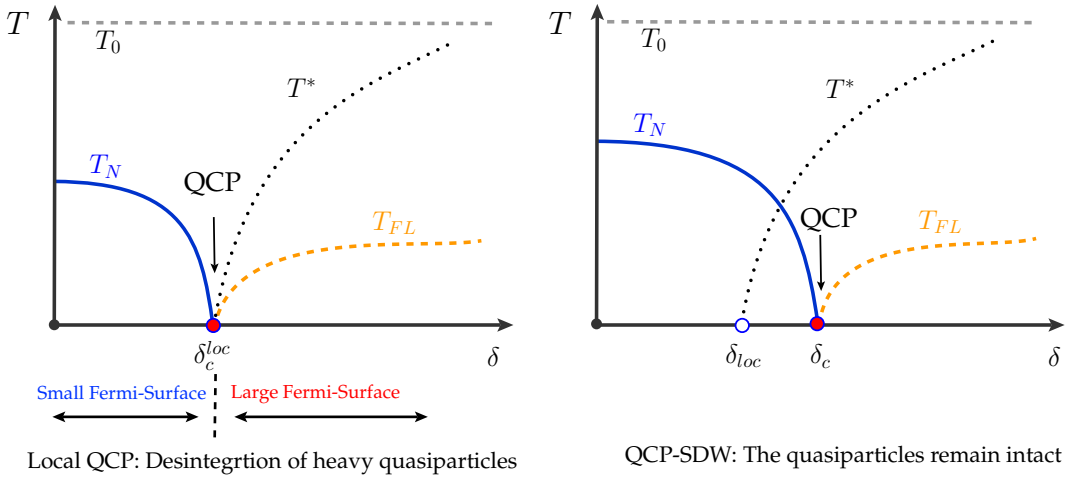

Figure 2.6 – Schematic phase diagrams for the two types of AFM quantum critical scenarios for HF systems. Left: The Kondo breakdown scenario [51, 52]. Right: The SDW scenario [1, 48, 49]. T_N represents the AFM ordering temperature, T_{FL} indicates the onset of the low temperature Fermi liquid regime and δ is the control parameter. T_0 represents the characteristic energy scale (the Kondo temperature), signifying the crossover from the high temperature incoherent state of local moments to the low temperature state in a Kondo lattice systems where moments are partially screened. The T^* energy line marks the crossover line between the local moments ($\delta < \delta_c$) and the quasiparticles ($\delta > \delta_c$) which are part of the Fermi surface. In fact, this energy scale separates the small and large Fermi surfaces.

2.3.2 Local quantum critical point scenario

In the SDW scenario of quantum criticality, the quasiparticle system undergoes a SDW instability at the QCP and the Kondo energy scale remains finite across the quantum phase transition. Recently, however, experimental results have indicated that the signature of heavy quasiparticles does not survive near the QCP [13, 12]. These discoveries have promoted theoretical descriptions which include the destruction of the Kondo effect at the QCP [51, 52, 53, 54, 55, 56]. The term "local quantum criticality" refers to the localization of the electronic excitations associated with the f-moments in which a destruction of Kondo screening of the f-moments coincides with the magnetic transition of the Kondo lattice. Thus, the breakdown of the Kondo effect at the QCP should be associated with a Fermi surface instability. Originally, based mainly on results from $YbRh_2Si_2$ [57], the nature of the Kondo breakdown was suggested to involve multiple energy scales. These multiple energy scales collapse to zero as the system is tuned through the QCP and it has been proposed that the Fermi surface changes from a large to a small one when the QCP is crossed from the paramagnetic side [14]. This is represented in Fig. 2.6 (left panel). The line associated with the energy scale T^* separates the incomplete Kondo screened state (left side of T^*) and complete Kondo screened state (right side of T^*). Thus, the T^* line marks the crossover from small to large Fermi surface: In fact, in the left side of T^* the local moments do not participate in the Fermi surface formation. This is different from what is expected in the SDW scenario, as shown in the right panel of the same figure [14]. Here, the T^* line has to vanish somewhere inside the AFM region of the phase diagram, but not at the QCP.

2.3.3 Global phase diagram

In the last years, new perspectives where proposed about the mechanism behind quantum criticality in HF systems, including the idea of a global phase diagram [58, 59, 60]. The scientific breakthrough was a work done on Ir- and Co-substituted $YbRh_2Si_2$ by Friedemann *et al.* [61]. The main results of this work are schematically summarized in the magnetic phase diagrams of Fig. 2.7. They represents the evolution of the fundamental energy scales in this systems, the AFM ordering temperature $T_N(H)$, the Kondo-destruction $T^*(H)$ crossover line, and the FL region below $T_{FL}(H)$ (the tuning parameter is here the magnetic field H). These scales were evidenced by several thermodynamic and transport measurements [57]. In $YbRh_2Si_2$ all energy scales converge to a single critical field at $T = 0$. In the Ir-substituted sample, T_N is suppressed, whereas in the Co-substituted sample T_N is enhanced. Surprisingly, the T^* scale does not change the position in the phase diagram in both systems. Therefore, it was inferred

that T^* is separated from T_N in $Yb(Rh_{0.94}Ir_{0.06})_2Si_2$, whereas T^* intersects T_N in $Yb(Rh_{0.93}Co_{0.07})_2Si_2$. Interestingly, both T^* and T_{FL} in the Ir- and Ge-substituted samples are separated from T_N [63, 62]. The NFL region between these energy scales has been proposed to have a spin-liquid ground state. The important point is that the Kondo-destruction energy scale seems not to be linked to the QCP, and in a KL system different QCPs are possible, which can be of SDW or local nature.

In two independent works, Q. Si and P. Coleman *et al.* proposed a possible explanation considering an extension of the Doniach phase diagram to a more "global phase diagram" for KL systems [58, 59, 60]. The phase diagram based on calculations on the AFM Kondo lattice by Q. Si [58] is shown in Fig. 2.8. This diagram has two parameters: The vertical axis is parametrized by $\mathcal{G}$ which characterizes the degree of quantum fluctuations or magnetic frustration of the local moments. Therefore increasing $\mathcal{G}$ reduces the T_N. The horizontal axis describes the strength of the Kondo coupling $\mathcal{J}_K$ between the local moments and the conduction electrons. It controls the degree of quantum fluctuations due to the spin-flip process associated with the Kondo coupling. The AF_S phase describes the small-Fermi surface AFM state and the AF_L correspond to the AFM state in presence of a Kondo

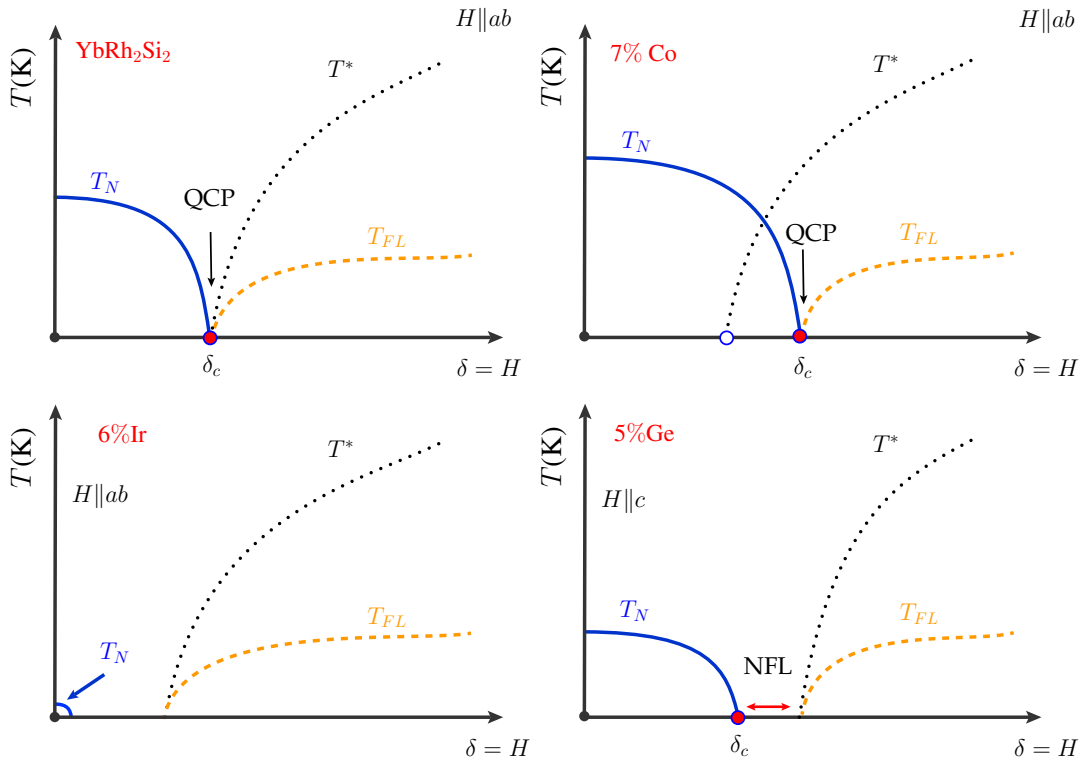

Figure 2.7 – Schematic $H-T$ phase diagrams of stoichiometric, Ir-, Co- and Ge- doped $YbRh_2Si_2$. These phase diagrams were taken from Refs. [61, 62].

screening. The P_L phase is the heavy Fermi liquid state with heavy quasiparticles and large Fermi surface, while the P_S phase is the paramagnetic state with small Fermi surface. The red line represents the line of QCPs of SWD nature while the blue line represents the QCPs of local nature. According to this, there are three possible routes for a system to go from the AF_S phase to the P_L phase:

- The transition between AF_S and P_L gives rise to a local QCP. A critical Kondo breakdown occurs at the AF QCP, giving rise to a sudden change of the Fermi surface and the vanishing of a Kondo-breakdown scale. This describes the case of stoichiometric $YbRh_2Si_2$.
- Trajectory $AF_S \rightarrow AF_L \rightarrow P_L$ describes the case of $Yb(Rh_{0.93}Co_{0.07})_2Si_2$ where the Kondo breakdown takes place inside the AFM phase and the Fermi surface changes not suddenly but like in a Lifshitz transition. The QCP at the $AF_L - P_L$ boundary falls in the SDW type.
- The $P_S - P_L$ transition could describe a spin liquid to heavy Fermi liquid QCP, like in the case of $Yb(Rh_{0.94}Ir_{0.06})_2Si_2$.

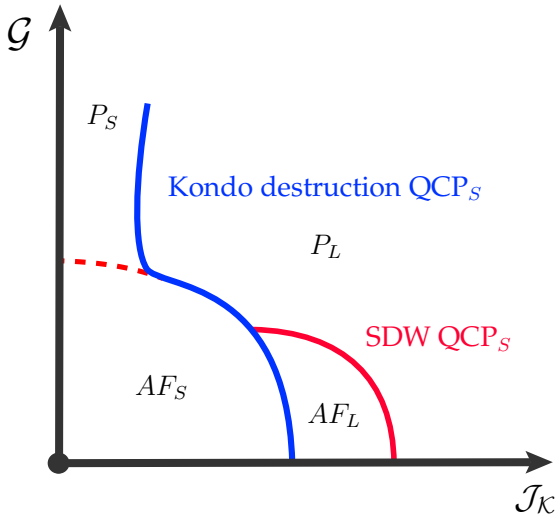

Figure 2.8 – Proposed theoretical phase diagram at $T = 0$ for AFM Kondo lattices [60]. $\mathcal{G}$ is a measure of the degree of quantum fluctuations or magnetic frustration. $\mathcal{J}_K$ describes the strength of the Kondo coupling between the local moments and the conduction electrons. The AF_S phase describes the small-Fermi surface AFM state and the AF_L correspond to the AFM state in presence of a Kondo screening. The P_L phase is the heavy Fermi liquid state with heavy quasiparticles and large Fermi surface, while the P_S phase is the paramagnetic state with small Fermi surface. The red line represents the line of QCPs of SWD nature while the blue line represents the QCPs of local nature.

A similar phase diagram is described by P. Coleman *et al.* in Ref. [59], where on the horizontal axis the parameter T_K/J is considered.

2.3.4 The Grüneisen ratio

The Grüneisen ratio has been successfully used as a tool for the identification of QCPs [8, 15, 64, 65]. The thermal Grüneisen ratio Γ is simply defined as ratio between the thermal expansion coefficient α and the molar specific heat C_p

$$\Gamma = \frac{\alpha}{C_p} = -\frac{(\partial S/\partial p)_T}{V_m T(\partial S/\partial T)_p} \tag{2.18}$$

where S is the entropy, V_m the molar volume and p the pressure. For a pressure-tuned quantum phase transition, the control parameter r can be linearized around the critical pressure $r = (p - p_c)/p_c$. The ratio $(\partial S/\partial p)_T = p_c^{-1}(\partial S/\partial r)_T$ explores then the dependence of the entropy on r. The corresponding quantity for a transition tuned by a magnetic field H with $r = (H - H_c)/H_c$ is $(\partial S/\partial H)_T = (\partial M/\partial T)_H$, were M is the total magnetization. We thus define the magnetic Grüneisen ratio as

$$\Gamma_H = -\frac{(\partial M/\partial T)_H}{C_H} = -\frac{1}{T}\frac{(\partial S/\partial H)_T}{(\partial S/\partial T)_H} = \frac{1}{T}\frac{\partial T}{\partial H}\Big|_S \tag{2.19}$$

which can be determined from the magnetocaloric effect, or measuring the magnetization *M(T)* and the specific heat *C(T)* separately.

In the work by L. Zhu *et al.* [15] it was demonstrated that, if scaling applies, when approaching a p-induced QCP the T-dependent Grüneisen ratio $\Gamma(T)$ diverges with the inverse of the control parameter

$$\Gamma(T \to 0, r) = -G_r \frac{1}{V_m(p - p_c)} \tag{2.20}$$

and at the critical pressure

$$\Gamma(T, r = r_c) = -G_T T^{-1/\nu z} \tag{2.21}$$

where the parameters ν (the correlation length exponent) and z (the dynamical critical exponent) are universal and depend only on the dimensionality of the critical fluctuations d and their nature ($z = 2$ for AFM and $z = 3$ for FM fluctuations). In addition, also the prefactors G_r and G_T depend strictly on these parameters. In other words, the temperature exponent of the Grüneisen ratio provides a direct means to measure νz and, as a result characterizes the nature of a QCP. For Γ_H with $r = (H - H_c)/H_c$ we have similar equations

$$\Gamma_H(T \to 0, r) = -G_r \frac{1}{(H - H_c)} \quad , \quad \Gamma_H(T, r = r_c) = -G_T T^{-1/\nu z}. \tag{2.22}$$

Again, in the $T \to 0$ limit, the prefactors are universal. As discussed in Refs. [15, 65] scaling is applicable under certain conditions: i) The system is dominated by a single energy scale E^*; ii) Sometimes non-critical contributions can dominate, like in the case of a AFM SDW QCP (see tab. 2.1). These contributions have to be carefully subtracted; iii) At the QCP more than a single diverging time scale can be present. This can indeed lead to a breakdown of simple scaling relations [66].

2.4 Spins are almost bosons

QPTs are intensively studied not only in metallic systems. Insulators show QPTs of different types. One of the most prominent example is the QPT in the dipolar-coupled Ising ferromagnet $LiHoF_4$ ($T_c = 1.53\,K$) driven by a transverse magnetic field at $T = 0$ [67]. There is another class of materials where a QPT is induced by the magnetic field: Low dimensional quantum magnets. Among them, dimer-based antiferromagnets [68] and quasi 1D arrangements of spin $S = 1$ (e.g., Haldane chains [69]). The central characteristic of these magnets is that they possess a non magnetic spin singlet ($S = 0$) ground state separated from the first excited triplet ($S = 1$) state by an energy gap Δ (see Fig. 2.9). The magnetic field eventually

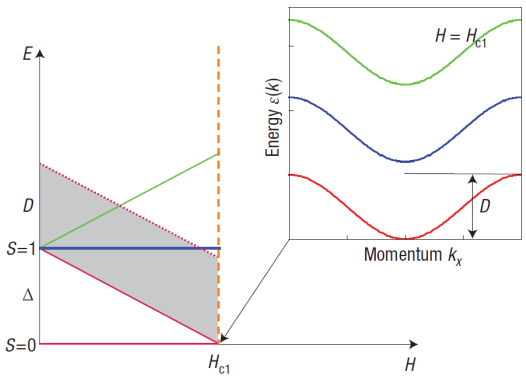

Figure 2.9 – Schematic representation of the Zeeman splitting of the triple modes with gap Δ and bandwidth D. At the field H_{c1} a field induced Bose-Einstein condensation of magnons occurs. The inset represents the triplons dispersion at H_{c1}. Figure taken from Ref. [70].

closes the gap at a critical field H_{c1} inducing a QPT into a XY AFM ordered state with finite magnetization and AFM magnon excitations. During the last decade, these materials have attracted much interest because the AFM ordering can be described as a Bose-Einstein condensation (BEC)[2] of magnons by mapping the spin-1 system into a gas of hardcore bosons [71]. These type of bosons can

[2]Bose-Einstein condensation occurs when the temperature of a gas of integer-spin particles (bosons) is low enough and thermodynamics causes a significant fraction of them to spontaneously enter a single quantum state. These particles form the condensate and they act collectively as a coherent classical wave.

undergo BEC and become superfluid. In this respect, the magnetic field acts as a chemical potential and tunes the boson density.

The first theoretical investigation of a possible BEC of magnons in quasi-one-dimensional systems was discussed by E. G. Batyev and L. S. Braginskii [72], and I. Affleck [73]. More than fifteen years later, field-induced antiferromagnetic order was observed experimentally in the gapped $S = 1/2$ dimer compound $TlCuCl_3$ [74, 68, 75] (see the Review article [76] by Giamarchi *et al.* and references therein). The magnetization measurements have shown that the magnetic subsystem of $TlCuCl_3$ consists of weakly antiferromagnetically coupled $S = 1/2$ spin dimers and the first excited state is separated from the ground state singlet by the energy gap $\Delta \approx 0.7$ meV. The QCP is at $H_{c1} \approx 5.7\,\mathrm{T}$. A series of experimental works could confirm the applicability of the BEC in this material and in many other quantum magnets with lattices of dimerized $S = 1/2$ Cu^{2+} (e.g., $BaCuSiO_6$ [77], $KCuCl_3$ [78], $TlCuCl_3$ [75, 68]) or $S = 1$ Ni chains (e.g., $Ni(C_5H_{14}N_2)_2N_3(PF_6)$ [79], $NiCl_2$-$4SC(NH_2)_2$ [80, 81, 82]). The correspondence between a Bose gas and a quantum antiferromagnet is given in Tab. 2.2 [76]. The general phase diagram of such materials is schematically represented in Fig. 2.10.

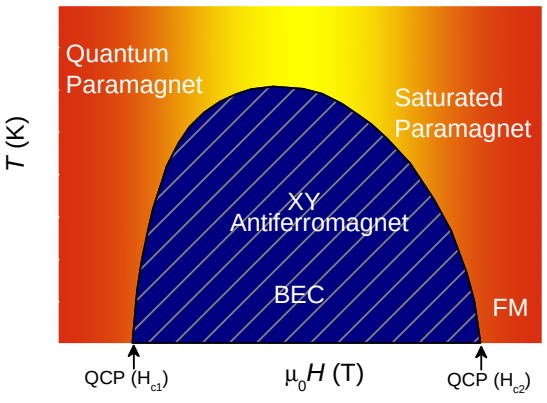

Figure 2.10 – Schematic phase diagram of a gapped quantum magnet. The phase boundary line divides the quantum paramagnet from the XY AFM ordered phase, i.e. the BEC. The magnetic field H induces two QPTs at H_{c1} and H_{c2}. The shape of the phase boundary line close to these critical fields is important to determine the nature of the ordered ground state.

Bose gas	Antiferromagnet
Bosons	Magnons
Boson number N	Spin component S^z
Charge conservation $U(1)$	Rotational invariance $O(2)$
Condensate wave function $\psi_i(r)$	Transverse magnetic order $\langle S_i^x + iS_i^y \rangle$
Chemical potential	Magnetic field

Table 2.2 – Correspondence between a Bose gas and a XY quantum antiferromagnet. Table taken from Ref. [70].

The starting point is the spin Hamiltonian of the magnetic system. In Chapter 5, the field-induced QCP of the quantum magnet $NiCl_2$-4SC$(NH_2)_2$, referred to as DTN, will be investigated. Therefore, we will adapt our description to the case of DTN where the magnetic Ni^{2+} ions with $S = 1$ are located on a body-centered tetragonal lattice. There is a large single-ion easy-plane anisotropy described by a parameter $D > 0$, not to confuse with the bandwidth in Fig. 2.9. Assuming $D >> J_{ij}$, which gives a non magnetic ground state at $H = 0$, the magnetic structure of DTN can be described by the Hamiltonian (the following calculations are based on Ref. [83]):

$$\mathcal{H} = \sum_{<ij>} J_{ij}\vec{S}_i\vec{S}_j + D\sum_i (S_i^z)^2 - g\mu_B\mu_0 H\sum_i S_i^z \tag{2.23}$$

where the first sum is taken over all bonds connecting the Ni sites i and j with exchange parameter J_{ij}. The magnetic field H is oriented along the single-ion anisotropy, i.e. along the crystallographic z direction, to keep the axial symmetry of the Hamiltonian. In the limit $J_{ij}/D \to 0$, the ground state of eq. 2.23 is nonmagnetic and is a direct product of spinors with $S_i^z = 0$ on each site i. The first excited state can be formed by creating a single spin excitations with $S_i^z \pm 1$ on each site i with a dispersionless spectrum (point at $H = 0$ in Fig. 2.9 and Fig. 2.11)

$$\omega_0(\vec{k}) = D.$$

We can now consider the $S_i^z \pm 1$ excitations as bosonic excitations

$$S_i^z = b_i^\dagger b_i - a_i^\dagger a_i \ , \ S_i^+ = (S_i^-)^\dagger = \sqrt{2}(b_i^\dagger + a_i) \ , \ S_i^x = \frac{1}{2}(S_i^+ + S_i^-) \ , \ S_i^y = \frac{1}{2}(S_i^+ - S_i^-)$$

where a_i and b_i are bosons representing -1 and +1 spin excitations on site i and S_i^+ either removes a down boson or creates an up boson on site i. Since we can not have more than 1 boson created at each site, we need the following constraints

$$\left\langle a_i^\dagger b_i^\dagger a_i b_i \right\rangle = 0 \quad , \quad \left\langle a_i^\dagger a_i \right\rangle \leq 1 \quad , \quad \left\langle b_i^\dagger b_i \right\rangle \leq 1,$$

which have to be fulfilled on each site simultaneously. We can formulate this with the help of an infinite repulsion U between any two bosons on each site. The Hamiltonian in Eq. 2.23 can then be mapped into the following one

$$\mathcal{H} = \sum_{<ij>} J_{ij}[(b_i^\dagger b_i b_j^\dagger b_j - b_i^\dagger b_i a_j^\dagger a_j - a_i^\dagger a_i b_j^\dagger b_j + a_i^\dagger a_i a_j^\dagger a_j) + (b_i^\dagger a_j^\dagger + b_i^\dagger b_j + a_i a_j^\dagger + a_i b_j$$
$$+ a_i^\dagger b_j^\dagger + a_i^\dagger a_j + b_i b_j^\dagger + b_i a_j)] + \sum_i (D - h_z) b_i^\dagger b_i + (D + h_z) a_i^\dagger a_i + \lim_{U\to\infty} \frac{U}{N} \sum_i (a_i^\dagger b_i^\dagger a_i b_i$$
$$+ a_i^\dagger a_i^\dagger a_i a_i + b_i^\dagger b_i^\dagger b_i b_i)$$

with $h_z = g\mu_B\mu_0 H$. This equation can be simplified if we consider that a -1 boson has a potential energy of an amount $(D + h_z)$ and we can therefore neglect the term $a_i^\dagger a_i$ and the three terms in the first part of the equation.

There are many ways to proceed. The goal is to obtain a description that can be used to fit the experimental measurable, in particular of the DTN compound. Assuming a low density of bosons, i.e. low temperature, we might transform our Hamiltonian into a Schwinger boson Hamiltonian [84] with new operators α and β which are boson fields corresponding to a spin down and up excitation. The resulting Hamiltonian is

$$\mathcal{H} = \tilde{E}_0 + \frac{1}{N}\sum_{\vec{k}}[(\omega(\vec{k}) - h_z)\beta_{\vec{k}}^\dagger\beta_{\vec{k}} + (\omega(\vec{k}) + h_z)\alpha_{\vec{k}}^\dagger\alpha_{\vec{k}}]$$

with ground state energy $\tilde{E}_0$ and parameters

$$\tilde{E}_0 = (\lambda - D)(s^2 - 1) + \frac{1}{N}\sum_{\vec{k}}[\omega(\vec{k}) - \lambda - s^2 J(\vec{k})] \tag{2.24}$$

$$\omega(\vec{k}) = \sqrt{\lambda[\lambda + 2s^2 J(\vec{k})]} \tag{2.25}$$

$$s^2 = 2 - \frac{1}{N}\sum_{\vec{k}}\frac{\lambda + s^2 J(\vec{k})}{\omega(\vec{k})} \tag{2.26}$$

$$D = \lambda(1 + \frac{1}{N}\sum_{\vec{k}}\frac{J(\vec{k})}{\omega(\vec{k})}) \tag{2.27}$$

$$J(\vec{k}) = \frac{1}{2}\sum_n J_n e^{i\vec{k}\vec{R}_n}. \tag{2.28}$$

Here, $J(\vec{k})$ is the dispersion of the spin excitations (Fourier transform of the exchange part of the Hamiltonian 2.23), $\vec{R}_n$ is the vector connecting a fixed site i with its neighbor site n, λ and s are variables that have to be determined self-consistently [84]. Meaningful results are obtained when $\lambda \approx D$ and $s \approx 1$. The magnetic field acts as chemical potential and when its energy is equal to the value of the excitation gap $\omega(\vec{Q}) - h_z$ ($\vec{Q}$ is the minimum position in $\vec{k}$ space), the system undergoes the QPT from a quantum paramagnetic to the 3D antiferromagnetically ordered state.

In the bosonic representation, this process can be viewed as a condensation of magnons carrying $S = 1$, obeying Bose-Einstein statistics [73, 85]. In spin space, the field-induced Bose-Einstein condensation of magnons corresponds to the order of the transverse spin components, perpendicular to the applied field, which spontaneously brakes the $O(2)$ symmetry of the Hamiltonian Eq. 2.23. The universality

class of the QCP can be determined by measuring the temperature dependence of thermodynamic quantities like the magnetization $M(T)$ or the specific heat $C(T)$ and the shape of the phase border line at the QCP [68]. Tab. 2.3 displays the expectation exponents for a XY antiferromagnet and the Ising QCP, both in three dimensions ($d = 3$). The BEC of magnons belongs to the 3D XY universality class with $d = 3$ and dynamical exponent $z = 2$.

Thermodynamics

Considering the partition function of the grand-canonical ensemble for noninteracting bosons

$$\mathcal{Z} = \prod_{i=1}^{\infty} \sum_{\nu_i=0}^{\nu_i^{max}} e^{-\frac{\nu_i(E_i-\mu)}{k_B T}} \tag{2.29}$$

where μ is the chemical potential, E_i the energy of the particles and ν_i their occupation number. For a system of bosons[3] we have $\nu_i^{max} = \infty$, then

$$\mathcal{Z} = \prod_{i=1}^{\infty} \frac{1}{1 - e^{-\frac{(E_i-\mu)}{k_B T}}}. \tag{2.30}$$

The free energy is therefore

$$F = -k_B T \ln(\mathcal{Z}) = -k_B T \sum_{i=1}^{\infty} \ln\left(1 - e^{-\frac{(E_i-\mu)}{k_B T}}\right)^{-1} = -k_B T \sum_{i=1}^{\infty} \ln Z_i. \tag{2.31}$$

[3] Fermions have $\nu_i^{max} = 1$

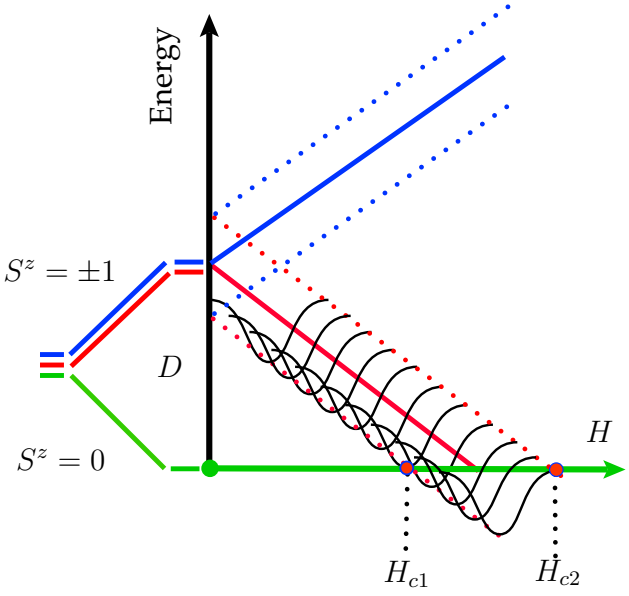

Figure 2.11 – Schematic representation of the Zeeman splitting of the $S^z = \pm 1$ excited states of Ni^{2+}-based quantum magnet like DTN. D is the single-ion anisotropy dominant energy, H_{c1} and H_{c2} are the critical fields which define the range of the XY AFM order (BEC phase), the black lines represents the dispersion of magnons.

In our case, the bosons are labeled by their crystal momentum $\vec{k}$ and in the continuum limit we can write

$$F = k_{\mathrm{B}}T \frac{1}{V_{Br.}} \int\limits_{1^{st}Br.} \ln(1 - e^{-\frac{(E_i-\mu)}{k_{\mathrm{B}}T}}) d^3k \tag{2.32}$$

and the integration is restricted to the first Brillouin zone. From the free energy relation, we can derive all thermodynamic quantities like, for instance, the magnetization and the heat capacity:

$$\begin{aligned} M &= -\frac{1}{V}\left(\frac{\partial F}{\partial B}\right) = -\frac{1}{V}\sum_i n(E_i)\frac{\partial E_i}{\partial B}, \\ C_V &= 2k_{\mathrm{B}}T\sum_i \frac{\partial \ln Z_i}{\partial T} + k_{\mathrm{B}}T^2 \sum_i \frac{\partial^2 \ln Z_i}{\partial T^2} \end{aligned} \tag{2.33}$$

where $H = B/\mu_0$ is the applied magnetic field and $n(E)$ is the Bose distribution function

$$n(E) = \left(e^{\frac{E_i-\mu}{k_{\mathrm{B}}T}} - 1\right)^{-1}.$$

For $J/D << 1$ we obtain

$$\begin{aligned} \omega(\vec{k}) &= D + J(\vec{k}) \\ J(\vec{k}) &= J_{\parallel}\cos k_z + J_{\perp}(\cos k_x + \cos k_y) \end{aligned} \tag{2.34}$$

assuming the body-centered tetragonal lattice of DTN and a cosine form of the dispersion [82, 86]. At low temperatures, only the up bosons at the dispersion minima ($k = \pm\pi$) contribute to the thermodynamic sum. Considering $\partial E_i/\partial B = \partial\omega(\vec{k})/\partial B = -g\mu_{\mathrm{B}}$, we can evaluate the average magnetic moment

$$m = (B,T) = \frac{V}{N}\cdot\frac{M}{g\mu_{\mathrm{B}}} = \frac{1}{V_{Br.}} \int\limits_{1^{st}Br.} d^3k\; n\left(\omega(\vec{k}) - h_z\right). \tag{2.35}$$

Thermodynamic variable	XY-AFM (BEC)	Ising-AFM
$M(H_c,T)$	$T^{3/2}$	T^2
$C(H_c,T)$	$T^{3/2}$	T^3
Phase line	$T_c \propto (H-H_c)^{2/3}$	$T_c \propto (H-H_c)^{1/2}$

Table 2.3 – Temperature dependencies of the thermodynamic quantities: magnetization $M(T)$ and specific heat $C(T)$ at the field induced QCP. The exponents are given for $d = 3$.

Considering Eqs. 2.34, the magnetization is small but finite for fields $H < H_{c1}$. Moreover, we know that in the DTN compound $J_\perp \approx 0$, i.e. $J_\perp << k_\mathrm{B}T$ and $J_\parallel$. We can then write

$$m(B,T) \approx \frac{1}{2\pi} \int_{-\pi}^{\pi} dk \left[e^{\frac{1}{k_\mathrm{B}T}(J_\parallel \cos(k) + D - h_z - \mu)} - 1 \right]^{-1}. \tag{2.36}$$

In the range $J_\perp << k_\mathrm{B}T << J_\parallel$ the magnetic moment is linear in T ($m(T) \propto T$), while at lower temperature $m(T) \propto T^{3/2}$. Fig. 2.12 shows the temperature dependence of the magnetic moment at a field slightly below the critical field H_{c1} calculated from Eq. 2.36.

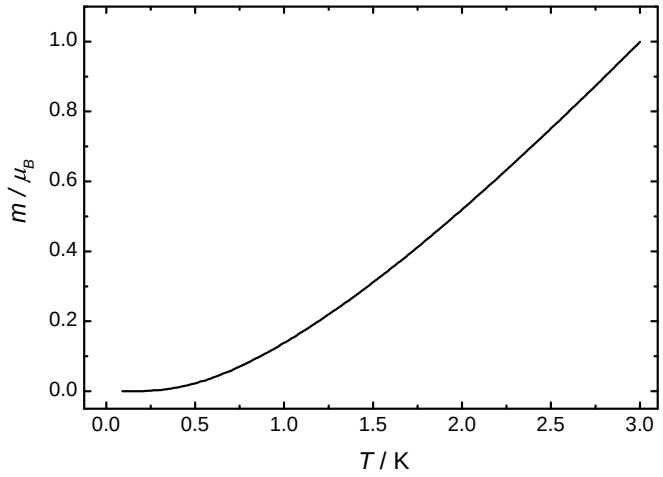

Figure 2.12 – Temperature dependence of the magnetic moment at a field slightly below the critical field H_{c1} calculated with the equation 2.36 and parameters: $D = 8.9\,\mathrm{K}$, $J_\parallel = 2.2\,\mathrm{K}$, $J_\perp = 0.18\,\mathrm{K}$, $g = 2.26$ valid for DTN [82, 86].

3 Experimental methods

Magnetic units Since we use magnetization measurements as a main characterization technique, it is instructive to give a brief survey of the magnetic units. In this context, it is interesting to read the publication of William Fuller Brown Jr. [87] and Bennetts *et al.* [88] where the authors explain the use and removal of various systems of units in the history of physics and technology. The magnetic flux density is measured in the SI unit system in Tesla (T), where 1 T = 1 Vs/m^2. In the cgs system, this corresponds precisely to 104 Gauss (G). The vacuum permeability in the cgs system is $\mu_0 = 1$, therefore the magnetic flux density B and the magnetic field H are used interchangeably. In fact, in the past, the magnetic field was measured in Gauss, until in 1928 the Oersted (Oe) was introduced as a new equivalent unit for the magnetic field. In the SI system the vacuum permeability is $\mu_0 = 4\pi \cdot 10^{-7}$ Vs/Am and we measure the magnetic field H in A/m. One A/m in vacuum is exactly $4\pi \cdot 10^{-7}$T. This is in the cgs system $4\pi \cdot 10^{-3}$ G or $\approx 1/80$ Oe.

The magnetization M is related to the magnetic induction by $B = \mu_0(H + M)$ in the SI-system, with M measured in A/m. In contrast, in the cgs system it is $B = H + 4\pi M$, therefore 1 A/m for M in SI corresponds to 10^{-3} G. The magnetic moment μ is measured in the SI system in Am^2. This is 1 Am^2 = 1 J/T $\approx 10^{23}\mu_B$. This is equal in cgs system to 10^3 erg/G or 10^3 emu. "Emu" is the so-called electromagnetic unit and is equivalent to 1 erg per Gauss. In this thesis the SI system is used. The susceptibility will be presented in m^3/mol, and the magnetization in μ_B per magnetic atom.

3.1 Magnetization

A magnetic moment μ in an externally-produced magnetic field $\boldsymbol{B}$ has a potential energy

$$E_p = -\mu \cdot \mathbf{B} \tag{3.1}$$

From this the units of the magnetic moment are J/T (emu in cgs). The magnetic moment of atoms or molecules is often quoted in terms of the Bohr magneton which is equal to the magnetic moment due to electron spin

$$\mu_B = \frac{eh}{4\pi m_e} = 9.27 \times 10^{-24}\,\mathrm{J/T}.$$

Material/Ordering	χ
Vacuum	0
Diamagnetic	Small and negative
Paramagnetic	Small and positive
Antiferromagnetic	Small and positive
Ferromagnetic	Large and positive
Ferrimagnetic	Large and positive

Table 3.1 – Variation of the susceptibility χ with the type of material and magnetic ordering.

The magnetization $\boldsymbol{M}$ is the vector field that expresses the density of permanent or induced magnetic moments in a magnetic material. The origin of the magnetic moments responsible for magnetization is microscopic, due to electric currents resulting from the motion of electrons in atoms.

The volume magnetization M, is a measure of the magnetic moment per unit volume

$$M = \frac{\mu}{V}. \tag{3.2}$$

How a material responds under the influence of a magnetic field is quantified by the susceptibility χ, which is the variation of the magnetization with an applied field

$$\chi = \frac{M}{H}. \tag{3.3}$$

The susceptibility of a material depends on its magnetic characteristics. Table 3.1 gives an indication of how χ varies with the type of material and magnetic ordering (if any).

3.1.1 Magnetization measurements

Magnetization is a key thermodynamic quantity for the study of condensed matter. Although neutron scattering (NS) is the right technique to image bulk excitations, magnetization measurements are essential to provide the field parameters and temperature range to search for such excitations. In other words, we may need magnetization measurements in order to know what we want to measure by NS spectroscopy. Magnetization measurements include a large range of different techniques (see Fig 3.1) depending on the temperature range and the type of material. We can divide magnetization measurements initially in two types: bulk and surface. The former case can be subdivided in local and global techniques. The local type includes:

- Muon spin Rotation (μSR)
- Mössbauer Spectroscopy
- Electron paramagnetic resonance (EPR)
- Nuclear magnetic resonance (NMR)
- Nuclear quadrupole resonance (NQR)

and the global techniques with which we investigate macroscopically the sample, include:

- Inductively coupled techniques
- Force methods.

On the other hand, the surface techniques include:

- Hall probe, SQUID on tip, etc.

The force techniques are the Gouy method and the Faraday magnetometer. Magnetization data in this thesis have been obtained using a MPMS SQUID (Quantum Design) and a high-precision Faraday magnetometer mounted in a ^{4}He-^{3}He dilution refrigerator. The theoretical principles of the Faraday magnetometer are outlined in Section 3.2.1 and its construction details in Section 3.2.1.3.

Among the various methods [89] inductive ones (sample extraction, VSM and field modulation techniques) are most commonly used for the magnetization measurements with a superconducting magnet. Except for the field modulation technique one must move the sample inside of a pick-up coil to drive a time varying magnetic flux. This action becomes a problem in the mK temperature regime because it produces heat and warms-up the sample. With the field modulation technique (AC method) one measures the differential susceptibility as a function of the applied field. This technique is usually used at low temperatures since the sample is not moved during the measurement.

The main advantage of the Faraday magnetometer compared to other methods is that the temperature of the sample can be exactly estimated due to the good thermal coupling with the mixing chamber and high magnetic fields can be used (up to 12 T). The infinitesimal displacement of the sample can be monitored by a capacitive cell. Such capacitive cell can be made from non-magnetic materials, simplifying the analysis of the data, since only a diamagnetic contribution needs to be subtracted. Another important advantage is that the sample can be easily

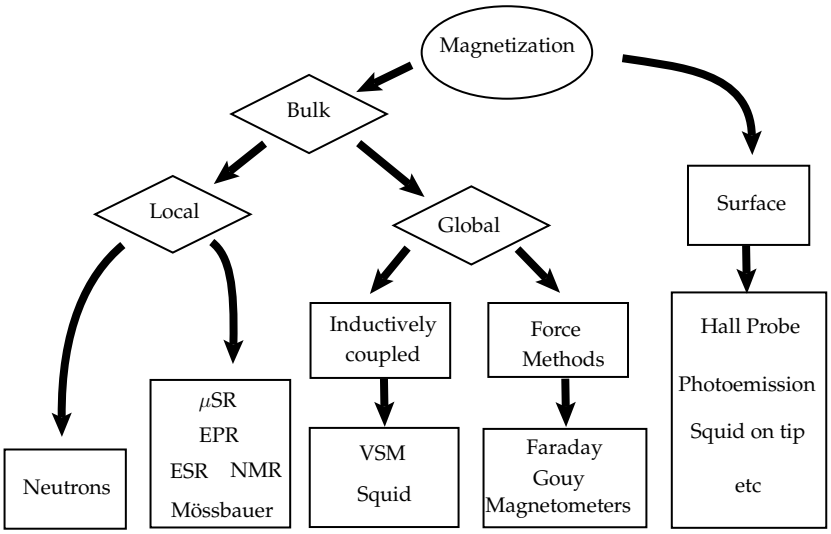

Figure 3.1 – Classification of different experimental methods to measure the magnetization of a sample.

oriented and quickly changed. Despite all these advantages there are some difficulties. One is that magnetically anisotropic samples will be subjected to a torque which will produce an additional signal. This signal can be larger than the magnetization signal, making it difficult to subtract. It is also important to note that working with high gradient fields can produce lateral instabilities [90], which can move the sample and affect the final magnetization measurement. All these issues will be described in detail in section 3.2.1.3.

3.2 Experimental techniques

The following sections give a brief review of the experimental methods used in this thesis as well as their operational principles and applications. In general, the methods used in this work for measuring the magnetization can be classified in two categories [91]: the force method where one measures the magnetic force exerted on a sample placed in an inhomogeneous magnetic field and the induction method where one measures the signal (voltage) induced by moving the sample with respect to the detecting coils. The first category is exemplified by the Faraday balance method [91]. A Faraday balance is a device for measuring magnetic susceptibility and it is often used in magneto-chemical studies because one can simultaneously observe changes in both magnetic properties and sample weight [92]. However, since the gradient is produced by the specially shaped poles (inhomogeneous field) of a large electromagnet, the method becomes unstable, when the field dependence

of the magnetization *M(H)* is measured. This is the case if the sample contains ferromagnetic material. The reason for this is that the field gradient, and therefore the sensitivity, is a function of the field which must be determined empirically. One finds that it decreases rapidly towards zero at low fields and is also unstable at high magnetic fields [93]. The second category is exemplified by the vibrating sample magnetometer (VSM) or the wide used superconducting quantum interference device (SQUID) magnetometer. This method has a high sensibility but can only be used in magnetic fields as high as 7 T and its application at temperatures below 2 K is rare.

3.2.1 Faraday magnetometer

3.2.1.1 Measurement of the force

In the Faraday method, the magnetization $\boldsymbol{M}$ is measured by observing the force $\boldsymbol{F}$ acting on a specimen of volume V placed in an inhomogeneous magnetic field $\boldsymbol{H}$. The relevant equation is:

$$\boldsymbol{F} = (\boldsymbol{M} \cdot \nabla)\mu_0 \boldsymbol{H}. \tag{3.4}$$

Such magnetic force can be measured capacitively by measuring the displacement produced by the sample on a variable parallel-plate capacitor, whose movable plate is suspended by elastic springs. Suppose that F is directed perpendicular to the plates, than the movable plate will be pushed until the restoring force of the springs balances with F, reaching equilibrium. The displacement of the plate is proportional to F and can be detected as a capacitance change ΔC.

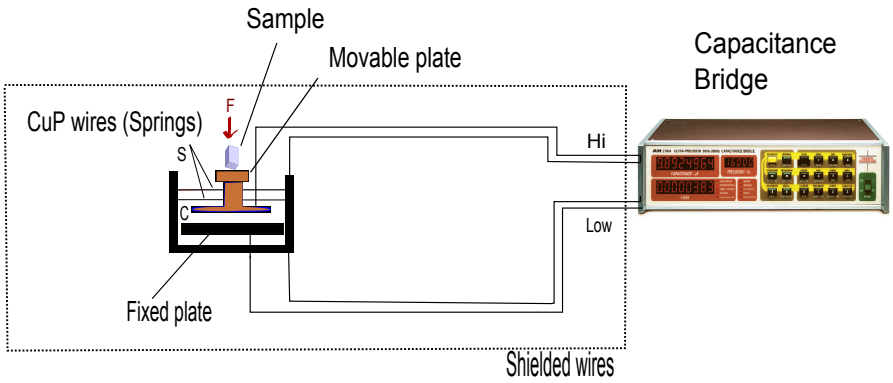

Figure 3.2 – Working principle of the measuring cell. The magnetic force $\boldsymbol{F}$ exerted on a sample situated in a spatially-varying field is detected as a change in the capacitance of a parallel plate capacitor, whose movable plate is suspended by elastic CuP wires acting as a spring.

Figure 3.2 shows schematically the working principle. In a pioneering work by Sakakibara *et al.* [16] a Faraday force magnetometer was designed for magnetization measurements. We used this work as a reference to design our magnetization cell. This method allows us to perform magnetic measurements in high magnetic fields and at mK temperatures.

3.2.1.2 Capacitive cell

The magnetic force can be measured by a capacitive method with a very sensitive capacitance cell able to detect small variations produced by the change in the magnetization. The measuring cell in which the sample holder is suspended by a crossed set of wires is shown in Fig. 3.3. This configuration is very sensitive to torque effects specially when we are measuring along the magnetic hard axis of a crystal. This is because just a single set of wires was used. Nevertheless, for magnetization along the easy axis the performance of the cell is very good, since no radial component exists and the torque, if is small, can always be subtracted.

We have modified the sample platform to reduce the torque contribution, which is proportional to the magnetization perpendicular to the applied field. The sample holder (gray component in Fig. 3.3) has been now suspended on a double set of wires as displayed in Fig. 3.2. The wires are clamped on two parallel bronze rings which are connected to the low-temperature stage of the cryostat. An image of the

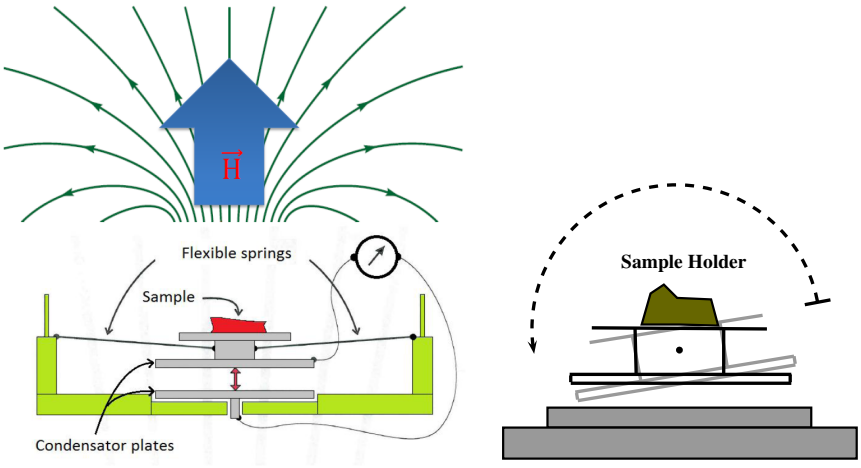

Figure 3.3 – Left: Schematic representation of the initial design of the capacitive cell. Right: Effect of the torque exerted on the sample holder due to the inhomogeneous mass distribution or to the crystal anisotropy.

cell design is shown in Fig. 3.4. The lower part of the sample holder is the upper plate of the capacitor. It is made of epoxy (Stycast 1266) and its electrode is formed by a thin layer of silver paint (Dupont 4922), which has been carefully polished

and covered by a thin layer of GE insulating varnish. This process is important in order to increase the sensitivity of the cell and achieve a large short-cut value of the capacitance. The total weight of the sample holder is 0.2134 g. The sample is located at the top of the Stycast holder and connected with the mixing chamber through a thin (0.0125 mm) silver foil as a thermal link. The upper capacitor plate

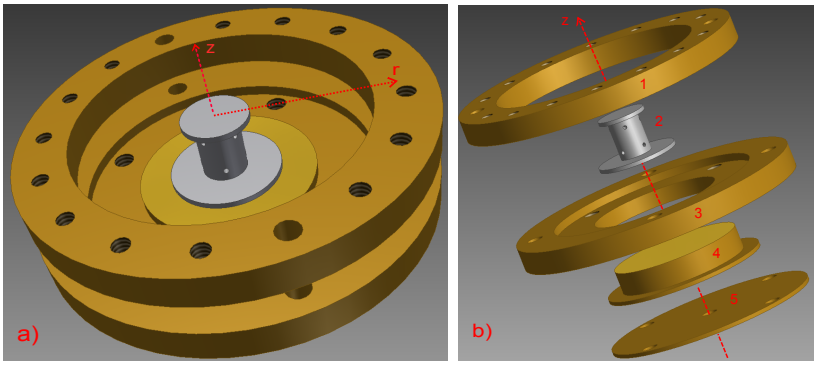

Figure 3.4 – Schematic representation of the capacitance cell. a) Complete assembled cell. b) Exploded view drawing of the magnetization cell and its parts: 1.- Upper ring 2.- Sample holder (movable plate) 3.- Lower ring 4.- Lower capacitor plate 5.- Locking plate.

is suspended by four phosphor - bronze (CuP) wires of 0.125 mm diameter with an initial tension of 0.5 N. Such wires are crossed in two separate (3 mm) planes in the z direction and with a difference of 45^o in the x-y plane (see Fig. 3.5). The diameter of the movable plate is 10 mm and the unloaded capacitance C_0 is 7.2 pF with a space between plates of about 0.1 mm. The lower capacitor plate is made of brass and polished (1 μm) to a mirror finish. This lower plate can be adjusted in the z direction for specific cases in which the magnetization will exceed the spatial movement of the upper plate, or simply to maximize the resolution (see Fig.3.9).

3.2.1.3 Design and performance of the cell

To design a reliable cell we need to consider the forces acting on a sample under the influence of a gradient field. If the sample is strongly anisotropic, $\boldsymbol{M}$ is not always parallel to the field $\boldsymbol{H}$ and may have a small radial component M_r. We assume $M_r << M_z \approx M \equiv |\boldsymbol{M}|$. Neglecting terms proportional to $\partial H_z/\partial r$, the forces will be then

$$F_z = M_z \frac{\partial H_G}{\partial z} \tag{3.5}$$

where H_G is the gradient field, and the radial component

$$F_r = -\frac{M_r}{2}\frac{\partial H_G}{\partial z}. \tag{3.6}$$

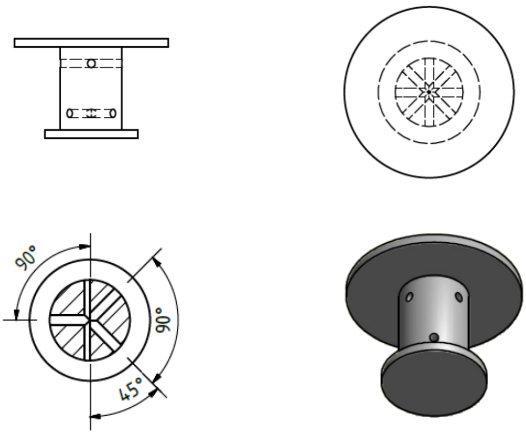

Figure 3.5 – Different views of the sample holder described in section 3.2.1.2. A robust sample holder and extra two holes for 2 set of CuP wires are the main differences from the initial design.

The component F_r is important for the lateral instability effect produced for high gradient fields [94]. In addition to the force the sample will experience a torque

$$\boldsymbol{N} = \boldsymbol{M} \times \boldsymbol{H}. \tag{3.7}$$

All forces and the torque contribute to the displacement of the capacitor plate, and the response ΔC may be written to a first approximation as

$$\Delta C = \upsilon F_z + \nu F_r + \omega |\boldsymbol{N}| \tag{3.8}$$

where the coefficients υ, ν and ω depend on the particular design of the cell. Other magnetization cells are made of different materials and based on different principles, for example cantilevers or diaphragms [95]. These kinds of magnetization cells present a strong torque signal, therefore a field dependence magnetization is always complicated to analyze when the torque response is of the same order or bigger than the magnetic signal. This usually happens in the case of extremely anisotropic materials, since $\boldsymbol{N}$ is very sensitive to a misalignment of the sample and is, therefore, not reproducible. We have tested two cells, cell 2 has a smaller sample holder (small background contribution) but is suspended on just a single set of wires. This configuration provides a large torque effect. Cell 3 has a bigger sample holder, but it is suspended on two sets of wires to reduce the torque effect. It can be seen in Fig. 3.7 that in the case of the new cell 3, tested with a sample $YbCo_2Si_2$ the effect of the torque is suppressed compared with the previous design (cell 2). The results in Fig. 3.7 were obtained under the same gradient field and temperature conditions for $H \| [100]$ and $H \| [001]$. The new configuration allows the sample holder to move preferentially in the z direction, so that the capacitor

plates are always parallel. It also avoids lateral instabilities that can modify the final capacitance [90]. The torque signal (red points) is an additional signal that needs to be subtracted from the raw capacitance data (black points) by comparing the signals with the gradient coils switched on and off. The displacement δ of the capacitance plate produced by the force F_z can be estimated by the formula:

$$\delta/F_z = \frac{L^3}{192nEI} \tag{3.9}$$

where n and L are the number and the effective length of the wires, respectively, E is the Young's modulus and I is the moment of inertia ($I = \pi D^4/64$) of the wire with diameter D. For the values of the new cell (L = 15 mm, D = 0.15 mm, n = 4, E = 120 GPa), the response of the cell can be estimated to be $\delta/F_z \approx 3$ mm/N, or $\Delta C/F_z \approx 300$ pF/N. The sensitivity of the cell can be also measured by putting a weight on it, or by observing the response due to a specimen whose magnetization is already know. We show in Fig. 3.8 the cell response to different weights obtained at room temperature (RT). The capacitance change was monitored by a capacitance bridge (Andeen-Hagerling, 2500A) in a three terminal configuration. The unloaded capacitance was 7.2 pF at RT and 5.4 pF at 4.2 K. Notice that ΔC is not linear with respect to weight, especially above $\Delta C/C_0 \approx 0.2$. If we neglect the edge effects of the capacitor, ΔC can be transformed to the displacement δ of the plate by the simple formula

$$\delta = \epsilon_0 A \left(\frac{1}{C_0} - \frac{1}{C} \right) \tag{3.10}$$

were A denotes the area of the plate, ϵ_0 is the permitivity of vacuum and $C = C_0 + \Delta C$ (see Fig. 3.8). A set of different weights was used (ASTM E617 Class 2, 1-500 mg) in order to gradually change the relative capacitance versus the distance between the plates. In the calibration with different weights (see Fig. 3.8) a linear

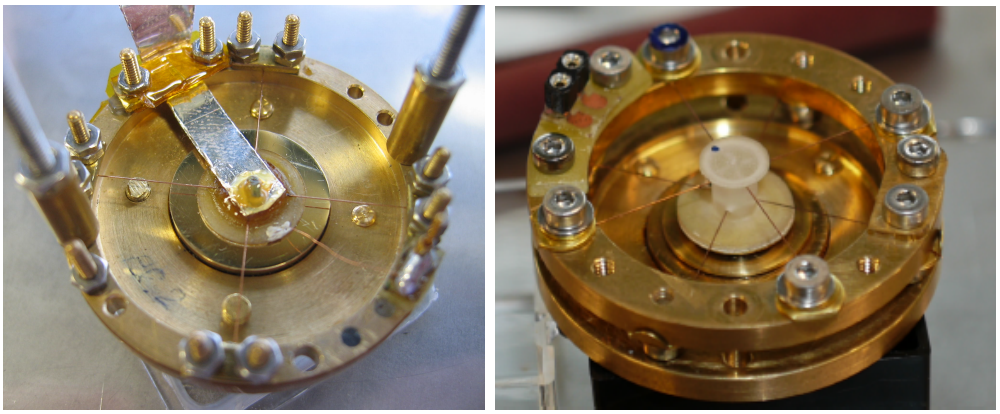

Figure 3.6 – Previous cell 2 (left) and new cell 3 (right).

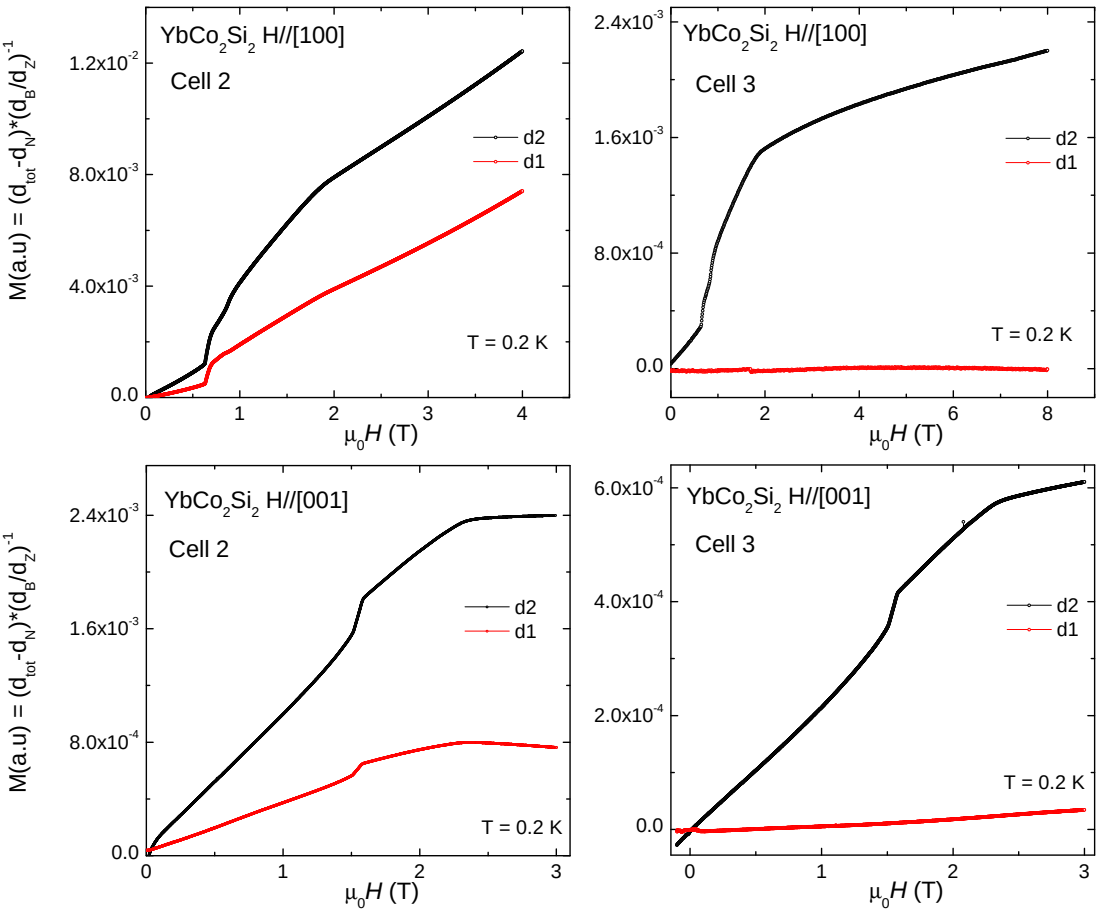

Figure 3.7 – Comparative analysis of the performance between the initial design (cell 2) and the new load cell (cell 3) developed in the present work, using $YbCo_2Si_2$ as a test material. The measurements were performed under the same conditions in gradient field and temperature. In the figure d_2 (black points) correspond to the displacement of the platform when the gradient field is not zero and d_1 (red points) when the gradient field is zero.

response for small weights up to 2 g can be observed. Usually we use this range in our magnetization measurements ($\delta \leq 5\mu$m).

3.2.1.4 Sensitivity

The sensitivity of the magnetometer is governed by the sensitivity of the capacitance cell itself, together with the maximum gradient that we can obtain and the resolution of the capacitance bridge. This low torque capacitance cell can detect force changes as small as $5 \cdot 10^{-6}$ Newtons. The maximum field gradient in the

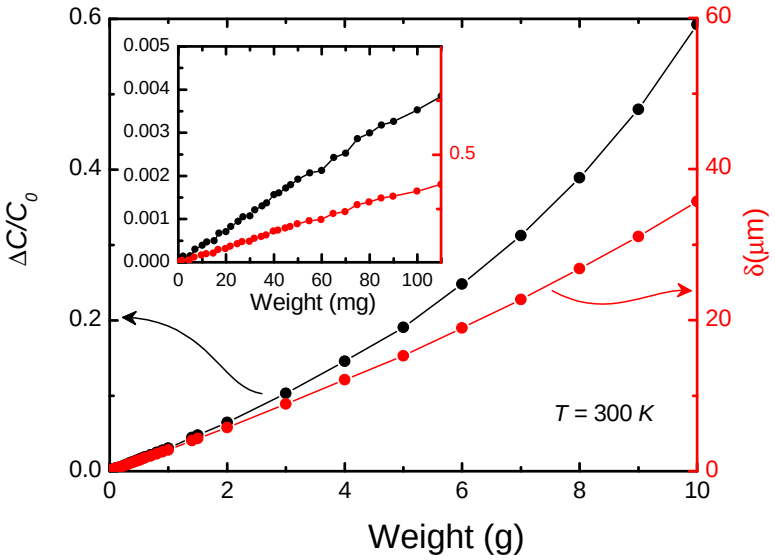

Figure 3.8 – Response of the load cell 3 to different weights, measured at room temperature. The black points are the observed capacitance change, while the red ones show the displacement of the movable plate of the cell, calculated from Eq. 3.10. The inset zooms in the values between 1 and 100 mg.

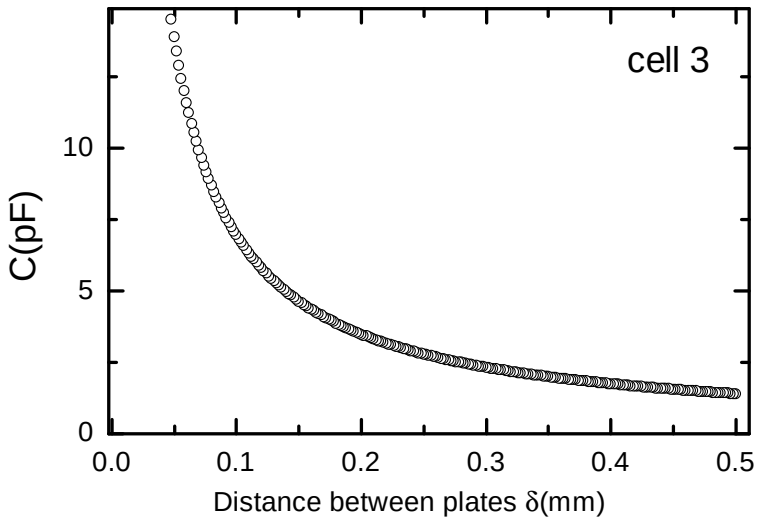

Figure 3.9 – Calculation of the capacitance vs. the displacement of the plates for cell 3, according to Eq. 3.10.

system is 10 T/m. Then the minimum detectable magnetic moment is of the order of 10^{-6} emu, (see Sec. 3.2.1.3). The sensitivity limits are determined by signal-to-noise ratio at the input circuit of the Andeen-Hagerling capacitive bridge. The

coils used to supply the gradient field ($\partial H_z/\partial z$) are shown in Fig. 3.13 as they are mounted inside the main magnet. The symmetry, size and sample position are crucial factors for an accurate measurement, since the force is a strong function of the spatial coordinates.

3.2.1.5 Background contributions

A measurement of the capacitance includes several contributions: sample magnetization, magnetization of all pieces of the sample holder and the contribution of the torque. A sample holder can produce a substantial contribution to the total signal. The holders used in this thesis have a single type of substrate, Stycast and are substantially larger in volume and mass than the sample itself. Fortunately, the Stycast is diamagnetic (see Fig. 3.12). Under applied fields its contribution is linear in field and temperature independent. Therefore the diamagnetic contribution can be easily substracted.

3.2.1.6 Calibration

Magnetization cells are generally calibrated with substances whose magnetization is known. The saturation moment of a small sphere of pure nickel is usually used as a secondary calibration standard for most magnetic measurements [96]. The two major reasons for choosing nickel are that it can be obtained with high purity and that the saturation moment of nickel is easily attained at low magnetic fields. The absolute accuracy of the instrument depends on the knowledge of the magnetic properties of the calibration standard and reproducibility of sample position.

This method is usually applied in cantilever magnetization cells in which the initial load capacitance never changes ($\approx$ 0.1 pF), since the samples are very small. We measure crystals between 5-30 mg. The initial capacitance in every new measurement may change from sample to sample. This change in the initial capacitance makes it difficult to get absolute units by calibration against a reference material. Another possibility of calibration is to compare the final field and temperature dependence magnetization measurement $M(H,T)$ against the measurements done in an SQUID. In this way we obtain the absolute magnetic units (see. Fig. 3.10). This method (calibration against other instrument) is more convenient and versatile since gives direct units without the necessity to calibrate the magnetization cell.

Figure 3.10 shows the result of the calibration obtained by comparing the response of a sample previously measured in the SQUID at 2 K and the measurement performed in the Faraday magnetometer at the same temperature with a vertical gradient field of 10 T/m.

The magnetization in Fig. 3.10 is extracted from the different of the field sweep with and without gradient field. The final data on this figure emerge from the difference of two curves as shown in Fig. 3.7 according to Eq. 3.11. The final magnetization then will be proportional to the net displacement (δ) of the upper capacitor plate when $\partial H_z/\partial z \neq 0$ after subtracting the displacement when $\partial H_z/\partial z = 0$ and will be defined by the formula

$$M \approx \left(\frac{\partial H_z}{\partial z}\right)^{-1} (d_2 - d_1). \tag{3.11}$$

The left panel of Figure 3.11 shows how the magnetic force $F \propto \Delta\, C$ is direct proportional to the gradient field. This can be easily understood by looking at the right panel of Fig. 3.11, in which it is shown the response of $YbRh_2Si_2$ and the linear dependence of the final capacitance against different gradient fields.

Figure 3.12 shows the magnetization of two empty cells between 0.05 K and 2 K : cell N.2 and 3. The magnetization contribution of the empty cell presents a diamagnetic behavior, which is consistent with the expected diamagnetism of the epoxy. In contrast, cell 2 shows a temperature dependence when the magnetic field was sweept. The non-linear response of the data for cell 2 is possibly due to the contribution of the phosphor-bronze wires which pass through the sample holder. In all measurements this contribution of the cell needs to be subtracted from the measured signal.

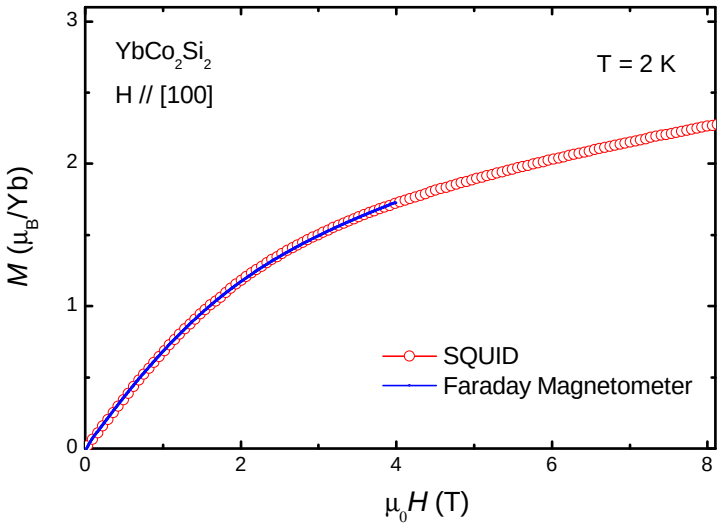

Figure 3.10 – Calibration against the result obtained with a SQUID at 2 K in $YbCo_2Si_2$.

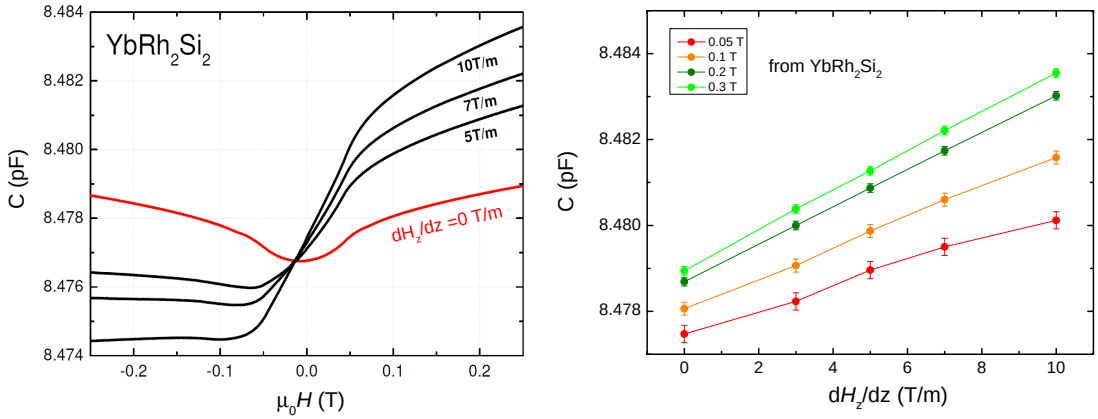

Figure 3.11 – Left: dependence of the capacitance for different gradient fields in $YbRh_2Si_2$. Right: dependence of the capacitance versus the strength of the gradient field.

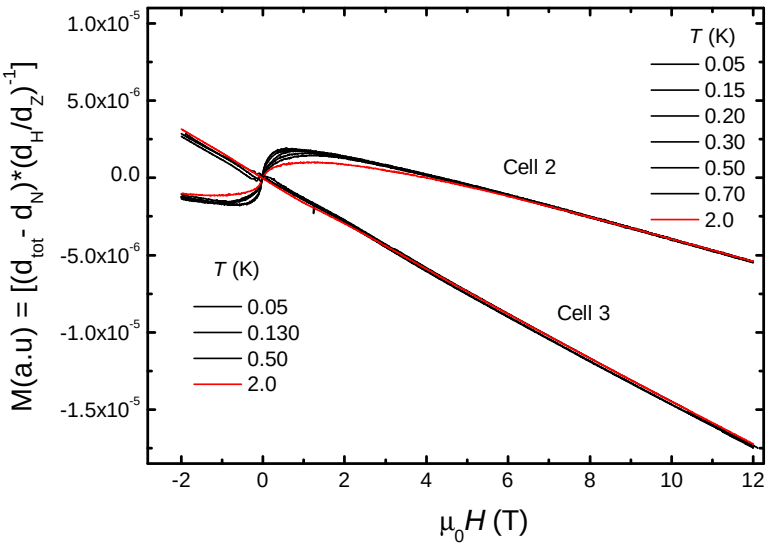

Figure 3.12 – Background contribution of cell 2 and 3. The final signal (M(a.u)) is the result of the total displacement d_{tot} minus the displacement produced by the torque d_N, multiplied by the inverse of the gradient field.

3.2.1.7 Magnets characteristics

In the Faraday method used for magnetization experiments [95, 97] the gradient field is usually produced by a solenoid magnet in which the sample is situated out of the center position. In this way, the same magnet produces the magnetization and the gradient field. This configuration has a strong position dependence of

the gradient field, and produces a poor reproducibility of the results. A much better method is to use gradient coils [98] in which the field gradient can be independently applied. We use superconducting magnets in gradient configuration to achieve high magnetic fields. The pair of superconducting coils are Oxford SC magnets with gradient coils (counter-wound split coils). A schematic picture is shown in Figure 3.13. The main coil produces magnetic fields (H_M) up to 12 T, with a homogeneity at the center better than 1 part in 10^4 over a 10 mm diameter in spherical volume. The gradient coils are able to produce a spatially varying magnetic field $\partial H_z/\partial z$ of 10 T/m. In our configuration, the gradient coils are wounded inside the main coil, and are driven by an independent power supply. The uniformity of the field gradient along the z axis is better than 0.5 % over $\pm$ 5 mm from the center.

The sample is located at the symmetry center of the gradient coils. At this position ($z = 0$) the leading terms of the z component of the vertical field gradient is expressed as

$$\left(\frac{\partial H_z}{\partial z}\right)_{z=0} = \frac{\partial H_G}{\partial z} + \frac{\partial H_M}{\partial z}. \tag{3.12}$$

For our magnet $\partial H_M/\partial z$ is expected to be very small (10^{-3} H_M [T/m]). This value is usually much smaller than $\partial H_G/\partial z$ even at the high fields and can therefore be ignored. It should be noted that, although the fields produced by the magnet may be axially symmetric, Eq. 3.12 with the condition $\nabla \cdot (\mu_0 \boldsymbol{H}) = 0$ leads to a radial component of the field H_r of the order

$$H_r \approx -\frac{r}{2}\frac{\partial H_G}{\partial z}. \tag{3.13}$$

3.2.1.8 Installation in a dilution refrigerator

The magnetization cell was installed in a ^{4}He - ^{3}He dilution refrigerator, the cooling power of which is 25 μW at $T = 100$ mK. The magnetization cell is attached to a silver cold finger which is thermally connected to the mixing chamber. In addition to the thermal link provided by the magnetization cell, the sample holder is directly connected to the cold finger with a silver foil of 10 μm thickness. The sample is positioned on the silver foil over the sample holder and fixed with grease (Apiezon N) or Varnish (GE-7031). The bending force of the silver foil is small compared to the restoring force in opposite direction of the load cell, and therefore does not disturb the measurement. The paramagnetic contribution (Pauli paramagnetism) of the silver foil can be neglected. We monitored the temperature of the sample with two of RuO_2 thermometers (LakeShore 2.2 kΩ Rx-102-A-AA). One is located

directly on the silver cold finger, near the silver foil and the second one on the mixing chamber, as shown in Figure 3.14.

Two small coaxial cables are used to electrically access the load cell. In an isothermal magnetization curve, the time varying field will induce eddy currents in the metallic parts of the cell and cell holder, which can raise the sample temperature. We have then to choose a sweep rate slow enough to maintain the temperature of a constant value and ensure isothermal condition. Despite the eddy currents we can make field dependent magnetization measurements at a base temperature of 40 mK with an uncertainty of ± 5 mK. The sharp peaks in the temperature around $H_M = 0$ (see Fig. 3.15) are caused by the flux jumps in the superconducting magnet.

3.2.2 SQUID magnetometer

One of the most sensitive magnetometry technique is the SQUID magnetometer. It uses a combination of superconducting materials and Josephson junctions to measure magnetic fields with resolutions up to $\sim 10^{-9}$ emu or greater [99]. In this work we have used MPMS SQUID and VSM SQUID magnetometers to measure the magnetization *M(H,T)* at high temperatures in order to calibrate the low-temperature magnetization measurements. The sample is usually fixed inside of a plastic straw. The set up is placed in a ^{4}He cryostat, in which temperatures

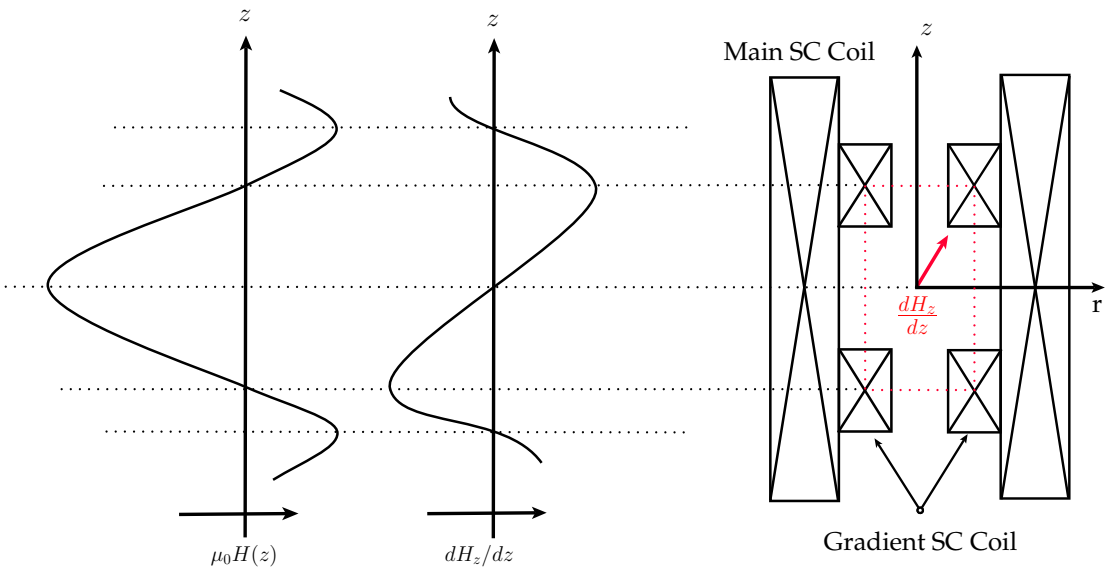

Figure 3.13 – Main and gradient field profiles in the plane of symmetry of the superconducting magnet as a function of the vertical coordinate z (left) and the schematic diagram of the superconducting set of coils used for the Faraday method (right).

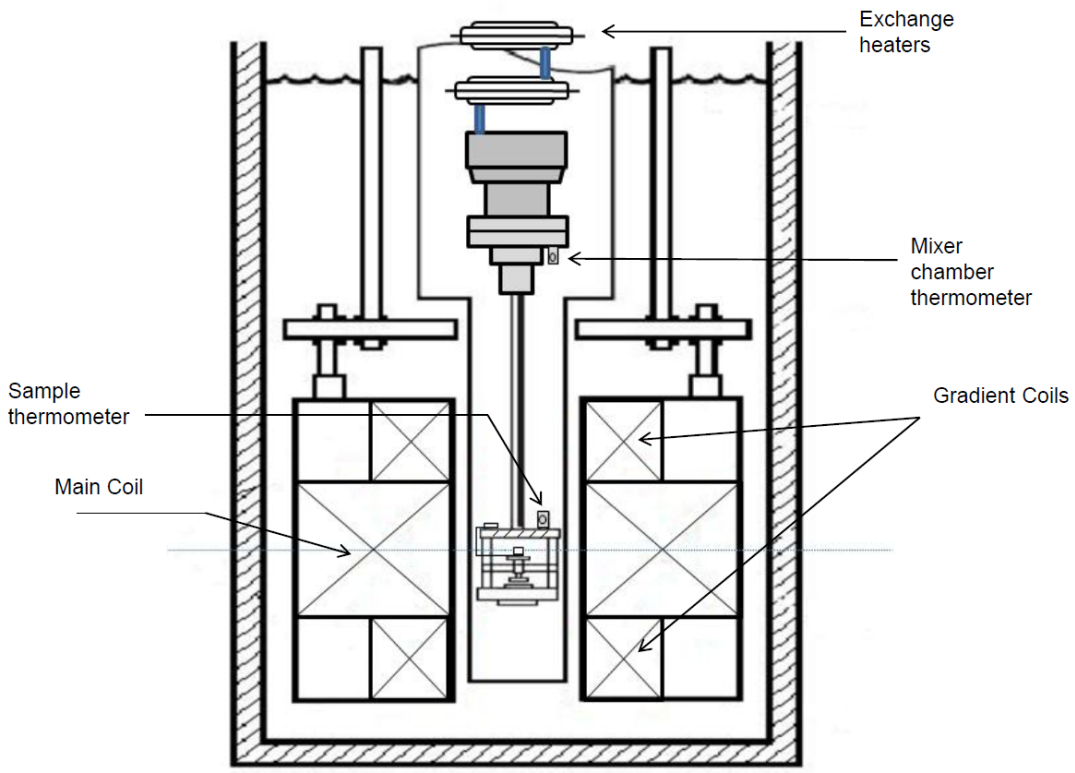

Figure 3.14 – Cross-sectional view of the Faraday magnetization cell installed in a conventional ^{4}He-^{3}He dilution refrigerator.

from 300 to 1.8 K can be achieved. A superconductor magnet inside the cryostat provides a magnetic field strength up to 7 T.

3.3 Magnetization measurements at high pressure

Like magnetic field, pressure can be used as control parameter in order to modify magnetic properties of a material. The application of pressure can produce important changes in the structural and electronic configuration of a crystal. Compared to isoelectronic substitution (chemical pressure) which introduces additional atomic disorder, hydrostatic pressure offers a clean way to tune the system through phase transitions. This technique is often used in the field of strongly correlated electron systems where high pressures are used in combination with low temperatures and high magnetic fields. Therefore, the measurements of magnetization under such conditions are very desirable. The type of pressure cell used here is a small piston-type cell (2.4 g) made of a non magnetic copper-beryllium alloy

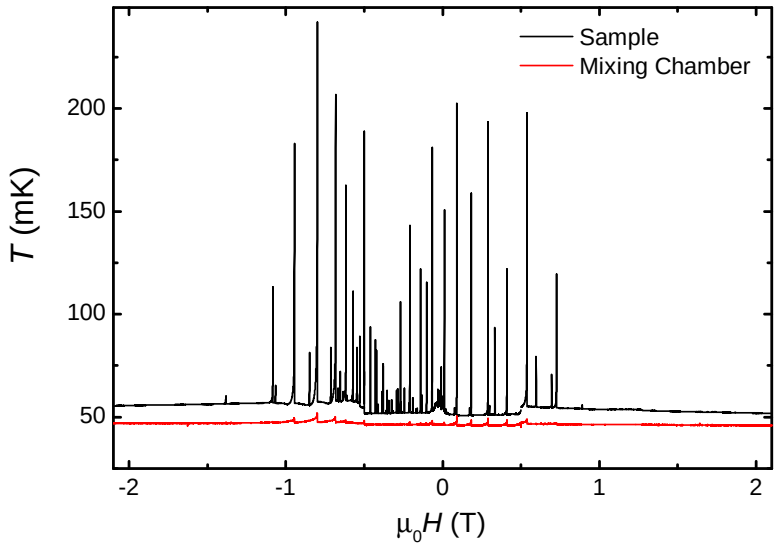

Figure 3.15 – Temperature reading of the sample T_s and mixing chamber T_M as the field is varied between - 2 and 2 T, obtained from the two RuO_2 thermometers installed near the sample and directly below the mixing chamber. The sharp peaks in T_s are caused by flux jumps in the superconducting magnet.

(Cu-Be), which can maintain their mechanical properties up to pressures of about 2 GPa. In this pressure cell even the piston is made of Cu-Be. Therefore, the contribution of the total cell to M can be easily subtracted from the raw data.

A major problem of magnetic measurements under pressure is the separation of the small changes in the magnetization of the sample from the magnetization of the manometer and pressure cell. One measures the total magnetization, which is the sum of the magnetization of the sample, pressure cell and pressure manometer (see Fig. 3.16). We have measured the pressure cell separately to be able to subtract this contribution and achieve a good accuracy of the absolute values.

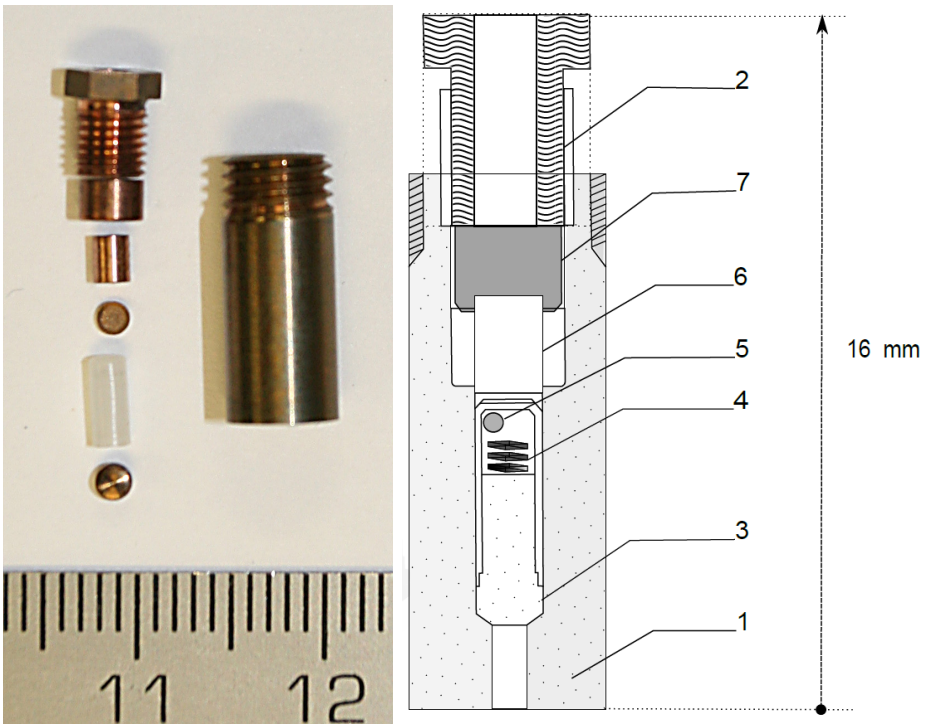

Figure 3.16 – Picture and schematic diagram of the miniaturized piston-cylinder type pressure cell used for magnetization measurements. The different components of the cell are indicated by numbers from 1 to 7. 1.-Body cell (CuBe), 2.-Locking nut, 3.-Plug (CuBe) and inner Cylinder, 4.-Samples, 5.- Manometer (Pb), 6.-Piston (CuBe) 7.-Backing Plate. Photo by R. Borth [100].

3.3.1 Experimental setup for $M(H,T)$ under pressure

Magnetization measurements under pressure were done in a dilution refrigerator cryostat as described in section 3.2.1.8, at low temperatures and high magnetic fields. The temperature range of the measurements is $0.05 \leq T \leq 4$ K, but we also used a MPMS to obtain $M(H,T)$ measurements in the temperature range $2 \leq T \leq 300$ K.

To determine the exact pressure inside the pressure cell, the SC transition temperature (T_c) of lead (Pb) was monitored. The pressure sensor is located inside the pressure cell near the sample. Another sensor is placed outside the cell in order to obtain the SC transition at normal pressure. The SC transition was monitored by $\chi_{AC}(T)$ measurements. The evolution of T_c for Pb is easily found in the literature [101]. To measure the magnetization of the sample under pressure we have positioned the pressure cell ($l = 16$ mm, $d = 6$ mm) on the sample holder in either

axial or longitudinal orientation with respect to the z axis. In this way, we were able to measure two crystallographic directions.

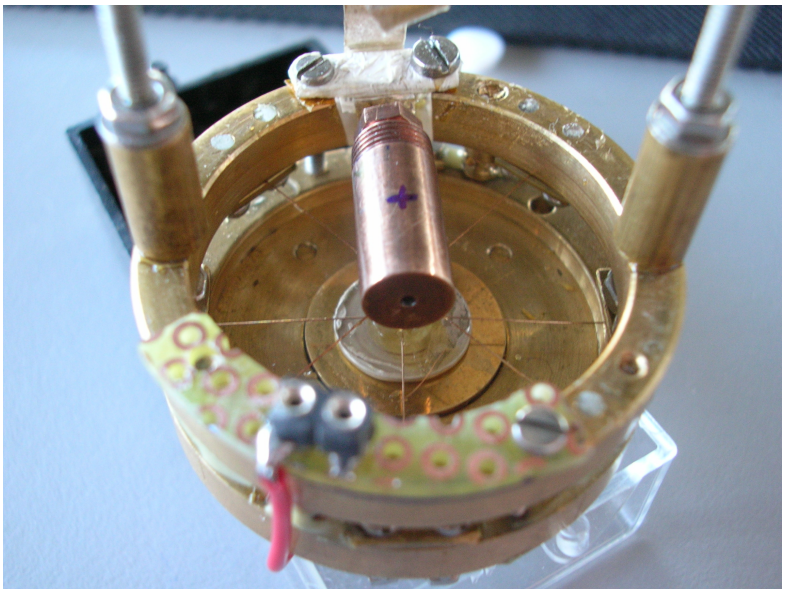

Figure 3.17 – Pressure cell mounted transversely on the magnetization cell. After the measurements, the contribution of the empty pressure cell was subtracted from the total magnetization.

4 $Yb(Rh_{1-x}Co_x)_2Si_2$

4.1 Introduction and motivation

The general understanding of quantum phase transitions (QPTs) is based on the concept of a single energy scale that fades continuously for $T \to 0$ (see Sec. 2.3). The conventional theoretical approach associates with this energy scale an order parameter that is defined finite inside a region of the phase diagram and zero elsewhere [1, 48, 49]. This region is separated from the rest by a 2^{nd}-order phase transition line which vanishes at $T = 0$, i.e., at the quantum critical point (QCP). In materials with magnetic phase transition temperatures close to zero, the energy scale is usually considered to be the ordering transition temperature - e.g., in the case of antiferromagnetic (AFM) systems, this is the Néel temperature T_N - and the order parameter is the staggered magnetization [5, 14]. In metals the magnetic order can be of the spin-density-wave (SDW) type and the same electrons which form the Fermi surface are involved in the QPT (see Sec. 2.3.1). This is the case of heavy-fermion compounds where the QPT separates a paramagnetic (PM) heavy Fermi liquid (FL) from an AFM metal. In these systems there are two principal energy scales: $k_B T_K$ and $k_B T_{RKKY}$ which derive from the respective interactions, the Kondo and the RKKY (see Secs. 2.2.2 and 2.2.3). T_K defines the temperature at which the localized f-electrons start to hybridize with the itinerant d-electrons to form a larger and heavier Fermi surface, T_{RKKY} is a measure of the inter-site exchange magnetic coupling. The interplay between these energy scales determines the magnetic ordering temperature T_N and characterizes the conventional QPT (see Sec. 2.2.4) [41]. In real systems, however, the situation can be rather more complex, due to the presence of multiple energy scales that can get involved in the QPT (see Sec. 2.3.2) [57]: Spin, charge, orbital and lattice degrees of freedom have to be considered. In addition, many materials show more than just a single magnetic phase transition. Therefore, experimental studies of quantum criticality become quite demanding but, on the other hand, promising for the discovery of novel correlated phases of condensed matter.

A prototypical example of such a complex system is the tetragonal $YbRh_2Si_2$, which is particularly suitable for studying QPTs [6, 102, 7]. In fact, this compound has a large $T_K \approx 25\,\mathrm{K}$ and a very small $T_N = 72\,\mathrm{mK}$ that can be suppressed by a magnetic field $\mu_0 H_N = 60\,\mathrm{mT}$ ($H \perp c$, with c being the magnetically hard axis) or chemical negative pressure ($P \approx -0.25\,\mathrm{GPa}$) [103, 104]. Three other intriguing features have recently been detected: (i) Another sharp

phase transition at $T_L = 2.2\,\mathrm{mK}$ [105], (ii) a kink in the magnetization at $H_0 \approx 10\,\mathrm{T}$ [106, 107], and (iii) a crossover energy scale $T^*(H)$ [13, 57]. The origin of the low-T transition is still unclear, but the comparison with the isoelectronic analogue $YbCo_2Si_2$ [108, 109] and the evolution of T_L observed in the series $Yb(Rh_{1-x}Co_x)_2Si_2$ (Co substitution corresponds to negative pressure) might suggest a second, possibly 1^{st}-order, AFM transition [110, 111, 112]. The feature at H_0 has been interpreted as field-induced suppression of the HF state, as hydrostatic pressure experiments have revealed a clear correspondence between H_0 and the Kondo scale T_K [106, 107]. Accurate de-Haas-van-Alphen experiments could show that the Fermi surface smoothly changes at H_0 suggesting a Lifshitz-like type of transition [113]. Meanwhile, thermopower experiments and renormalized band structure calculations have undoubtedly demonstrated that the anomaly at H_0 is caused by the field-induced shift of a van-Hove singularity (in the quasiparticle density of states) through the Fermi level, causing two consecutive Lifshitz transitions [114, 115]. Finally, there is the crossover line $T^*(H)$ which has been found in measurements of the Hall-effect [13] and various other thermodynamic properties [57]. The full width at half maximum (FWHM) of these crossovers is proportional to temperature. This suggests a step-like change of the Hall coefficient at $T = 0$ implying a Fermi surface reconstruction. This finding inspired a series of new theoretical proposals which considered the Fermi surface collapse due to the critical breakdown of the Kondo screening effect at the field-induced AFM QCP, including degrees of freedom other than fluctuations of the order parameter [52, 51, 53, 116]. In addition, recent detailed experiments have shown that the FWHM is proportional to temperature and therefore consistent with the energy over temperature scaling of the quantum-critical single-electron fluctuation spectrum [61].

However, experimental evidence that the energy scale $T^*(H)$ does not change much under applied pressure [117, 118], while the other energy scales $T_L(H)$, $T_N(H)$ and $T_0(H)$ are very pressure sensitive [103, 104, 112], has reopened the debate on how to interpret the experimental results. Three possibilities are currently considered: (i) The $T^*(H)$ line represents a change in the Fermi surface and inside the magnetic phase it is seen as a Lifshitz transition where the two magnetic phases have different topology [58, 59]; (ii) it represents the effect of a Zeeman-induced Lifshitz transition [119, 120, 121]; (iii) recent inelastic neutron scattering experiments associate the electron spin resonance signal [122] seen in $YbRh_2Si_2$ with a field-induced mesoscopic spin resonance, which evolves in field like the $T^*(H)$ line [123].

A detailed study of the magnetic fluctuations at the QCP is hindered by the lack of knowledge of the magnetically ordered structure which is due to the very low T_N and the unexpectedly small ordered moment ($10^{-3}\mu_B$/Yb) [124]. One way

to overcome this problem is to stabilize the AFM order by applying hydrostatic or chemical pressure, thus enhancing T_N and the size of the ordered moment. This has been successfully realized by substituting isoelectronic Co for Rh [125]: In fact, the whole series $Yb(Rh_{1-x}Co_x)_2Si_2$ crystallizes in the tetragonal $ThCr_2Si_2$-structure (space group I4/mmm) [110, 112]. The complete substitution of Rh by Co eventually leads to the stoichiometric compound $YbCo_2Si_2$, which is easier to study, since its $T_N = 1.7\,\mathrm{K}$ [126, 111] with almost localized $4f$ electrons and $T_K << T_{RKKY}$ [110, 112]. The knowledge of its magnetically ordered structure will possibly give some hints about the magnetic structure in $YbRh_2Si_2$, provided that the Yb Kramers-doublet ground state is the same in both compounds.

In the following Sec. 4.2 we follow the evolution of the three aforementioned energy scales under the effect of chemical pressure (Co substitution) by means of magnetization measurements in magnetic fields as high as 12 T and temperatures down to 0.05 K [16]. This allow us to observe the evolution of itinerant to local magnetism by monitoring the magnetic moment from the small value of about $\approx 0.1\,\mu_B$ in $YbRh_2Si_2$ to $\approx 1.4\,\mu_B$ in $YbCo_2Si_2$, for $H \perp c$, and the evolution of the magnetic ordered ground state.

In Sec. 4.3 we focus on the nature of the field-induced QCP in $Yb(Rh_{0.93}Co_{0.07})_2Si_2$, which is supposed to be of itinerant character (see Sec. 2.3.3), i.e. to be described by the SDW scenario. This is done by calculating the magnetic Grüneisen ratio (see Sec. 2.3.4), the analysis of which provides direct evidence of the presence of a QCP and information about its nature. A similar analysis is done in Sec. 4.4 with very demanding experiments on $YbRh_2Si_2$ under a hydrostatic pressure of 1.5 GPa, which corresponds to a chemical Co substitution of $x \approx 0.1$, i.e. near to $x = 0.07$.

Finally, in Sec. 4.5 the low-temperature $H-T$ magnetic phase diagram of high-quality single crystals of $YbCo_2Si_2$ is derived by applying the magnetic field along three crystallographic directions: [100], [110] and [001]. These data can be used to test the CEF calculations (see Sec. 2.1.1) by providing the values of the saturation magnetization and clarify the evolution of the magnetic structure in an applied magnetic field.

4.1.1 The heavy-fermion compound $YbRh_2Si_2$

The heavy fermion (HF) compound $YbRh_2Si_2$ crystallizes in the body-center tetragonal structure $ThCr_2Si_2$ (see fig 4.1) (space group $I4/mmm$) with lattice parameters $a = 4.007\,\text{Å}$ and $c = 9.858\,\text{Å}$ [6]. The Yb ions in $YbRh_2Si_2$ are in the trivalent state with $J = 7/2$ split into four Kramers doublets due to the crystalline electric field (CEF) (cf. Sec. 2.1.1) [6]. Inelastic neutron scattering (INS) experiments have shown that the ground state is separated from the three excited doublets by approximately 17, 25, and 43 meV corresponding to 200, 290, and

500 K [127]. Similar values have be measured by Stock *et al.* [123]. This was also recently observed in Scanning Tunneling Microscopy (STM) [128]. The suscepti-

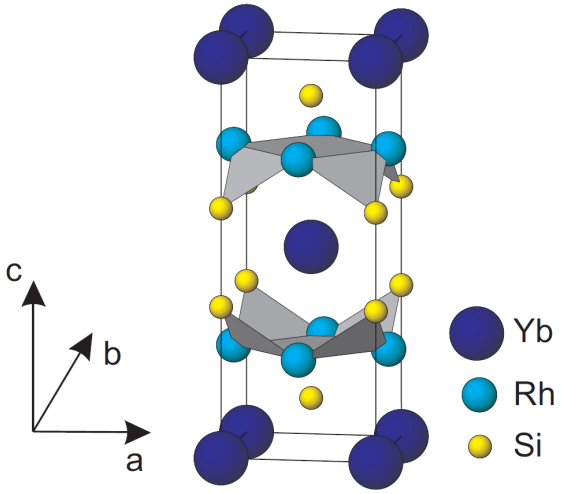

Figure 4.1 – Body-center tetragonal crystal structure of $YbRh_2Si_2$ (space group $I4/mmm$).

bility χ follows a Curie-Weiss behavior above 200 K for magnetic fields along both crystallographic directions, $H\|c$ and $H \perp c$ with an effective magnetic moment $\mu_{\text{eff}} = 4.4\mu_{\text{B}}$, which is close to the magnetic moment expected for a free Yb^{3+} ion ($4.54\mu_{\mathbf{B}}$). The Weiss temperatures $\Theta_W(H\|c) = -180\,\text{K}$ and $\Theta_W(H \perp c) = -9\,\text{K}$ indicate a strong magnetocrystalline anisotropy and point to an AFM ground state, or at least a ground state with AFM interactions [129]. At low temperatures, $\chi_{\perp c}$ is very large and about 20 times larger than $\chi_{\|c}$ [130]. This and the value of the Sommerfeld-Wilson ratio of about 30 indicate the presence of strong ferromagnetic fluctuations [63]. At T_N a sharp peak is observed in $\chi_{\perp c}$ (see Fig. 4.2a) below which antiferromagnetism sets in. The ordered moment has been reported to be very small ($10^{-3}\mu_{\text{B}}$/Yb) [124].

The electrical resistivity ρ(T) exhibits a weak negative temperature dependence at high-T decreases sharply below 100 K indicating the development of coherence effects, characteristic of Kondo lattice systems. The characteristic Kondo temperature $T_K \approx 25 - 29\,\text{K}$ was determined from the magnetic entropy (cf. inset of Fig. 4.2c) and thermopower experiments [6, 131]. In zero field and at ambient pressure ρ(T) follows a quasi-linear behavior below 10 K indicating strong non-Fermi-liquid (NFL) behavior (cf. Fig. 4.2b) [7]. A pronounced kink at T_N marks the onset of the AFM ordering below which ρ(T) follows a T^2 behavior expected for a Fermi liquid. This is confirmed by the large and constant Sommerfeld coefficient $\gamma_0 = C_{el}/T(T \to 0) = 1.8\,\text{J/K}^2\text{mol}$ [7] which evidences the HF character of

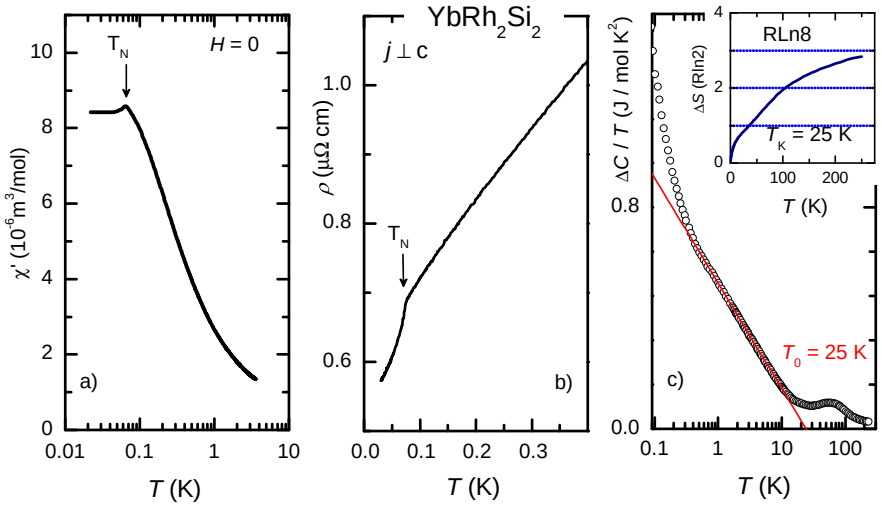

Figure 4.2 – a) Ac-susceptibility measured in zero external magnetic field H and a modulation field of about 11 μT applied perpendicular to the c-axis [132]. The arrow indicates the peak at the Néel temperature T_N. b) T-dependence of the resistivity in zero field which is $\propto T$ above T_N and $\propto T^2$ below T_N. c) Contribution of the $4f$-electrons to the specific heat, plotted as $\Delta C/T$ vs. $log(T_0/T)$ from Ref. [107]. The red line is a logarithmic fit to the data between 0.3 and 10 K. The inset shows the evolution of the entropy $S(T)$ with temperature which reaches the expected value of R$ln8$ for a $J = 7/2$ Yb^{3+} ion at about 300 K. The magnetic specific heat data shows a broad Schottky anomaly at $\approx 60-70$ K which is consistent with the CEF schema proposed by Stockert *et al.* [127].

$YbRh_2Si_2$. The specific heat measurements reveal strongly enhanced values and a logarithmic increase of the $4f$-electron $C_{el}(T)/T$ (see Fig. 4.2c)[1] being a further hallmark of the presence of spin fluctuations and the emergence of NFL behavior. The logarithmic increase of C_{el}/T towards lower temperatures can be described by a function proportional to $log(T_0/T)$ where $T_0 \approx 25$ K can be considered the characteristic spin-fluctuation temperature according to Ref. [49]. Most interestingly, below $T = 0.3$ K, C_{el}/T increases strongly than a logarithmic function following a power law $C_{el}/T \propto T^{0.34}$. This additional upturn was ascribed to the breakup of the heavy quasiparticles at the QCP [7]. The AFM phase transition is characterized by an extremely sharp anomaly at T_N [7, 133] below which a tiny amount of entropy, about 0.03R$ln2$, is released [107] in agreement with the small ordered moment.

[1] The electronic contribution $C_{el}(T)$ is derived by subtracting the non-magnetic contribution of $LuRh_2Si_2$ from the total specific heat of $YbRh_2Si_2$.

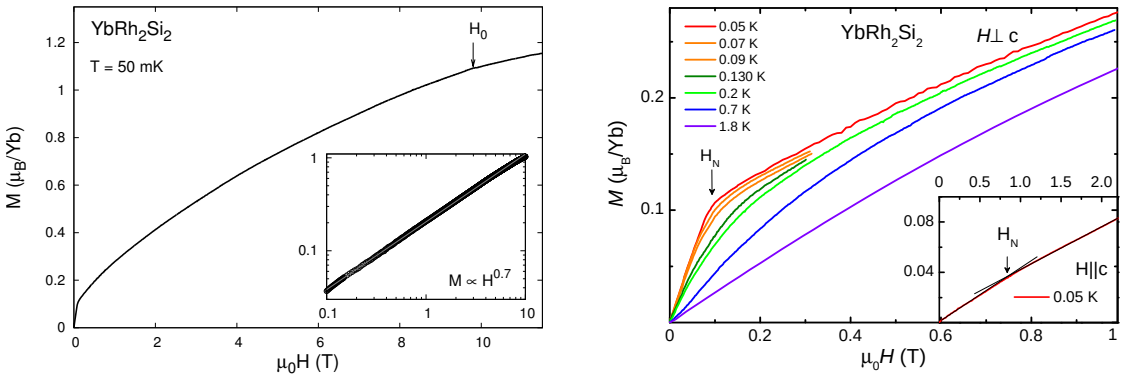

Figure 4.3 – Left: Isothermal magnetization measurements of $YbRh_2Si_2$ at 0.05 K for fields perpendicular to the c direction ($H \perp c$) up to 12 T. The arrow indicates the position of H_0. The inset shows the same data in a double logarithmic scale to emphasize that $M \propto H^{0.7}$. Right: Isothermal magnetization measurements of $YbRh_2Si_2$ at various low temperatures below and above T_N with $H \perp c$. The arrow marks the position of the critical field H_N . The inset shows a magnetization measurement at 0.05 K with field parallel to the c direction ($H \| c$). The black straight lines have been drawn to emphasize the kink at H_N .

The magnetization isotherms $M(H)$ of $YbRh_2Si_2$ are quite rich of features (see Fig. 4.3). At 0.05 K $M(H)$ shows a pronounced kink at about 0.06 T which remains sharp even above T_N. This feature has been associated with the presence of a crossover energy scale $T^*(H)$. This crossover sharpens on cooling and at $T = 0$ marks the abrupt change of the Fermi surface at the AFM-QCP as evidenced by Hall-effect experiments [13, 61] in agreement with the predictions for the local Kondo breakdown scenario [52, 51, 134, 116] (see text below). For $H > H_N$ the magnetization increases steeply following a power law $M \propto H^{0.7}$ (see inset of Fig. 4.3) up to $H_0 \approx 10$ T where it shows a kink and the slope of M vs. H strongly decreases. The increase of M between 0.1 and 10 T is too strong to be associated with Pauli paramagnetism, but it indicates the continuous suppression of the Kondo effect which increases the measured magnetic moment. The value of M at H_0 is about 1.1 μ_B, and it is still smaller than the saturation value of about 1.7 μ_B expected for the Γ_7 ground state as deduced from ESR [122, 135] (with a $g_{ESR} = 3.6$) and INS experiments [127, 123]. In fact, $YbRh_2Si_2$ shows a well defined ESR signal with properties similarly observed for local Yb^{3+} ions in metallic environments. The signal is observed well below the Kondo temperature T_K, where the magnetic Yb^{3+} moments are supposed to be screened and no ESR signal is expected. It is the first observation of an ESR signal of the Kondo ion in a Kondo-lattice system; the origin of the signal is yet unexplained [122], although recent INS experiments associate the ESR signal with a field-induced mesoscopic spin reso-

nance [123]. The feature at H_0 was initially associated with the destruction of the heavy-fermion state and localization of the f-electrons [106, 107]. Subsequently, the continuous decrease of the dHvA frequency across this transition was interpreted as a Lifshitz transition induced by strong spin-splitting [113]. Meanwhile, renormalized band structure calculations [114] supported by thermopower, Hall effect, magnetoresistance and thermodynamic measurements [115] have undoubtedly demonstrated that the feature at H_0 is split into two field-induced topological changes of the Fermi surface, i.e. Lifshitz transitions, which involve Fermi surfaces of $d + f$ character. This means that the f-electrons are still not fully localized above H_0.

The magnetization is very anisotropic. Small magnetic fields $\mu_0 H_N = 0.06\,\mathrm{T}$ with $H \perp c$ and $\mu_0 H_N = 0.66\,\mathrm{T}$ with $H \| c$ are sufficient to suppress T_N to zero (cf. magnetic phase diagrams in Fig. 4.4). At these fields the measured magnetic moments are very small, $0.1\mu_\mathrm{B}$/Yb for $H \perp c$ and $0.04\mu_\mathrm{B}$/Yb for $H \| c$, as shown in Fig. 4.3. This indicates the strong Kondo effect which almost completely screens the Yb moments of the doublet ground state. At the critical field H_N the resistivity $\rho(T)$ shows NFL T-linear behavior (see orange area in Fig. 4.4a) and the specific heat C_{el}/T diverges for $T \to 0$ following a power law $T^{-0.34}$[7]. These discoveries have been taken as evidence for the presence of an AFM-QCP in $YbRh_2Si_2$. These temperature dependences do not agree with the conventional SDW scenario (see Sec. 2.3.1), but a local Kondo breakdown scenario (see Sec. 2.3.2) was proposed [52, 51, 134, 116]. In the Kondo breakdown scenario the Kondo effect which is responsible for the formation of heavy quasiparticles breaks down and a Fermi surface reconstruction at the QCP should occur. At the QCP the quasiparticle will disintegrate into its localized spin and delocalized charge degrees of freedom. Such a break up of the heavy electrons is responsible for the peculiar NFL behavior observed in $YbRh_2Si_2$. Such a scenario has been supported by Hall-effect, transport and thermodynamic experiments, which have identified a crossover energy scale $T^*(H)$ which vanishes at the QCP and where the Hall effect shows an abrupt change at $T \to 0$ [13, 57, 61]. The results of all these experiments have been summarized in the phase diagram of Fig. 4.4b. Across the T^* line the Fermi surface changes from a small volume at low fields to a large volume at higher fields. Here, the heavy Fermi-liquid regime is recovered below T_{FL}, as evidenced by a constant Sommerfeld coefficient γ and $\rho \propto T^2$ (see blue area in Fig. 4.4a). In addition, the divergent behavior of the thermal $\Gamma(T)$ and magnetic $\Gamma_H(T)$ Grüneisen ratios at the QCP in $YbRh_2Si_2$ (see Sec. 2.3.4), divergencies that are in contrast with the conventional SDW model, might support the local scenario [8, 118]. In particular, at an AFM-QCP the SDW scenario predicts $\nu z = 1$ with ν the spatial correlation-length exponent and z the dynamical exponent. For the case of $YbRh_2Si_2$ a value

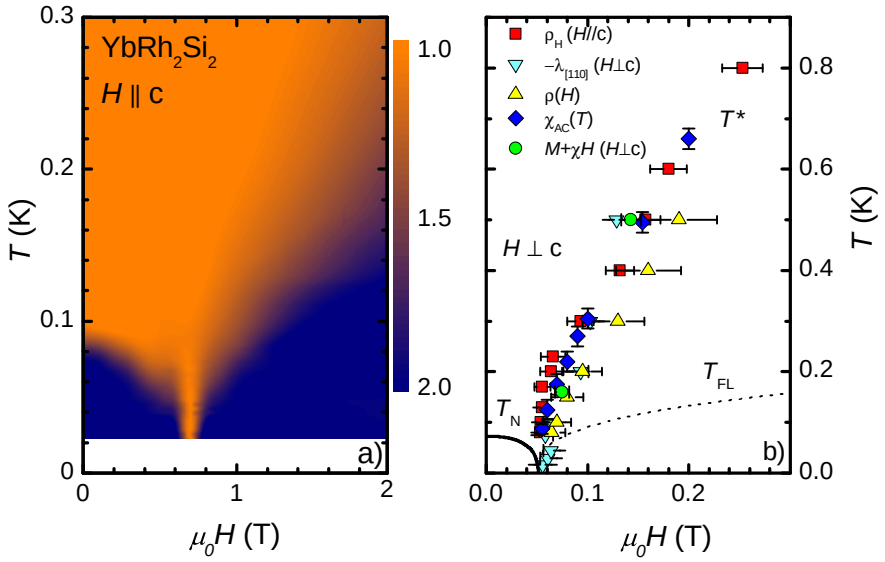

Figure 4.4 – a) Magnetic phase diagram of $YbRh_2Si_2$ with $H \| c$ from Ref. [7]: Color plot showing the temperature and field dependence of the exponent ϵ of the resistivity $\rho = \rho_0 + AT^{\epsilon}$: The orange area indicates the NFL behavior, i.e. $\rho(T) \propto T$, while the blue area indicates the FL behavior, i.e. $\rho(T) \propto T^2$. This plot evidences clearly the presence of a QCP at $\mu_0 H_N = 0.66\,\mathrm{T}$ (with $H \| c$). The blue area on the left is the AFM ordered region. b) Magnetic phase diagram of $YbRh_2Si_2$ with $H \perp c$ from Ref. [57]. The energy scale $T^*(H)$ was obtained from Hall resistivity $\rho_H(H)$, magnetostriction coefficient $\lambda(H)$, magnetoresistance $\rho(H)$, ac-susceptibility $\chi_{\mathrm{AC}}(T)$ and magnetization $M + (\partial M/\partial H)H$ measurements. T_N is the Néel temperature and T_{FL} is the temperature below which $\rho(T) \propto T^2$ marking the FL ground state.

of $\nu z = 0.7$ was found from measurements of the thermal [8] and magnetic [118] Grüneisen ratios.

4.1.2 The antiferromagnet $YbCo_2Si_2$

$YbCo_2Si_2$ has already been investigated by several groups (see Refs. [126, 136, 137, 138]), but all of these studies are based on polycrystalline material and do not focus on the low temperature properties. The first evidence of magnetic order in $YbCo_2Si_2$ was observed by Hodges in ^{170}Yb Mössbauer spectroscopy experiments on polycrystalline materials [126]. He found AFM order below 1.7 K with the easy magnetization in the basal plane and a saturated moment of 1.4 μ_B/Yb. Moreover, he suggested that the magnetic moments lie in directions close to the basal plane. These results could be explained in terms of a Yb^{3+} valence state experiencing a tetragonal crystalline electrical field (CEF), resulting in a Kramers-doublet Γ_7 as ground state. This agrees well with high-temperature ($T > 100\,\mathrm{K}$)

susceptibility measurements, which follow a Curie-Weiss behavior with an effective moment of 4.7 μ_B/Yb and a Weiss temperature θ_W of -4 K and -160 K for the magnetic field H parallel and perpendicular to the basal plane, respectively; no magnetic contribution from Co has been observed [110, 112]. A similar fit at temperatures between 2 and 4 K leads to a reduced effective moment of 3.6 μ_B/Yb for $H \perp c$. INS experiments revealed that the excited Kramers doublets are 4, 12.5 and 30.5 meV away from the ground state doublet. An exact analysis of the CEF level scheme has been proposed in Ref. [112]: Using the Weiss temperatures $\theta_W^{ab} \approx -4\,\mathrm{K}$ and $\theta_W^{c} \approx -160\,\mathrm{K}$ from the high-temperature Curie-Weiss fits of the magnetic susceptibilities (see Fig. 4.5), the CEF coefficient $B_2^0 O_2^0$ of the CEF Hamiltonian in Eq. 2.3 can be estimated from equation 2.7 (see Tab. 4.1). Taking

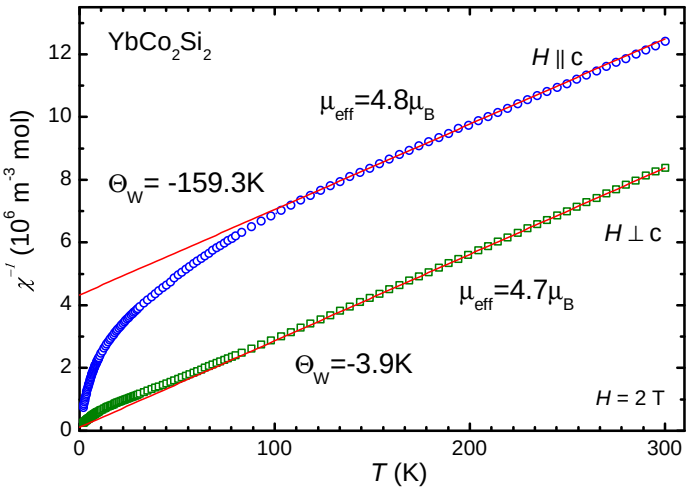

Figure 4.5 – Inverse magnetic dc susceptibility of single crystalline $YbCo_2Si_2$ measured in an applied field of 2 T. The solid lines represent the Curie-Weiss law (Eq. 2.6).

Table 4.1 – Crystal field parameters for $YbCo_2Si_2$ in meV [111]

B_2^0	B_4^0	B_4^4	B_6^0	B_6^4
0.75	$6.162 \cdot 10^{-3}$	$5.022 \cdot 10^{-2}$	$-1.159 \cdot 10^{-4}$	$2.242 \cdot 10^{-4}$

into account the energy splittings (INS experiments) and the values of α and α' that can be extracted from ESR [139] experiments - these measurements lead to $g_{ab} \approx 2.8$ and $g_c \approx 1.4$ - the CEF parameters corresponding to a single solution could be derived and are listed in table 4.1. The ground state wave function is:

$$|\Gamma_{7,1}> = 0.891|\pm 3/2> - 0.454|\mp 5/2> \tag{4.1}$$

and the CEF level scheme is shown in Fig. 4.6.

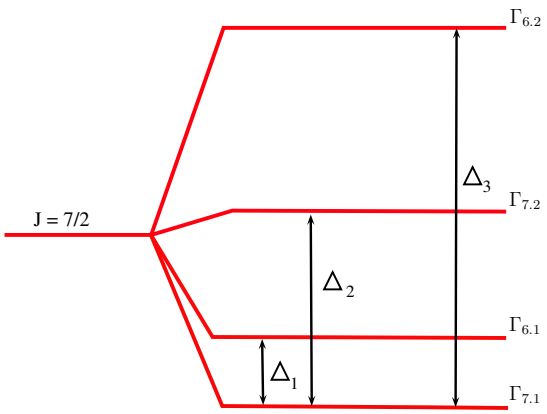

Figure 4.6 – Schematic crystal-field level scheme proposed by Klingner *et al.* [111]. $\Delta_1 = 4$meV, $\Delta_2 = 12.5$meV and $\Delta_3 = 30.5$meV are the CEF excitation energies determined in neutron scattering experiments [138].

An external magnetic field removes the degeneracy and the Zeeman Hamiltonian $H = -\boldsymbol{\mu} \cdot \boldsymbol{B}$ with magnetic moment $\boldsymbol{\mu} = -g_J \mu_B \boldsymbol{J}$ can be treated as 1^{st} order perturbation. With field parallel to the c axis, $B//c$, the magnetic moment (i.e., the saturation magnetization) is:

$$\mu_c = - < j_c > g_J \mu_B = \frac{8}{7} \cdot 0.68 \mu_B = 0.77 \mu_B \tag{4.2}$$

and the ESR g-factor is accordingly

$$g_c(ESR) = 2 g_J < j_z >= 2 \mu_c = 1.54. \tag{4.3}$$

With field perpendicular to the c axis, $B \perp c$, the magnetic moment is:

$$\mu_{ab} = - < j_{ab} > g_J \mu_B = \frac{8}{7} \cdot 1.4 \mu_B = 1.6 \mu_B \tag{4.4}$$

and the ESR g-factor is

$$g_{ab}(ESR) = 2 g_J < j_{ab} >= 2 \mu_{ab} = 3.2. \tag{4.5}$$

This fits reasonably good with our experimental results displayed in section 4.5.2. A similar ground state is currently considered in $YbRh_2Si_2$ [127, 140].

A second AFM phase transition has been observed in $YbCo_2Si_2$ at a temperature $T_L = 0.9$ K by means of magnetization, resistivity and specific-heat measurements (e.g., see Fig.4.7) [108, 141, 112]. While the phase transition at T_N is second order, the sudden drop at T_L and the latent heat observed in the heat capacity in

zero field point to a first order nature of the phase transition (see Fig. 4.7) [112]. Both transition temperatures are suppressed by a field larger than 2 T, and the $H-T$ magnetic phase diagrams become very complex, showing a strong basal plane anisotropy [141]. The entropy above both transitions confirms a Kramers doublet ground state and the local character of the Yb $4f$ quasi-hole. In fact, the Kondo temperature has been estimated to be lower than 1 K and this system is dominated by the RKKY exchange interaction since about 75% of the ground state entropy has been found below T_N [110, 111]. The $\gamma_0 = 0.13\,\mathrm{J/K^2mol}$ value indicates a weak hybridization of the local $4f$ moments with the conduction electrons and therefore the system cannot be considered a HF system.

The fact that Yb seems to have a similar Γ_7 ground state in both $YbCo_2Si_2$ and $YbRh_2Si_2$, represents a unique opportunity to make a direct comparison between these two compounds. Further experiments in neutron diffraction measurements on our $YbCo_2Si_2$ single crystals might be the key experiments in order to clarify the magnetic structure and the magnetic excitations in $YbRh_2Si_2$. Powder neutron diffraction studies, performed in the intermediate and low-T AFM states, have detected magnetic peaks and suggested that the propagation vector $\mathbf{Q}$ changes its periodicity between the two phases [142]. In addition, preliminary neutron scattering experiments seem to indicate that the propagation vector $\mathbf{Q}$ is incommensurate below T_N, Q_2= (0.25, 0.08, 1) for $0.9 < T < 1.7$ K and becomes commensurate below T_L, Q_1=(0.25, 0.25, 1) for T≤0.9 K [143].

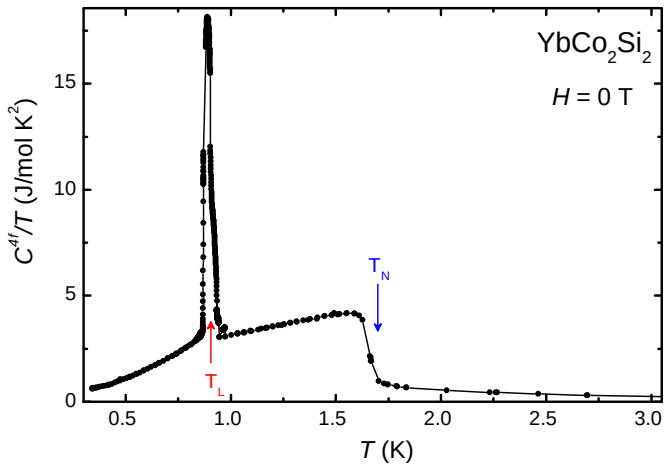

Figure 4.7 – Specific heat measurement of $YbCo_2Si_2$ in zero field. The $T_N = 1.7$ K and $T_L = 0.91$ K transitions are marked by a vertical arrow. The T_L is a clearly first-order phase transition. Data from Ref. [110].

4.1.3 Isoelectronic substitution of Co for Rh: $Yb(Rh_{1-x}Co_x)_2Si_2$

Inelastic neutron scattering experiments are adequate tool to investigate quantum critical fluctuations in $YbRh_2Si_2$. Although recently significant progresses have been done with coaligned single crystals (reaching a sample mass of about 3 g) [123], a comprehensive and satisfying study is still missing. The low transition temperature and also the extremely small ordered moment prevent experimentalists to achieve this goal. To overcome these difficulties, INS experiments should be carried out under pressure, since T_N and the corresponding ordered moment increase with increasing pressure in Yb-based compounds (see Sec. 2.1) [144, 145]. Such experiments have not been successful yet. However, isoelectronic substitution of Rh by Co leads to a similar effect as pressure. Recently, the crystal growing process has been optimized in order to produce single crystals of $Yb(Rh_{1-x}Co_x)_2Si_2$, which all crystallize in the tetragonal $ThCr_2Si_2$-type structure: Several high-quality single crystals with a Co content x varying between 0.03 and 1 have been synthesized [110, 112]. The analysis of the crystallographic parameters a and c of the $Yb(Rh_{1-x}Co_x)_2Si_2$ series indicates positive chemical pressure with increasing x. The ratio c/a decreases with increasing unit cell volume and

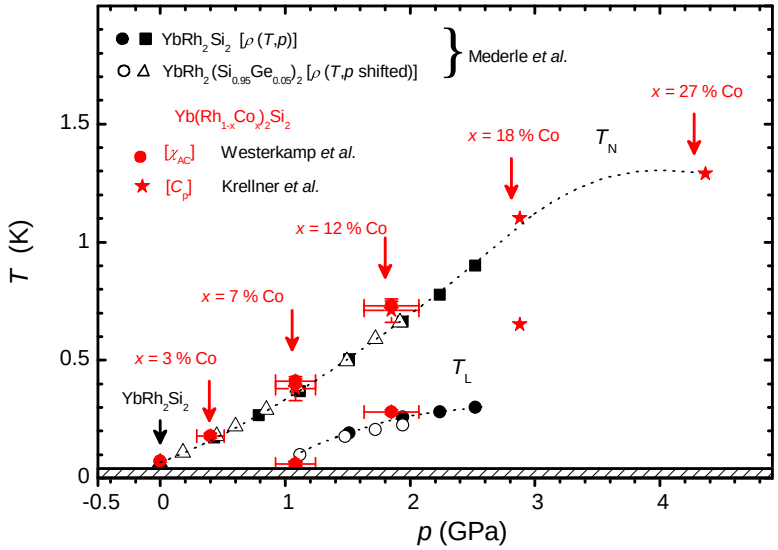

Figure 4.8 – Equivalence of external and chemical pressure in $YbRh_2Si_2$. The Néel temperature T_N of $YbRh_2Si_2$ is taken from Mederle *et al.* [144, 103] in agreement with Knebel *et al.* [145]. Above 1GPa a second transition is observed at T_L. The transition temperatures for $Yb(Rh_{1-x}Co_x)_2Si_2$ were determined by Westerkamp *et al.* with ac-susceptibility [132] and Krellner *et al.* [146] with specific heat measurements. The pressure values for $Yb(Rh_{1-x}Co_x)_2Si_2$ has been calculated using the measured lattice parameters and the bulk modulus of $YbRh_2Si_2$ [147].

changes slope above $x = 0.27$ indicating that a comparison between hydrostatic and chemical pressure is only possible for $x \geq 0.38$ to some extent. Moreover, from analysis of the low-T entropy it could be stated that the Yb^{3+} CEF ground state is a Kramers doublet for the complete series.

As expected for low Co content, the increasing of x stabilizes the magnetic order enhancing T_N and the value of the ordered moment [125, 117]. This is illustrated in Fig. 4.8 for $p < 5$ GPa where the transition temperatures T_N and T_L have been plotted versus the hydrostatic (from Refs. [144, 103, 145]) and chemical pressure (from Refs. [132, 146]). The pressure values for $Yb(Rh_{1-x}Co_x)_2Si_2$ has been calculated using the measured lattice parameters and the bulk modulus (190 GPa) of $YbRh_2Si_2$ [147]. The values of the transition temperatures measured under hydro-

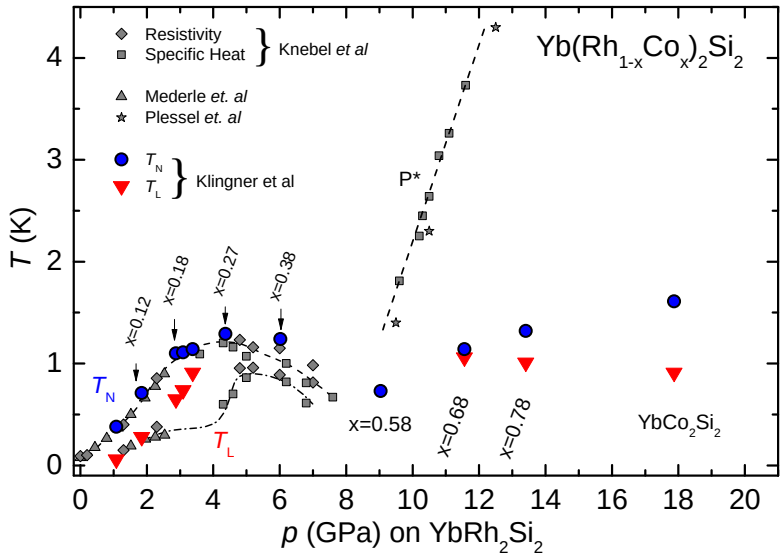

Figure 4.9 – $x - T$ phase diagram of $Yb(Rh_{1-x}Co_x)_2Si_2$ obtained from Refs. [144, 103, 147, 145, 132, 112]. The gray points were obtained under hydrostatic pressure while the colored ones correspond to $Yb(Rh_{1-x}Co_x)_2Si_2$. The P^* dashed line marks the modification from a low-moment to a high-moment state as suggested by Plessel *et al.* [147].

static pressure match quite well those of the Co-doped samples up to a pressure of about 2.5 GPa. Above this pressure the correspondence can not be observed anymore [112].

A comprehensive study of the evolution of magnetism in $Yb(Rh_{1-x}Co_x)_2Si_2$ at intermediate and high temperatures was performed by Klingner *et al.* [112]. By means of susceptibility, resistivity and specific heat measurements a complete $x-T$ phase diagram was drawn. This is shown in Fig. 4.9. The phase diagram can be divided in 4 different x regions: (I) for $0 \leq x \leq 0.12$, T_N and T_L measured in

$Yb(Rh_{1-x}Co_x)_2Si_2$ excellently agree with those measured under hydrostatic pressure; (II) for $0.12 < x < 0.27$, T_N and T_L increase and join at $x = 0.27$, while under hydrostatic pressure both phase transitions come closer at 5 GPa but never join; (III) for $0.27 \leq x \leq 0.58$ T_N and T_L decrease monotonically towards a minimum near $x = 0.58$. The sample with $x = 0.27$ shows a single phase transition down to 20 mK, while in the $x = 0.58$ sample recent measurements indicate the presence of a second transition below T_N [148]; (IV) above $x = 0.58$, hydrostatic pressure experiments suggested a modification from a low-moment (LM) to a high-moment (HM) state along the P^* dashed line. This is not observed in $Yb(Rh_{1-x}Co_x)_2Si_2$ indicating a smooth rather than abrupt change from LM to HM. Hydrostatic and chemical pressure can definitely not be compared for $x > 0.58$, anymore.

The evolution of the magnetic ground state in $Yb(Rh_{1-x}Co_x)_2Si_2$ is characterized by the interplay between the two characteristic energy scales: Kondo (T_K) and RKKY (T_{RKKY}). Both energies decrease with increasing pressure in Yb-based intermetallic systems [149] (see Sec. 2.1). Previous comparisons between chemical and hydrostatic pressure on Yb-based systems have already discussed this phenomena [150, 151]. Klingner *et al.* have shown that the Kondo temperature strongly decreases from 25 K in $YbRh_2Si_2$ to values below 1 K for $x > 0.4$, while T_{RKKY} assumes an almost constant value of about 2 K throughout the whole series [112]. This is beautifully shown in Fig. 4.10 where T_{4f}, i.e. the temperature at which the entropy reaches $0.5Rln2$, the Sommerfeld coefficient γ_0 and the temperature at which the coherence maximum T_{max} in the resistivity $\rho(T)$ appears are plotted as a function of x [112]. This agrees with the fact that both temperatures have a different dependence on the hybridization strength parameter J - faster exponential decrease for T_K and a quadratic decrease for T_{RKKY}- which in turn is modified by the pressure (see Sec. 2.2.4). It is evident the change of relevant energy scale from the Kondo into a dominant T_{RKKY} for concentrations $x > 0.4$. The use of chemical pressure in $Yb(Rh_{1-x}Co_x)_2Si_2$ offers the possibility to investigate the evolution from itinerant to local magnetism by modifying J. Moreover, the analysis of the Weiss temperature θ_W from fits of the low-T magnetic susceptibilities of $Yb(Rh_{1-x}Co_x)_2Si_2$ samples with $B \perp c$ has shown that ferromagnetic correlations increase with increasing x achieving a maximum in the range $0.27 \leq x \leq 0.38$ where θ_W is positive. Additional experiments have confirmed the sample with $x = 0.27$ to be a ferromagnet with moments along the c-axis. This discovery is not a surprise when we consider that in $YbRh_2Si_2$ strong ferromagnetic fluctuations have been detected [153, 63] and Knebel *et al.* have proposed a ferromagnetic ground state above 5 GPa [145].

Quantum criticality of isoeletronic substituted $YbRh_2Si_2$ was extensively studied by Friedemann *et al.* [117, 154] using electrical resistivity, ac-susceptibility and magnetization. Rhodium in $YbRh_2Si_2$ was initially doped with iridium (negative

pressure) and cobalt (positive pressure). In Ref. [117] the authors have specifically studied the influence of chemical pressure on the field-induced QCP. A 3D phase diagram which summarizes the major findings of Ref. [117] is shown in Fig 4.11. These findings are: (i) The AF state is stabilized through the application of positive chemical pressure, as expected. (ii) The position of the suggested breakdown of the Kondo effect manifesting itself as a Fermi surface reconstruction depends only weakly on chemical pressure, although the Kondo effect itself is known to be strongly pressure dependent. (iii) For positive pressure, the AF QCP at H_N is located in the regime with intact Kondo screening ($H_N > H^*$) where the SDW theory is expected to be applicable. (iv) For negative chemical pressure, on the other hand, H_N is separated from H^* towards lower fields with an intermediate spin-liquid (SL) type of ground state emerging. Obviously, here, AF order and the FL ground state are not connected by a single QCP, but are separated by a SL region. Moreover, it needs to be understood why in pure $YbRh_2Si_2$, the AF QCP is "locked-in" by the Kondo breakdown. In the framework of the local critical scenario a coincidence of the two occurs as a natural consequence of reduced dimensionality of the AF quantum critical fluctuations [51], whereas the intersection observed in 7% Co is predicted in the 3D case.

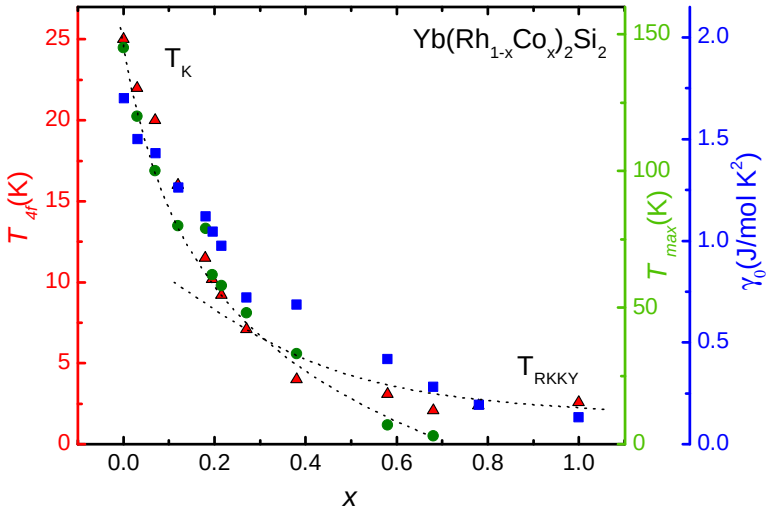

Figure 4.10 – Evolution of the characteristic energy scales T_K and T_{RKKY} with x in $Yb(Rh_{1-x}Co_x)_2Si_2$. These have been estimated from T_{4f}, i.e. the temperature at which the entropy reaches $0.5Rln2$, the Sommerfeld coefficient γ_0 and the temperature of the coherence maximum T_{max} in the resistivity. Figure from Refs. [110, 112].

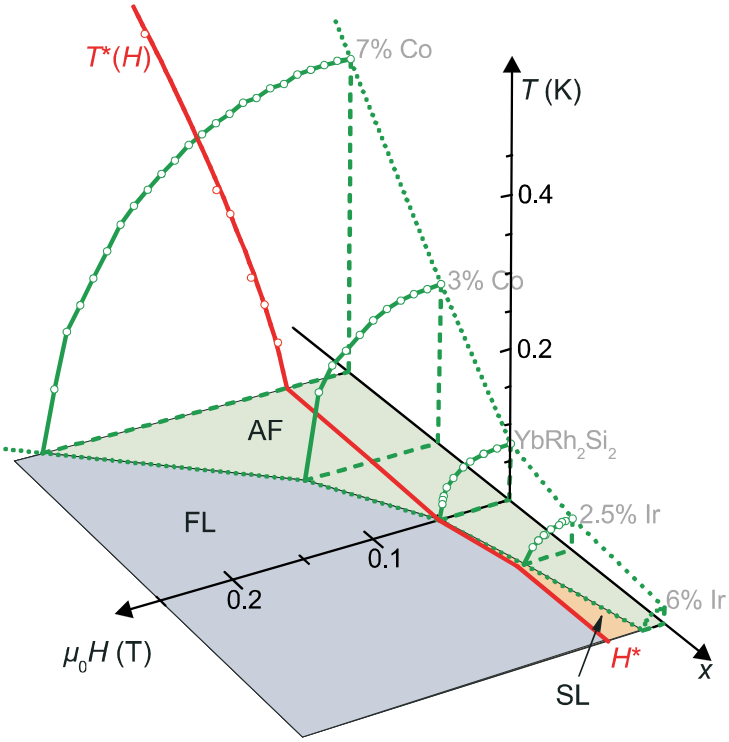

Figure 4.11 – Evolution of the $H-T$ phase diagram of $YbRh_2Si_2$ under positive (Co substitution) and negative (Ir substitution) chemical pressure. The zero temperature plane displays H versus the chemical pressure x. The green lines indicate the antiferromagnetic (AF) phase transition border lines. The red line represents the x-dependence of the Kondo-breakdown line for $T^*(H) \to 0$. The orange area represents the spin-liquid (SL) ground state while the gray area indicates the Fermi-liquid (FL) ground state. This figure was taken from Ref. [152].

4.2 Itinerant vs. local magnetism in $Yb(Rh_{1-x}Co_x)_2Si_2$

In this section, the evolution of the magnetism from a more itinerant character in $YbRh_2Si_2$ towards the more local character in $YbCo_2Si_2$ is analyzed by means of magnetization measurements of $Yb(Rh_{1-x}Co_x)_2Si_2$ single crystals at low temperatures. The magnetic field is mostly applied along the magnetic easy axis, i.e. $H \perp c$. All measurements were carried out in the Faraday magnetometer (see Sec. 3.2.1). From these measurements the values of the magnetic moment $\mu_N(H_N)$ just above the critical field H_N which suppresses the magnetic ordered state as well as the magnetic moment $\mu_{H0}(H_0)$ at the H_0 anomaly (close to the saturation magnetization μ_{sat}) at higher fields can be extracted. The comparison of these values with the measured ESR g-factor and with the energy scales extracted from

Fig. 4.10 allows to derive conclusions about the itinerant/local character of the magnetism and about the evolution of the Fermi surface in $Yb(Rh_{1-x}Co_x)_2Si_2$.

4.2.1 Magnetization of $Yb(Rh_{1-x}Co_x)_2Si_2$ with $0 \leq x \leq 0.27$

4.2.1.1 $YbRh_2Si_2$ and $Yb(Rh_{0.93}Co_{0.07})_2Si_2$

The magnetization curves for $YbRh_2Si_2$ at low temperatures have been shown and discussed in Sec. 4.1.1. Here, selected measurements have been chosen to compare them with those for $Yb(Rh_{0.93}Co_{0.07})_2Si_2$. Single crystals of $Yb(Rh_{0.93}Co_{0.07})_2Si_2$ have been already investigated by Westerkamp *et al.* [125] and Friedemann *et al.* [117]. Two phase transitions in zero field at $T_N = 0.4\,\mathrm{K}$ and $T_L = 0.06\,\mathrm{K}$ were observed in ac-susceptibility and resistivity. The transition at T_N can be

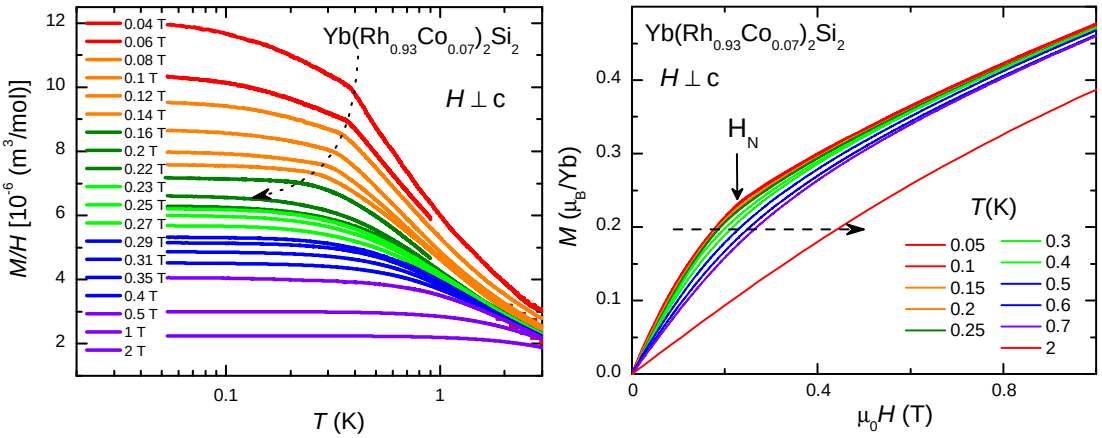

Figure 4.12 – Left: Temperature dependence of dc-susceptibility $\chi = M/H$ for $Yb(Rh_{0.93}Co_{0.07})_2Si_2$. The AFM phase transition T_N is marked by an arrow. Right: Field dependence of the magnetization at different temperatures. The kink at H_N marks the phase transition from an AFM into the paramagnetic state.

suppressed to zero temperature by a magnetic field $H_N(T = 0) = 0.23\,\mathrm{T}$ while the transition at T_L splits into two transitions in field which have critical fields $H_{L1} = (0.02)\,\mathrm{T}$ and $H_{L2} = (0.05)\,\mathrm{T}$, respectively. From the H-dependence of the ordering temperatures and the little chemical pressure that 7% of cobalt exerts, it has been concluded that both transitions are AFM. A maximum in the ac-susceptibility in field was associated with the T^* line and it was demonstrated that it remains at the same position found in the stoichiometric $YbRh_2Si_2$. Therefore the AFM border line $T_N(H)$ and the T^* intercept each other and the $T^*(H)$ line falls inside the AFM ordered region of the phase diagram [117].

The left panel of Fig. 4.12 shows the temperature dependence of the uniform susceptibility $\chi = M/H$ in several fields with $H \perp c$. The kink at $T_N = 0.4\,\mathrm{K}$ marks the onset of the AFM state. Surprisingly, M/H keeps increasing below T_N and saturate at a high value of $12 \times 10^{-6}\,\mathrm{m}^3/\mathrm{mol}$ indicating the presence of strong FM fluctuations. No other signature of phase transition below T_N is further observed. T_N shifts to lower temperatures as the external magnetic field is increased (see dashed arrow in Fig. 4.12, left). A magnetic field of 0.23 T is enough to suppress the AFM order to zero. The field dependence of the magnetization at temperature below and above T_N is shown in the right panel of Fig. 4.12. At 0.05 K it shows a sudden increase of the magnetic moment for very small fields and at 0.23 T a kink at H_N marks the transition into the paramagnetic state. The transition at H_N can be followed up to 0.3 K although it becomes smooth. Above H_N the value of the magnetic moment is small $\mu_N(H_N) \approx 0.23\mu_\mathrm{B}/\mathrm{Yb}$ but almost four times larger than that of $YbRh_2Si_2$. For $H > H_N$, the magnetization strongly increases indicating that $M(H)$ is far from its saturation value. For higher temperatures no other feature was found and at the lowest temperature no hysteresis effects could be detected.

We focus now on the energy scale $T^*(H)$. To get more insights into its nature, we have performed the analysis proposed in Ref. [13, 57] for the two single crystals: $YbRh_2Si_2$ and $Yb(Rh_{0.93}Co_{0.07})_2Si_2$. In analogy with the Hall-effect signatures observed at $T^*(H)$, it has been proposed to fit M vs. H with the integral of the following step function:

$$f(H,T) = A_2 - \frac{A_2 - A_1}{1 + (H/H^*)^p} \tag{4.6}$$

where parameters A_1 and A_2 denote the linear slope of M vs. H before and after the kink, which is associated with H^* (cf. Fig. 4.13). Since M vs. H is not linear for $H \geq H^*$, the authors suggested to fit the quantity $\tilde{M} = M + (dM/dH)H$ vs. H which represents the derivative of the magnetic free energy and is linear at least up to 2 T (right frames of Fig. 4.13). There is a disadvantage to do that: The kink is shifted to lower fields, e.g., in $YbRh_2Si_2$ the kink observed at 0.1 T is shifted to ≈ 0.05 T showing that the position of $H^*(T)$ stricktly depends on how it is defined. This could have fundamental consequences: For instance, the fact that at 50 mK in the stoichiometric crystal the critical fields H_N and H^* almost coincide would imply that at temperatures lower that 50 mK these energy scales might intersect each other (this hypothesis is currently being investigated by measurements of the Hall effect under pressure). For Co concentrations higher than 7% this analysis could not be performed anymore because of the strong influence of the H_L transition on the curvature of M vs. H. In the right frames of Fig. 4.13 the black lines are the fit to the data performed by integrating equation 4.6. The little humps are a consequence of the metamagnetic-like transition at H_N.

The results of such fits are summarized in Fig. 4.14. The data for $YbRh_2Si_2$ agree well with those in Fig. 4.4b and the FWHM of the crossover fit function is proportional to T as it was found in recent Hall effect measurements by Friedemann *et al.* [61]. With $x = 0.07$ the AFM ordered region expands while the crossover field H^*, associated with the energy scale $T^*(H)$, is slightly influenced by the chemical substitution, as observed in Ref. [117]. In the $Yb(Rh_{0.93}Co_{0.07})_2Si_2$ sample $T^*(H)$ follows an almost linear H dependence outside the AFM phase, deviates from linearity at $T < T_N(0)$ and ends clearly inside the magnetic phase.

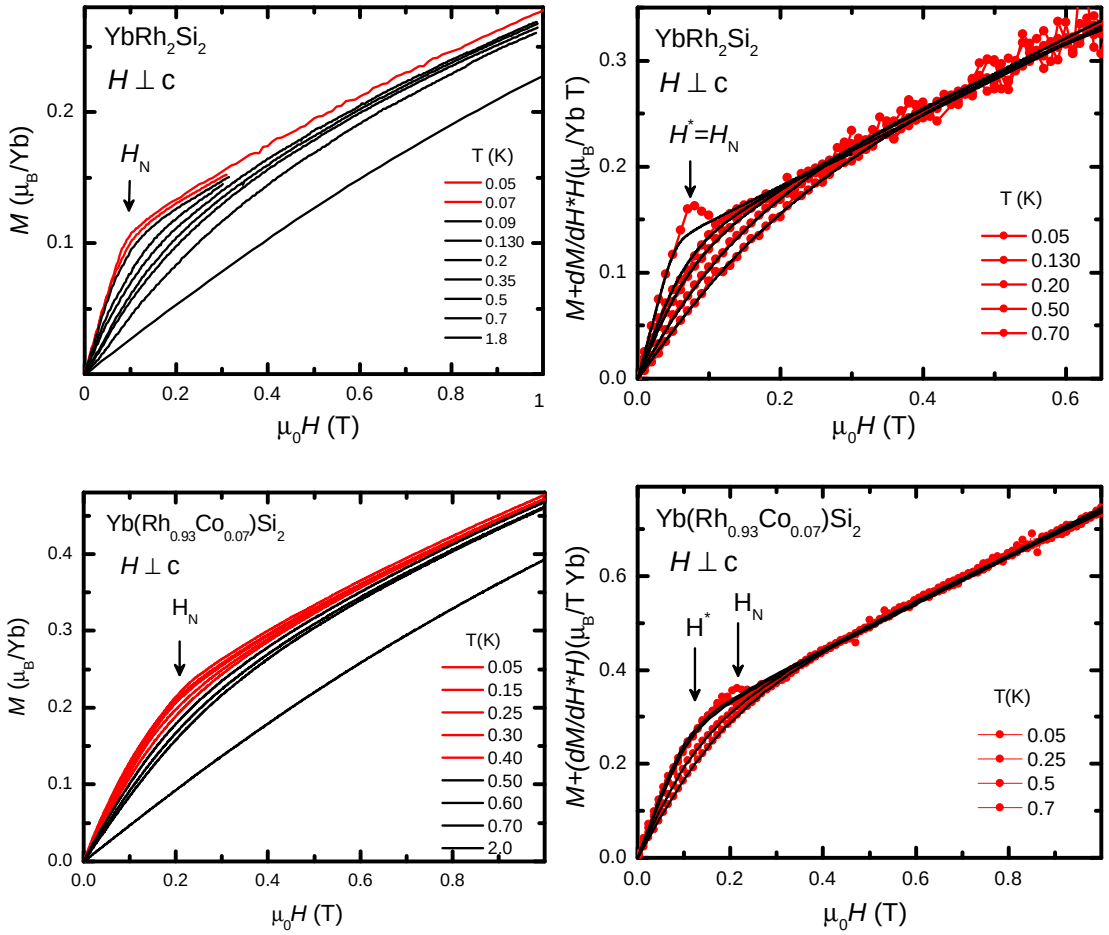

Figure 4.13 – Left: Magnetization isotherms for two single crystals with field $H \perp c$ axis. Red lines indicate measurements at temperatures $T < T_N$. H_N and H^* are the fields associated with T_N and T^* at 50 mK. In $YbRh_2Si_2$ the two fields almost coincide. Right: $\tilde{M} = M + (dM/dH)H$ vs. H for the same two single crystals. The little humps, visible just above H_N, denote the phase transition and their shape is a consequence of how $\tilde{M}$ is calculated.

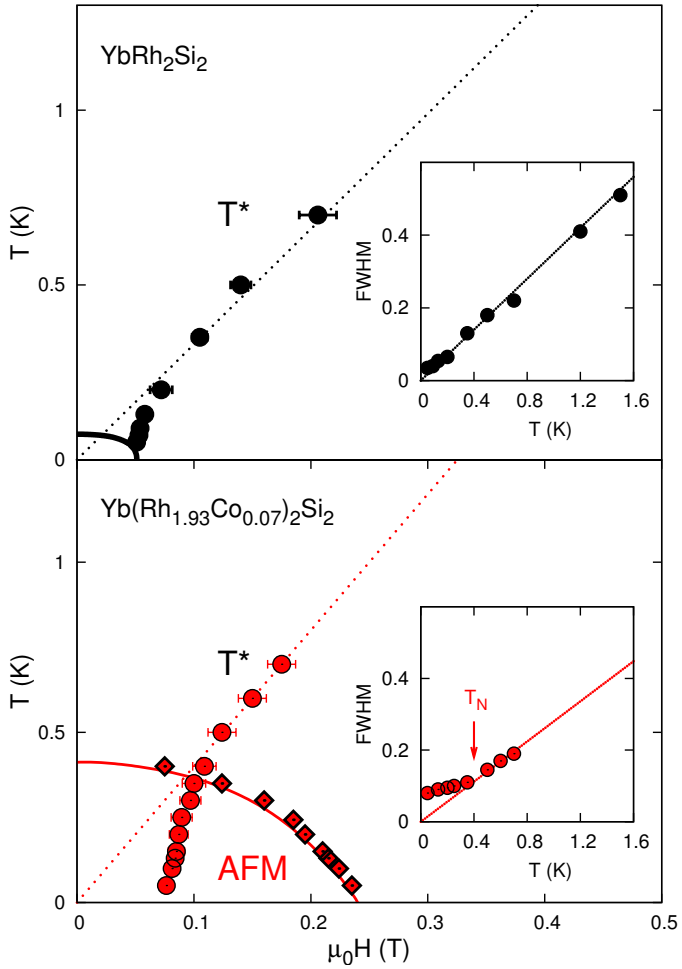

Figure 4.14 – Magnetic phase diagrams from magnetization measurements. The data points for the T^* line comes from the fitting of the crossover function (equation 4.6). The dotted lines are guides to the eye. The inset display the FWHM of the crossover function plotted over the temperature.

The FWHM of the crossover fit function also depends linearly on field outside the phase, but remains constant inside, suggesting either that such an analysis is valid only for $T \geq T_N(0)$, where it is not influenced by the ordered magnetic structure, or that the Fermi surface changes continuously at $T = 0$ inside the magnetic phase. Anyway, the fact that the $T^*(H)$ line ends inside the AFM ordered phase has two important consequences: i) there are two field-induced QCPs, one associated with the $T^*(H)$ line and the other with $T_N(H)$, ii) the latter must have itinerant character and should be described by the SDW model (see Sec. 2.3.1). Quantum criticality at this QCP is analyzed in Sec. 4.3 by means of the magnetic Grüneisen ratio (see Sec. 2.3.4).

4.2.1.2 $Yb(Rh_{0.88}Co_{0.12})_2Si_2$

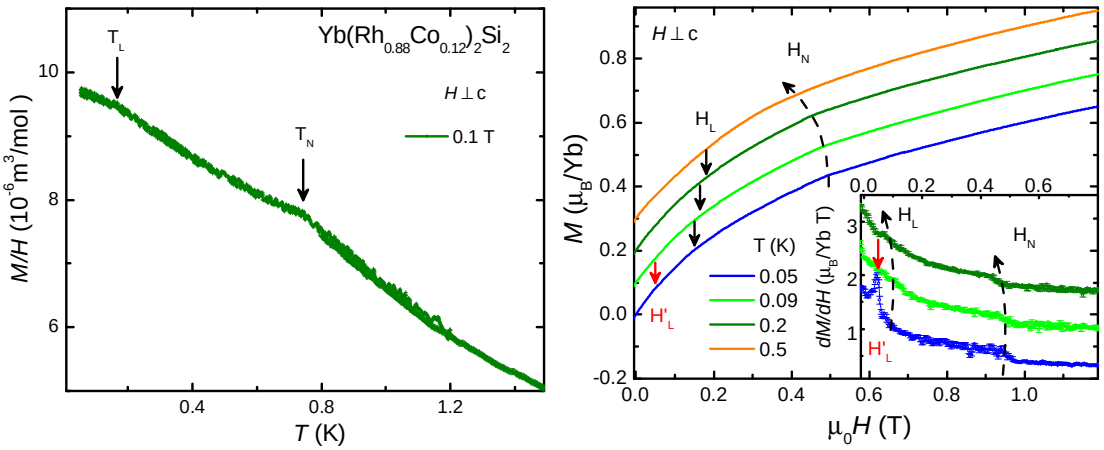

Figure 4.15 – Left: Temperature dependence of the susceptibility $\chi = M/H$ at 0.1 T. Two kinks marked by arrows indicate the transition temperatures T_N and T_L. Right: Isothermal magnetization curves at selected temperatures below and above T_N and T_L. The curves are shifted by $0.1\mu_B$/Yb. The arrows indicate kinks which are associated with the critical fields H'_L and H_N. This is better shown in the derivative dM/dH plotted in the inset.

The sample with $x = 0.12$ has been already investigated by means of ac-susceptibility and shows a similar behavior as the one with $x = 0.07$ [125]. At $T_N = 0.78$ K AFM order sets in and below T_N another, possibly AFM, phase transition has been detected at $T_L = 0.28$ K. This is reproduced in the dc-susceptibiliy data taken at 0.1 T and shown in Fig. 4.15 (left panel). The arrows indicate the kinks at T_N and T_L where the susceptibility changes slope. Like in the $x = 0.07$ sample, the susceptibility keeps increasing below T_L. A magnetic field of about 0.5 T is enough to suppress T_N to zero while a field of $\mu_0 H_L = 0.05$ T suppresses T_L to zero in a similar fashion. This is well shown in Fig. 4.15 (right panel) where the magnetization isotherms at selected temperatures are depicted. M vs. H at 0.05 K features three kinks that we associate with H'_L, H_L and H_N. A better understanding in given by the derivative dM/dH, displayed in the inset, which shows a peak at $H_{,L}$ and a drops at H_L and H_N. This is in agreement with the ac-susceptibility $\chi'(H)$ measured at 0.02 K by T. Westerkamp where the broad drop in $\chi'(H)$ at 0.12 T was associated with a second transition, indicating that T_L splits in two branches in field [132]. Above H_N the value of the magnetic moment is still small $\mu_N(H_N) \approx 0.45\mu_B$/Yb but double of that in $Yb(Rh_{0.93}Co_{0.07})_2Si_2$. The value of $\mu_N(H_N)$ seems to increase linearly with the value of T_N. For $H > H_N$, the magnetization strongly increases indicating that $M(H)$ is far from its saturation value.

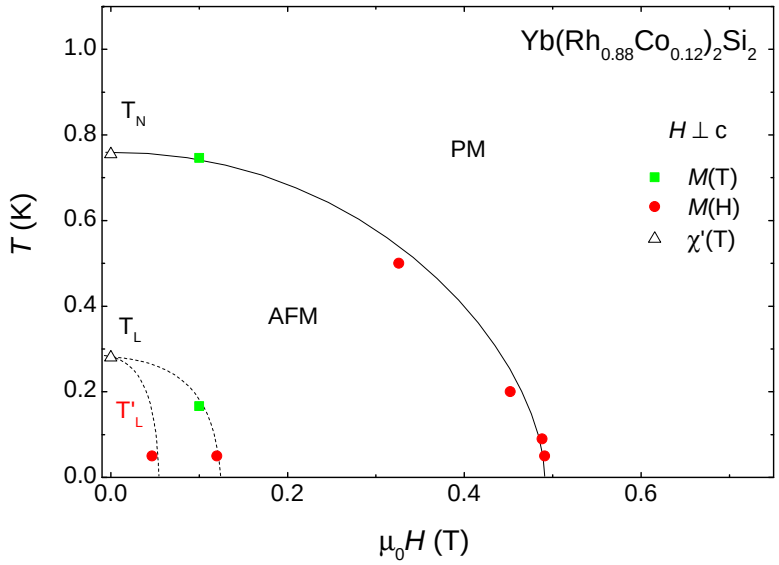

Figure 4.16 – $T-H$ phase diagram of $Yb(Rh_{0.88}Co_{0.12})_2Si_2$. The Néel temperature in zero field was determined by ac-susceptibility (△) [125]. The black line represents a fit to the data with an empirical elliptic function to estimate the critical field $H_N(T=0) = 0.49\,\mathrm{T}$. The black dashed lines are the phase boundary lines taken from Ref. [125].

For higher temperatures no other feature was found and at the lowest temperature no hysteresis effects could be detected. For this and higher cobalt concentrations the analysis performed using equation 4.6 could not be performed anymore, because of the high H_L and the stronger curvature of M vs. H. However, the T^* line could be observed as a maximum in the ac-susceptibility by T. Westerkamp and it seems to be at a similar position in the phase diagram as for the $x = 0.07$ sample [132]. The resulting phase diagram is shown in Fig. 4.16, were the ordered phases are considered to be AFM.

4.2.1.3 $Yb(Rh_{0.82}Co_{0.18})_2Si_2$

We focus now on the next Co concentration $x = 0.18$. $Yb(Rh_{0.82}Co_{0.18})_2Si_2$ has not been investigated before. It features two anomalies similar to those observed for $x = 0.12$ and $x = 0.07$. This is shown in Fig. 4.17 (left panel). The arrows indicate the phase transitions at T_N (red) and T_L (blue). At T_N the susceptibility shows a weak kink, whereas at T_L it shows a pronounced drop typical for AFM ordering, and saturates at a quite high value of $9 \times 10^{-6}\,\mathrm{m^3/mol}$. A magnetic field of about $0.7\,\mathrm{T}$ suppresses T_N to zero, while the field splits T_L into two branches which are suppressed at critical fields $H'_L = 0.15\,\mathrm{T}$ and $H_L = 0.22\,\mathrm{T}$, similar to what was seen in $Yb(Rh_{0.88}Co_{0.12})_2Si_2$. This is shown in Fig. 4.17 (right panel) where the

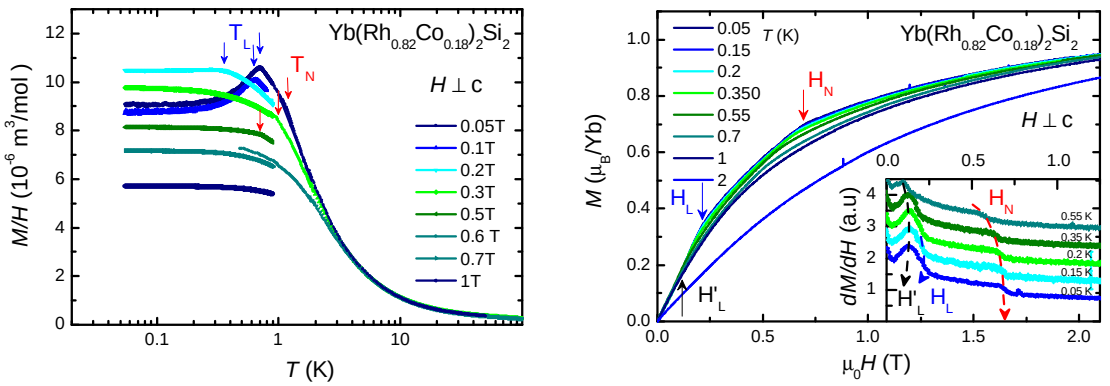

Figure 4.17 – Left: Temperature dependence of the susceptibility of $Yb(Rh_{0.82}Co_{0.18})_2Si_2$ measured at different fields. The black arrows marks the kinks indicating the onset of the AFM ordering at T_N. The red arrows marks the second transition at T_L below which $\chi(T)$ decreases rapidly. Right: Isothermal magnetization curves where two clear features are observed at H_N and H_L. The first is a smooth metamagnetic-like increase of the magnetization whereas the second one is a small kink. This is emphasized in the derivative $dM/dH(H)$ plotted in the inset. Another kink can be identified at H'_L as in the sample with $x = 0.12$.

magnetization isotherms at selected temperatures are depicted. M vs. H at 0.05 K features a metamagnetic-like increase of the magnetization followed by a first kink and another kink at higher fields that we associate with H_N. This is emphasized in the derivative dM/dH plotted in the inset. dM/dH shoes a peak at $\mu_0 H'_L = 0.15$ T, a drop at $\mu_0 H_L = 0.22$ T and another drop at $H_N = 0.7$ T. Fig. 4.18 (left panel) displays two magnetization isotherms taken at the lowest measured temperature of 0.05 K to show that there is no hysteresis. The magnetic moment at H_N starts to become quite large $\mu_N(H_N) \approx 0.7\mu_B$/Yb, indicative that Co doping weakens the Kondo interaction faster than it does with the RKKY interaction (cf. Fig. 4.10). However, this value is still far from the saturation one. This is supported by the high value of the Sommerfeld coefficient $\gamma_0 = 1.3$ J/K^{2}mol [110], which gives an indication of the effective mass of the quasiparticles. The final magnetic phase diagram is shown in Fig. 4.18 (right panel). This magnetic phase diagram was also confirmed by resistivity and ac-susceptibility measurements [155]. As for $x = 0.12$ three border lines can be identified. The region between $T_N(H)$ and $T_L(H)$ can be likely associated with an AFM order, while the ground state below $T_L(H)$ is still unknown. However, the $\chi(T)$ measurements strongly suggests another AFM phase.

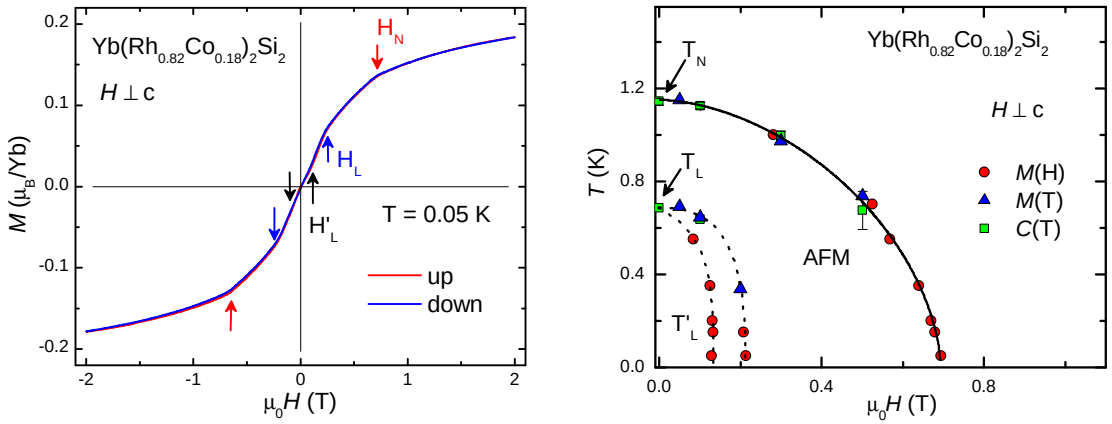

Figure 4.18 – Left: Magnetization curves between -2 and 2 T taken by sweeping up and down the magnetic field to show that there is no hysteresis at the lowest measured temperature of 0.05 K. Right: $T-H$ phase diagram of $Yb(Rh_{0.82}Co_{0.18})_2Si_2$. The green triangles are data points from specific heat measurements from Ref. [110]. The black line represents a fit to the data with an empirical elliptic function to estimate the critical field $H_N(T=0)=0.7\,\mathrm{T}$.

4.2.1.4 $Yb(Rh_{0.73}Co_{0.27})_2Si_2$

The sample with $x=0.27$ is somehow unique in the series $Yb(Rh_{1-x}Co_x)_2Si_2$. As reported by Klingner *et al.* [112] this material shows just a single phase transition at $T_N = 1.3\,\mathrm{K}$ in contrast to all other samples with lower Co content[2]. As introduced in Sec. 4.1.3, at $x=0.27$, which corresponds to a hydrostatic pressure of about 4.3 GPa (see phase diagram in Fig. 4.9), T_N and T_L appear to merge to a single magnetic transition, while in the pressure experiments by Knebel *et al.* two distinct phase transitions were observed up to 7 GPa [145]. Moreover, pressure experiments on $YbRh_2Si_2$ have showed that the unit cell c/a-ratio is constant up to the highest applied pressures of 21 GPa [147], while in $Yb(Rh_{1-x}Co_x)_2Si_2$ an increase of c/a has been seen with decreasing unit cell volume with a change of slope exactly at $x=0.27$ [112]. Finally, $Yb(Rh_{0.73}Co_{0.27})_2Si_2$ is at the position of the $x-T$ phase diagram where the RKKY energy scale prevails over the Kondo one (cf. Fig. 4.10) and where the low-T Curie-Weiss fits give slightly positive values of the Weiss temperature ($\Theta_W^{2-4\,\mathrm{K}} = 0.1\,\mathrm{K}$ for $x=0.27$) indicating strong FM correlations [112]. The high-T Curie-Weiss fits still give negative Weiss temperatures (cf. Fig. 4.23, right panel), because it is dominated by the CEF effects.

[2] The label T_N was historically given to this transition temperature because it was thought to be AFM. In this section we demonstrate that it is FM. However, we keep here the nomenclature.

Our magnetization measurements with $H \perp c$ reproduces exactly this scenario. The susceptibility χ vs. T of $Yb(Rh_{0.73}Co_{0.27})_2Si_2$ taken at different fields between 0.1 and 2 T is shown in Fig. 4.19 (top left panel). At a small field of 0.1 T a single phase transition is observed as a sharp peak (black arrow) in $\chi(T)$ down to 0.05 K. This is confirmed by recent ac-susceptibility and resistivity measurements performed by S. Lausberg down to 0.02 K [156]. With increasing H the transition is shifted systematically to lower temperatures. M vs. H taken at several temperatures between 0.05 and 2 K in shown in Fig. 4.19 (top right panel). At 0.05 K the magnetization grows linearly in field and features a sharp kink at $\mu_0 H_N = 0.55$ T after which it increases with a much lower slope. With increasing T the kink is shifted to lower fields, in agreement with behavior of $\chi(T)$. The magnetic moment at H_N, $\mu_N(H_N) \approx 0.85\mu_B$/Yb, is larger than in $Yb(Rh_{0.82}Co_{0.18})_2Si_2$, confirming the continuous suppression of the Kondo effect with increasing x. The resulting

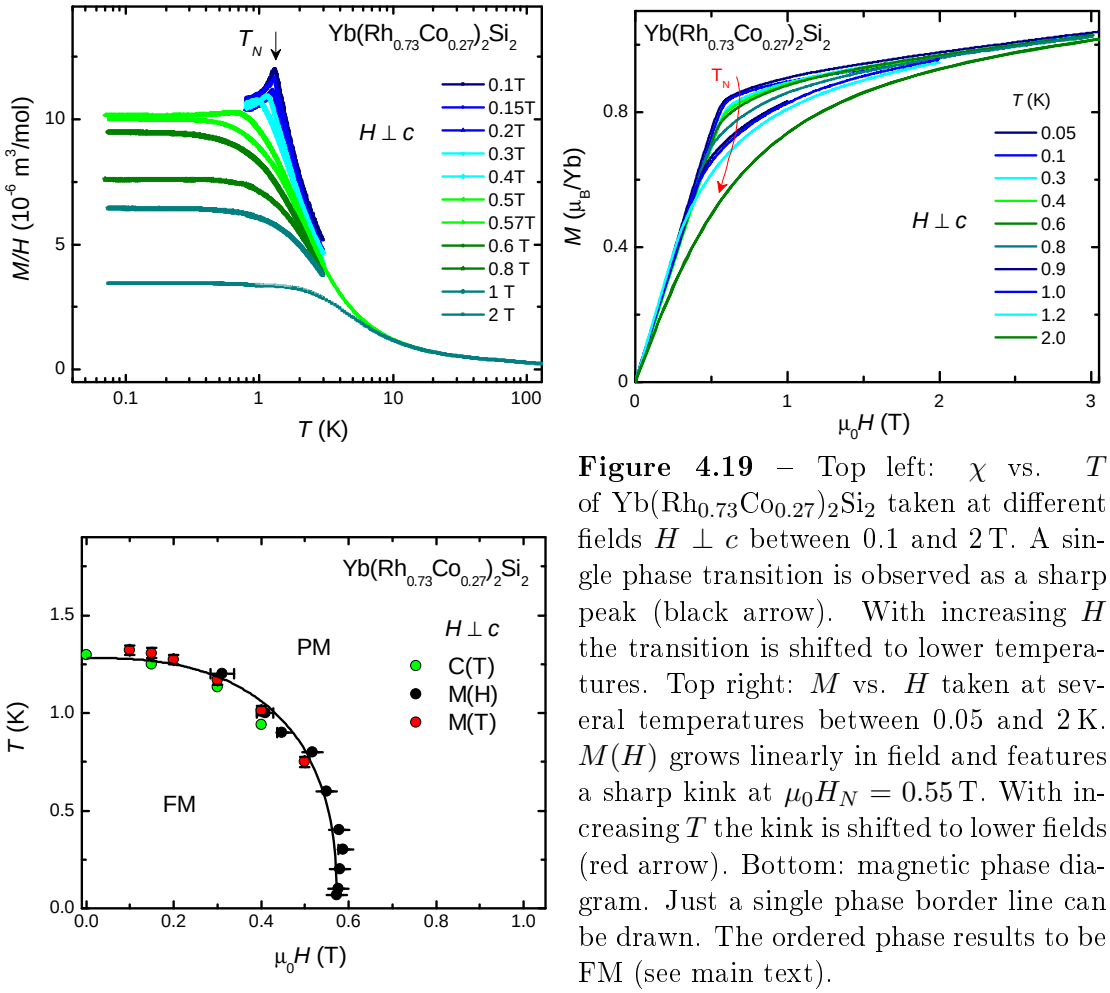

Figure 4.19 – Top left: χ vs. T of $Yb(Rh_{0.73}Co_{0.27})_2Si_2$ taken at different fields $H \perp c$ between 0.1 and 2 T. A single phase transition is observed as a sharp peak (black arrow). With increasing H the transition is shifted to lower temperatures. Top right: M vs. H taken at several temperatures between 0.05 and 2 K. $M(H)$ grows linearly in field and features a sharp kink at $\mu_0 H_N = 0.55$ T. With increasing T the kink is shifted to lower fields (red arrow). Bottom: magnetic phase diagram. Just a single phase border line can be drawn. The ordered phase results to be FM (see main text).

magnetic phase diagram is displayed in Fig. 4.19 (bottom panel). Just a single phase border line can be drawn. This line is expected for an antiferromagnet, i.e. the transition shifts to lower temperatures as the field increases, as for $x < 0.27$ samples. Interestingly, the phase border line is very steep close to the critical field of 0.55 T and might suggest a first order phase transition at $H_N(T = 0)$. Moreover, the line is now well fitted by an almost circular function (see black line in the bottom panel of Fig. 4.19 and Fig. 4.20) and not an elliptic function like for all other sample with smaller x. This is illustrated in Fig. 4.20 where a 3D plot of the outer border line for $0 \leq x \leq 0.27$ obtained from our data is plotted. The $T_N(x)$ line at $H = 0$ and the magnetic moment $\mu_N(H_N)$ increase monotonically with x and reaches a maximum at $x = 0.27$ (cf. Fig. 4.9). On the other side, the critical field $H_N(x)$ at $T = 0$ increases almost linearly in x up to $x = 0.18$, but then drops suddenly at $x = 0.27$. This might indicate a relevant change in the magnetic ordered structure. This observation and the peculiar fact that in $Yb(Rh_{0.73}Co_{0.27})_2Si_2$ the ac-susceptibility measured down to 1.8 K along the magnetocrystalline easy axis starts to become smaller than the ac-susceptibility along the hard axis (a similar behavior was observed in the low-T ferromagnet $YbNi_4P_2$ [157]) motivated

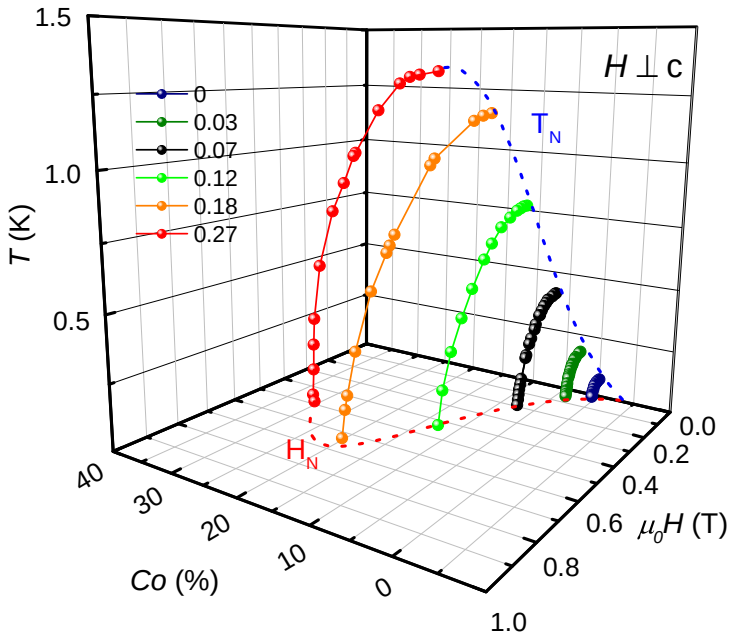

Figure 4.20 – 3D $H - T$ magnetic phase diagram of the series of $Yb(Rh_{1-x}Co_x)_2Si_2$ compounds vs. Co content. For simplicity only the T_N transition is depicted. It can be observed how the magnetic order increase as the cobalt content is increased, the critical field H_N is also increased until a value of ≈ 0.7 T but short after 0.18 decrease to 0.58 T.

S. Lausberg *et al.* [156] to characterize this material along the c-axis (hard-axis). Surprisingly, measurements of the heat capacity and ac-susceptibility have demonstrated that $Yb(Rh_{0.73}Co_{0.27})_2Si_2$ orders ferromagnetically along the c-axis below 1.3 K.

The magnetization measurements at low temperatures for $H \| c$, performed in collaboration with A. Hannaske, are shown in Fig. 4.21. In the left panel the

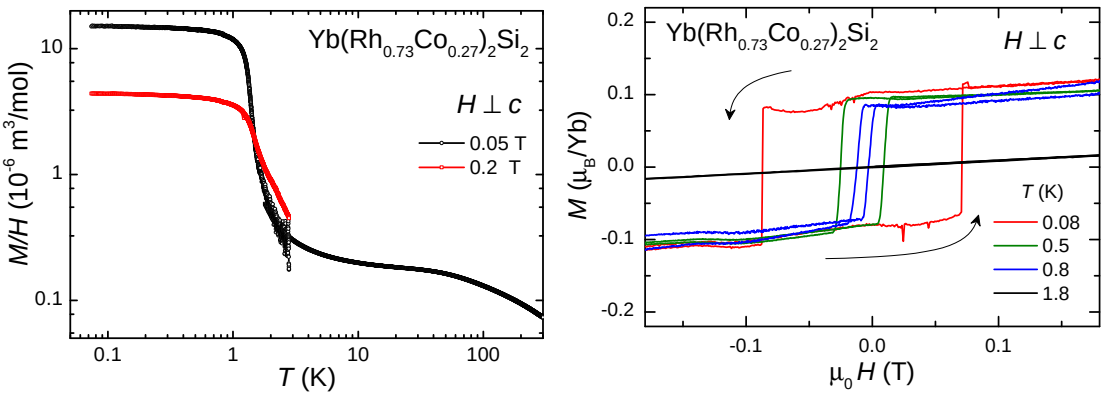

Figure 4.21 – Left: χ vs. T in a double-logarithmic scale. The increase of $\chi(T)$ at $T_N = 1.3$ K indicates the onset of FM order. Right: M vs. H isotherms with hysteresis at temperatures below T_N while at 1.8 K the hysteretic behavior is not present anymore.

temperature dependence of M/H at small fields of 0.05 and 0.2 T is shown. M/H increases at T_N up to a value of about 13×10^{-6} m^3/mol as expected for a ferromagnet. We did not consider the demagnetization factor. The "smoking gun" experiment for a FM material is the field dependent magnetization which is shown in the right panel of Fig. 4.21. It reveals a clear hysteresis at $H = 0$ below 1.3 K, evidencing that the ground state of the compound is indeed FM. Although the transition temperature for $Yb(Rh_{0.73}Co_{0.27})_2Si_2$ should be labeled T_C (FM Curie temperature), we have labeled it T_N (AFM Néel temperature) since it represents the x-evolution of the T_N measured in the pure system ($x = 0$). The behavior of M vs. H indicates that the FM moments are aligned along the c-axis.

The discovery of pressure induce ferromagnetism in $YbRh_2Si_2$ is surprising but, as a matter of fact, consistent with all findings observed before. Strong FM fluctuations in $YbRh_2Si_2$ were previously seen by Ishida *et al.* [153] and Gegenwart *et al.* [63], Knebel *et al.* [145] suggested FM order above 5 GPa and finally Klingner *et al.* [112] measured a positive Weiss temperature at $x = 0.27$. Neutron scattering experiments failed to see the ordered state since the magnetic neutron intensity in masked by the strong elastic peak at $\mathbf{Q} = 0$ [158].

4.2.1.5 Summary

The evolution of magnetism in $Yb(Rh_{1-x}Co_x)_2Si_2$ for $0 \leq x \leq 0.27$ along the magnetic easy axis, i.e. $H \perp c$, is shown in Fig. 4.22 and can be summarized as follows: With increasing Co content the magnetic uniform susceptibility M/H at a constant temperature, e.g. 2 K, increases with increasing x. In addition both observed transition temperatures T_N and T_L become higher with larger x. This results from the continuous suppression of the Kondo screening and the smooth decreasing of the RKKY interaction with increasing x (see Sec. 4.1.3). The value of the susceptibility at 0.05 K seems to be approximately the same for all concentrations, i.e. between 8 and 11×10^{-6} m^3/mol. The behavior of the susceptibility suggests AFM order below T_N and T_L since it shows a peak or kink at both transitions and AFM order is established in $YbRh_2Si_2$. However, FM order has been found in the sample with $x = 0.27$ with ordered moment along the c-axis (explaining the peak in the susceptibility measured with $H \perp c$) and this raises the question whether in the samples with $0 < x < 0.27$ the magnetic order below T_L is FM or not.

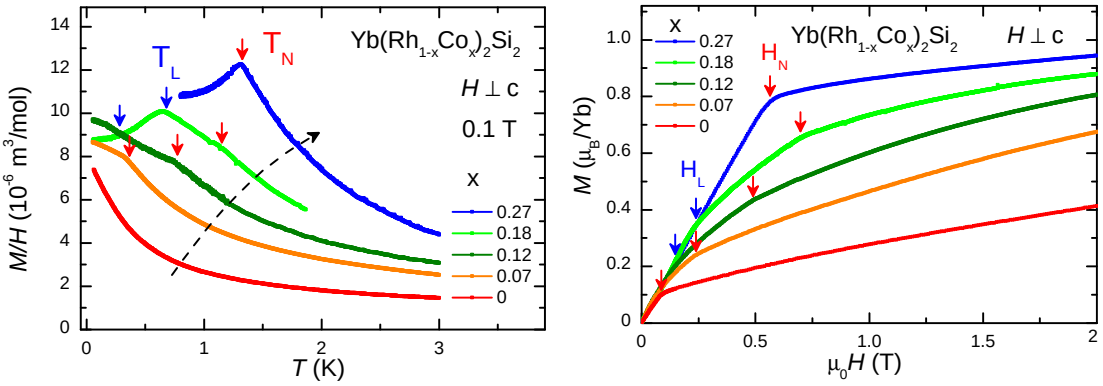

Figure 4.22 – Left: Basal plane susceptibility M/H of $Yb(Rh_{1-x}Co_x)_2Si_2$ for the $0 \leq x \leq 0.27$ single crystals plotted as a function of T. The black arrow indicates the increasing susceptibility with increasing x. Red and blue arrows show the position of T_N and T_L, respectively. The data for $YbRh_2Si_2$ are taken from Ref. [159]. Right: H-dependence of the magnetization for the same set of samples. The magnetic moment at H_N, $\mu_N(H_N)$, increases with increasing Co content.

Isothermal magnetization measurements (see Fig. 4.22, right panel) also show a consistent behavior with the scenario of Ref. [112]. M increases linearly with H and features kinks at the critical fields H_N and H_L. In the sample with $x = 0.27$ just a single kink is observed and no hysteresis, suggesting that the FM moments are aligned along the c-axis where a hysteresis was observed (cf, Fig. 4.21). Outside the ordered phase the magnetic moment at H_N, $\mu_N(H_N)$, increases with increasing Co

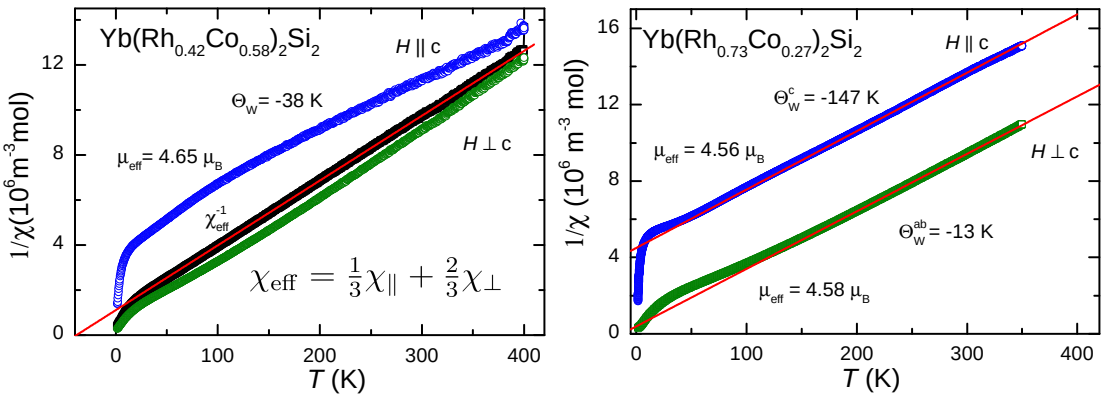

Figure 4.23 – Left: Inverse of the magnetic susceptibility $\chi_{\parallel}$ with $H \| c$ (blue circles) and $\chi_{\perp}$ with $H \perp c$ (green circles) plotted as a function of T along with the averaged value χ_{eff}^{-1} defined in eq. 4.7. The data were taken between 1.8 and 300 K in a constant magnetic field of 2 T. The straight red line represents the Curie-Weiss law. Right: Same plot for $Yb(Rh_{0.73}Co_{0.27})_2Si_2$. The solid lines represent the Curie-Weiss fits performed between 200 and 300 K.

content and reaches a value of $\approx 0.85\mu_B$/Yb for $Yb(Rh_{0.73}Co_{0.27})_2Si_2$. This value is still smaller than the saturation magnetization expected for the Yb^{3+} ion in the tetragonal CEF environment (see Secs. 2.1.1 and 4.1.2).

4.2.2 Magnetization of $Yb(Rh_{1-x}Co_x)_2Si_2$ with $x = 0.58$ and $x = 1$

The next Co concentration studied here is $x = 0.58$, which corresponds to a chemical pressure of about 9 GPa and is located in the $x - T$ phase diagram of Fig. 4.9 at the minimum of $T_N(x)$ and where the P^* line begins. It was suggested by Plessel *et al.* that this line marks the modification from a low-moment state into the high-moment state [147], but this effect does not take place in $Yb(Rh_{1-x}Co_x)_2Si_2$. Taking into account that $Yb(Rh_{0.73}Co_{0.27})_2Si_2$ is FM while the pure $YbCo_2Si_2$ is AFM, it is interesting to investigate the evolution from FM to AFM starting with $x = 0.58$.

The first peculiar feature of $Yb(Rh_{0.42}Co_{0.58})_2Si_2$ is the high-T magnetic susceptibility. In all samples with $0 \leq x \leq 0.27$ and in $YbCo_2Si_2$, both inverse susceptibilities $\chi_{\parallel}^{-1}$ (with $H \| c$) and $\chi_{\perp}^{-1}$ (with $H \perp c$) follows a Curie Weiss behavior above 200 K [110, 111, 112], as shown, e.g., in the right panel of Fig. 4.23 for the $x = 0.27$ sample. In $Yb(Rh_{0.42}Co_{0.58})_2Si_2$ both susceptibilities deviate from the Curie-Weiss behavior as displayed in the left panel of Fig. 4.23. A broad maximum in the $\chi_{\parallel}^{-1}$ vs. T curve can be seen around 100 K. This behavior is associated with

a modification of the CEF scheme for this material compared to that of the other concentrations. However, the calculated averaged susceptibility

$$\chi = \frac{1}{3}\chi_{\parallel} + \frac{2}{3}\chi_{\perp} \tag{4.7}$$

follows the expected Curie-Weiss behavior between 50 and 300 K with an effective moment $\mu_{\text{eff}} \approx (4.56 \pm 0.1)\mu_{\text{B}}$, close to that of the free Yb^{3+} ion, and a Weiss temperature of −38 K.

The low-T measurements were performed first with $H \perp c$, more precisely with $H \| [110]$. The data are shown in Fig. 4.24. The left panel shows the susceptibility $\chi = M/H$ measured at several fields from 0.05 to 4 T. At 0.05 T, two anomalies can be observed. A sharp peak at $T_N = 0.82$ K and a smooth kink at $T_L = 0.65$ K

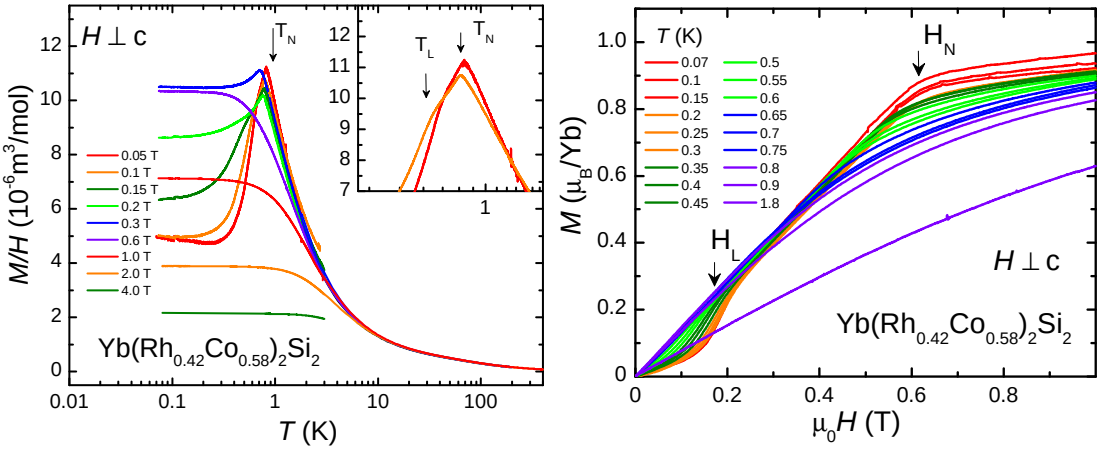

Figure 4.24 – Left: T- dependence of the susceptibility $\chi = M/H$ of $Yb(Rh_{0.42}Co_{0.58})_2Si_2$ measured at different fields between 0.05 and 4 T perpendicular to the c-axis. The inset zooms into the region of the peaks. Right: Isothermal magnetization curves at many temperatures to systematically investigate the magnetic phase diagram. The critical field H_L is associated with the metamagnetic-like transition and H_N is associated with the kink after which the magnetization saturates.

which disappears at fields larger than 0.1 T.[3] This is emphasized in the inset of the same panel. The pronounced peak at T_N persists up to a magnetic field of 0.6 T where the susceptibility assumes a high value of about $10.5 \times 10^{-6}\,\text{m}^3/\text{mol}$. The phase transition at T_L was not seen in the heat capacity measurements of Ref. [112], possibly because both transitions are in a narrow temperature region

[3] We use the same nomenclature for the two transition temperatures, like in the case of the $x = 0.27$ compound, in agreement with Ref. [112], although one of the transitions is FM.

and the feature at T_L is very weak. A consistent picture is give by the magnetization isotherms shown in the right panel of Fig. 4.24. M vs. H at 0.05 K features a metamagnetic-like increase at $\mu_0 H_L = 0.2$ T and a sharp kink at $\mu_0 H_N = 0.6$ T. The magnetic moment at H_N, $\mu_N(H_N) \approx 0.9\mu_B$/Yb is slightly larger than that in $Yb(Rh_{0.73}Co_{0.27})_2Si_2$. Both anomalies at H_L and H_N can be followed in the derivative dM/dH up to 0.7 K. The resulting points are plotted in the phase diagram of Fig. 4.25 (left panel). Both phase border lines follow a behavior expected for

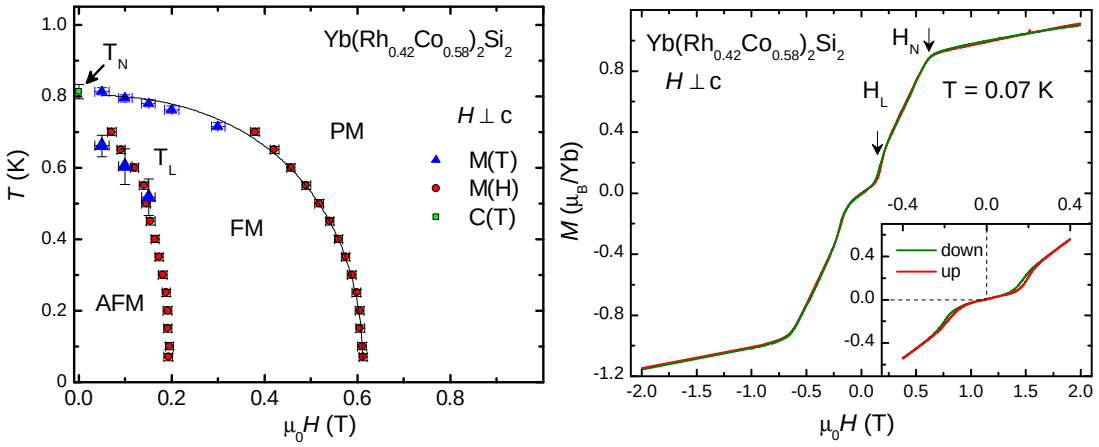

Figure 4.25 – Magnetic phase diagram of $Yb(Rh_{0.42}Co_{0.58})_2Si_2$ with $H\|[100]$. Two phase transition lines $T_N(H)$ and $T_L(H)$ are derived from field and temperature dependencies of the magnetization and from the specific heat of Ref. [148]. Isothermal magnetization measurements at 0.07 K where the field was swept up and down between -0.4 and 0.4 T. The inset is a zoom in the field region where a slight hysteresis at H_L is observed.

an antiferromagnet. This does not rule out the presence of a FM phase, as it was demonstrated for $Yb(Rh_{0.73}Co_{0.27})_2Si_2$. We checked that at $H = 0$ no remanent magnetization is present. Two subsequent field sweeps (up and down) were carried out at 0.07 K and the results are shown in the right panel of Fig. 4.25. Only tiny hysteresis were observed across $H_L(H)$ but no hysteresis at $H = 0$. A similar effect was observed in $YbCo_2Si_2$ where the commensurate AFM ground state is changed into a incommensurate AFM one by a field applied along the [100] direction (see. Fig. 4.51) [108, 109]. This suggests that the ground state might be similar to that of $YbCo_2Si_2$. Measurements along the c-axis provide, however, a different picture. The susceptibility and magnetization are shown in Fig. 4.26 on the left and right panels, respectively. The temperature dependence of the susceptibility for $H\|c$ shows a strong increase up to values close to 100×10^{-6} m^3/mol at $T_N = 0.82$ K

which indicates the onset of FM order. Just below T_N, M/H decreases strongly suggesting another transition into an AFM or canted AFM ground state. This is corroborated by the field dependence of the magnetization at selected temperatures. At 0.7 K, i.e. between T_L and T_N, a remanent magnetization of about $0.01\,\mu_B$/Yb with no hysteresis is measured, evidencing the FM state. Below T_L,

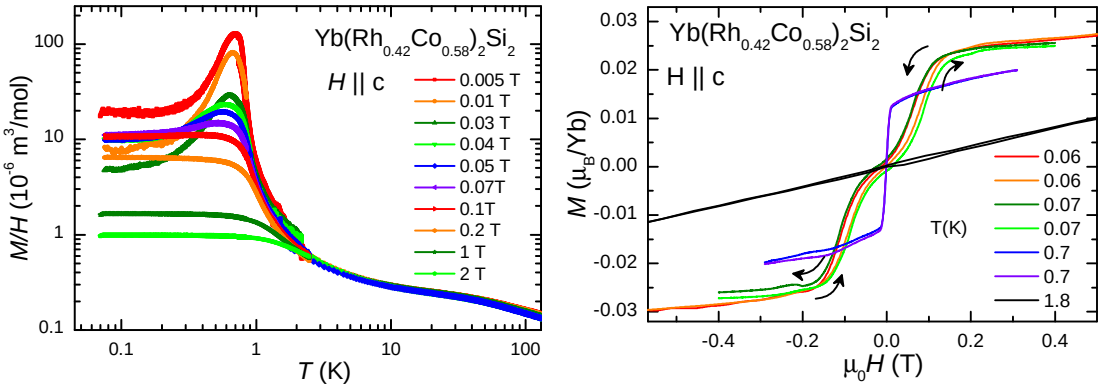

Figure 4.26 – Left: Temperature dependence of the magnetization of $Yb(Rh_{0.42}Co_{0.58})_2Si_2$ divided by field for $H \| c$. The strong increase of M/H up to values close to $100 \times 10^{-6}\,m^3/mol$ at $T_N = 0.82\,K$ indicates the onset of FM order. The pronounced peak indicate the lower AFM ground state. Right: Field dependence of the magnetization at selected temperatures. At 0.7 K, i.e. between T_L and T_N, a remanent magnetization of about $0.01\,\mu_B$/Yb with no hysteresis is observed, evidencing the FM state. Below T_L, M vs. H shows metamagnetic-like transitions with a tiny remanent magnetization. Measurements from Ref. [158].

M vs. H shows metamagnetic-like transitions with a tiny remanent magnetization indicating that the ground state has switched from FM to AFM or, possibly, canted AFM since at $H = 0$ a remanent moment is still visible.

The magnetization of a single crystal with $x = 1$, i.e. $YbCo_2Si_2$, is studied in great detail in this thesis. All measurements are shown and discussed in Sec. 4.5. For the sake of discussing the evolution of magnetism from more itinerant to more local in $Yb(Rh_{1-x}Co_x)_2Si_2$ we need just to mention that $YbCo_2Si_2$ behaves simply like a local antiferromagnet. The value of the magnetization just above H_N is 1.4 μ_B/Yb with $H \perp c$ and is in agreement with the saturated moment calculated by Hodges [126] and by Klingner *et al.* [112], confirming the local magnetic behavior of the Yb $4f$ quasi-holes.

4.2.3 Evolution from itinerant to local magnetism

So far we have focused the attention on the physics of $Yb(Rh_{1-x}Co_x)_2Si_2$ at low magnetic fields, where the Kondo effect is not completely suppressed and every crystal shows at $H = 0$ a magnetic ordered ground state caused by the RKKY interaction. In this section a comprehensive magnetization study of the relevant energy scales under chemical pressure and at higher fields (with $H \perp c$) will be presented, in order to show the evolution from the more itinerant character of magnetism in $YbRh_2Si_2$ to the more local character at high chemical pressure, i.e. in $YbCo_2Si_2$, and at high fields where the magnetization reaches its saturation value. The largest value of the field used for the magnetization measurements is 12 T (see Sec. 3.2.1).

At low fields ($H \perp c$) and small Co content, the H-dependence of the magnetization has been already shown in Fig. 4.22. $M(H)$ increases linearly and shows kinks at the critical fields H_L and H_N. For $H > H_N$ the system is paramagnetic (PM) and the ground state is a heavy-fermion Fermi liquid [102, 7, 107, 111]. At

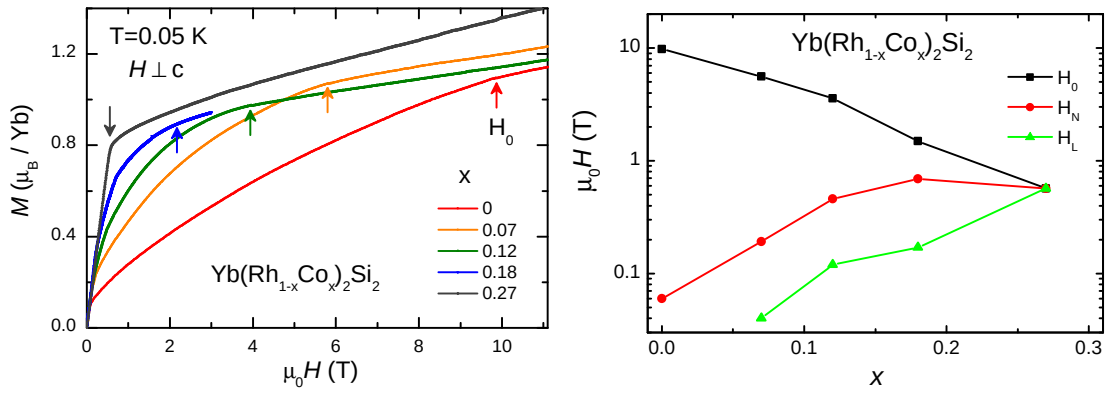

Figure 4.27 – Left: high-field magnetization curves for for $0 \leq x \leq 0.27$ taken at 0.05 K for $H \perp c$. The upward arrows indicate the position of the kink associated with the field H_0. The downward arrows mark the critical field H_N. Right: evolution of the critical fields H_L, H_N and H_0 with Co content x for $0 \leq x \leq 0.27$. All converge to the same point at $x = 0.27$.

higher x, the critical fields H_L and H_N assume larger values and above them the ground state is a Fermi liquid but the heavy-fermion character is strongly reduced, e.g. in $YbCo_2Si_2$ $\gamma_0 = 0.13\,J/K^2mol$. In fact, the RKKY interaction dominates over the Kondo interaction (cf. Sec. 4.1.3).

The high-field part of the magnetization at 0.05 K for $Yb(Rh_{1-x}Co_x)_2Si_2$ is shown in Fig. 4.27 (left panel) exemplary for $0 \leq x \leq 0.27$. For $x > 0.27$ the magnetization at $H > H_N$ behaves similarly to that of $Yb(Rh_{0.73}Co_{0.27})_2Si_2$ with

the only difference that the moment $\mu_N(H_N)$ increases with increasing x. Above H_N, M vs. H exhibits a strong negative curvature in all samples with $x < 0.27$ until it reaches the field H_0 (indicated by arrows in Fig. 4.27), after which $M(H)$ increases linearly in field. No other feature could be seen in measurements of $M(H)$ up to 35 T [107]. As explained in Sec. 4.1.1, the kink in magnetization at H_0 is the signature of field-induced Lifshitz transitions due to the shift of a van-Hove singularity in the renormalized band structure density of states across the Fermi level [160, 107, 161, 113, 114, 115]. The reduction of the effective quasiparticle mass and the fact that H_0 scales under pressure with the Kondo temperature was initially associated with the destruction of the heavy-fermion state and localization of the f-electrons [106, 107] and this is still an essential part of the Lifshitz transitions [114]. The new findings (see Fig. 4.29) show that the f electrons are not fully localized above H_0 and the Kondo effect is not completely suppressed. This is corroborated by the value of the magnetic moment at H_0, $\mu_{H_0}(H_0) \approx 1.2\,\mu_B/\mathrm{Yb}$, i.e. much smaller than the expected saturation value of about $1.7\mu_B/\mathrm{Yb}$ [107]. However, increasing the field up to H_0 leads to a strong de-renormalization of the quasiparticles and, therefore, to a strong reduction of the density of states at E_F.

Fig. 4.27 shows that H_0 is strongly affected by chemical doping, i.e. it decreases with increasing x while the kink becomes rounded, possibly because of disorder. This agrees with pressure experiments [106]. At $x \geq 0.27$ just a single kink in magnetization at H_N is observed. The critical fields H_L, H_N and H_0 for $0 \leq x \leq 0.27$ are plotted in Fig. 4.27 (right panel). Interestingly, all three fields converge at $x = 0.27$ suggesting that the van-Hove singularity disappears from the renormalized band structure for $x \geq 0.27$. This can easily been explained within the Kondo model, assuming that for $x \geq 0.27$ T_K becomes weaker than T_{RKKY}. Then the RKKY interaction forces the system into a localized magnetic state and prevents the formation of the so-called large Fermi surface. As a result, for $x \geq 0.27$, the system retains at zero field as well as high fields the localized Fermi surface.

The pressure dependence of H_0 of $\mathrm{Yb(Rh_{1-x}Co_x)_2Si_2}$ is plotted in Fig. 4.28 together with the Kondo temperature T_K in a semi-logarithmic scale. The pressure dependence of the field H_0 shows a smooth exponential decrease as the pressure is increased, as T_K does. This is in agreement with the band structure calculations which show that the field does not only move the van-Hove singularity across the Fermi level, but it simultaneously lowers the renormalized density of states as a consequence of the suppression of the hybridization, i.e. the Kondo effect. Such exponential behavior can be observed only until $x = 0.27$ where H_0 coincides with H_N. The complete localization of the $4f$ quasi-holes might continuously happen at much higher values of the field [162].

Since the evolution of the measured magnetic moment $\mu(H, x)$ with field and pressure reflects the competition between T_K and T_{RKKY} in $Yb(Rh_{1-x}Co_x)_2Si_2$, it is very useful to draw a phase diagram where on the abscissa we have the chemical pressure x and on the ordinate the magnetic moments $\mu_N(H_N)$ and $\mu_{H_0}(H_0)$ measured at H_N and H_0, respectively. This is shown in Fig. 4.29. In addition, we can take advantage of recent measurements of the ESR g-factor published in Ref. [139] from which we can add $\mu_{sat}(H_{sat}) = g_{\mathrm{ESR}}/2$ (taken at 5 K) on our plot. In fact, despite the high value of $T_K \approx 25$ K, a sharp ESR signal was observed below T_K with pronounced Yb^{3+} character [122]. Although the Kondo temperature decreases by an order of magnitude with increasing x in $Yb(Rh_{1-x}Co_x)_2Si_2$, all crystals of the series show a well defined ESR signal below 20 K with properties typical of a local Yb^{3+} spin (see Fig. 4.29) [163, 139]. It is important for our analysis that the g-factor shows an uniform variation with x (see Sec. 4.1.2). Therefore, the plotted $g_{\mathrm{ESR}}/2$ values are a reliable estimation of the ground state saturation magnetization $\mu_{sat}(H_{sat})$ of the fully localized $4f$ state.

Fig. 4.29 is the key result of our study and represents the field (H) and pressure (x) evolution of magnetism in $Yb(Rh_{1-x}Co_x)_2Si_2$. This phase diagram is separated in four regions. The LO-MO region represents the magnetically ordered AFM state with a localized small Fermi surface. At small x the region IT-HF represents the

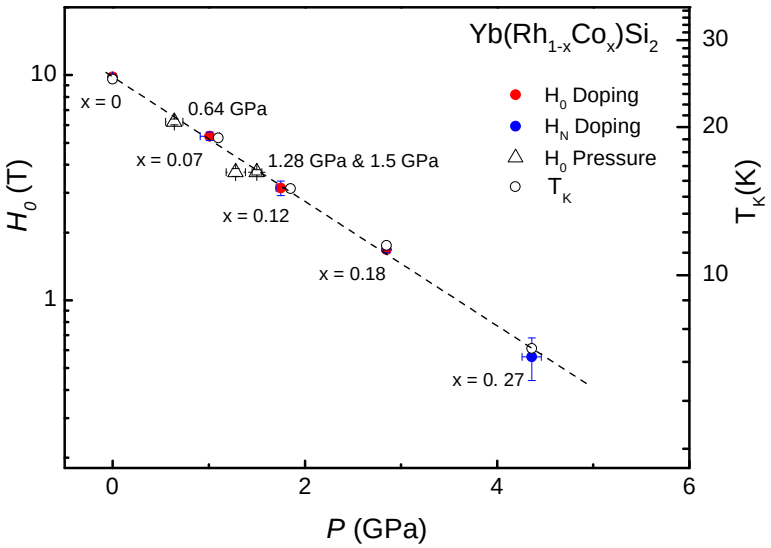

Figure 4.28 – Pressure dependence of the high-field transition in the series of $Yb(Rh_{1-x}Co_x)_2Si_2$ plotted together with the Kondo temperature T_K (right scale) in a semi-logarithmic representation. The pressure dependence of the field H_0 shows a smooth exponential decrease as the pressure is increased, as T_K does. Such exponential behavior can be observed only until $x = 0.27$ where H_0 coincides with H_N.

itinerant heavy-fermion ground state, which is characterized by $T_K > T_{RKKY}$ and an itinerant renormalized large Fermi surface. Above μ_{H_0} the system enters the region RN-LO with a change of the Fermi surface into a small localized, but still renormalized, Fermi surface. The Kondo effect is here not completely suppressed. At even higher fields, the system reaches the saturation moment $\mu_{sat} = g_{\mathrm{ESR}}/2$ where it enters the LO region which is characterized by the non-renormalized small local Fermi surface. At zero pressure and at $H > H_N \approx 60\mathrm{mT}$ the Kondo energy scale dominates over the RKKY one, almost screening the magnetic Yb^{3+} moments and leaving AFM order just below 0.07 K with a very small $\mu_N(H_N) \approx 0.1\,\mu_B/\mathrm{Yb}$. The system shows itinerant magnetism and heavy-fermion character in the regions IT-HF. We do not discuss here the properties of the AFM-QCP and the physics associated with the Kondo-breakdown energy scale $T^*(H^*)$, since it seems not to be very affected by pressure and we consider fields $H > H^*$. With increasing pressure, i.e. increasing the strength of the hybridization J, the magnetic moment $\mu_N(x)$ increases rapidly as a consequence of the rapid (exponential in J, see Sec. 2.2.4) decrease of the Kondo temperature T_K. T_{RKKY} also decreases but in a smoother way (quadratic in J, see Sec. 2.2.4). Furthermore, in this region T_{RKKY} can not

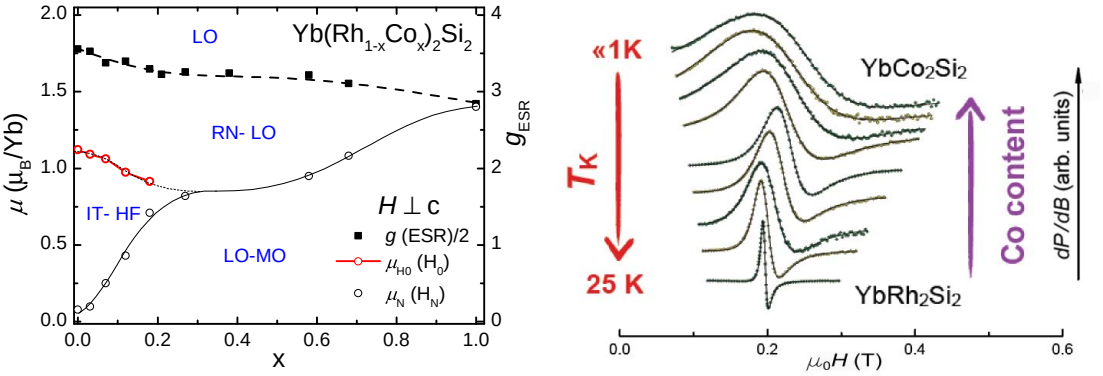

Figure 4.29 – Left: Phase diagram of $Yb(Rh_{1-x}Co_x)_2Si_2$ where the Co content x, i.e. chemical pressure, is plotted on the abscissa versus the magnetic moments $\mu_N(H_N)$ and $\mu_{H_0}(H_0)$ measured at H_N and H_0, respectively. The empty circles indicate the fields $\mu_{H_0}(H_0)$ and $\mu_N(H_N)$ while the filled squares indicate the values of $\mu_{sat}(H_{sat}) = g_{\mathrm{ESR}}/2$ (at 5 K) from Ref. [139]. The phase diagram is separated in four regions: LO-MO (localized electron and magnetic ordered), IT-HF (itinerant electron and heavy-fermion behavior with large renormalized Fermi surface), RN-LO (localized electron with small renormalized Fermi surface) and LO (localized electron with non-renormalized Fermi surface). Right: Evolution of the ESR spectra ($H \perp c$) in $Yb(Rh_{1-x}Co_x)_2Si_2$ single crystals for different cobalt concentrations, from Ref. [139]. The solid lines represent metallic Lorentzian line shapes. The narrowing of the ESR line with decreasing x is associated with the increasing of the Kondo interaction [139].

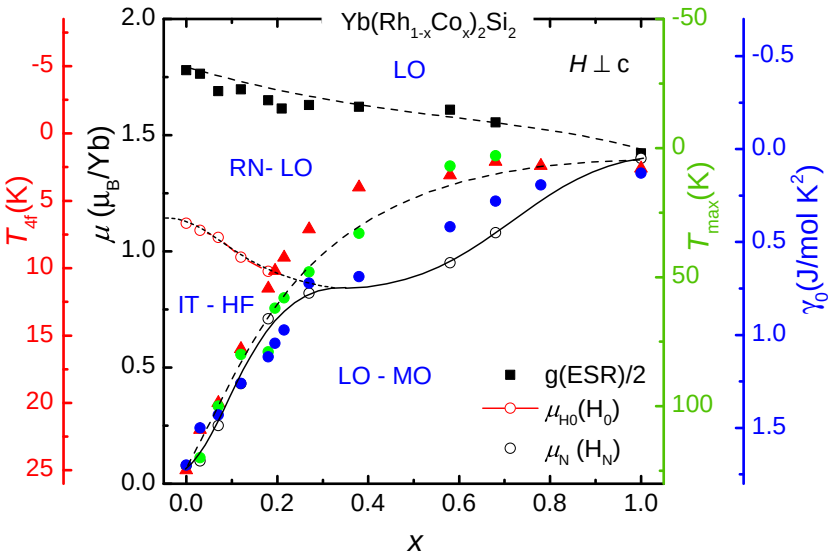

Figure 4.30 – Same plot as Fig. 4.29 with the additional inverse of the characteristic energy scales T_{4f}, T_{max}, γ_0 taken from Fig. 4.10, the scales of which are fixed by the two pure Rh and Co compounds.

be extracted from experimental data. Therefore, the region LO-MO expands with increasing x. Above $x = 0.27$ the RKKY interaction dominates substantially over the Kondo interaction and $\mu_N(x)$ vs. x still increases, but only weakly. Between $x = 0.27$ and $x = 1$ the system still shows some weak heavy-fermion character in the region RN-LO, while at $x = 1$ the pressure is enough to eventually localize the $4f$-electrons where $\mu_N = \mu_{sat}$. This demonstrates the fact that magnetism evolves continuously from itinerant to local in $Yb(Rh_{1-x}Co_x)_2Si_2$. The magnetic field has a similar effect, but the interesting fact is that evolution from itinerant to local takes place in two steps. A small field suppresses T_{RKKY} and the system enters the IT-HF region characterized by HF behavior and a large renormalized Fermi surface [113, 114] (the local-to-itinerant field-induced transition at the AFM-QCP is located at very low fields, about 0.06 T, and we discuss here the region with $H \geq 0.1$). Then, the field induces two Lifshitz transitions [115] where dHvA measurements indicate that the Fermi surface changes from large to small [113], but it is still the renormalized one [114]. Finally the fully localization of the f electrons takes place smoothly at even higher fields where the magnetic moment achieves its saturation value. This intriguing behavior has its origin in the complex Kondo effect mechanism in Kondo lattices. Both the coherence effects resulting from the lattice periodicity as well as the de-renormalization of the quasiparticles, which reflects the break-up of the local Kondo singlets, have to be taken into account.

It is now instructive to plot the inverse of the characteristic energy scales T_{4f}, T_{max}, γ_0 into the phase diagram (see Fig. 4.30). Surprisingly, we can perfectly scale the evolution of the energy scale with $\mu_N(x)$. This emphasizes the crossover from the region where the Kondo energy scale dominates (with more itinerant character) to that where the RKKY energy scale dominates (with more local character).

4.3 Field-induced QCP in $Yb(Rh_{0.93}Co_{0.07})_2Si_2$

The discovery of pronounced NFL behavior in a broad temperature region above the field-induced QCP in $YbRh_2Si_2$ has encouraged a large number of works with the purpose of characterizing the nature of such a QCP [6, 7]. As a matter of fact, there are only two well studied scenarios with which we can attempt to describe the experimental data of $YbRh_2Si_2$: the conventional "itinerant" SDW scenario (see Sec. 2.3.1) and the unconventional and recently proposed "local" scenario (see Sec. 2.3.2). Many of $YbRh_2Si_2$ properties are well described by the local scenario [8, 61]. According to this scenario [51] and experimental evidence [13, 107], the phase transition at the QCP is accompanied by a Fermi surface reconstruction due to the breakdown of the Kondo effect. This has been suggested to happen at the $T^*(H)$ crossover energy scale at which the moments from local become itinerant (see Sec. 4.1.1). One of the fundamental question that has still to be answered is why the energy scale $T^*(H)$ is almost pressure independent [117]. Within the

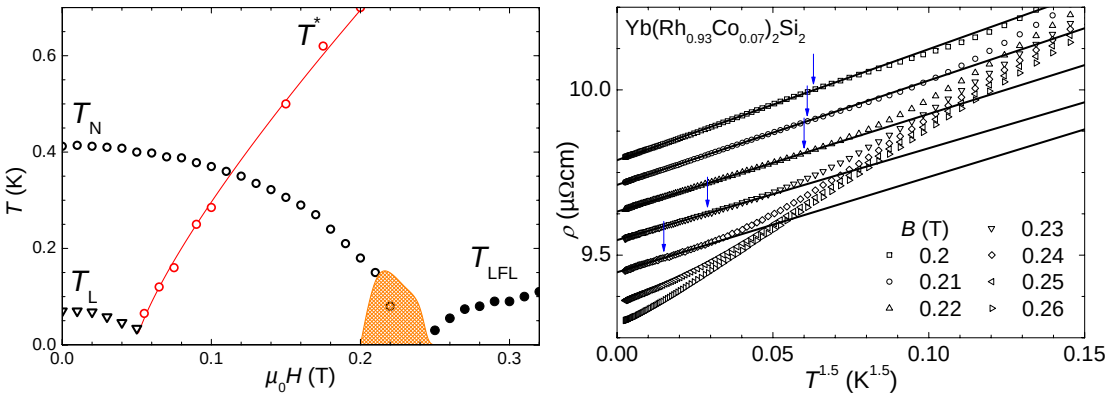

Figure 4.31 – Left: Phase diagram of the $Yb(Rh_{0.93}Co_{0.07})_2Si_2$ compound with $H \perp c$ obtained from resistivity measurements. It is similar to the phase diagram of Fig. 4.14 but, here, the phase line $T_L(H)$ and the FL line are included. The yellow region is the region where the electrical resistivity $\rho \propto T^{1.5}$ (see right panel). Right: $\rho(T)$ plotted over $T^{1.5}$. The arrows marks the end of linearity. Figures taken from Ref. [154].

simplest model, in a local scenario the $T^*(H)$ must vanish at the AFM QCP, but

for more complex model, e.g. with the presence of frustration, T_N and T^* can be separated (see Sec. 2.3.3). The work of Friedemann *et al.* , which is summarized in Fig. 4.11 [152], suggests that there is a global phase diagram (see Sec. 2.3.3 and Refs. [58, 60, 59]) where the field H^* separates a region where the moments are part of the large Fermi surface (itinerant) and a region where they are local (with small Fermi surface). The nature of the QCPs is different in these two regions. It is therefore desired to investigate the nature of such QCPs in both regions. In this chapter, we focus on positive pressure (7% Co substitution) where the AFM QCP at H_N is located in the regime with intact Kondo screening ($H_N > H^*$) where the SDW theory is expected to be applicable. We show measurements of the uniform magnetization as well as of the specific heat, from which we can deduce the magnetic Grüneisen ratio Γ_H. $\Gamma_H(T)$ vs. T should diverge at a field-induced QCP (i.e., at $H_N(0)$) where Γ_H vs. H changes its sign manifesting an accumulation of entropy due to the presence of quantum fluctuations [15, 65].

The nature of the QCP at $\mu_0 H_N(0) = 0.22$ T in $Yb(Rh_{0.93}Co_{0.07})_2Si_2$ was already investigated in Ref. [117] and in the Supplementary Information of the same article. The SDW model seems to be the adequate to describe the behavior of the resistivity, where we expect $\rho(T) \propto T^{3/2}$ for an antiferromagnet with 3D fluctuations, and the corresponding field dependence of the Néel temperature $T_N(H) = (H_N - H)^\epsilon$ predicts an exponent $\epsilon = 2/3$ [5] where the experimental result gives $\epsilon = 0.65$. However, the region of the phase diagram where the $T^{3/2}$ power law in resistivity is observed is rather broad and not sharp as expected at a QCP. This is illustrated in the left panel of Fig. 4.31 (yellow region). Such a broadening is possibly due to disorder and we might than expect a spin-glass ground state in $Yb(Rh_{0.93}Co_{0.07})_2Si_2$, since for a spin-glass the resistivity is also expected to follow a $T^{3/2}$ power law [164]. On the other side, the phase transition at T_N does not show any frequency dependence [132] and it looks like a second order phase transition in the specific heat (see Fig. 4.32 [157]). The model experiment to provide evidence of the presence of quantum critical fluctuations is the measure of the critical magnetic Grüneisen ratio (see Sec. 2.3.4):

$$\Gamma_H = -\frac{1}{T}\frac{(\partial S/\partial H)_T}{(\partial S/\partial T)_H} = -\frac{(\partial M/\partial T)_H}{C_H} = \frac{1}{T}\frac{\partial T}{\partial H}\Big|_S \tag{4.8}$$

which can be determined by measurements of the magnetization and specific heat or directly by magnetocaloric effect experiments [157]. According to Refs. [15, 65], this quantity diverges when approaching any field-induced QCP with power law functions

$$\Gamma_H(T, H = H_N) \propto T^{-1/\nu z} \quad \text{and} \quad \Gamma_H(T = 0, H) = -G_r(H - H_N)^{-1} \tag{4.9}$$

where the parameters ν (the correlation length exponent) and z (the dynamical critical exponent) are universal and depend only on the dimensionality of the

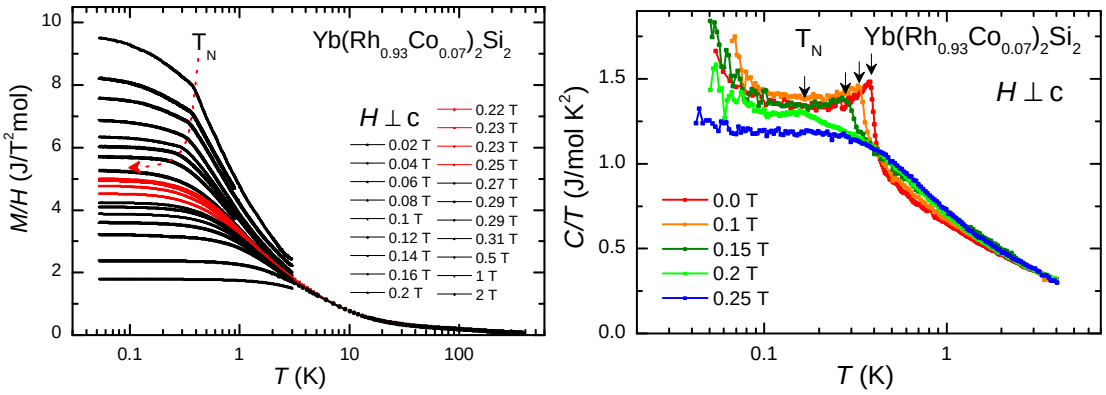

Figure 4.32 – Uniform susceptibility (left panel) and specific heat measurements (right panel) of a single crystal of $Yb(Rh_{0.93}Co_{0.07})_2Si_2$ plotted as a function temperature [157]. In M/H vs. T, the red lines correspond to the fields where Friedemann *et al.* have observed the $T^{1.5}$ dependence in the electrical resistivity. The dashed line represents the AFM transition temperature T_N. At the critical field both $M(T)/H$ and $C(T)/T$ tends to saturate to a constant value at low temperatures.

critical fluctuations d and their nature ($z = 2$ for AFM and $z = 3$ for FM fluctuations). In addition, also the prefactor G_r depends strictly only on these parameters, $G_r = \nu(d - z)$, which provide a fully determination of the nature of the QCP. For instance, when scaling applies within the SDW scenario $\nu = 1/2$ and for a system with 3D AFM critical fluctuations, $d = 3$ and $z = 2$, we simply expect $\Gamma \propto 1/T$ (cf. Tab. 2.1). In $YbRh_2Si_2$ it was found $\Gamma_H \propto T^{-0.7}$ at low temperatures (below 0.3 K) and $G_r = -0.3$ [118] which do not agree with the SDW scenario, but seems to agree with the Kondo-breakdown QCP proposed in Ref. [165].

We have used measurements of the magnetization $M(T, H)$ and specific heat $C(T, H)$ to determine Γ_H. The temperature dependence of both measurements is shown in Fig. 4.32. The magnetization measurements are the same as those presented in Fig. 4.12 but, here, we have marked in red the curves close to the QCP at $\mu_0 H_N(0) \approx 0.22$ T. A quick examination of the uniform susceptibility $\chi = M(T)/H$ in Fig.4.32 (left panel) around the critical field (in the range $0.22 \leq \mu_0 H \leq 0.25$ T) makes clear that there is not divergence of $M(T)/H$, since the curves tend to saturate to a constant value towards the lowest temperature of 0.05 K. Also the specific heat coefficient $C(T)/T$ (right panel of Fig.4.32) follows a similar behavior. In both cases, M/H and C/T at the critical field of 0.22 T feature a smooth crossover around $T \approx 0.3$ K below which they flatten. To obtain Γ_H we need to calculate the derivative of the magnetization with respect to temperature. This is shown in Fig. 4.33 together with $C(T)/T$ and $\Gamma_H(T)$ in a double logarithmic representation to emphazise the putative power-law behavior.

No divergence is seen in $-(dM/dT)/T$ vs. T but the magnetic Grüneisen ratio $\Gamma_H(T)$ rises steeply below 1 K and exhibits a crossover into a smooth logarithmic behavior below 0.3 K (see Fig. 4.34). For a AFM system with 3D fluctuations we expect from the SDW theory $\Gamma_H \propto T^{-1}$. This might be realized for $T > 0.3$ K (when a non critical background is subtracted) but not below 0.3 K. Even in the case of 2D AFM fluctuations the theory predicts $\Gamma_H \propto loglog(1/T)/Tlog(1/T)$ (see Tab. 2.1) which does definitely not agree with the experimental data below 0.3 K. One possible explanation is that 0.22 T might not be the field where the fluctuations become critical. To proof this assumption, we have performed the same analysis for all fields close to 0.22 T. We have found the very same behavior: For instance, in Fig. 4.34 we have plotted $\Gamma_H(T)$ vs. $log(T)$ for a field of 0.25 T. We have also included the magnetic Grüneisen ratio calculated from measurements of the magnetocaloric effect performed by A. Steppke [157]. This is because the magnetocaloric effect shows the largest divergence of $\Gamma_H(T)$ at this field. Both results match surprisingly well although they have been obtained from three measurement techniques and two different samples of the same batch. Not just the temperature dependence is the same but also the absolute values. In the plot we have included the T^{-1} power law, too. There is indeed not a big difference between the behavior at 0.22 T and that at 0.25 T.

We can therefore conclude that the magnetic Grüneisen ratio does not show a critical divergence at $H_N(0)$ and this means that we do not have a QCP.

A second possibility might be the fact that, since the susceptibility keeps increasing below T_N for $H < H_N$ (see Fig. 4.32), the quantum fluctuations might become critical inside the AFM phase, possibly at the critical field $H_L(0)$ or at $H^*(0)$. Since $H_L(0) \approx H^*(0)$ it is difficult to decide whether the fluctuations of the magnetic order-to-disorder transition or those of the small-to-large Fermi surfaces are responsible for the critical behavior. There is another intriguing aspect that has to be considered. For fields larger than the critical field the uniform susceptibility $\chi = M/H$ saturates at low temperature to a constant value as expected for a Fermi liquid (cf. Sec. 2.2.1). For a Kondo lattice the value of the Pauli susceptibility in the PM regime $\chi_0 = \chi(T \to 0)$ is proportional to the Sommerfeld coefficient γ_0 and therefore to the effective mass m^* of the quasiparticles. Resistivity measurements by Friedemann *et al.* [154] on $Yb(Rh_{0.93}Co_{0.07})_2Si_2$ have shown that the quasiparticle-quasiparticle scattering cross section A, where in a Fermi liquid $\rho = \rho_0 + AT^2$ and $A \propto (m^*)^2$, strongly diverges when $H_N(0)$ is approached from the PM side, following a function

$$A(H) \propto (H - H_{cr})^{-1} \tag{4.10}$$

and a critical field $\mu_0 H_{cr} \approx 0.13$ T which is surprisingly inside the AFM phase. A similar analysis can be done with the $\chi_0(H)$ values of the magnetic susceptibility

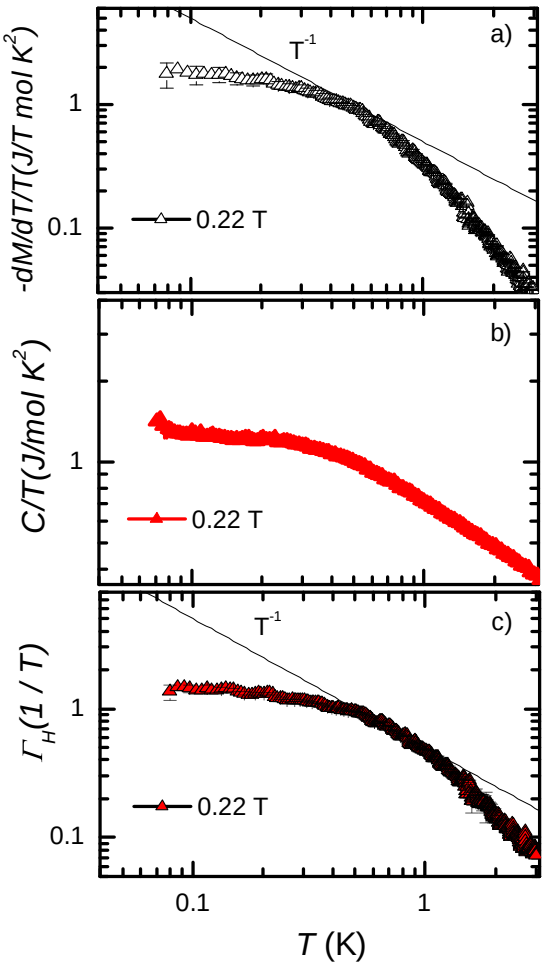

Figure 4.33 – a) Temperature derivative of the magnetization $-(dM/dT)/T$ of $Yb(Rh_{0.93}Co_{0.07})_2Si_2$ plotted over the temperature at the critical field $\mu_0 H_N = 0.22\,\mathrm{T}$. b) Electronic specific heat coefficient $C(T)/T$ of the same sample plotted over the temperature. The data were taken from Ref. [157]. c) Calculated magnetic Grüneisen ratio Γ_H from the data of panel a) and b). $-(dM/dT)/T$ and $C(T)/T$ exhibit a crossover towards a constant value below 0.3 K, whereas Γ_H increases smoothly with decreasing T following a logarithmic behavior.

data of Fig. 4.32. Since in a Fermi liquid $\chi_0 \propto m^*$ we attempt to fit our data for $H > H_N(0)$ with the following function

$$\chi_0 \propto \frac{1}{(H - H_{cr})^{\epsilon}} \tag{4.11}$$

which yields a critical field $H_{cr} \approx 0$ and $\epsilon \approx 1/2$ (see Fig. 4.35). There is a slight kink at 0.22 T which, however, does not influence the fit coefficients too much

(see inset of Fig. 4.35). In the SDW scenario we expect $m^* \propto (H - H_{cr})^{(d-z)/2}$ (see Sec. 2.3.1), therefore we can conclude that this result matches nicely the one obtained by resistivity experiments where $\epsilon \approx 1$, i.e. $\chi_0 \propto A^{1/2} \propto m^*$ and suggests $d = 2$ and $z = 3$ which imply a 2D FM QCP at a field close to zero. The quantum criticality seen from the PM side of the phase diagram seems to be more sensitive to FM fluctuations than to AFM ones. In fact, we know that in pure $YbRh_2Si_2$ FM fluctuations have been observed [63] and also under pressure the magnetic order changes from AFM to FM (cf. section 4.2.1). In addition, even in the antiferromagnet $CeCu_{6-x}Au_x$ such a possibility was considered, based on neutron scattering results [166]. It is worth mentioning that high magnetic fields promote FM fluctuations instead of AFM ones in $YbRh_2Si_2$, as shown by K. Ishida *et al.* [153]. Therefore, our analysis of χ_0, which is taken from high fields, might be more influenced by FM fluctuations than by AFM ones.

It is therefore important to plot $-(dM/dT)/T$ vs. T inside the AFM phase and compare these curves with those at fields close to $H_N(0)$. This is shown in Fig. 4.36 in a double-logarithmic representation. We have also plotted a T^{-1} function as a guide to the eye. This figure emphasizes how, for higher fields than the critical field, the curve tends to saturate to a constant value below 1 K. Nevertheless, as we approach the critical field $\mu_0 H_N(0) = 0.22$ T the crossover region is shifted to lower temperatures. As soon as the ordered state is reached, the value of

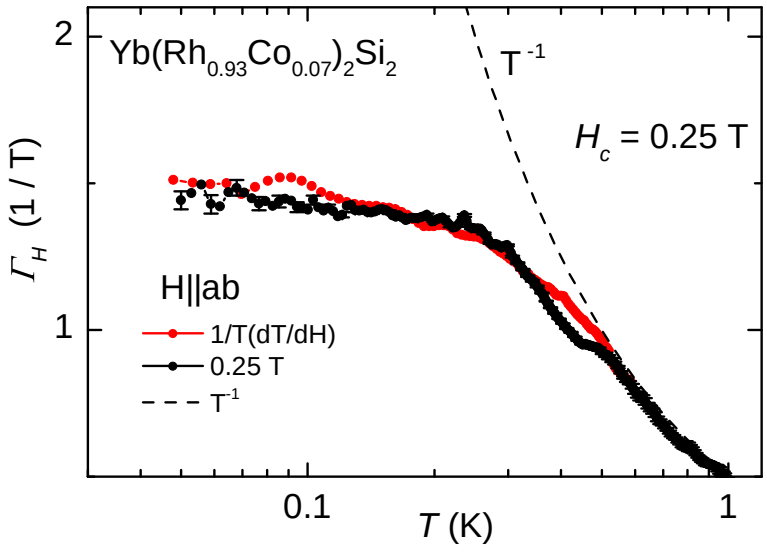

Figure 4.34 – Magnetic Grüneisen ratio $\Gamma_H(T)$ obtained from $-(dM/dT)/T$ and $C_H(T)$ (black points) data as well as from magnetocaloric effect measurements (red points) [157] plotted as a function of the temperature. The dashed line is just a guide to the eye, indicating that the data do not follow a T^{-1} power-law function.

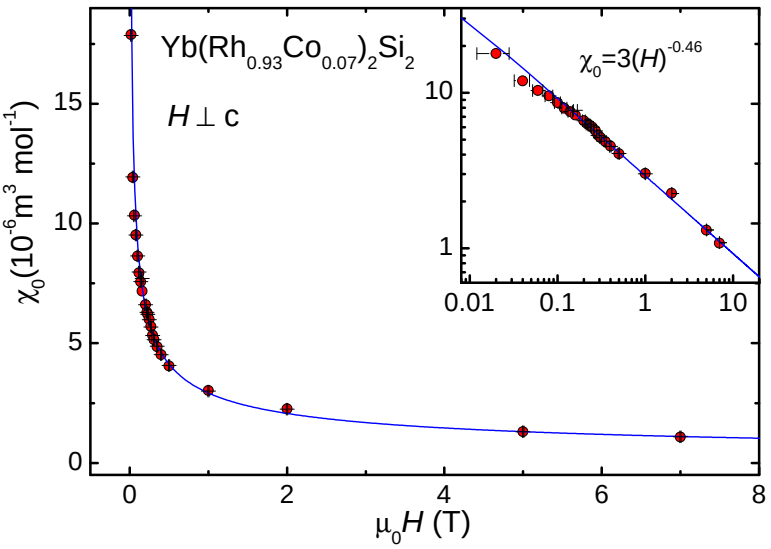

Figure 4.35 – Field dependence of the value χ_0 of the susceptibility for $T \to 0$ (taken at 0.05 K) from the measurements shown in Fig. 4.32. The solid blue line represents a fit according with equation 4.11. The inset shows the same data and fit in a double logarithmic representation to emphasize the quality of the fit and the slight kink at 0.22 T.

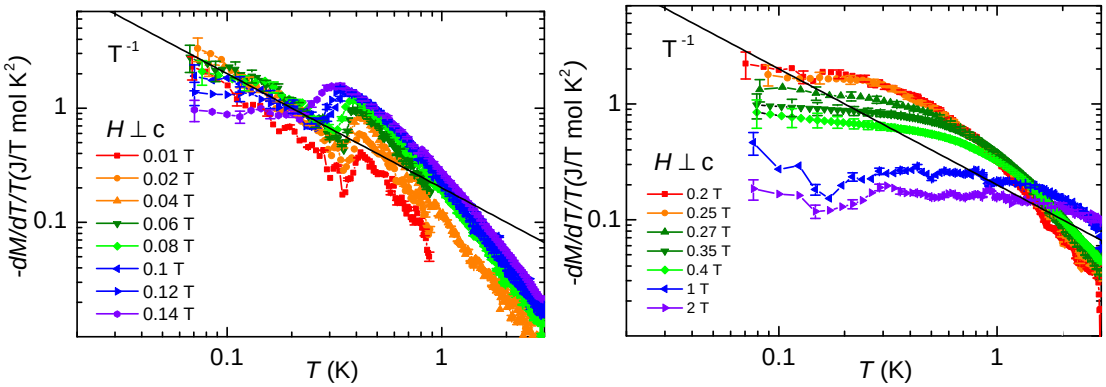

Figure 4.36 – Left: Temperature derivative of the magnetization $-(dM/dT)/T$ for fields $\mu_0 H \leq 0.14$ T, i.e. well inside the ordered state. At $H \approx H_L$ and below T_N, $-(dM/dT)/T \propto T^{-1}$. The black line is a guide to the eye. Right: $-(dM/dT)/T$ vs. T for fields close and above the critical field $\mu_0 H_N(0) = 0.22$ T. None of the curves follows a T^{-1} power-law behavior.

the quantity $-(dM/dT)/T$ changes dramatically due to the effect of the phase

transition and saturate for fields between 0.1 and 0.2 T. However, at fields close to $\mu_0 H_L(0) \approx 0.06$ T, below T_N, $-(dM/dT)/T$ diverges following a T^{-1} power law. Assuming $C(T)/T$ to be constant at these fields below T_N, we can infer the presence of a 3D AFM SDW QCP at 0.06 T in $Yb(Rh_{0.93}Co_{0.07})_2Si_2$ in disagreement with the analysis of χ_0. Although all results seem not to agree consistently with just a single set of universal parameters within the SDW model, we can surely state that the clearest divergencies are seen inside the AFM ordered state at fields close to 0.06 T. As previously mentioned, we do not know if this divergences are a consequence of the fluctuations of the magnetic order-to-disorder transition at $H_L(0)$ or those of the small-to-large Fermi surfaces at $H^*(0)$ since $H_L(0) \approx H^*(0)$.

Another simple explanation for the lack of critical fluctuations at $H_N(0)$ is the presence of disorder in the sample. Disorder scattering might influence the critical slowing down of the fluctuations below 0.3 K explaining the crossover from a quasi T^{-1} behavior of Γ_H into a weak $-log(T)$. To test this scenario we have performed very challenging measurements of the magnetization and specific heat under hydrostatic pressure, since 7% of Co substitution represents a pressure of about 1 GPa (cf. Fig. 4.8). The measurements and the analysis of the results are presented in the next section.

4.4 $YbRh_2Si_2$ under hydrostatic pressure

As mentioned in Sec. 4.1.1, magnetization measurements under the hydrostatic pressure of 0.64 and 1.28 GPa on $YbRh_2Si_2$ were already performed by Y. Tokiwa *et al.* at different temperatures and high magnetic fields [106, 159]. The main results were the observation of the field-induced suppression of the HF state at H_0, as hydrostatic pressure experiments have revealed a clear correspondence between H_0 and the Kondo scale T_K [106, 107], and the confirmation that the energy scale $T^*(H)$ is almost pressure independent [159, 117]. Unfortunately, the lack of specific heat data under pressure did not permit to calculate $\Gamma_H(T, H)$. In the following section we will show measurements of the magnetization of a single crystal of $YbRh_2Si_2$ under a pressure of 1.5 GPa (see Sec. 3.3) as well as specific heat results taken from the same sample inside the very same pressure cell performed by R. Borth [100] in the group of Dr. Michael Nicklas. We will compare our analysis with that performed for the $Yb(Rh_{0.93}Co_{0.07})_2Si_2$ crystal since a pressure of 1.5 GPa corresponds to a Co substitution of about 10% (cf. Fig. 4.8). Since up to a Co concentration of 12% (≈ 2 GPa) the physical properties of the pure system under pressure and of $Yb(Rh_{1-x}Co_x)_2Si_2$ seem to be equivalent, such a comparison is justified.

The magnetization measurements were performed in two steps, as described in the experimental Sec. 3.3, first by measuring the magnetization of the pressurized

sample together with the pressure cell (and the pressure gauge) and after that, by measuring the contribution of the empty pressure cell which is eventually substracted. A miniature CuBe piston-cylinder pressure cell, which contained 21.2 mg of 12 high-quality single crystals of $YbRh_2Si_2$, was mounted on the Faraday magnetometer (Sec. 3.2.1). The complete pressure cell has a relative small magnetization, and the ratio of the contribution from the empty cell is less than 45% of the contribution of the samples at high magnetic fields.

4.4.1 Magnetization vs. field

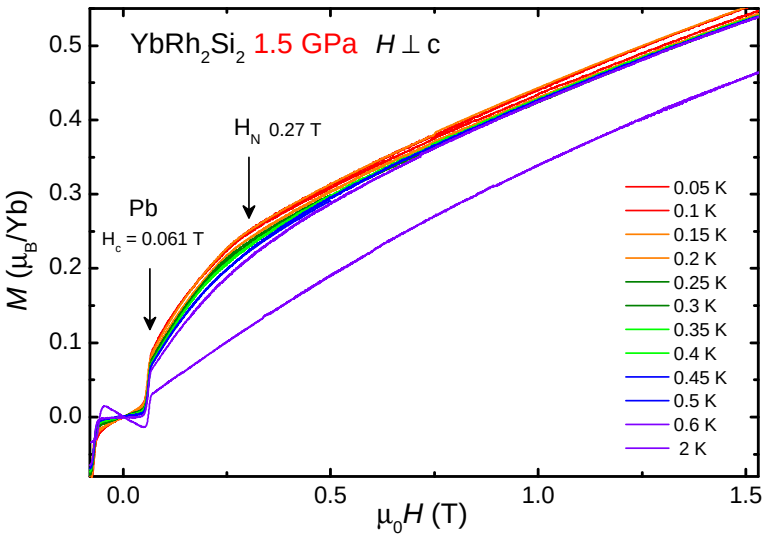

Figure 4.37 – Isothermal magnetization measurements at several temperatures of $YbRh_2Si_2$ for $H \perp c$ under a hydrostatic pressure of 1.5 GPa. The arrows indicate the critical field $H_N \approx 0.27\,\mathrm{T}$ at which the AFM order is suppressed at 0.05 K and the critical field $\mu_0 H_c \approx 0.061\,\mathrm{T}$ of superconducting lead used as a manometer to estimate the inner pressure.

Fig. 4.37 shows the isothermal magnetization measurements performed with the field perpendicular to the crystallographic c-axis at different temperatures and under a hydrostatic pressure of 1.5 GPa. At 0.05 K, two anomalies can be seen in $M(H)$, a step like at $\mu_0 H_c \approx 0.061\,\mathrm{T}$ and a kink at $\mu_0 H_N \approx 0.27\,\mathrm{T}$. The first one corresponds to the superconducting critical field of lead (Pb) used as manometer to estimate the internal pressure, while the second one marks the suppression of the AFM order by the magnetic field, that sets in below $T_N = 0.55\,\mathrm{K}$. Assuming a good agreement between hydrostatic pressure and Co substitution (cf. Fig. 4.8) we expect another feature to be present at about 0.05 T which should correspond to the critical field of the magnetic transition at T_L. Unfortunately, this feature is

obscured by the strong effect at H_c. Since this effect is very strong and sensitive to the remanent field of the superconducting magnet (a few mT), we were not able to substract it correctly. The feature at H_c remains sharp up to 2 K since

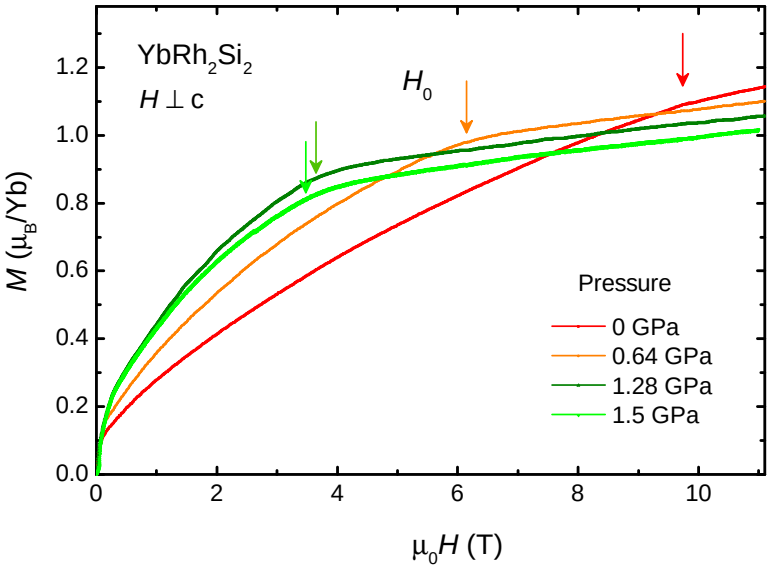

Figure 4.38 – High-field curves of the field dependence of the magnetization in $YbRh_2Si_2$ at different hydrostatic pressures. The field H_0, associated with the Lifshitz transitions is marked by arrows. The data at 0.64 and 1.28 GPa were taken from Ref. [106].

the superconducting transition of lead at 1.5 GPa is at 6.64 K [167]. The kink at H_N becomes rapidly smeared with increasing temperature. Nevertheless, the transition can be followed up to 0.4 K. These data look quite similar to those for $Yb(Rh_{0.93}Co_{0.07})_2Si_2$ and $Yb(Rh_{0.88}Co_{0.12})_2Si_2$ of Fig. 4.12 and 4.15, respectively, confirming the good agreement between hydrostatic pressure and Co substitution. Although the kink in the magnetization curves broadens rapidly with increasing temperature, $M(H)$ exhibits a strong non linear field dependence even for $T \geq T_N$. This behavior is also observed in $YbRh_2Si_2$ (see Fig. 4.3).

At higher fields, the kink associated with H_0 is found at about 4 T, confirming that H_0 is shifted to lower fields under pressure. This is shown in Fig.4.38 where we have plotted the magnetization of $YbRh_2Si_2$ at 0, 0.64, 1.28 and 1.5 GPa. The data at 0.64 and 1.28 GPa were taken from Ref. [106]. The arrows indicate the positions of H_0 which are 6.2, 3.7, and 3.5 T for 0.64, 1.28 and 1.5 GPa, respectively. Surprisingly, the curves for 1.28 and 1.5 GPa are very similar with a similar value for H_0, which is remarkable since H_0 is very sensitive to pressure [106]. A more detailed discussion about this issue is given in Sec. 4.4.2. However, our data seem to be consistent with the specific heat results taken at the same pressure by R. Borth [100]. In fact, in Fig. 4.39 we have plotted the field dependence of

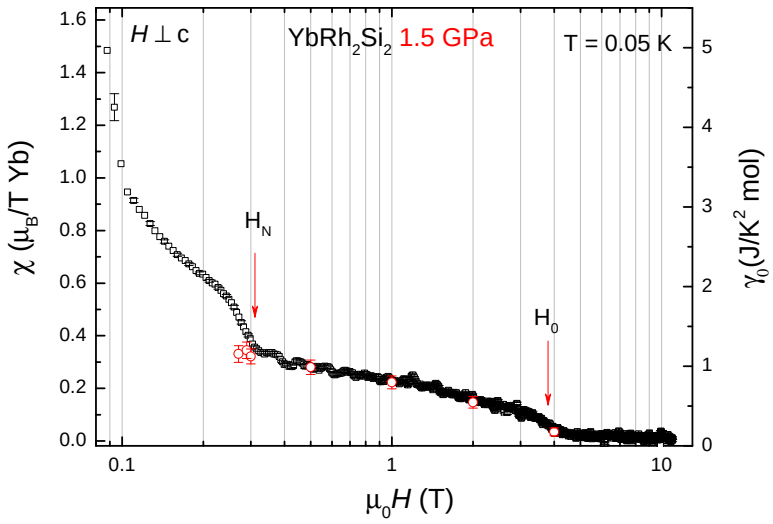

Figure 4.39 – Field dependence of the differential susceptibility $\chi(H) = dM(H)/dH$ of $YbRh_2Si_2$ at 1.5 GPa and 0.05 K. The sudden decreases of $\chi(H)$, marked by the red arrows, indicate the transitions at H_N and H_0. The differential susceptibility χ_0 at $T \approx 0$ (black points) is proportional to the Sommerfeld coefficient γ_0 (red points) indicating the reduction of the quasiparticle effective mass $m^* \propto \chi_0 \propto \gamma_0$ with field in the Fermi-liquid ground state [100].

the differential susceptibility $\chi(H) = dM(H)/dH$ of $YbRh_2Si_2$ at 1.5 GPa and 0.05 K. The sudden decreases of $\chi(H)$, marked by the red arrows, indicate the transitions at H_N and H_0. The differential susceptibility χ_0 at $T \approx 0$ (black points) is proportional to the Sommerfeld coefficient γ_0 (red points) indicating the reduction of the quasiparticle effective mass $m^* \propto \chi_0 \propto \gamma_0$ with field in the Fermi-liquid ground state. The very same behavior was observed in $YbRh_2Si_2$ at zero pressure [106, 107].

4.4.2 Comparison with 1.28 GPa

The remarkable similarity between our data at 1.5 GPa and the data at 1.28 GPa of Refs. [106, 159] motivated us to compare them in more detail. In the left panel of Fig. 4.40 we have plotted the low- and high-field magnetization curves at 0.05 K, the same displayed in Fig. 4.38, for 1.28 and 1.5 GPa. It can be clearly seen that they match each other. In particular, the critical fields H_N are almost identical, 0.28 and 0.27 T for 1.28 and 1.5 GPa, respectively. This behavior is quite anomalous since a difference of 0.22 GPa between the two pressures should yield a relevant difference in H_N (see Fig. 4.20). We therefore conclude that there was an error in the exact estimation of the 1.28 GPa value of the pressure in Refs. [106, 159]. The same conclusion can be drawn from the $H - T$ magnetic

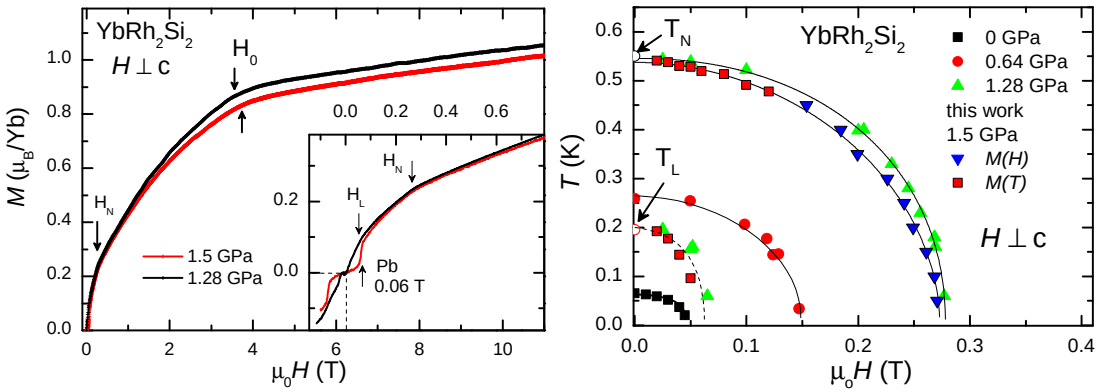

Figure 4.40 – Left: Same curves as Fig. 4.38 for 1.28 and 1.5 GPa. The inset emphasizes that at low fields the data show the very same behavior despite the superconducting transition. Right: $H-T$ magnetic phase diagram of $YbRh_2Si_2$ at different pressures for $H \perp c$. The points at 1.5 GPa were taken from magnetization and specific heat data, while the points at 0.64 and 1.28 GPa were adapted from Refs. [106, 118]. Both $T_N(H)$ and $T_L(H)$ at 1.28 and 1.5 GPa follows exactly the same behavior.

phase diagram shown in the right panel of Fig. 4.40. The AFM phase transition

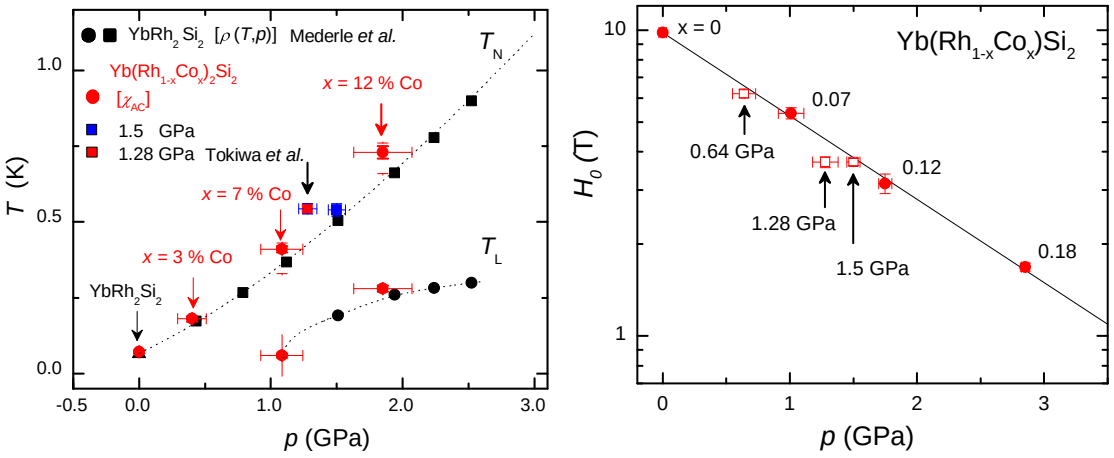

Figure 4.41 – Left: Fig. 4.8 on which we have plotted the T_N values for 1.28 and 1.5 GPa. The point for 1.28 GPa does not fit into the expected behavior. Right: Pressure dependence of H_0 in $YbRh_2Si_2$. Also here the point for 1.28 GPa is not on the fit line.

boundary line has been determined from the kinks in both isothermal $M(H)$ and

isofield $M(T)$ magnetization measurements. The T_L phase boundary line has been determined by the kinks in $M(T)$ at very low fields ($\mu_0 H < 0.06$) together with the specific heat measurements performed by R. Borth [100]. Both $T_N(H)$ and $T_L(H)$ at 1.28 and 1.5 GPa follows exactly the same behavior. Tokiwa *et al.* used tin (Sn) as a manometer. Since the critical field of Sn ($\approx$ 300 G) is much smaller than that of Pb ($\approx$ 800 G), it is possible that the remanent field of the superconducting magnet of the SQUID did consistently affect the value of T_c needed to estimate the pressure.

To add more evidence for our conclusion, we have plotted the T_N values for 1.28 and 1.5 GPa in Fig. 4.41 (left panel). In addition we have plotted the values for H_0 over pressure in the right panel of Fig. 4.41. It can straightforwardly be seen that the values for 1.28 K do not fit into the expected behavior. In particular, looking at the T_N vs. pressure phase diagram for the doping series $Yb(Rh_{1-x}Co_x)_2Si_2$, our pressures are located in a quasi-linear pressure dependence region (between 7 and 12% Co), where a difference of 0.22 GPa should yield an increase in T_N of $\approx$ 0.1 K.

4.4.3 Magnetization vs. temperature

The uniform susceptibility $\chi = M(T)/H$ at different fields of $YbRh_2Si_2$ at 1.5 GPa is shown in Fig. 4.42. In this temperature range the measurements are not affected

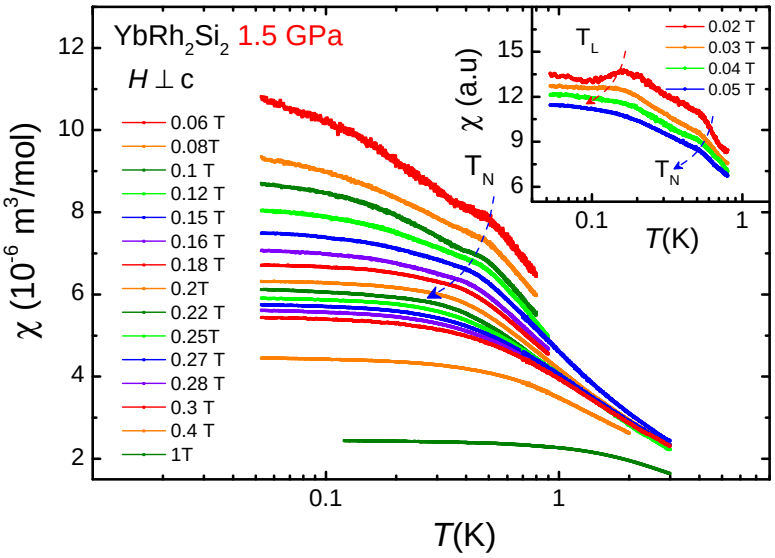

Figure 4.42 – Uniform susceptibility of $YbRh_2Si_2$ under 1.5 GPa at several magnetic fields with $H \perp c$. The transition at T_N associated with the onset of the AFM order is marked by the dashed line. The transition temperature in zero field is 0.55 K. Inset: low-field data. The transition at $T_L = 0.2$ K can be seen as a kink in $\chi(T)$ (red dashed arrow).

by the superconducting transition of lead, because $T_c = 6.64\,\mathrm{K}$ [167]. In small fields, as in Fig. 4.12, we can clearly see the onset of the AFM order in form of a kink at $T_N = 0.55\,\mathrm{K}$ marked by the dashed arrow. Even the transition at $T_L = 0.2\,\mathrm{K}$ is visible in the inset of the same figure. As the field is increased the transitions become less pronounced and the susceptibility tends to saturate into a constant value at low temperatures. More precisely, for fields between 0.06 and 0.1 T, $\chi(T)$ keeps increasing below T_N like in $Yb(Rh_{0.93}Co_{0.07})_2Si_2$. Above 0.1 T, $\chi(T)$ saturates below a temperature which varies from 0.1 up to 0.4 K inferring a Fermi-liquid ground state. The Curie-Weiss analysis of the inverse susceptibility

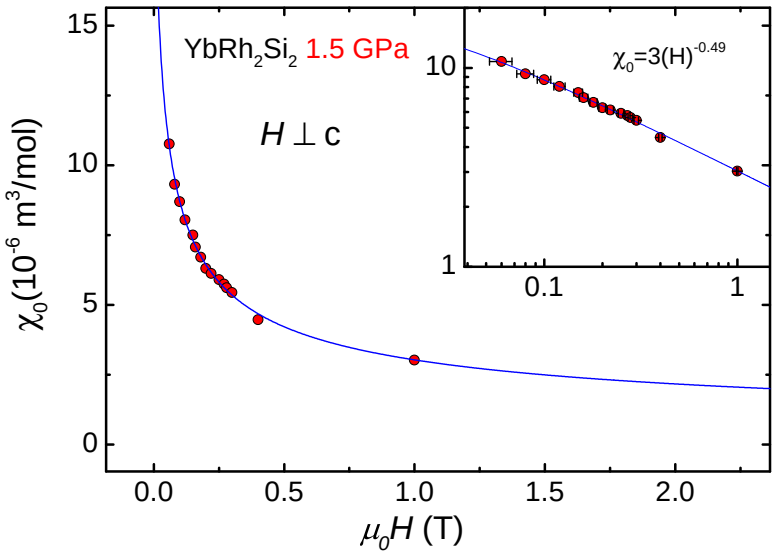

Figure 4.43 – Field dependence of the value χ_0 of the susceptibility for $T \to 0$ (taken at 0.06 K) from the measurements shown in Fig. 4.42. The solid blue line represents a fit according with equation 4.11. The inset shows the same data and fit in a double logarithmic representation to emphasize the quality of the fit. A slight kink might be identified at 0.27 T.

at low temperatures (between 2 and 4 K) gives an effective magnetic moment of $2.6\,\mu_B$ and a Weiss temperature of $-1.5\,\mathrm{K}$, values very similar to those estimated in $Yb(Rh_{0.93}Co_{0.07})_2Si_2$ [112].

Extracting the χ_0 susceptibility values for $T \to 0$, we can attempt to perform the same analysis done in Sec. 4.3 for $Yb(Rh_{0.93}Co_{0.07})_2Si_2$. The extracted values are plotted in Fig. 4.43 together with a fit to the data with the equation 4.11 (blue line). The function 4.11 can well describe the data yielding a critical field $H_{cr} \approx 0$ and $\epsilon \approx 1/2$ in good agreement with the results shown in Fig. 4.35 for $Yb(Rh_{0.93}Co_{0.07})_2Si_2$. This suggests that the critical fluctuations are strong inside the AFM phase at a field close to zero and their character is FM and 2D.

Like in $Yb(Rh_{0.93}Co_{0.07})_2Si_2$, this imply that at $\mu_0 H_N = 0.27\,\mathrm{T}$ there is no QCP or at least the critical fluctuations are not strong. As already mentioned, high magnetic fields promote FM fluctuations instead of AFM ones in $YbRh_2Si_2$, as shown by K. Ishida *et al.* [153] and this could explain why this analysis yields parameters compatible with an FM character of the fluctuations. To test this scenario we have calculated the magnetic Grüneisen ratio at fields below and above H_N and compared the results with those for $Yb(Rh_{0.93}Co_{0.07})_2Si_2$, which are shown in Sec. 4.3.

4.4.4 Field-induced QCP at 1.5 GPa

In the previous section 4.3, the quantity $-(\partial M/\partial T)_H/T$ was introduced, which is needed to calculate the magnetic Grüneisen ratio Γ_H (see Eq. 4.8). In Fig. 4.44 such quantity is calculated from the data of Fig. 4.42. The results are split in two panels, the left one for $0.06 \leq \mu_0 H \leq 0.22\,\mathrm{T}$ (inside the AFM phase) and the right one for $0.25 \leq \mu_0 H \leq 1\,\mathrm{T}$ (at the putative field-induced QCP and outside the AFM phase). The putative field-induced QCP is at $\mu_0 H_N = 0.27\,\mathrm{T}$. Similarly

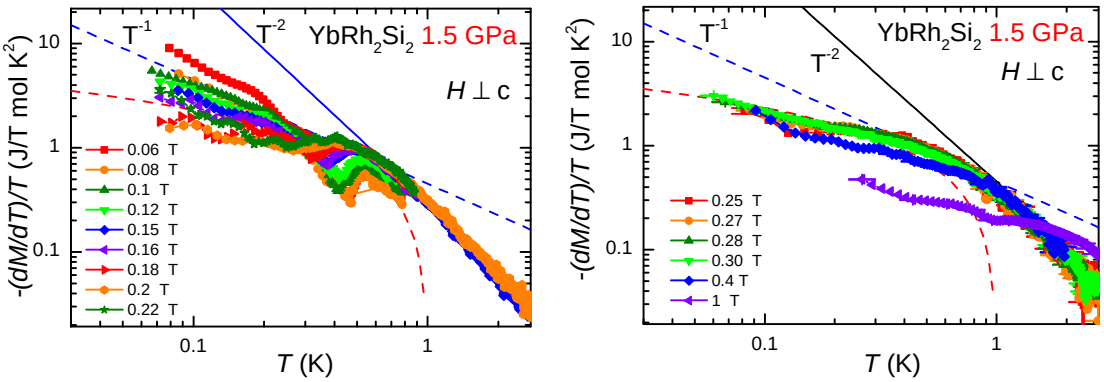

Figure 4.44 – Left: $-(dM/dT)/T$ vs. T for fields $0.06 \leq \mu_0 H \leq 0.22\,\mathrm{T}$ (inside the AFM phase). Right: $-(dM/dT)/T$ vs. T for fields $0.25 \leq \mu_0 H \leq 1\,\mathrm{T}$ (at the field-induced QCP and outside the AFM phase). The lines are guides to the eye. The red dashed line is $\propto -log(T)$.

to what was seen in $Yb(Rh_{0.93}Co_{0.07})_2Si_2$, the quantity $-(dM/dT)/T$ do not show any strong divergence at fields close to 0.27 T. Nevertheless, at high temperatures $-(dM(T)/dT)/T$ is proportional to T^{-2} and below 1 K decreases substantially and eventually follows a $-log(T)$ behavior (red dashed line in Fig. 4.44) down to the lowest temperature. We can not attribute this behavior to the presence of disorder, like in $Yb(Rh_{0.93}Co_{0.07})_2Si_2$, but it seems to be intrinsic. In all fields close to the critical field of 0.27 T this behavior is observed (cf. right panel of Fig. 4.44).

However, for small fields the temperature dependence of $-(dM/dT)/T$ is stronger and follows a T^{-1} at 0.06 T, like in $Yb(Rh_{0.93}Co_{0.07})_2Si_2$ (cf. Fig. 4.36), which is the critical field associated either with the transition at T_L or with the crossover energy T^*.

The specific heat was measured at the same fields as the magnetization on the very same pressure cell. Selected results are plotted in Fig. 4.45 (right panel) as $C(T)/T$ vs. T in a double logarithmic representation. The T_N and T_L phase transitions (not shown) in zero field match quite well those previously reported by Mederle *et al.* at the same hydrostatic pressure [144]. The application of a magnetic field leads to the suppression of the AFM ordered state at the critical field of 0.27 T. Here, the data saturates below 0.25 K and remains constant down to the lowest temperature. In the vicinity of a QCP, a system is known to show

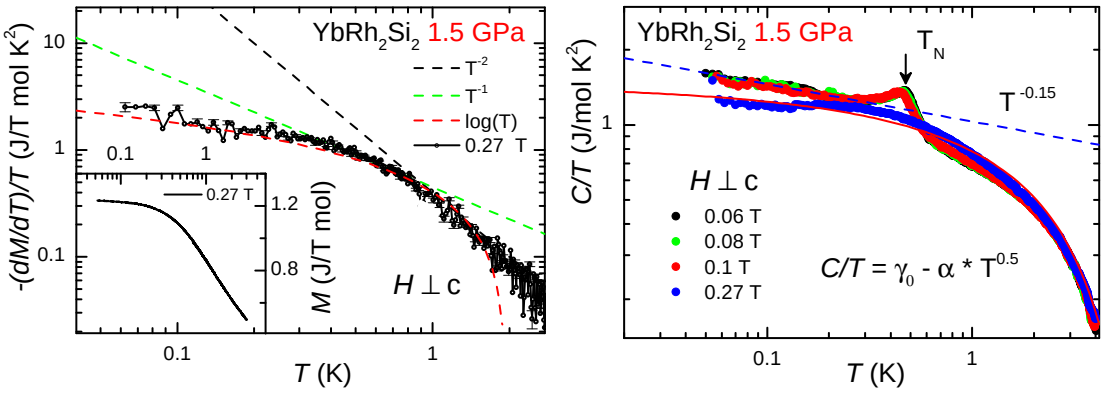

Figure 4.45 – Left: Temperature derivative of the magnetization plotted as $-(dM/dT)/T$ vs. T at the critical field $\mu_0 H_N = 0.27$ T for $YbRh_2Si_2$ at 1.5 GPa. The curve initially increases with a slope proportional to T^{-2} which flattens into a $-log(T)$ behavior below 1 K. Right: Temperature dependence of the specific heat C/T of $YbRh_2Si_2$ at 1.5 GPa for four fields [100]. After the subtraction of the nuclear contribution C_N [157], $C(T)/T$ at the critical field 0.27 T is nearly constant below 0.3 K. For a 3D AFM QCP, C/T consists of a non critical γ_0 and a critical contribution $C/T \propto -\sqrt{T}$ [49, 15]. The solid red line represents a fit to the data according to the equation $C/T = \gamma_0 - \alpha \cdot \sqrt{T}$ which might fit to the data at 0.27 T. The fit parameters are $\gamma_0 = 1.45$ J K^{-2} mol^{-1} and $\alpha = 0.6691$ J mol^{-1} K$^{-3/2}$. For the lower fields, below T_N, C/T follows a $T^{-0.15}$ dependence which is close to a $-log(T)$.

deviations in the Sommerfeld coefficient $\gamma = C/T$ from the Fermi liquid theory (see Tab. 2.1), where it is expected to be constant. For instance, for a 3D itinerant FM QCP, C/T is expected to be proportional to $-log(T)$, while for a 3D AFM QCP, C/T consists of a non critical γ_0 and a critical contribution $C/T \propto -\sqrt{T}$ [49, 15]. The solid red line in the right panel of Fig. 4.45 represents a fit to the data

according to the equation $C/T = \gamma_0 - \alpha \cdot \sqrt{T}$ which might fit to the data at 0.27 T. For the lower fields, below T_N, C/T follows $T^{-0.15}$ dependence which is close to a $-log(T)$. The weak T-dependence of C/T at 0.06 T is in contrast to the strong T^{-1} power-law dependence of $-(dM(T)/dT)/T$. This suggests that Γ_H might be proportional to T^{-1} as expected for a 3D AFM QCP.

4.4.5 The magnetic Grüneisen ratio

As explained in Sec. 2.3.4 and Ref. [15], a divergence in the Grüneisen ratio can be considered as direct evidence of the presence of quantum critical fluctuations and therefore can prove the existence of quantum critical points. The temperature dependence of the magnetic Grüneisen ratio $\Gamma_H(T) = -(\partial M(T)/\partial T)_H/C(T)_H$ of $YbRh_2Si_2$ at 1.5 GPa for fields $0.06 \leq \mu_0 H \leq 0.4$ T, i.e. below and above the critical field $\mu_0 H_N = 0.27$ T, is displayed in Fig. 4.46. The data are plotted in a double logarithmic representation to emphasize the power-law behavior.

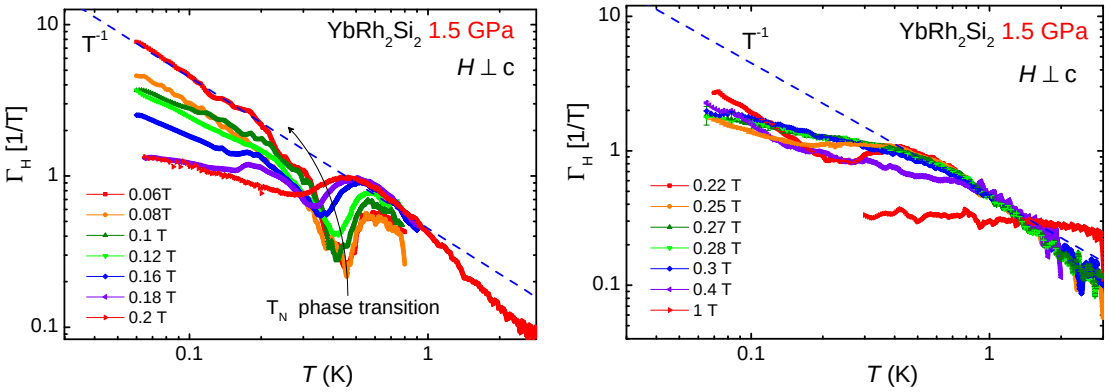

Figure 4.46 – Left: Temperature dependence of the magnetic Grüneisen ratio $\Gamma_H(T) = -(\partial M(T)/\partial T)_H/C(T)_H$ of $YbRh_2Si_2$ at 1.5 GPa for fields $0.06 \leq \mu_0 H \leq 0.2$ T, i.e. below the critical field $\mu_0 H_N = 0.27$ T. The data are plotted in a double logarithmic representation to emphasize the power-law behavior. Right: Same as in the left panel but for fields $0.22 \leq \mu_0 H \leq 0.4$ T, close and above $\mu_0 H_N = 0.27$ T.

For fields $0.22 \leq \mu_0 H \leq 0.4$ T, i.e. close and above the AFM critical field $\mu_0 H_N = 0.27$ T, $\Gamma_H(T) \propto T^{-2}$ above 1 K. But below 1 K it flattens and all curves seem to be proportional to a $-log(T)$ function at low T or a power law with a very small exponent (see analysis in Fig. 4.47). Such a weak divergence is not expected in 3D antiferromagnets at the QCP in either the SDW [15] or the local [165] scenario. Since the system at H_N is expected to be itinerant (cf. discussion in Sec. 4.1.3) it should follow the SDW model, with $\Gamma \propto T^{-1}$ in 3D or $\Gamma_H \propto T^{-1}$ with logarithmic corrections in 2D (see Tab. 2.1). But this is not the case. The

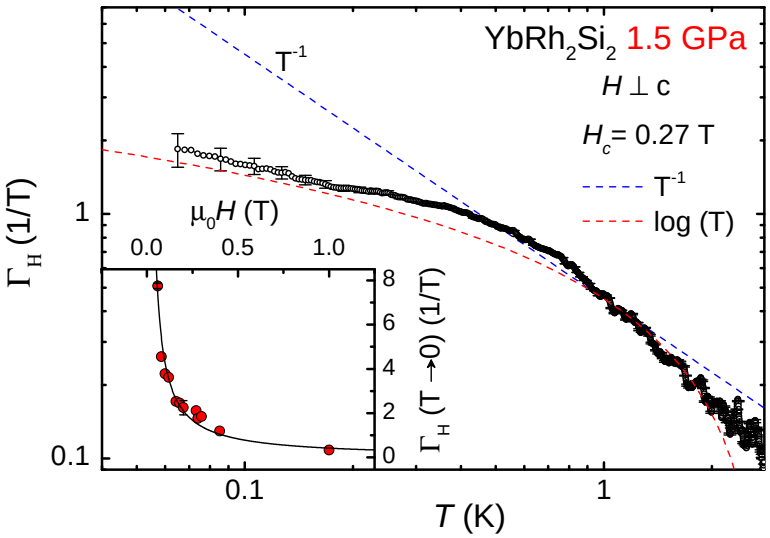

Figure 4.47 – Magnetic Grüneisen ratio of $YbRh_2Si_2$ at 1.5 GPa at the AFM critical field $\mu_0 H_N = 0.27\,\mathrm{T}$. $\Gamma_H(T) \propto T^{-2}$ above 1 K, but below 1 K it flattens and all curves seem to be proportional to a $-log(T)$ function at low T or a power law with a very small exponent of -0.15. The inset shows the field dependence of $\Gamma_H = -G_r(H - H_{cr})^{-1}$ taken at 0.06 K, according to Eq. 4.9. A fit to the data gives $G_r = -0.42$ and $H_{cr} \approx 0.004\,\mathrm{T}$.

weak temperature divergence of $\Gamma_H(T)$ can not be attributed to the presence of disorder, since the samples are of the best quality, and it is therefore an intrinsic property of $YbRh_2Si_2$ at H_N.

The T^{-1} power law is indeed found inside the AFM phase, in particular at 0.06 T. In fact, $\Gamma_H(T)$ keeps increasing inside the AFM phase with a larger slope at the smallest fields. The log-log representation in the left panel of Fig. 4.46 emphasizes such behavior. As it was conclude for the $Yb(Rh_{0.93}Co_{0.07})_2Si_2$ system, we may state that the critical divergencies are observed not at the AFM field-induced QCP but inside the AFM phase at another critical field of about 0.06 T. This field coincides with the critical field of the transition at $T_L(H)$ or with the critical field associated with the Kondo-breakdown crossover line $T^*(H)$ [159]. Since $\Gamma_H = T^{-1/(\nu z)}$ in the SDW scenario, we can extract $z = 2$, since $\nu = 1/2$, which imply an AFM QCP. More information can be deduced from the H-dependence of Γ_H. The inset of Fig. 4.47 shows the field dependence of Γ_H taken at 0.06 K. According to Eq. 4.9, $\Gamma_H = -G_r(H - H_{cr})^{-1}$ with $G_r = \nu(d - z)$. A fit to the data gives $G_r = -0.42$ and $H_{cr} \approx 0.004\,\mathrm{T}$. This is consistent with $z = 2$ when $d \approx 3$ inferring a 3D AFM QCP at a field which is in the range $0 \leq \mu_0 H_{cr} \leq 0.06\,\mathrm{T}$. Unfortunately, a clear statement about the meaning of these parameters and the nature of the QCP inside the AFM phase can not here be given, since these numbers are affected

by the magnetic phase below T_N and, in addition, we did not subtract the non-critical contribution to $\Gamma_H(T,H)$ which can not be correctly estimated.

4.5 The magnetic phase diagrams of $YbCo_2Si_2$

In this section an investigation of the magnetic properties of the high quality single crystals of the $YbCo_2Si_2$ compound by means of dc-magnetization measurements is presented. The low-temperature $H-T$ magnetic phase diagram is derived by applying the magnetic field along three crystallographic directions: [100], [110] and [001]. These data can be used to test the CEF calculations by providing the values of the saturation magnetization and clarify the evolution of the magnetic structure in an applied magnetic field. The results obtained here by dc-magnetization are complementary to those obtained in magnetoresistance [141] and neutron scattering [142, 143] experiments. The interpretation of the data is done by taking into account all these results. This work might be the first step to help identifying the ordered state in the homologue $YbRh_2Si_2$.

The single crystals investigated here has been grown with In-flux technique as fully described in Ref. [112]. They have a residual resistance ratio (RRR = $\rho_{300K}/\rho_{0.35K}$) of 2 at 0.35 K. Its shape is square, with sides parallel to the crystallographic direction [100], which made it easy to align. The dc-magnetization (M) has been measured with a high resolution Faraday magnetometer as described in section 3.2.1, in magnetic fields as high as 4 T and temperatures down to 0.05 K. The ac-susceptibility measurements were performed in a Quantum Design Physical Properties Measurement System (PPMS) in temperatures down to 2 K and magnetic fields up to 3 T. A few measurements have been carried out down to 0.5 K in a ^{3}He option (iQuantum Corporation) for a 7 T-SQUID (Quantum Design). The measurements were made on two different crystals: for the directions $H\|[100]$ and $H\|[001]$ a crystal with a mass of 8.44 mg in the Faraday magnetometer and other crystal from the same batch with 35 mg for the direction $H\|[110]$ in the ^{3}He SQUID.

4.5.1 Magnetization vs. temperature

Figure 4.49 shows the temperature dependence of the uniform susceptibility $\chi = M/H$ in several magnetic fields along the three crystallographic directions. Two features can be identified in all three field directions: A sharp kink at $T_N = 1.75$ K and a distinct drop at $T_L = 0.9$ K. At T_N AFM order sets in but $\chi(T)$ indicates a different antiferromagnetically ordered structure below T_L, as suggested in Ref. [142]. The shape of the magnetization curves reminds to that observed in $YbRh_2Si_2$, (cf. Ref. [105]), pointing to an AFM nature of the phase transition at T_L in $YbRh_2Si_2$. Both T_N and T_L, shift to lower temperatures with increasing

H along the [100] and [001] directions, whereas for $H\|[110]$ T_L remains almost constant in T. For H parallel to [100] and [110] and at fields higher than 0.1 T, the sharp cusp at T_N changes into a plateau, where $\chi(T)$ remains almost constant down to a temperature T'_N (cf. curve at 0.5 T for $H\|[100]$ and curve at 0.55 T for $H\|[110]$ of Fig. 4.49). The lower transition becomes broader in T as the external field is enhanced, and it disappears for fields $H \geq 1$ T along the two directions [100] and [110], but a field of about 1.6 T is necessary to suppress T_L along [001] [108]. A field $H \geq 2$ T is necessary to suppress T_N to zero, where $\chi(T)$ becomes nearly constant in all three directions.

The strong basal anisotropy noticed in the magnetoresistance measurements [141] is confirmed by the different behavior of the isofield curves taken along [100] and [110]. The curves look very similar for $H \leq 0.3$ T but in higher fields the susceptibility along [100] still keeps decreasing below T_L, while along [110] it increases steeply. The picture proposed in Ref. [141] is that the phase transition at T_L is the one where the propagation vector $\mathbf{Q}$ changes from incommensurate to commensurate; the kink at T'_N and the features observed for $H\|[110]$ at $H \approx 0.4$ T would indicate a possible reorientation of the moments without any change in $\mathbf{Q}$. This could explain why χ changes behavior above 0.4 T. Along [001], just two anomalies at T_N and T_L are observed, which are systematically suppressed by fields of 1.6 and 2.35 T, respectively.

It is worth noting that, below T_L and in low fields parallel to [100], the susceptibility follows a T^4 dependence, as shown in Fig. 4.50. This temperature dependence is probably due to spin wave excitations and depends strictly on their dispersion. However, the knowledge of the low-T propagation vector can help us to perform calculations to check this power law, as well as those obtained in specific-heat and resistivity measurements [112, 141].

Figure 4.48 – Photography of a $YbCo_2Si_2$ single crystal on millimeter paper.

4.5.2 Magnetization vs. field

To investigate the phase transition lines in more detail, we measured the field dependence of M at different temperatures. The results are shown in figures 4.51 to 4.53 with the respective derivatives dM/dH. The isothermal curves of Fig 4.51 at 0.05 K, $H\|[100]$ show two metamagnetic-like steps at about 0.65 T and 0.85 T,

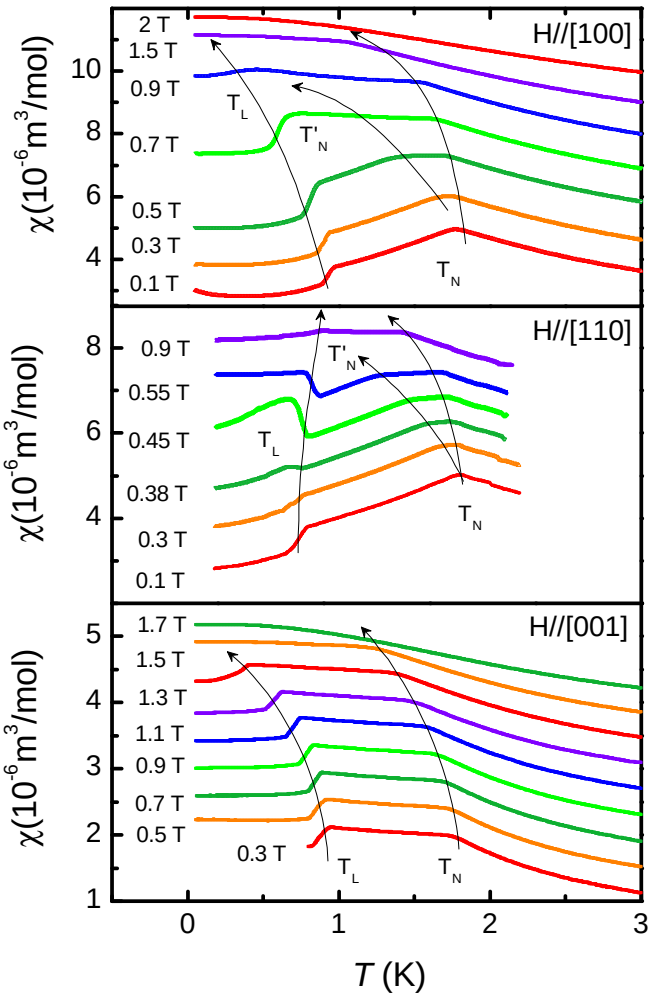

Figure 4.49 – Magnetic susceptibility $\chi = M/H$, plotted as a function of T, in external magnetic fields applied along three crystallographic directions. In every frame, all curves have been shifted for clarity by a constant factor with respect to that at the lowest field. T_N denotes the upper AFM transition temperature, T_L the lower one. T'_N defines the temperature down to which the susceptibility stays constant below T_N and successively decreases. The arrows indicate the evolution of the transition temperatures with increasing magnetic field.

followed by a kink at $H_N = 1.9$ T, which is associated with the transition at H_N (upper frame). Measuring M, while sweeping the field up and down, a small hysteresis is observed across the second phase transition at 0.85 T (cf. inset of the same frame). At H_N the transition is continuous. At a slightly higher temperature $T \approx 0.2$ K, the hysteresis vanishes. By further increasing T, the two steps merge into one at 0.65 K and afterward split again at 0.8 K without showing any hysteresis. This is well illustrated in the bottom frames of Fig. 4.51, where dM/dH is plotted as a function of H. We have assigned the critical fields of the metamagnetic-like transitions to the fields corresponding to the maxima of dM/dH and for the transition at H_N we considered the inflection points in dM/dH. Moreover, from the evolution of these anomalies in field we have associated the fields of the first and second step with the signatures seen at T'_N and T_L, namely H'_N and H_L. These signatures indicate that the nature of the phase line T'_N(H) may be of the second order while the one of T_L(H) is of the first order. This does not contradict the interpretation given in Ref. [143] that at 0.65 T the field modifies the orientation of the moments (either through a spin-flop transition or depopulating unfavored AFM domains, that causes the strong change of slope in M vs. H) without modifying the propagation vector $\mathbf{Q}$, whereas at 0.85 T it is the change of $\mathbf{Q}$, that causes the tiny hysteresis effect. This scenario seems to be confirmed by neutron scattering experiments on single crystals performed in magnetic field [143].

The value of the magnetization just above H_N is 1.4 μ_B/Yb, which is in agreement with the saturated moment calculated by Hodges [126] and by Klingner *et al.* [112], confirming the local magnetic behavior of the Yb $4f$ holes. Above H_N, M increases further possibly because of the van Vleck contributions to M.

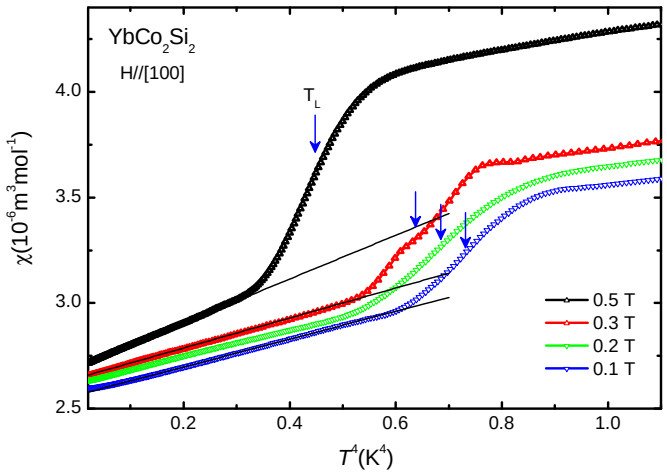

Figure 4.50 – Uniform susceptibility plotted as a function of T^4 to emphasize the behavior below the lower AFM transition temperature T_L (indicated by arrows).

The results of the M vs. H measurements with H along the [110] direction are shown in Fig. 4.52. At all temperatures lower than T_N, a metamagnetic-like step is observed at almost the same field of 0.45 T with no detectable hysteresis, although the temperatures at which these data have been taken are higher than 0.05 K, as shown in the inset of Fig. 4.51. The expected saturation magnetization of 1.4 μ_B/Yb is achieved at $H_N \approx 1.75$ T for a temperature of 0.5 K, below which we did not carry out further measurements. At 1.4 K the signature of such

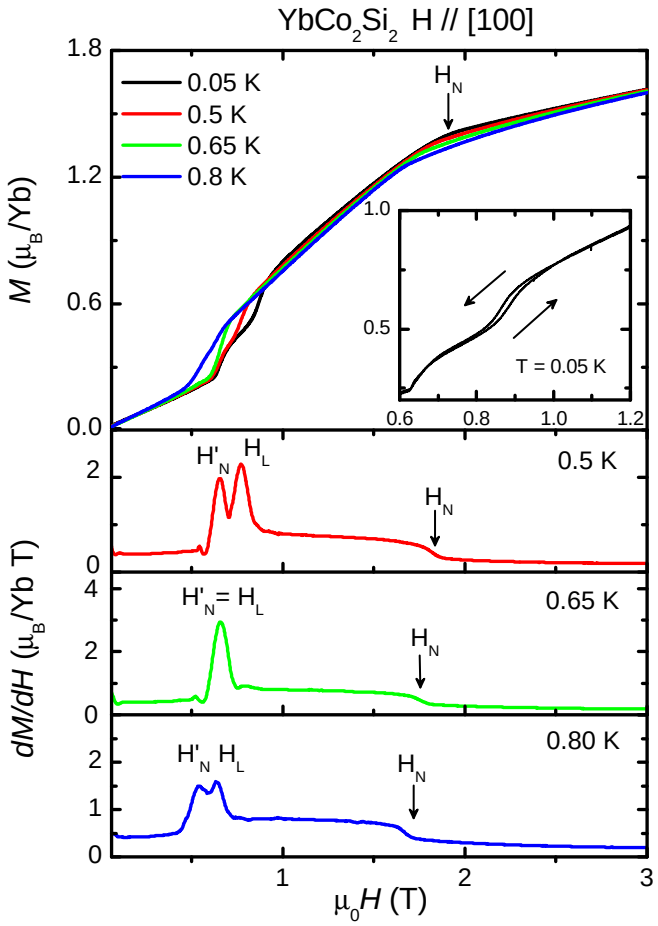

Figure 4.51 – Upper frame: M vs. H at four selected temperatures with $H\|[100]$. H_N denotes the critical field associated with the transition at T_N. In the inset we zoom on the metamagnetic-like transitions to emphasize the hysteresis loop at 0.05 K; the arrows indicate the field sweep direction. In the lower frames, the derivative of the isotherm magnetization is plotted at 0.5, 0.65 and 0.8 K. The two metamagnetic-like transitions visible at 0.5 K join each other to become one at 0.65 K and split again at 0.8 K. This feature is accentuated in dM/dH (in form of peaks). We have associated the fields H'_N and H_L with the transitions at T'_N and T_L, respectively.

anomaly is very weak and can only be observed in the derivative (cf. bottom frame of Fig. 4.52). Since only a metamagnetic-like transition is seen along the [110] direction, one may ask whether this transition represents the reorientation of the moments or a change in **Q**. Since this feature seems to be present also above T_L, we tend to associate it with H'_N.

The Fig. 4.53 shows representative curves of the magnetization as a function of the field (upper frame) and its derivative (lower frame) for $H\|[001]$. Also in these measurements only a single step could be discerned before the magnetization reaches its saturation value of 0.68 μ_B/Yb with a kink at 2.35 T for $T = 0.05$ K. The saturated moment matches very well with that calculated within the CEF

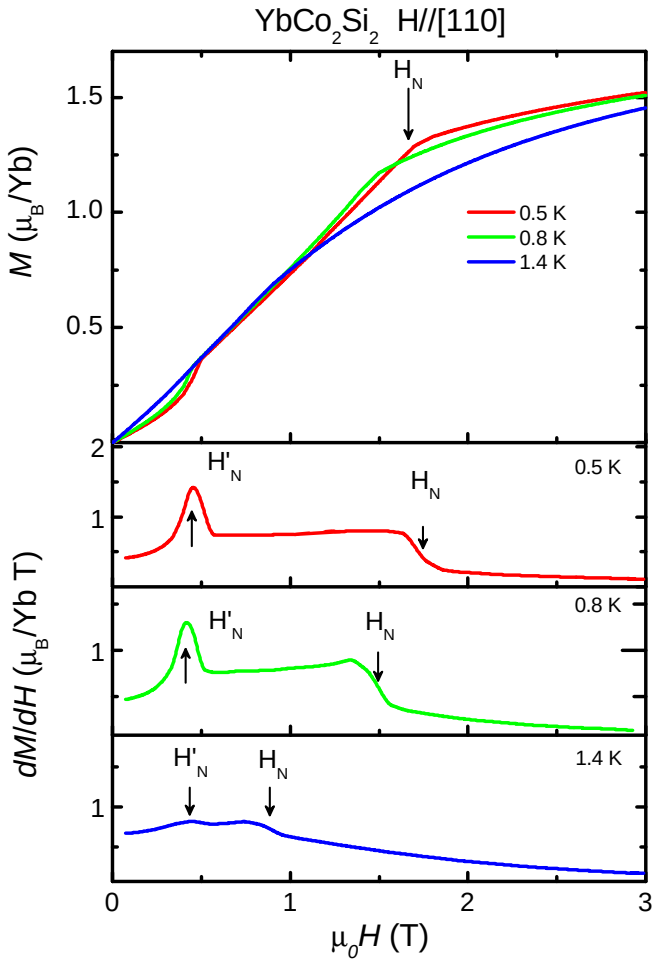

Figure 4.52 – Upper frame: M vs. H at three selected temperatures with $H\|[110]$. Lower frames: dM/dH vs. H at the same three temperatures. H_N and H'_N denote the critical fields associated with the transitions at T_N and T'_N, respectively.

model in Ref.[112]. In this case we have associated the metamagnetic-like step in M vs. H with the phase transition at T_L, although here no hysteresis could be resolved. This association is derived directly from the shape of the phase lines plotted in Fig. 4.54. Both the isothermal and isofield measurements show features at the same phase transition lines where the propagation vector **Q** is believed to change. In the lower frame of Fig. 4.53 we have plotted dM/dH vs. H to emphasize that the signatures at H_L and H_N broaden and the peak intensity is reduced, as expected from the evolution of the phase transition lines.

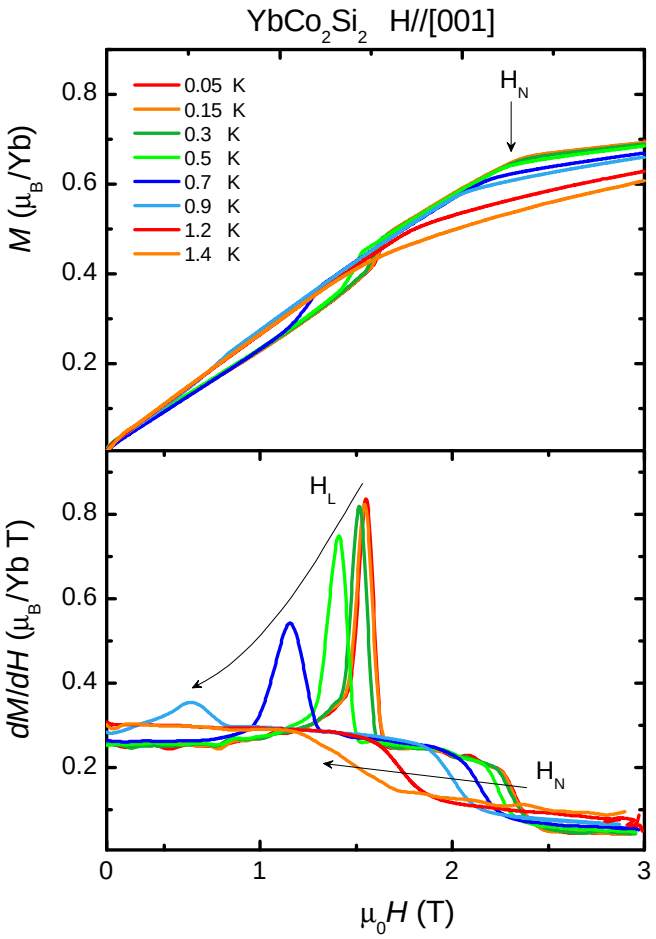

Figure 4.53 – Upper frame: M vs. H at six selected temperatures with $H\|[001]$. Lower frames: dM/dH vs. H at the same six temperatures. H_N and H_L denote the critical fields associated with the transitions at T_N and T_L, respectively. The arrows indicate the evolution of the critical fields with increasing temperature.

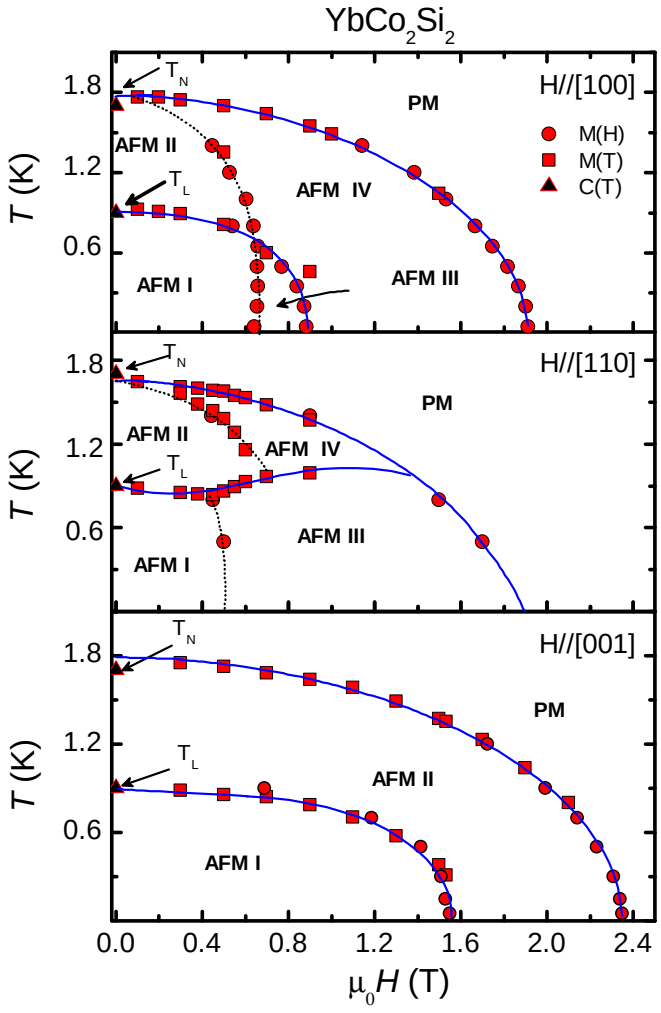

Figure 4.54 – Magnetic phase diagram of $YbCo_2Si_2$ with $H\|[100]$, [110] and [001]. The square and circle points have been extracted from isofield and isothermal measurements of M, respectively. PM indicates the paramagnetic region while AFM the antiferromagnetic one. The four different AFM phases are labeled from I to IV. The full lines represent phase transition lines at which the propagation vector $\mathbf{Q}$ changes, whereas the dashed lines mark the reorientation of the moments. The border between the PM and the AFM regions has been fitted with the curve: $[H_N(T)/H_N(0)]^n + [T/T_N(0)]^n = 1$, where $T_N(0) = 1.77$ K, $\mu_0 H_N(0) = 1.9$, 1.88 and 2.35 T and n = 1.9, 1.78 and 1.94 for $H\|[100]$, [110] and [001], respectively. The differences in the evolution of T_N at $\mu_0 H(T) = 0$ between $H\|[100]$, $H\|[001]$ and $H\|[110]$ come from the fact that the magnetization measurements were performed in two different crystals from the same batch.

4.5.3 $H - T$ phase diagrams

The deduced magnetic $H - T$ phase diagram with H applied along the three crystallographic directions [100], [110] and [001] is shown in Fig. 4.54. The squares and circles indicate anomalies observed in M vs. T and M vs. H, respectively. The outer second order phase-transition boundary line, which separates the AFM from the paramagnetic (PM) phase, can be followed from 1.75 K in zero field up to the critical fields $\mu_0 H_N(0) = 1.9$, 1.88 and 2.35 T along the three directions. The data along these lines can well be described by an empirical curve $[H_N(T)/H_N(0)]^n + [T/T_N(0)]^n = 1$ with n close to 2. The exponents are displayed in the caption of Fig. 4.54. For $H//[110]$ T_N at zero field is slightly smaller than that measured along [100] or [001]. This is due to the fact that the isofield measurements were performed in the SQUID on a second sample of the same batch [110].

Inside the magnetic phase, four AFM regions can be identified when the field is applied along the basal plane (upper panels), while for $H//[001]$ only two regions have been observed (lower panel). We start our description from the lower panel of Fig. 4.54. Since the two AFM phase transitions at T_N and T_L in zero field have been established to be of the second and first order and involve a change of the propagation vector **Q** [111, 142, 143], it is straightforward to draw continuous lines on the points and consider the two regions AFM I and II as regions with different **Q**. On the other hand, for $H//[100]$ the $T_N(H)$ line seems to split in field separating the regions AFM II and IV and AFM I and III by a second-order-like phase transition indicated by a kink at T'_N or a metamagnetic-like step at H'_N without hysteresis (see Figs. 4.49 and 4.51). In addition, the boundaries between the phases I and II and between the phases III and IV appear to be first order lines (see Fig. 4.51). For this reason we have drawn a continuous line, which we think separates the regions with different **Q**. A similar interpretation can be considered for $H//[110]$, but in this case the line separating the two magnetic structures is almost constant in temperature. Recent neutron scattering experiments performed in magnetic field seem to support such a scenario [143]. Taking into account all our findings and the results of Refs. [141, 142, 143] we might interpret our data as follows: Region II is characterized by AFM order with an incommensurate arrangement of the moments, which then assumes a commensurate structure in region I through a first order phase transition. By applying a magnetic field along [001], the arrangement of the moments undergoes a metamagnetic-like transition changing the propagation vector and becoming fully polarized above 2.35 T. The same feature is expected across the continuous line inside the magnetic ordered phase for $H//[100]$ (upper panel of Fig. 4.54), e.g. between the AFM III and AFM IV. For $H//[100]$ and [110] the magnetic field modifies the orientation of the moments at $T'_N(H)$ (dashed lines in Fig. 4.54), either through a spin-flop transition or depopulating unfavored AFM domains, without modifying the propagation vector **Q**. However,

in Ref. [143] a significant difference between the behavior of the magnetoresistance across the dashed lines for temperatures lower and higher than $T_L(H)$ was observed: For $T > T_L(H)$ the magnetoresistance shows a kink at $T'_N(H)$ suggesting a continuous transition, e.g. a depopulation of unfavored AFM domains, while for $T < T_L(H)$ the magnetoresistance shows a distinct drop inferring a spin-flop transition, possibly into a structure with a ferromagnetic component. The fact that only for $H//[001]$ no reorientation of the moments is observed, suggests that the moments may lie in directions close to the basal plane, as previously suggested by Hodges [126]. Our interpretation assumes that the AFM structure allows multiple domains and that the dashed lines in Fig. 4.54 may indicate a simple domains depopulation effect. Another and more suggestive possibility is that of a double-**Q** structure as has been found, e.g., in $GdNi_2B_2C$ [168]. The same principle holds for such a kind of structure in which the field somehow favors one or the other propagation vector.

In summary, in this section the magnetic phase diagram of single crystals of $YbCo_2Si_2$ was explored by means of isothermal and isofield magnetization measurements with the magnetic field oriented along the crystallographic directions [100], [110] and [001]. In a small field $\mu_0 H = 0.1$ T two AFM phase transitions were detected at $T_N = 1.75$ K and $T_L = 0.9$ K, in the form of a sharp cusp and a sudden drop in $\chi = M/H$. These signatures confirm that the phase transitions are second order at T_N and first order at T_L. The shape of the magnetization curves are similar to those observed in $YbRh_2Si_2$ pointing to an AFM nature of the phase transition at T_L in $YbRh_2Si_2$. The AFM order is completely suppressed by fields close to 2 T where the magnetization reaches its saturation values $M_s(H\|[100])$ and $M_s(H\|[110]) \approx 1.4\mu_B$ and $M_s(H\|[001]) \approx 0.68\mu_B$ which match quite well with those calculated for the Γ_7 ground state proposed in Ref. [112] confirming the trivalent state of the Yb ions in $YbCo_2Si_2$. Inside the AFM phase, two main regions can be identified along all directions where the propagation vector **Q** assumes two different values. For H parallel to [100] and [110] (the magnetic structure is anisotropic in the basal plane), however, these regions are separated by another line, which seems to correspond to the line where the magnetic moments reorient, and separates AFM domains; in the case of an AFM double-**Q** structure we would observe the same features and the available neutrons scattering results needs to clarify this point. For H parallel to [001] only two AFM phases have been observed, implying that the moments might lay in directions close to the basal plane.

4.5.4 Ac-susceptibility

Finally, I would like to briefly compare ac-susceptibility $\chi'(T)$ measurements on $YbCo_2Si_2$ with those performed on $YbRh_2Si_2$ [125]. In the latter compound a maximum was observed in the temperature dependence of $\chi'(T)$ in magnetic field

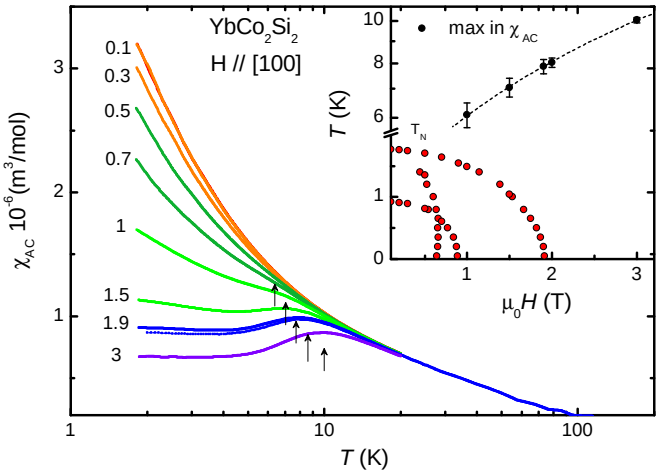

Figure 4.55 – Temperature dependence of the ac-susceptibility $\chi'(T)$ measured at different applied magnetic fields. The arrows indicate the maximum observed only at high fields. Inset: Magnetic phase diagram with $H\|[100]$ in which we have included the points extracted from the maxima of $\chi'(T)$.

and it was associated with an energy scale $T^*(H)$ interpreted as the energy where the Kondo effect breaks down due to the presence of a field-induced QCP at H_N. The $T^*(H)$ line vanishes for $T \to 0$ at the QCP [57]. In $YbCo_2Si_2$ we observe a similar effect, i.e., maxima in $\chi'(T)$ which are indicated by arrows in Fig. 4.55. Plotting the maxima on the phase diagram (inset of the same figure) we can deduce from the evolution of the points that the similar energy scale $T^*(H)$ for $YbCo_2Si_2$ is not approaching the critical field H_N. In $YbRh_2Si_2$ the maxima undoubtedly represents the thermally activated excitation of the Γ_7 doublet split by the Zeeman effect.

A straightforward comparison between the two systems cannot be done, since $YbCo_2Si_2$ is a system where the Yb quasi-holes are almost localized while in $YbRh_2Si_2$ they are almost delocalized. It would be however interesting to study the evolution of this energy scale while varying the Co content, as has already been done in Ref. [125] and [117] for low Co concentrations.

4.6 Conclusions

In this Chapter, seven high-quality single crystals of the series $Yb(Rh_{1-x}Co_x)_2Si_2$ (with $x = 0, 0.07, 0.12, 0.18, 0.27, 0.58$ and 1) were investigated by means of magnetization measurements in a temperature range $0 \leq T \leq 4\,\mathrm{K}$ and field range $0 \leq \mu_0 H \leq 12\,\mathrm{T}$.

We have investigated the evolution of magnetism from itinerant (with $x = 0$ and $H > H_N$) to local (with $x = 1$) in $Yb(Rh_{1-x}Co_x)_2Si_2$ (Sec. 4.2) and drawn an instructive magnetic moment μ vs. chemical pressure x phase diagram (see Fig. 4.30). At zero pressure and at $H > H_N$ the Kondo energy scale dominates over the RKKY one, almost screening the magnetic Yb^{3+} moments and leaving AFM order just below 0.07 K and a very small ordered moment $\mu(H_N) \approx 0.1\,\mu_B/Yb$. The system shows itinerant magnetism and heavy-fermion character. At the critical field H_N of the AFM phase a QCP is found with pronounced NFL properties and an associated energy scale $T^*(H^*)$ where the Kondo effect breaks down and a Fermi surface reconstruction takes place (Sec. 2.3.2). This energy scale separates a region where the magnetic moments have local character from a region where they have itinerant character (see Fig. 4.11). One of the first observations is that this energy scale seems not to be very affected by pressure. With increasing pressure, i.e. decreasing the strength of the hybridization J, the magnetic moment $\mu(x)$ increases rapidly as a consequence of the rapid decrease of the Kondo temperature T_K. T_{RKKY} also decreases but in a smoother way. Therefore, at above $x = 0.27$ the RKKY interaction dominates substantially over the Kondo interaction and $\mu(x)$ vs. x still increases, but weakly. Between $x = 0.27$ and $x = 1$ the systems still show weak heavy-fermion character, while at $x = 1$ the pressure is enough to eventually localize the $4f$-electrons and we obtain $\mu = \mu_{sat}$. This demonstrates the fact that magnetism evolves continuously from itinerant to local in $Yb(Rh_{1-x}Co_x)_2Si_2$. On the other hand, the evolution from itinerant to local magnetism induced by magnetic field takes place in two steps. First, the field induces Lifshitz transitions where the Fermi surface changes from large to small as a result of the shift of a van-Hove singularity across the Fermi level and then the fully localization of the f electrons takes place smoothly at even higher fields where the magnetic moment achieves its saturation value. Hence, both the coherence effects resulting from the lattice periodicity as well as the de-renormalization of the quasiparticles, which is reflects the break-up of the local Kondo singlets, have to be taken into account.

The physics of the antiferromagnet $YbCo_2Si_2$, i.e. at high x, can completely be understood, if one considers Yb local moments and the CEF schema shown in Sec. 4.1.2. On the other side, the physics of pure $YbRh_2Si_2$ and small x is much more problematic, due to the itinerant character of magnetism and the vicinity of the system to a QCP. We have tried to characterize the field-induced AFM QCP at the critical field H_N in $Yb(Rh_{0.93}Co_{0.07})_2Si_2$ (Sec. 4.3) and in pure $YbRh_2Si_2$ under a pressure of 1.5 GPa (Sec. 4.4) by means of a measure of the magnetic Grüneisen ratio $\Gamma_H(T, H)$. This QCP is located in the itinerant part of the phase diagram and supposed to be described by the SDW scenario (Sec. 2.3.1). We have found very similar results in $Yb(Rh_{0.93}Co_{0.07})_2Si_2$ and in $YbRh_2Si_2$ under 1.5 GPa demonstrating that, for small $x \leq 0.12$, chemical pressure is equivalent to

hydrostatic pressure. At H_N, $\Gamma_H(T) \propto -log(T)$ and therefore does not diverge as expected ($\Gamma \propto T^{-1}$ in 3D AFM QCP). However, at fields well below H_N, $\Gamma_H(T) \propto T^{-1}$ inferring a 3D AFM QCP at a field which is in the range $0 \leq \mu_0 H_{cr} \leq 0.06\,\mathrm{T}$. Unfortunately, a clear statement about the nature of the QCP inside the AFM phase can not here be given, since the extracted parameters are affected by the magnetic phase below T_N and, in addition, we did not subtract the non-critical contribution to $\Gamma_H(T, H)$ which can not be correctly estimated.

5 $NiCl_2$-4SC$(NH_2)_2$

5.1 Introduction and motivation

This section is dedicated to the study of the field-induced quantum phase transition in the strongly anisotropic quasi-one dimensional $S = 1$ Ni^{2+} chain $NiCl_2$-4SC$(NH_2)_2$ (dichloro-tetrakis-thiourea-nickel(II)), better know as DTN (see Fig. 5.1). Differently from theories of QPTs in metals, the theory of QPTs in magnetic insulators, like DTN, seems to be better understood and to match often the experimental evidence. The QPTs in DTN are induced by magnetic field. In fact, DTN enters a XY AFM ordered state below 1.2 K between moderate fields

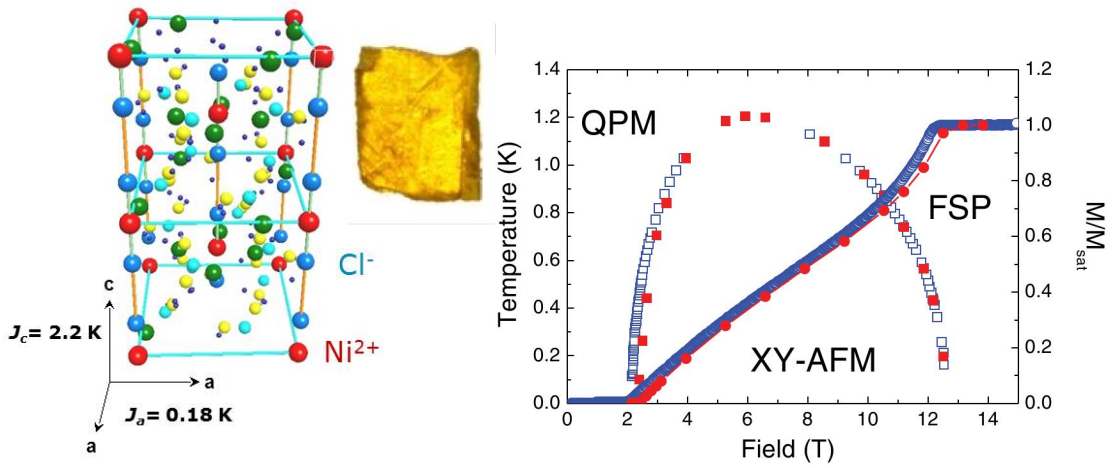

Figure 5.1 – Left: Body-centered tetragonal crystal structure of DTN with chains of Ni-Cl-Cl-Ni atoms arranged along the crystallographic c direction. The AFM exchange constants between neighboring spins are $J_c = 2.2$ K along the chains and about 10 times smaller, $J_{ab} = 0.18$ K, in the ab-plane. DTN crystals are yellow (inset). Right: Field dependence of the magnetization at 16 mK (right scale). The phase boundary line between the quantum paramagnetic (QPM) phase, the XY AFM phase and the fully spin-polarized (FSP) phase was obtained by magnetocaloric-effect measurements (open squares). The solid squares and circles were obtained by Monte Carlo calculations. Figure taken from Ref. [86].

$\mu_0 H_{c1} \approx 2\,\mathrm{T}$ and $\mu_0 H_{c2} \approx 12.5\,\mathrm{T}$. In this prospect, quantum magnets like DTN are suitable materials to be investigated by means of magnetization measurements.

DTN has a body-centered tetragonal crystal structure with chains of Ni-Cl-Cl-Ni atoms arranged along the crystallographic c direction (see Fig. 5.1). The magnetic Ni^{2+} atoms carry spin $S = 1$ due to an almost completely quenched orbital momentum. The dominant single-ion anisotropy constant $D/k_\mathrm{B} = 8.9\,\mathrm{K}$, and the AFM exchange constants between neighboring spins $J_c/k_\mathrm{B} = 2.2\,\mathrm{K}$ (along the chains) and $J_{ab}/k_\mathrm{B} = 0.18\,\mathrm{K}$, (in the ab-plane) were obtained by neutron scattering and ESR experiments [82, 86]. The gyromagnetic factor g parallel to the c-axis was estimated to be 2.26 by ESR experiments [86]. The ground state at $H = 0$ is non magnetic $(S = 1, S^z = 0)$ and is separated from the first excited state $(S = 1, S^z = \pm 1)$ by an energy gap Δ (see Fig. 2.11 of Sec. 2.4). The magnetic field eventually closes the gap at a critical field H_{c1} inducing a QPT into a XY AFM ordered state with finite magnetization and AFM magnon excitations. The magnetization then rises up to the saturated value at H_{c2} (cf. right panel of Fig. 5.1).

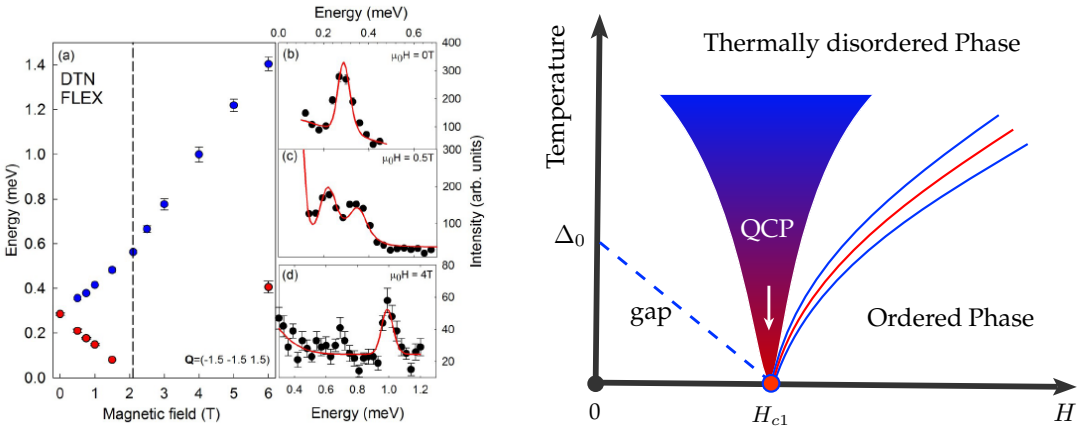

Figure 5.2 – Left: Energy of the spin excited doublet plotted as function of the applied magnetic field parallel to the crystallographic c-axis and measured at wave vector $Q = (-1.5, -1.5, 1.5)$. The energy of the scans in magnetic field are shown in the subplots (b), (c) and (d). Right: Schematic view of the phase boundary line of a gapped quantum magnet. The dotted line shows the energy of the spin gap shifted linearly by the Zeeman effect. The blue-red conical region indicates the region of enhanced quantum fluctuations at $T > 0$. The red solid line represents the phase boundary between the paramagnetic and the XY-AFM phase, while the two blue lines represent the region with strong thermal fluctuations. Figure taken from Ref. [169].

The first microscopic evidence that the zero-field magnetic excitations in DTN are doublet states was found by N. Tsyrulin by means of neutron spectroscopy [169]. He observed how the energy levels of the doublet excited state split linearly with increasing field, (see left panel of Fig. 5.2). This figure shows the magnetic excitation spectrum as a function of energy for different magnetic fields. At $\mu_0 H_{c1} \approx 2\,\mathrm{T}$ the magnetic sublattice undergoes a second order phase transition into a XY AFM order. This XY AFM order can be described as a Bose-Einstein condensation of magnons by mapping the spin-1 system into a gas of hardcore bosons [71]. This analogy between ultra cold diluted atomic gases and BEC in quantum magnets was theoretical predicted by Matsubara and Matsuda in 1953 [71] and observed experimentally in the gapped $S = 1/2$ dimer compound $TlCuCl_3$ [74, 68, 75, 76]. An overview of the theory is given in Sec. 2.4. The DTN system can be fully described by the Hamiltonian 2.23 in Sec. 2.4 and all thermodynamical quantities can be calculated, as done, e.g., in Eqs. 2.33. The expectation values for critical exponents at the field-induced QCP at H_{c1} can be obtained analytically and numerically. The universality class of the QCP can be determined by measuring the temperature dependence of thermodynamic quantities like the magnetization $M(T)$ or the specific heat $C(T)$ and the shape of the phase border line in the vicinity of the QCP [68]. Tab. 2.3 of Sec. 2.4 displays the expectation exponents for a XY antiferromagnet and the Ising QCP, both in three dimentions ($d = 3$). The BEC of magnons belongs to the 3D XY universality class with $d = 3$ and dynamical exponent $z = 2$. In addition, by using $M(T)$ and $C(T)$, the temperature dependence of the magnetic Grüneisen ratio $\Gamma_H(T)$ can be obtained and compared with the expected behavior $\Gamma_H(T) \propto T^{-1/\nu z}$ at the QCP (cf. Sec. 2.3.4).

5.2 Results

In the following, dc-magnetization measurements on a single crystal of $NiCl_2$-$4SC(NH_2)_2$ by means of the high-resolution Faraday magnetometer (described in Sec. 3.2.1) are presented. In addition, specific heat measurements performed by A. Steppke [157] with the compensated heath-pulse technique [170] on the same sample are shown and used to calculate the magnetic Grüneisen parameter (see Sec. 2.3.4). All measurements were performed down to 50 mK an up to 5 T. We have accurately determined the phase diagram boundary line and performed an accurate analysis of the temperature dependence of $M(T)$ and $C(T)$ in order to obtain critical exponents that are compared to those predicted for the XY-AFM and Ising universality classes. A detailed analysis of the Grüneisen parameter at the quantum critical point is also given.

5.2.1 Magnetization

Fig. 5.3 shows the magnetization $M(H)$ curves obtained in magnetic field up to 5 T applied along the c-axis at temperatures between 0.05 and 0.5 K. The magnetization increases linearly and very slightly from $H = 0$ up to the critical field $\mu_0 H_{c1} = 2.12$ T at which it changes slope[1]. The kink in M vs. H can clearly be observed at the phase transition where the spin gap closes and the XY-AFM order sets in. For $H > H_{c1}$ the magnetization increases linearly as expected (see right panel of Fig. 5.1). With increasing T, the kink is shifted to higher fields as

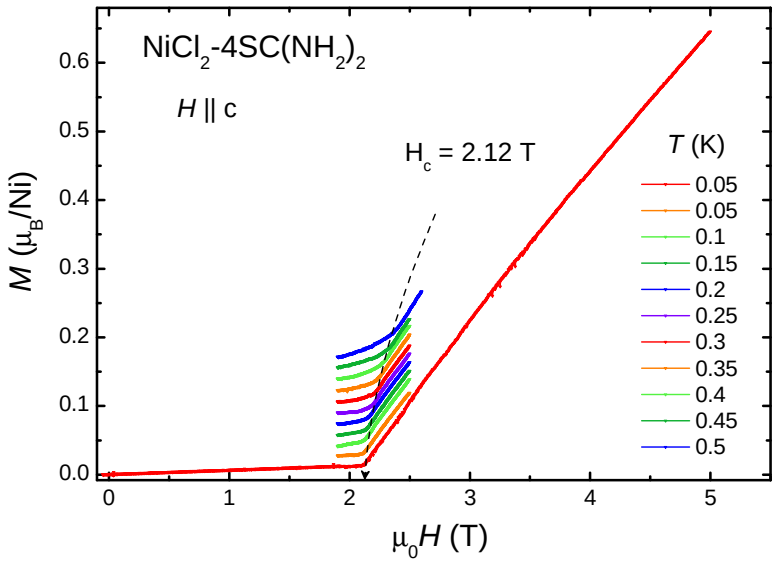

Figure 5.3 – Magnetization M plotted as a function of the magnetic field $H \| c$ at different temperatures. The curves are vertically shifted by $0.014 \mu_B$/Ni for better visibility. The dashed arrow indicates the evolution of the critical field H_{c1}, at which M vs. H shows a kink.

expected from the shape of the phase diagram (see right panel of Fig. 5.1). The field at which the phase transition occurs can be accurately obtained from the position of the peak of the second derivative of the magnetization with respect to field d^2M/dH^2. This peak sharpens as the temperature is reduced. In Fig. 5.4, d^2M/dH^2 vs. H is shown for the measurement done at the lowest temperature of

[1] In our publication, i.e. Ref. [171], the increasing of $M(H)$ for $H < H_{c1}$ is associated to a misalignment of the sample of less than 1.2°, which gives a contribution $M(H \perp c)$ to the magnetization, and the data were corrected. This is because the ground state is a singlet between $H = 0$ and H_{c1} and the magnetization should be zero. This correction results in a slightly different value of the critical field, i.e. 2.08 T. In this section the raw data are analyzed with $\mu_0 H_{c1} = 2.12$ T. There is no difference between our analysis and that performed in Ref. [171] as well as in the conclusions.

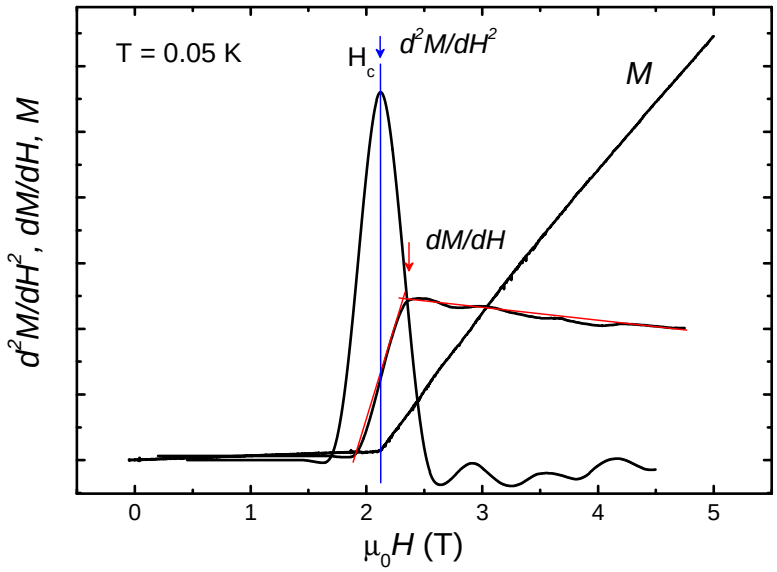

Figure 5.4 – First and second derivative of $M(H)$ with respect to H, plotted as a function of H for the measurement taken at 0.05 K. The sharp peak in the second derivative marks the position of the critical field H_{c1} (blue line).

0.05 K. The vertical line indicates the correct position of H_{c1}, which is 2.12 T. This method of extracting the critical field is significantly more accurate and reliable than the method used by Paduan-Filho *et al.* [172] in which only the first derivative is taken into account. The thermodynamic validation of such an argument is explained in the Ref. [173].

The temperature dependence of the magnetization $M(T)$ is presented in Fig. 5.5 at several magnetic fields below and above the critical field H_{c1}. The transition to the XY-AFM ordered state is marked by a dip in $M(T)$ which is a phase transition of second order surrounded by thermal fluctuations, similar to what was observed previously by Paduan-Filho *et al.* [81]. Inside the ordered state the spins of nickel are in a canted configuration (↖↗↖↗), and the magnetization for $T \to 0$ increases with increasing field. When the temperature is increased at values close to the single-ion anisotropy constant $D/k_B \approx 9$ K the magnetization shows a maximum (at about 5 K), indicating the presence of the spin gap. Neglecting the exchange interaction parameters between the Ni sites we can simplify the Hamiltonian 2.23 as

$$\mathcal{H} = \sum_i [D(S_i^z)^2 - g\mu_B\mu_0 H S_i^z] \tag{5.1}$$

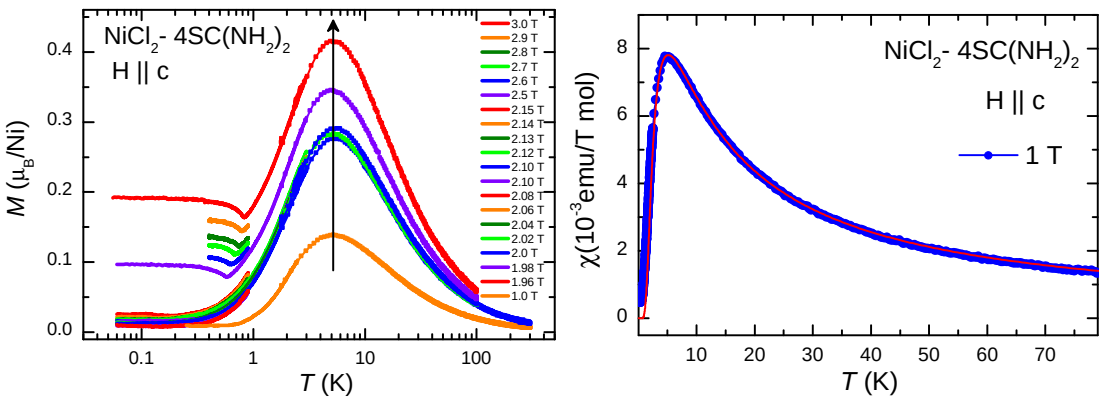

Figure 5.5 – Left: Magnetization curves as a function of temperature for several magnetic fields applied along the c-axis. The maxima at about 5 K indicate the spin gap. The onset of magnetic order at low temperatures is marked by a dip [81]. Right: Temperature dependence of the magnetic susceptibility at 1 T along the crystallographic c-axis. The solid line is a fit to the data with Eq. 5.2.

where only the single-ion anisotropy is taken into account [80]. The susceptibility along the c-axis can be calculated and is

$$\chi_{H\parallel c} = \frac{2\mu_0 N_A(\mu_B g)^2}{k_B T(2 + e^{D/k_B T})} \tag{5.2}$$

where N_A is the Avogadro number, μ_B is the Bohr magneton and D is the single ion anisotropy constant. The susceptibility at high temperatures follows the Curie-Weiss law and below 5 K it decreases exponentially to zero due to the opening of the spin gap. A fit of the measured curve at 1 T with Eq. 5.2 is displayed in the right panel of Fig. 5.5. Eq. 5.2 reproduces quite well the data. Only at very low temperatures the fit deviates slightly due to the impact of the exchange interaction and the fact that at 1 T the measured magnetization is not zero. The fit gives a value for D/k_B of ≈ 8.23 K, which is very close to the published data [82, 86].

5.2.2 Comparison between theory and experiment

Using the measurements displayed in Figs. 5.3 and 5.5, we can extract the points of the phase transitions for fields close to H_{c1} at low temperature. According to the expectation values summarized in Tab. 2.3, the phase boundary line should follow $T_c \propto (H - H_c)^{1/\alpha}$ with $\alpha = 3/2$ for a XY-AFM (BEC) or $\alpha = 2$ for an Ising antiferromagnet. Fitting our data we could find the universality class of the quantum critical point provided we fit the data in the lowest temperature range,

where thermal fluctuations are negligible. Fig. 5.6 shows the extracted data as well as two fitting functions. The blue line is a fit over all points by keeping the parameters free. The fit suggests $\alpha \approx 2$ and seems to describe quite well the experimental data down to the critical field of 2.12 T. The red line is a fit of the data in the field range delimited by the black arrows (below 500 mK) by keeping the exponent $\alpha = 3/2$ fixed. This fit also matches quite well the data. At low temperature it is therefore difficult to discern between the XY or the Ising scenarios (see inset of Fig 5.6). It has to be mentioned, that investigations of the

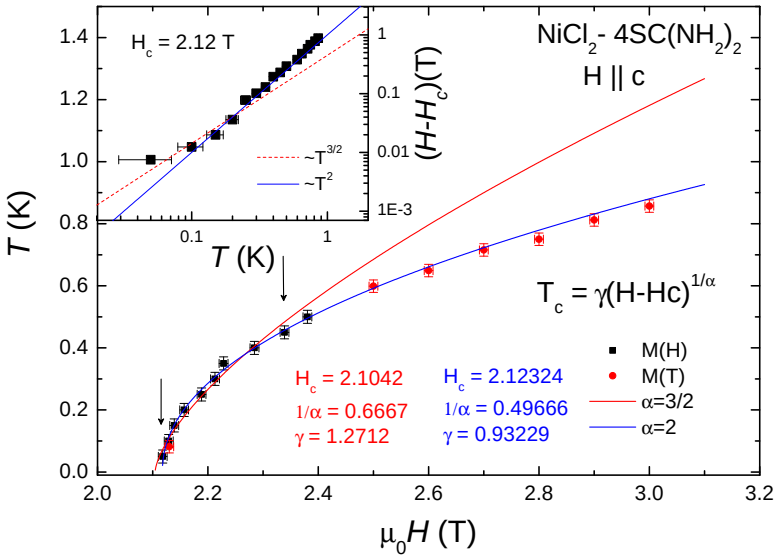

Figure 5.6 – Phase transition boundary line extracted from measurements displayed in Figs. 5.3 and 5.5. The solid lines are fits with equation $T_c = \gamma(H - H_c)^{1/\alpha}$. At high temperature the fit with $\alpha \approx 2$ seems to describe quite well the experimental data. At lower temperature, in particular in the field range delimited by the arrows, both fits match quite well the data. The T dependence of α is shown in the inset by the plot of $H - H_c$ vs. T on double logarithmic scales.

exact shape of the phase boundary close to H_{c1} down to 1 mK was successfully performed by detailed AC susceptibility measurements by L. Yin *et al.* [174]. They found that below 300 mK the universality class is of a BEC. Up to date, this is the solely experimental observation consistent with a field induced BEC-QCP in this material. Our measurements go down to only 50 mK and below 300 mK only few points can be used for the fit. In addition, as shown in Fig. 2.12 of Sec. 2.4, the theoretical calculation for the magnetization of DTN at H_{c1} (after having used experimental parameters) shows that the BEC critical exponents can be observed only below $J_\perp/k_B \approx 0.18$ K. Below this temperature, $M(T) \propto T^{3/2}$, which is the signature of the presence of quantum critical fluctuations.

To check this theoretical prediction (see Tab. 2.3) we have plotted in Fig. 5.7 the magnetization $M(T)$ as a function of $T^{3/2}$ for magnetic fields $H \| c$ between 1 and 3 T. The curves are shifted vertically by $0.014\,\mu_B$/Ni for clarity. The arrows mark the onset of the XY-AFM state while the continuous dashed region marks the position in temperature where $M(T)$ deviates from the $T^{3/2}$ behavior and becomes constant. We can observe that at lower fields the curves do not show a power law dependence inside the quantum paramagnetic state but the magnetization is almost constant at low T. Nevertheless, as we approach to the critical field $\mu_0 H_{c1} = 2.12\,\mathrm{T}$, the magnetization develops a $T^{3/2}$-behavior at low temperatures over a decade in temperature ($0.1 \leq T \leq 1\,\mathrm{K}$), in agreement with the expected behavior for a BEC QCP in 3 dimensions. No T^2 proportionality is observed.

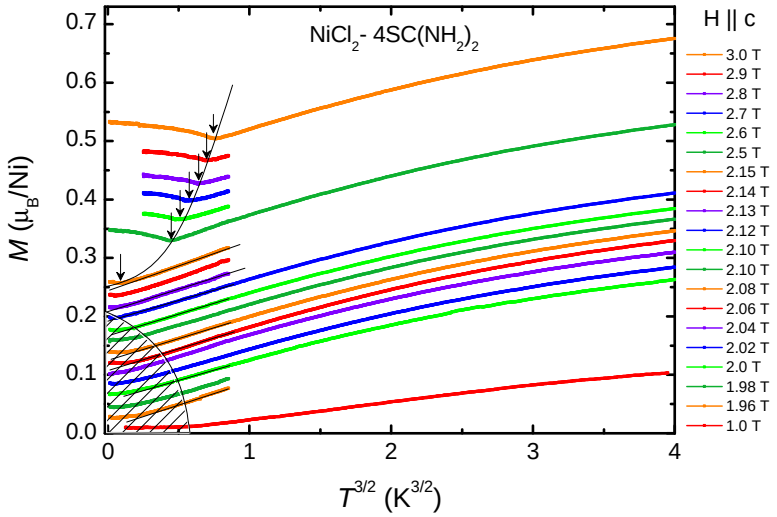

Figure 5.7 – Magnetization plotted as a function of $T^{3/2}$ for magnetic fields $H \| c$ between 1 and 3 T. The curves are shifted vertically by $0.014\,\mu_B$/Ni for clarity. The arrows mark the onset of the XY-AFM state. The continuous dashed region marks the position in temperature where $M(T)$ deviates from the $T^{3/2}$ behavior.

This results clearly indicate the presence of a QCP and that its universality class is that of an XY antiferromagnet, in contrast to the T^2 dependence for an Ising magnet.

To further support this point, we have fitted the magnetization at 2.08 T, slightly below H_{c1}, with the function 2.35 of Sec. 2.4 with $\mu_0 H \approx 2\,\mathrm{T}$, $\mu \approx 0$, $J_\parallel/k_B = 2.2\,\mathrm{K}$, $J_\perp/k_B = 0.18\,\mathrm{K}$, $D/k_B = 8.9\,\mathrm{K}$, plus an additional offset $m_0 = 0.013\,\mu_B$. No big difference can be seen between the fit in 1D and that in 3D. The initial parameters are unchanged apart of the gyromagnetic ratio g which is 2.8 in 1D and $g = 2.65$ in 3D in very good agreement with the experiments [86]. The data with the fit are shown in Fig. 5.8. We observe that the analytic results agree

well with the experimental data below 2 K. The small offset can be caused by a misalignment of the sample as explained in Ref. [171]. At higher temperatures, the calculations deviate significantly as expected. We can conclude that the analytical solution describes the temperature behavior of the magnetization quite nicely at low temperatures.

5.2.3 Magnetic phase diagram

We can now summarize all findings in a magnetic phase diagram. Figure 5.9 shows the experimental phase diagram of DTN for $H \| c$ derived from magnetization measurements. The left side of the phase diagram corresponds to the QPM region where $M(T) \propto T^{n>3/2}$ while the right side corresponds to the XY-AFM region (see right panel of Fig. 5.1). The central part is the typical QCP conical region where $M(T) \propto T^{3/2}$ indicating that quantum fluctuations linked to the QCP at $\mu_0 H_{c1} = 2.12\,\mathrm{T}$ are dominating. The phase boundary line between the QPM and the AFM regions agrees well with those determined in previous magnetization measurements [81, 172].

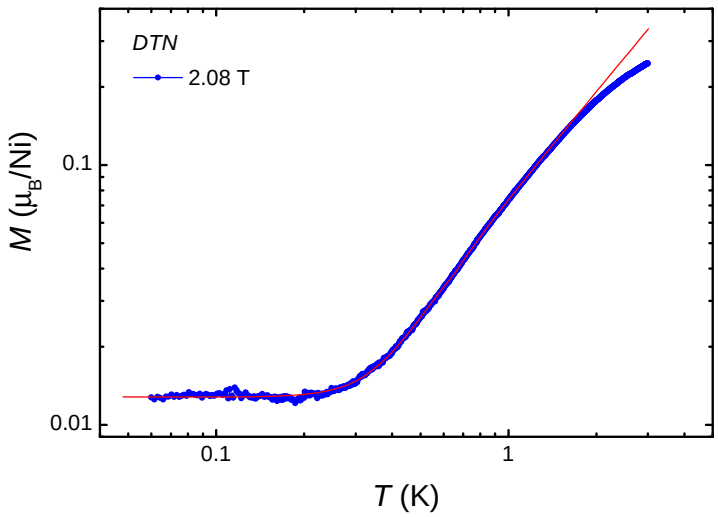

Figure 5.8 – T-dependence of the magnetization at a magnetic field $\mu_0 H = 2.08\,T$, slightly below H_{c1}. The solid lines are fit to the data performed using Eq. 2.35, considering both 3D and 1D integral, with $\mu_0 H \approx 2\,\mathrm{T}$, $\mu \approx 0$, $J_\parallel/k_\mathrm{B} = 2.2\,\mathrm{K}$, $J_\perp/k_\mathrm{B} = 0.18\,\mathrm{K}$, $D/k_\mathrm{B} = 8.9\,\mathrm{K}$, plus an additional offset $m_0 = 0.013\,\mu_\mathrm{B}$. No big difference can be observed. From the fit we obtain a gyromagnetic ratio $g = 2.8$ in 1D and $g = 2.65$ in 3D in very good agreement with the experiments [86].

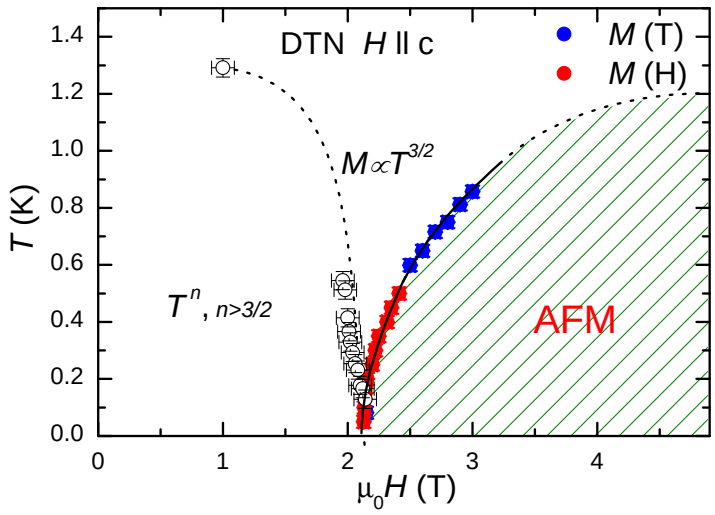

Figure 5.9 – Experimental magnetic phase diagram of DTN for $H \| c$ derived from magnetization measurements. The left side of the phase diagram corresponds to the QPM region while the right side to the XY-AFM region (see right panel of Fig. 5.1). The central part is the typical QCP conical region where $M(T) \propto T^{3/2}$ indicating that quantum fluctuations linked to the QCP at H_{c1} are dominating. The squares of the left side of the phase diagram were extracted from the point were the magnetization deviates from the $T^{3/2}$ behavior (see. Fig 5.7).

5.2.4 Specific heat

To investigate in more detail the properties of the QCP at H_{c1} it is important to measure the temperature dependence of the magnetic Grüneisen ratio, as explained in Sec. 2.3.4. However, a measurement of the specific heat is needed. A. Steppke has performed such a measurement down to 50 mK. The raw data are displayed in Fig. 5.10 (black points). The specific heat of DNT contains three contributions: nuclear Schottky, magnetic Schottky and a quantum critical contribution at low T. The phonon contribution is negligibly small in the temperature range below 1 K. The Schottky contributions can be subtracted from the total C/T since $C_S/T \propto T^{-3}$ is very large below 300 mK (cf. Fig. 5.10). The remaining magnetic specific heat C_{mag} should follow a $T^{3/2}$ power law at low temperature which results from quantum critical fluctuations at the QCP (cf. Tab. 2.3). This is not the case, at least for $T > 0.2$ K. There are possibly two reasons for this behavior: i) the $T^{3/2}$ law is due to quantum fluctuations of the QCP which are seen in the calculations at temperatures well below $J_c/k_B = 2.2$ K and in the experiments for $T < 0.3$ K [174], ii) $C(T)/T$ is influenced by two broad humps, the one at 2.5 K is due to the population of the $S^z = \pm 1$ excited states and the other at 0.5 K might be the dimensionality crossover from 3D to 1D since $J_c/k_B = 0.18$ K. However, analytical

and quantum Monte Carlo calculations seems to reproduce nicely the behavior of $C_{mag}(T)/T$ vs. T, suggesting that in the $T \to 0$ limit $C_{mag} \propto \sqrt{T}$ [171].

5.2.5 The magnetic Grüneisen ratio

As elucidated in Sec. 2.3.4, the magnetic Grüneisen parameter, Γ_H, can be derived by magnetization and specific heat measurements according to

$$\Gamma_H = -\frac{(\partial M/\partial T)}{C_H} \quad , \quad \Gamma_H(T, H = H_{c1}) \propto T^{-1/\nu z} \tag{5.3}$$

where the parameters ν (the correlation length exponent) and z (the dynamical critical exponent) are universal and depends only on the dimensionality of the critical fluctuations d and their nature ($z = 2$ for AFM and $z = 3$ for FM fluctuations) [15, 65]. In the case of a XY antiferromagnet or BEC we expect $\nu = 1/2$ and $z = 2$, which yields $\Gamma_H \propto 1/T$. Fig. 5.11 shows the magnetic Grüneisen ratio Γ_H estimated from the magnetization and specific heat data at 2.08 T presented in Fig. 5.7 and 5.10. $\Gamma_H \propto 1/T$ below 1.5 K as expected for a XY-AFM QCP. This is in good agreement with the behavior seen in Fig. 5.8. The fact that the specific heat does not strictly follow a $\sqrt{T}$ behavior seems to not affect the Grüneisen ratio possibly because $\partial M(T)/\partial T$ is more singular than $C(T)_H$.

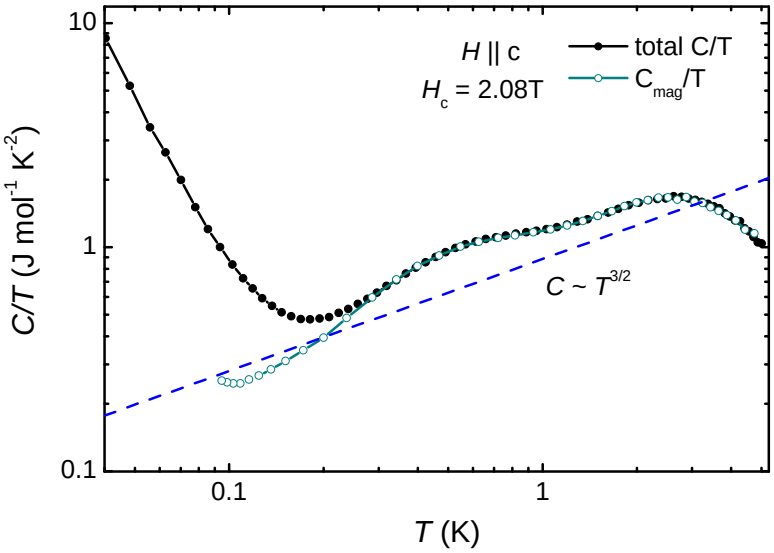

Figure 5.10 – Total C/T and magnetic C_{mag}/T (after the subtraction of the nuclear Schottky contribution) specific heat plotted as a function of temperature T at the critical field $H_{c1} = 2.08$ T for the specific heat set-up in a log-log representation [171, 157].

5.3 Conclusions

In this chapter a comprehensive experimental study of the magnetization and specific heat in the vicinity of the field-induced QCP ($H_{c1} \approx 2.12\,\mathrm{T}$) of $NiCl_2$-$4SC(NH_2)_2$ (DTN) was presented. We could identify the boundary line points of the phase transition between the quantum paramagnetic phase and the 3-dimensional XY-AFM phase, which can be described within the formalism of a Bose-Einstein condensation (BEC) of magnons. We found the phase line $T_c \propto (H - H_c)^{2/3}$ at low temperatures and a $T^{3/2}$ behavior in the magnetization at H_{c1}, which are all in agreement with the universality class of a BEC QCP. We have performed analytical calculations of the magnetization for low temperatures, which nicely reproduce the temperature dependence of the magnetization. Furthermore, the magnetic Grüneisen ratio was calculated from the experimental data and it diverges with a $1/T$ power law as expected for a BEC QCP. All in all, theory and experiments confirm the existence of a XY-AFM QCP at H_{c1} and this investigation is a remarkable example how theory can describe the experimental evidence in great detail.

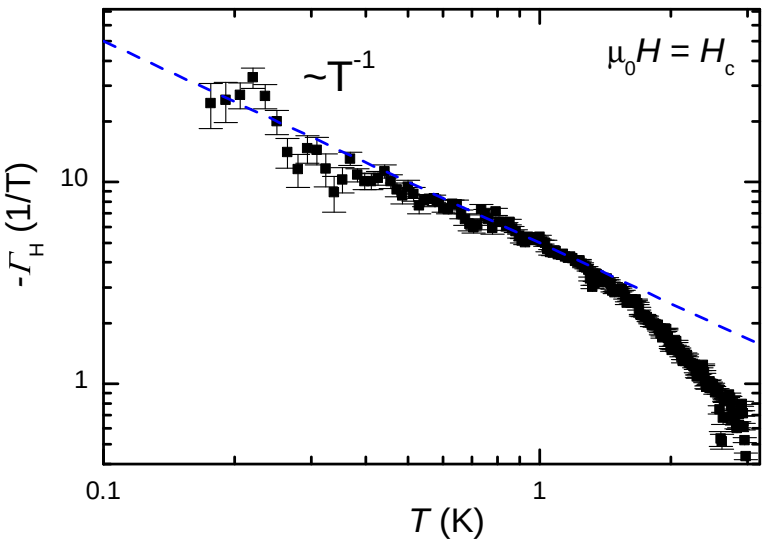

Figure 5.11 – Magnetic Grüneisen ratio Γ_H estimated from the magnetization and specific heat data at 2.08 T (see Fig. 5.7 and Fig. 5.10). $\Gamma_H \propto 1/T$ below 1.5 K as expected for a XY-AFM QCP. This is in agreement with the behavior seen in Fig. 5.8.

6 General conclusions

The central topic of this PhD thesis has been the study of magnetic quantum phase transitions (QPTs) in the heavy fermion (HF) system $Yb(Rh_{1-x}Co_x)_2Si_2$ and in the quantum magnet $NiCl_2$-$4SC(NH_2)_2$. The magnetic field H has been chosen as tuning parameter and the physical quantity, that was measured, is the magnetization M. To do this a high-resolution Faraday magnetometer was set up in a dilution refrigerator to be able to measure $M(T, H)$ up to 12 T and down to 0.05 K. The magnetic Grüneisen ratio Γ_H, i.e. the ratio between the field dependence of the entropy and the temperature dependence of the entropy, was used to identify the presence of field-induced quantum critical points (QCPs). This ratio can be expressed as a function of M and the specific heat at constant H, $\Gamma_H = -(\partial M/\partial T)_H/C_H$.

The evolution of magnetism from itinerant (with slightly Co-doped) to local (with $x = 1$) in $Yb(Rh_{1-x}Co_x)_2Si_2$ was investigated and an instructive magnetic moment μ vs. chemical pressure x phase diagram was drawn. At zero pressure and at $H > H_N$ the Kondo energy scale dominates over the RKKY one, almost screening the magnetic Yb^{3+} moments and leaving AFM order just below 0.07 K and a very small ordered moment. The system shows itinerant magnetism and HF character. At the critical field H_N of the AFM phase a QCP is found with pronounced NFL properties and an associated energy scale $T^*(H^*)$ where the Kondo effect breaks down and a Fermi surface reconstruction takes place. One of our first observations is that this energy scale seems not to be very affected by pressure as predicted by the theoretical "local QCP scenario". The QPT at H^* seems to be a continuous QPT inside the AFM phase, similar to a Lifshitz transition. Recent theoretical models, which include the effect of frustration, predict this behavior associating the QPT inside the AFM phase with a Kondo-destruction topological transition with a continuous change of the Fermi surface at $T = 0$ in agreement with our findings. With increasing pressure, i.e. decreasing the strength of the hybridization J, the magnetic moment $\mu(x)$ increases rapidly as a consequence of the rapid decrease of the Kondo temperature T_K. T_{RKKY} also decreases but in a smoother way. Therefore, at above $x = 0.27$ the RKKY interaction dominates substantially over the Kondo interaction and $\mu(x)$ vs. x still increases, but weakly. Between $x = 0.27$ and $x = 1$ the system still shows weak heavy-fermion character, while at $x = 1$ the pressure is enough to eventually localize the $4f$-electrons and we obtain $\mu = \mu_{sat}$. This demonstrates the fact that magnetism evolves continuously from itinerant to local in $Yb(Rh_{1-x}Co_x)_2Si_2$. On the other hand, the evolution

from itinerant to local magnetism induced by magnetic field takes place in two steps. First, the field induces Lifshitz transitions where the Fermi surface changes from large to small as a result of the shift of a van-Hove singularity across the Fermi level and then the fully localization of the f electrons takes place smoothly at even higher fields where the magnetic moment achieves its saturation value. Hence, both the coherence effects resulting from the lattice periodicity as well as the de-renormalization of the quasiparticles, which is reflects the break-up of the local Kondo singlets, have to be taken into account.

The physics of the antiferromagnet $YbCo_2Si_2$, i.e. at $x = 1$, could completely be understood within the framework of crystal field effects and a local $4f$-electron model. The magnetic phase diagram of single crystals of $YbCo_2Si_2$ was explored along the crystallographic directions [100], [110] and [001]. In a small field $\mu_0 H = 0.1$ T two AFM phase transitions were detected at $T_N = 1.75$ K and $T_L = 0.9$ K. The AFM order is completely suppressed by fields close to 2 T where the magnetization reaches its saturation values $M_s(H\|[100])$ and $M_s(H\|[110]) \approx 1.4\mu_B$ and $M_s(H\|[001]) \approx 0.68\mu_B$ which match quite well those calculated for the Γ_7 ground state, confirming the trivalent state of the Yb ions. Inside the AFM phase, two main regions can be identified along all crystallographic directions where the propagation vector $\mathbf{Q}$ assumes two different values. For H parallel to [100] and [110], however, these regions are separated by another line, which seems to correspond to the line where the magnetic moments reorient, and separates AFM domains. For H parallel to [001] only two AFM phases have been observed, implying that the moments might lay in directions close to the basal plane.

Another important achievement is the investigation of the field-induced QPT at the critical field H_N between the AFM phase and the PM one in $Yb(Rh_{0.93}Co_{0.07})_2Si_2$ and in pure $YbRh_2Si_2$ under a pressure of 1.5 GPa. The magnetic Grüneisen ratio $\Gamma_H(T, H)$ behaves in a very similar way in both compounds demonstrating that, for small x, chemical pressure is equivalent to hydrostatic pressure and the effect of disorder on our results can be definitively neglected. At H_N, $\Gamma_H(T) \propto -log(T)$ implying no QCP. The expected divergence for a 3D AFM QCP is $\Gamma \propto T^{-1}$. In addition, at fields well below H_N, $\Gamma_H(T) \propto T^{-1}$ inferring a 3D AFM QCP at this field which is in the range $0 \leq 0.06$ T. Unfortunately, a clear statement about the nature of the QCP inside the AFM phase cannot be given, since the extracted parameters are affected by the magnetic phase below T_N.

In the quantum magnet $NiCl_2$-$4SC(NH_2)_2$, the field-induced QCP at the critical field $H_c \approx 2.12$ T was investigated. We have identified the boundary line of the phase transition between the quantum paramagnetic phase and the 3-dimensional XY-AFM phase. The phase line $T_c \propto (H - H_c)^{3/2}$ at low temperatures and the $T^{3/2}$ behavior in the magnetization at H_{c1} were observed. Interestingly, the quan-

tum phase transition can be described within the formalism of a Bose-Einstein condensation (BEC) of magnons. We have performed analytical calculations of the magnetization for low temperatures, which nicely reproduce the temperature dependence of the magnetization for the universality class of a BEC QCP. Furthermore, the magnetic Grüneisen ratio was calculated from the experimental data and it diverges with a $1/T$ power law as expected for a BEC QCP. In this insulating material it seems that the theory of quantum phase transitions can reliably describe the experiments and the existence of a XY-AFM QCP at H_{c1} is confirmed.

In summary, the behavior of the magnetization across field-induced QPTs was examined in detail in two different systems: an insulating quantum magnet and a metallic heavy-fermion system. Although the state-of-the-art theory of quantum phase transitions can reasonably well describe QPTs in insulating materials, it can not describe the unusual behavior observed at QPTs in metals, e.g. the absence of a QCP at the field-induced QPT in $Yb(Rh_{0.93}Co_{0.07})_2Si_2$ as well as at the field-induced QPT in the pure $YbRh_2Si_2$ under pressure.

Appendix 1

The ground state in magnetic field of $YbCo_2Si_2$

Considering Yb^{+3} valence state for $YbCo_2Si_2$ experiencing a crystalline electric field (CEF) in a tetragonal symmetry, with a total angular momentum $J = 7/2$ (Landé factor $g_J = 8/7$), the wave-function of a CEF doublet can be either

$$|\psi_1 >= a|\pm 5/2 > +b|\mp 3/2 > \tag{1}$$

or

$$|\psi_2 >= a|\pm 7/2 > +b|\mp 1/2 > \tag{2}$$

with coefficient a and b between 0 and 1 which fulfill the $a^2 + b^2 = 1$ normalization. These can be represented in the basis of $|j_z >$ and their eigenfunctions can be written as:

$$|\Gamma_{7,1} > \;\; = \;\; 0.891|\pm 3/2 > -0.454|\mp 5/2 >$$

If an external magnetic field is applied the degeneracy is removed and the Zeeman Hamiltonian can be written as: $H = -\boldsymbol{\mu} \cdot \boldsymbol{B}$ with magnetic moment $\boldsymbol{\mu} = -g_J \mu_B \boldsymbol{J}$. Considering the operators of the total angular momentum :

$$\begin{aligned} j_z|j,m > &= m|j,m > \\ j_x|j,m > &= \frac{1}{2}(j_+ + j_-)|j,m > \\ j_\pm|j,m > &= [j(j+1) - m(m\pm)1)]^{1/2}\,|j,m \pm 1 > \end{aligned}$$

the effect of an external magnetic field $\boldsymbol{H}$ on these wave-functions can be calculated for the [100] and [001] directions.

Field parallel to the z axis: $\boldsymbol{H} \parallel z$

The Hamiltonian is $H_z = g_J \mu_B j_z B_z$ and the corresponding expectation value of the two energy levels are:

$$\begin{aligned} E(a) =< \Gamma_{7,1}(a)|H_z|\Gamma_{7,1}(a) > &= g_J\mu_B B < \Gamma_{7,1}(a)|j_z|\Gamma_{7,1}(a) >= 0.68 g_J \mu_B B_z \\ with < \Gamma_{7,1}(a)|j_z|\Gamma_{7,1}(a) > &= (0.891)^2(\frac{3}{2}) + (-0.454)^2(-\frac{5}{2}) = +0.68 \\ E(b) =< \Gamma_{7,1}(b)|H_z|\Gamma_{7,1}(b) > &= g_J\mu_B B < \Gamma_{7,1}(b)|j_z|\Gamma_{7,1}(b) >= -0.68 g_J \mu_B B_z \\ with < \Gamma_{7,1}(b)|j_z|\Gamma_{7,1}(b) > &= (0.891)^2(-\frac{3}{2}) + (-0.454)^2(\frac{5}{2}) = -0.68. \end{aligned}$$

The other matrix elements are zero:

$$< +3/2|j_z|5/2 >=< +3/2|j_z|-5/2 >=< +-3/2|j_z|5/2 >=< -3/2|j_z|-5/2 >= 0.$$

The ground state wave function is therefore $|\Gamma_{7,1}(b) >$ with eigenvalue $E(b)$ and the magnetic moment of the lower state (i.e. saturation magnetization) is:

$$\mu_z = - < j_z > g_J \mu_B = \frac{8}{7} \cdot 0.68 \mu_B = 0.77 \mu_B. \tag{3}$$

The ESR g-factor is

$$g_z(ESR) = \frac{E(a) - E(b)}{\mu_B B_z} = 2 g_J < j_z >= 2\mu_z = 1.54 \tag{4}$$

Field perpendicular to the z axis: $\boldsymbol{H} \perp z$

The Hamiltonian is $H_x = g_J \mu_B j_x B_z$ and the corresponding matrix elements which are not zero are:

$$\begin{aligned} j_+|+3/2> &= \alpha_1|+5/2> \\ j_+|-5/2> &= \alpha_2|-3/2> \\ j_-|+5/2> &= \alpha_3|+3/2> \\ j_-|-3/2> &= \alpha_4|-5/2> \end{aligned}$$

$$with \qquad \alpha_1 = \left[\frac{7}{2}\left(\frac{7}{2}+1\right) - \frac{3}{2}\left(\frac{3}{2}+1\right)\right]^{1/2} = \alpha_2 = \alpha_3 = \alpha_4 = 2\sqrt{3}.$$

The eigenfunction of the J_x operator are therefore linear combinations of $|\Gamma_{7,1}(a)>$ and $|\Gamma_{7,1}(b)>$:

$$\begin{aligned} |\Gamma_{7,1}(c)> &= \frac{1}{\sqrt{2}}\left(|\Gamma_{7,1}(a)> + |\Gamma_{7,1}(b)>\right) \\ |\Gamma_{7,1}(d)> &= \frac{1}{\sqrt{2}}\left(|\Gamma_{7,1}(a)> - |\Gamma_{7,1}(b)>\right). \end{aligned}$$

The eigenvalues are:

$$\begin{aligned} <\Gamma_{7,1}(c)|J_x|\Gamma_{7,1}(c)> &= \frac{1}{2}\frac{1}{\sqrt{2}}\frac{1}{\sqrt{2}}[(-)(0.891\cdot 0.454)\cdot 4\cdot 2\sqrt{3}] = -1.4 \\ <\Gamma_{7,1}(d)|J_x|\Gamma_{7,1}(d)> &= \frac{1}{2}\frac{1}{\sqrt{2}}\frac{1}{\sqrt{2}}[(+)(0.891\cdot 0.454)\cdot 4\cdot 2\sqrt{3}] = +1.4. \end{aligned}$$

The ground state wave function is therefore $|\Gamma_{7,1}(c)>$ with eigenvalue $E(c) = -1.4 g_J \mu_B B_x$. The magnetic moment (i.e. saturation magnetization) for this case is:

$$\mu_z = -<j_z> g_J \mu_B = \frac{8}{7}\cdot 1.4\mu_B = 1.6\mu_B. \tag{5}$$

The ESR g-factor is

$$g_z(ESR) = \frac{E(d)-E(c)}{\mu_B B_x} = 2g_J <j_x> = 2\mu_x = 3.2. \tag{6}$$

Appendix 2

Table of Conversions for magnetic properties

Table 1 – Units for magnetic properties

Quantity	Symbol	cgs unit Gaussian	Conversion factor	SI
flux density magnetic induction	$\boldsymbol{B}$	Gauss (G)	10^{-4}	Tesla (T), Wb/m^2
Magnetic flux	ϕ	maxwell G cm^2	10^{-8}	Wb, (V s)
Magnetic field strength	$\boldsymbol{H}$	Oerested (Oe)	$10^3/4\pi$	A/m
Magnetization	$\boldsymbol{M}$	emu/cm	10^3	A/m
Magnetic moment	$\boldsymbol{m}$	emu	10^{-3}	A/m^2, J/T
Molar susceptibility	χ	cm^3/mol, emu/mol	$4\pi\times10^{-6}$	m^3/mol
Permeability	μ_0	dimensionless	$4\pi\times10^{-7}$	H/m,Wb/A·m
Demagnetization factor	$\boldsymbol{D}$, $\boldsymbol{N}$	dimensionless	$1/4\pi$	dimensionless

Bibliography

[1] Hertz, J. A.: *Quantum critical phenomena.* Physical Review B, **14 (1976), 3**, pp. 1165. 1, 16, 18, 51

[2] Mathur, N. D.; Grosche, F. M.; Julian, S. R.; Walker, I. R.; Freye, D. M.; Haselwimmer, R. K. W.; and Lonzarich, G. G.: *Magnetically mediated superconductivity in heavy fermion compounds.* Nature, **394 (1998), 6688**, pp. 39. 1

[3] Yuan, H. Q.; Grosche, F. M.; Deppe, M.; Geibel, C.; Sparn, G.; and Steglich, F.: *Observation of Two Distinct Superconducting Phases in $CeCu_2Si_2$.* Science, **302 (2003), 5653**, pp. 2104. 1

[4] Bonn, D. A.: *Are high-temperature superconductors exotic?* Nature Phys., **2 (2006)**, pp. 159. 1

[5] Loehneysen, H. v.; Rosch, A.; Vojta, M.; and Woelfle, P.: *Fermi-liquid instabilities at magnetic quantum phase transitions.* Reviews of Modern Physics, **79 (2007), 3**, pp. 1015. 1, 16, 51, 90

[6] Trovarelli, O.; Geibel, C.; Mederle, S.; Langhammer, C.; Grosche, F. M.; Gegenwart, P.; Lang, M.; Sparn, G.; and Steglich, F.: *$YbRh_2Si_2$ Pronounced Non-Fermi-Liquid Effects above a Low-Lying Magnetic Phase Transition.* Physical Review Letters, **85 (2000), 3**, p. 626. 2, 51, 54, 88

[7] Custers, J.; Gegenwart, P.; Wilhelm, H.; Neumaier, K.; Tokiwa, Y.; Trovarelli, O.; Geibel, C.; Steglich, F.; Pépin, C.; and Coleman, P.: *The break-up of heavy electrons at a quantum critical point.* Nature, **424 (2003), 6948**, pp. 524. 2, 51, 55, 56, 57, 58, 83, 88

[8] Küchler, R.; Oeschler, N.; Gegenwart, P.; Cichorek, T.; Neumaier, K.; Tegus, O.; Geibel, C.; Mydosh, J. A.; Steglich, F.; Zhu, L.; and Si, Q.: *Divergence of the Grüneisen Ratio at Quantum Critical Points in Heavy Fermion Metals.* Physical Review Letters, **91 (2003), 6**, p. 066405. 2, 13, 16, 21, 58, 88

[9] Stockert, O.; Faulhaber, E.; Zwicknagl, G.; Stüßer, N.; Jeevan, H. S.; Deppe, M.; Borth, R.; Küchler, R.; Loewenhaupt, M.; Geibel, C.; and Steglich, F.: *Nature of the A Phase in $CeCu_2Si_2$.* Phys. Rev. Lett., **92 (2004)**, p. 136401. 2, 16

[10] Miyake, K. and Ikeda, H.: *True Meaning of "Localized" f-Electrons Measured by dHvA Experiments in Ce-Based Heavy Fermion Metals.* Journal of the Physical Society of Japan, **75 (2006), 3**, p. 033704. 2

[11] Schröder, A.; Aeppli, G.; Coldea, R.; Adams, M.; Stockert, O.; Lohneysen, H.; Bucher, E.; Ramazashvili, R.; and Coleman, P.: *Onset of antiferromagnetism in heavy-fermion metals.* Nature, **407 (2000), 6802**, pp. 351. 2, 17

[12] Shishido, H.; Settai, R.; Harima, H.; and Ōnuki, Y.: *A Drastic Change of the Fermi Surface at a Critical Pressure in $CeRhIn_5$: dHvA Study under Pressure.* Journal of the Physical Society of Japan, **74 (2005), 4**, pp. 1103. 2, 17

[13] Paschen, S.; Luhmann, T.; Wirth, S.; Gegenwart, P.; Trovarelli, O.; Geibel, C.; Steglich, F.; Coleman, P.; and Si, Q.: *Hall-effect evolution across a heavy-fermion quantum critical point.* Nature, **432 (2004), 7019**, pp. 881. 2, 17, 52, 56, 57, 68, 88

[14] Gegenwart, P.; Si, Q.; and Steglich, F.: *Quantum criticality in heavy-fermion metals.* Nat Phys, **4 (2008), 3**, pp. 186. 2, 16, 18, 51

[15] Zhu, L.; Garst, M.; Rosch, A.; and Si, Q.: *Universally Diverging Grüneisen Parameter and the Magnetocaloric Effect Close to Quantum Critical Points.* Physical Review Letters, **91 (2003), 6**, p. 066404. 2, 16, 17, 21, 22, 89, 90, 104, 105, 131

[16] Sakakibara, T.; Mitamura, H.; Amitsuka, T. T.; and Hiroshi: *Faraday Force Magnetometer for High-Sensitivity Magnetization Measurements at Very Low Temperatures and High Fields.* Japanese Journal of Applied Physics, **33 (1994)**, pp. 5067. 3, 35, 53

[17] Goltsev, A. V. and Abd-Elmeguid, M. M.: *Origin of the pressure dependence of the Kondo temperature in Ce- and Yb-based heavy-fermion compounds.* Journal of Physics: Condensed Matter, **17 (2005), 11**, pp. S813. 5

[18] Newman, D. J. and Ng, B.: *Crystal Field Handbook.* Cambridge University Press, illustrated edition ed. (**2000**). 6

[19] Du Trémolet de Lacheisserie, E.; Gignoux, D.; and Schlenker, M.: *Magnetism: I - Fundamentals.* Springer (**2002**). 6

[20] Hutchings, M.; Seitz, F.; and Turnbull, D.: *Point-Charge Calculations of Energy Levels of Magnetic Ions in Crystalline Electric Fields. Advances in*

Research and Applications, vol. Volume 16, Academic Press (**1964**), pp. 227–273. 6

[21] Bowden, G. J.; Bunbury, D. S. P.; and McCausland, M. A. H.: *Crystal fields and magnetic anisotropy in the molecular field approximation. I. General considerations*. Journal of Physics C: Solid State Physics, **4 (1971), 13**, p. 1840. 7

[22] Willers, T.: *Spectroscopic Investigations of the Crystal Field and Kondo Effect in 4f Heavy-Fermion Systems*. Ph.D. thesis, Universität zu Köln (**2011**). 7

[23] Hewson, A. C.: *The Kondo Problem to Heavy Fermions*. Cambridge University Press (**1997**). 8, 10

[24] Coleman, P.: *Heavy Fermions: electrons at the edge of magnetism*. cond-mat/0612006, **(2006)**, handbook of Magnetism and Advanced Magnetic Materials. Edited by Helmut Kronmuller and Stuart Parkin. Vol 1: Fundamentals and Theory. John Wiley and Sons, 95-148 (2007). 8, 13

[25] Andres, K.; Graebner, J. E.; and Ott, H. R.: *4f-Virtual-Bound-State Formation in $CeAl_3$ at Low Temperatures*. Physical Review Letters, **35 (1975), 26**, pp. 1779. 8

[26] Stewart, G. R.: *Heavy-fermion systems*. Reviews of Modern Physics, **56 (1984), 4**, p. 755. 8

[27] Landau, L. D.: *The theory of a Fermi liquid*. Sov. Phys. JETP, **3 (1957), 6**, pp. 920. 8

[28] Fulde, P.: *Electron Correlations in Molecules and Solids*. Bd. 100, Springer Series in Solid-State Science, Springer, Berlin (**1995**). 9

[29] Fisk, Z.; Hess, D. W.; Pethick, C. J.; Pines, D.; Smith, J. L.; Thompson, J. D.; and Willis, J. O.: *Heavy-Electron Metals: New Highly Correlated States of Matter*. Science, **239 (1988), 4835**, pp. 33 . 9

[30] Kadowaki, K. and Woods, S. B.: *Universal relationship of the resistivity and specific heat in heavy-Fermion compounds*. Solid State Communications, **58 (1986), 8**, pp. 507. 9

[31] de Haas, W.; de Boer, J.; and van dën Berg, G.: *The electrical resistance of gold, copper and lead at low temperatures*. Physica, **1 (1934), 7–12**, pp. 1115. 9

[32] Kondo, J.: *Resistence Minimum in Dilute Magnetic Alloys*. Prog. Theor. Phys., **32 (1964)**, p. 32. 10

[33] Hewson, A. C.: *Renormalized perturbation expansions and Fermi liquid theory*. Physical Review Letters, **70 (1993), 25**, pp. 4007. 10

[34] Wilson, K. G.: *The renormalization group: Critical phenomena and the Kondo problem*. Reviews of Modern Physics, **47 (1975), 4**, pp. 773. 10

[35] Andrei, N.: *Diagonalization of the Kondo Hamiltonian*. Phys. Rev. Lett., **45 (1980)**, pp. 379. 10

[36] Wiegmann, P. B.: *Exact solution of the s-d exchange model (Kondo problem)*. Journal of Physics C: Solid State Physics, **14 (1981), 10**, pp. 1463. 10

[37] Coqblin, B. and Schrieffer, J. R.: *Exchange Interaction in Alloys with Cerium Impurities*. Physical Review, **185 (1969), 2**, pp. 847. 10

[38] Hirst, L.: *Theory of the coupling between conduction electrons and moments of 3d and 4f ions in metals*. Advances in Physics, **27 (1978), 2**, pp. 231. 10

[39] Ruderman, M. A. and Kittel, C.: *Indirect Exchange Coupling of Nuclear Magnetic Moments by Conduction Electrons*. Physical Review, **96 (1954), 1**, p. 99. 11

[40] Opel, M.: *Grundlagen des Magnetism "Vorlesungsskript"*. TU München (**2005**). 12

[41] Doniach, S.: *The Kondo lattice and weak antiferromagnetism*. Physica B+C, **91 (1977)**, pp. 231. 12, 51

[42] Stewart, G. R.: *Non-Fermi-liquid behavior in d- and f-electron metals*. Reviews of Modern Physics, **73 (2001), 4**, p. 797. 13

[43] Landau, L. D.; Lifschitz, E. M.; Ziesche, P.; and Lenk, R.: *Lehrbuch der Theoretischen Physik*, vol. 5, Statistische Physik. Akademie-Verlag Berlin (**1987**). 14

[44] Vojta, M.: *Quantum phase transitions*. Reports on Progress in Physics, **66 (2003), 12**, pp. 2069. 15

[45] Aeppli, G. and Soh, Y.-A.: *Quantum Criticality in a Clean Metal*. Science, **294 (2001), 5541**, pp. 315 . 15

[46] Sachdev, S. and Keimer, B.: *Quantum criticality*. Physics Today, **64 (2011)**, p. 29. 15

[47] *Quantum phase transitions*. Nat. Phys., **4 (2008), 3**. 15

[48] Millis, A. J.: *Effect of a nonzero temperature on quantum critical points in itinerant fermion systems*. Phys. Rev. B, **48 (1993)**, pp. 7183. 16, 18, 51

[49] Moriya, T. and Takimoto, T.: *Anomalous Properties around Magnetic Instability in Heavy Electron Systems*. Journal of the Physical Society of Japan, **64 (1995)**, pp. 960. 16, 17, 18, 51, 55, 104

[50] Lonzarich, G. G.: *Electron*. Cambridge University Press, Cambridge, UK (**1997**). 16, 17

[51] Si, Q.; Rabello, M. S.; Ingersent, K.; and Smith, J. L.: *Locally critical quantum phase transitions in strongly correlated metals*. Nature, **413 (2001), 6858**, pp. 804. 17, 18, 52, 56, 57, 66, 88

[52] Coleman, P.; Pépin, C.; Si, Q.; and Ramazashvili, R.: *How do Fermi liquids get heavy and die?* Journal of Physics: Condensed Matter, **13 (2001), 35**, pp. R723. 17, 18, 52, 56, 57

[53] Senthil, T.; Sachdev, S.; and Vojta, M.: *Fractionalized Fermi Liquids*. Phys. Rev. Lett., **90 (2003), 21**, p. 216403. 17, 52

[54] Senthil, T.; Vojta, M.; and Sachdev, S.: *Weak magnetism and non-Fermi liquids near heavy-fermion critical points*. Phys. Rev. B, **69 (2004)**, p. 035111. 17

[55] Paul, I.; Pépin, C.; and Norman, M. R.: *Kondo Breakdown and Hybridization Fluctuations in the Kondo-Heisenberg Lattice*. Phys. Rev. Lett., **98 (2007)**, p. 026402. 17

[56] Pépin, C.: *Kondo Breakdown as a Selective Mott Transition in the Anderson Lattice*. Phys. Rev. Lett., **98 (2007)**, p. 206401. 17

[57] Gegenwart, P.; Westerkamp, T.; Krellner, C.; Tokiwa, Y.; Paschen, S.; Geibel, C.; Steglich, F.; Abrahams, E.; and Si, Q.: *Multiple Energy Scales at a Quantum Critical Point*. Science, **315 (2007), 5814**, pp. 969. 17, 19, 51, 52, 57, 58, 68, 117

[58] Si, Q.: *Global magnetic phase diagram and local quantum criticality in heavy fermion metals*. Physica B, **378-380 (2006)**, pp. 23. 18, 20, 52, 89

[59] Coleman, P. and Nevidomskyy, A. H.: *Frustration and the Kondo Effect in Heavy Fermion Materials*. Journal of Low Temperature Physics, **161 (2010), 1-2**, pp. 182. 18, 20, 21, 52, 89

[60] Si, Q.: *Quantum criticality and global phase diagram of magnetic heavy fermions*. physica status solidi (b), **247 (2010), 3**, pp. 476. 18, 20, 89

[61] Friedemann, S.; Oeschler, N.; Wirth, S.; Krellner, C.; Geibel, C.; Steglich, F.; Paschen, S.; Kirchner, S.; and Si, Q.: *Fermi-surface collapse and dynamical scaling near a quantum-critical point*. Proceedings of the National Academy of Sciences, **(2010)**. 19, 52, 56, 57, 70, 88

[62] Custers, J.; Gegenwart, P.; Geibel, C.; Steglich, F.; Coleman, P.; and Paschen, S.: *Evidence for a Non-Fermi-Liquid Phase in Ge-Substituted $YbRh_2Si_2$*. Physical Review Letters, **104 (2010), 18**, p. 186402. 19

[63] Gegenwart, P.; Custers, J.; Tokiwa, Y.; Geibel, C.; and Steglich, F.: *Ferromagnetic Quantum Critical Fluctuations in $YbRh_2(Si_{0.95}Ge_{0.05})_2$*. Physical Review Letters, **94 (2005), 7**, p. 076402. 19, 54, 65, 77, 94

[64] Küchler, R.; Gegenwart, P.; Heuser, K.; Scheidt, E.; Stewart, G. R.; and Steglich, F.: *Grüneisen Ratio Divergence at the Quantum Critical Point in $CeCu_{6-x}Ag_x$*. Physical Review Letters, **93 (2004), 9**, p. 096402. 21

[65] Garst, M. and Rosch, A.: *Sign change of the Grüneisen parameter and magnetocaloric effect near quantum critical points*. Physical Review B, **72 (2005), 20**. 21, 22, 89, 90, 131

[66] Belitz, D.; Kirkpatrick, T. R.; Mercaldo, M. T.; and Sessions, S. L.: *Local field theory for disordered itinerant quantum ferromagnets*. Physical Review B, **63 (2001), 17**, p. 174427. 22

[67] Bitko, D.; Rosenbaum, T. F.; and Aeppli, G.: *Quantum Critical Behavior for a Model Magnet*. Phys. Rev. Lett., **77 (1996)**, pp. 940. 22

[68] Nikuni, T.; Oshikawa, M.; Oosawa, A.; and Tanaka, H.: *Bose-Einstein Condensation of Dilute Magnons in $TlCuCl_3$*. Physical Review Letters, **84 (2000), 25**, p. 5868. 22, 23, 26, 123

[69] Haldane, F. D. M.: *Nonlinear Field Theory of Large-Spin Heisenberg Antiferromagnets: Semiclassically Quantized Solitons of the One-Dimensional Easy-Axis Néel State*. Phys. Rev. Lett., **50 (1983)**, pp. 1153. 22

[70] Giamarchi, T.: *Quantum Phase Transitions in quasi-one dimensional systems*. (CRC Press / Taylor&Francis, 2010, to appear) (**2010**). 23

[71] Matsubara, T. and Matsuda, H.: *A Lattice Model of Liquid Helium, I.* Progress of Theoretical Physics, **16 (1956), 6**, pp. 569. 23, 123

[72] Batyev, E. G. and Braginskii, L. S.: *Antiferrornagnet in a strong magnetic field: analogy with Bose gas.* Sov. Phys. JETP, **60, (1984)**, p. 781786. 23

[73] Affleck, I.: *Bose condensation in quasi-one-dimensional antiferromagnets in strong fields.* Physical Review B, **43 (1991), 4**, p. 3215. 23, 26

[74] Giamarchi, T. and Tsvelik, A. M.: *Coupled ladders in a magnetic field.* Physical Review B, **59 (1999), 17**, pp. 11398. 23, 123

[75] Ruegg, C.; Cavadini, N.; Furrer, A.; Gudel, H.-U.; Kramer, K.; Mutka, H.; Wildes, A.; Habicht, K.; and Vorderwisch, P.: *Bose-Einstein condensation of the triplet states in the magnetic insulator $TlCuCl_3$.* Nature, **423 (2003), 6935**, pp. 62. 23, 123

[76] Giamarchi, T.; Ruegg, C.; and Tchernyshyov, O.: *Bose-Einstein condensation in magnetic insulators.* Nat Phys, **4 (2008), 3**, pp. 198. 23, 123

[77] Jaime, M.; Correa, V. F.; Harrison, N.; Batista, C. D.; Kawashima, N.; Kazuma, Y.; Jorge, G. A.; Stern, R.; Heinmaa, I.; Zvyagin, S. A.; Sasago, Y.; and Uchinokura, K.: *Magnetic-Field-Induced Condensation of Triplons in Han Purple Pigment* $BaCuSi_2O_6$. Phys. Rev. Lett., **93 (2004)**, p. 087203. 23

[78] Oosawa, A.; Takamasu, T.; Tatani, K.; Abe, H.; Tsujii, N.; Suzuki, O.; Tanaka, H.; Kido, G.; and Kindo, K.: *Field-induced magnetic ordering in the quantum spin system $KCuCl_3$.* Physical Review B, **66 (2002), 10**, p. 104405. 23

[79] Hagiwara, M.; Honda, Z.; Katsumata, K.; Kolezhuk, A. K.; and Mikeska, H.-J.: *Zeeman Levels with Exotic Field Dependence in the High Field Phase of an $S = 1$ Heisenberg Antiferromagnetic Chain.* Phys. Rev. Lett., **91 (2003)**, p. 177601. 23

[80] Paduan-Filho, A.; Chirico, R. D.; Joung, K. O.; and Carlin, R. L.: *Field-induced magnetic ordering in uniaxial nickel systems: A second example.* The Journal of Chemical Physics, **74 (1981), 7**, pp. 4103. 23, 126

[81] Paduan-Filho, A.; Gratens, X.; and Oliveira, N. F.: *Field-induced magnetic ordering in $NiCl_2$-4SC$(NH_2)_2$.* Physical Review B, **69 (2004), 2**, p. 020405. 23, 125, 126, 130

[82] Zapf, V. S.; Zocco, D.; Hansen, B. R.; Jaime, M.; Harrison, N.; Batista, C. D.; Kenzelmann, M.; Niedermayer, C.; Lacerda, A.; and Paduan-Filho, A.: *Bose-Einstein Condensation of S=1 Nickel Spin Degrees of Freedom in*

$NiCl_2$-4SC$(NH_2)_2$. Physical Review Letters, **96 (2006), 7**, p. 077204. 23, 28, 29, 122, 126

[83] Schmidt, B.: *private communication* (**2012**). 24

[84] Kohama, Y.; Sologubenko, A. V.; Dilley, N. R.; Zapf, V. S.; Jaime, M.; Mydosh, J. A.; Paduan-Filho, A.; Al-Hassanieh, K. A.; Sengupta, P.; Gangadharaiah, S.; Chernyshev, A. L.; and Batista, C. D.: *Thermal Transport and Strong Mass Renormalization in $NiCl_2$-4SC$(NH_2)_2$*. Phys. Rev. Lett., **106 (2011)**, p. 037203. 25, 26

[85] Sørensen, E. and Affleck, I.: *Large-scale numerical evidence for Bose condensation in the S=1 antiferromagnetic chain in a strong field*. Physical Review Letters, **71 (1993), 10**, pp. 1633. 26

[86] Zvyagin, S. A.; Wosnitza, J.; Batista, C. D.; Tsukamoto, M.; Kawashima, N.; Krzystek, J.; Zapf, V. S.; Jaime, M.; Oliveira, N. F.; and Paduan-Filho, A.: *Magnetic Excitations in the Spin-1 Anisotropic Heisenberg Antiferromagnetic Chain System $NiCl_2$-4SC$(NH_2)_2$*. Physical Review Letters, **98 (2007), 4**, p. 047205. 28, 29, 121, 122, 126, 129

[87] Brown, W.: *Tutorial paper on dimensions and units*. Magnetics, IEEE Transactions on, **20 (1984), 1**, pp. 112. 31

[88] Bennett, L. H.: *Comments on Units in Magnetism*. Journal of Research of the National Bureau of Standards J. Res. Nat. Bur. Std., 83(1), p. 9, (1978)., **83 (1978), 1**, pp. 9. 31

[89] Foner, S.: *Measurement of Magnetic Properties and Quantities*. WILEY-VCH Verlag GmbH & Co KGaA (**2003**). 33

[90] Stewart, A. M.: *Prediction of lateral instabilities in the Faraday magnetometer*. Journal of Physics E: Scientific Instruments, **3 (1970), 3**, pp. 251. 34, 39

[91] Zijlstra, H.: *Experimental Methods in Magnetism: Generation & Computation of Magnetic Fields*. American Elsevier Pub. NY/North-Holland Pub. Co (**1967**). 34

[92] Richardson, J. T. and Beauxis, J. O.: *Automatic Magnetic Susceptibility Apparatus*. Review of Scientific Instruments, **34 (1963), 8**, pp. 877. 34

[93] Stewart, A. M.: *The superconducting Faraday magnetometer: error forces and lateral stability*. Journal of Physics E: Scientific Instruments, **8 (1975), 1**, p. 55. 35

[94] Lewis, R. T.: *A Faraday Type Magnetometer with an Adjustable Field Independent Gradient*. Review of Scientific Instruments, **42 (1971), 1**, pp. 31. 38

[95] Swanson, A. G.; Ma, Y. P.; Brooks, J. S.; Markiewicz, R. M.; and Miura, N.: *Diaphragm magnetometer for dc measurements in high magnetic fields*. Review of Scientific Instruments, **61 (1990), 2**, pp. 848. 38, 44

[96] Shull, R. D.; McMichael, R. D.; Swartzendruber, L. J.; and Leigh, S. D.: *Absolute magnetic moment measurements of nickel spheres*. Journal of Applied Physics, **87 (2000), 9**, p. 5992. 42

[97] Brooks, J. S.; Naughton, M. J.; Ma, Y. P.; Chaikin, P. M.; and Chamberlin, R. V.: *Small sample magnetometers for simultaneous magnetic and resistive measurements at low temperatures and high magnetic fields*. Review of Scientific Instruments, **58 (1987), 1**, p. 117. 44

[98] Wolf, W. P.: *Force on an Anisotropic Paramagnetic Crystal in an Inhomogeneous Magnetic Field*. Journal of Applied Physics, **28 (1957), 7**, p. 780. 44

[99] Clarke, J.: *SQUID*. Scientific American, **271 (1994), 2**, p. 46. 47

[100] Borth, R.: *private communication* (**2012**). 49, 96, 98, 99, 104

[101] Eiling, A. and Schilling, J. S.: *Pressure and temperature dependence of electrical resistivity of Pb and Sn from 1-300K and 0-10 GPa use as continuous resistive pressure monitor accurate over wide temperature range; superconductivity under pressure in Pb, Sn and In*. Journal of Physics F: Metal Physics, **11 (1981), 3**, pp. 623. 50

[102] Gegenwart, P.; Custers, J.; Geibel, C.; Neumaier, K.; Tayama, T.; Tenya, K.; Trovarelli, O.; and Steglich, F.: *Magnetic-Field Induced Quantum Critical Point in $YbRh_2Si_2$*. Physical Review Letters, **89 (2002), 5**, p. 056402. 51, 83

[103] Mederle, S.; Borth, R.; Geibel, C.; Grosche, F. M.; Sparn, G.; Trovarelli, O.; and Steglich, F.: *An unconventional metallic state in $YbRh_2(Si_{1-x}Ge_x)_2$ a high pressure study*. Journal of Physics: Condensed Matter, **14 (2002), 44**, pp. 10731. 52, 62, 63, 64

[104] Macovei, M. E.; Nicklas, M.; Krellner, C.; Geibel, C.; and Steglich, F.: *Effect of pressure and Ir substitution in $YbRh_2Si_2$*. J. Phys.: Condens. Matter, **20 (2008), 50**, p. 505205. 52

[105] Schuberth, E.; Tippmann, M.; Kath, M.; Krellner, C.; Geibel, C.; Westerkamp, T.; Klingner, C.; and Steglich, F.: *Magnetization measurements on $YbRh_2Si_2$ at very low temperatures*. Journal of Physics: Conference Series, **150 (2009), 4**, p. 042178. 52, 107

[106] Tokiwa, Y.; Gegenwart, P.; Radu, T.; Ferstl, J.; Sparn, G.; Geibel, C.; and Steglich, F.: *Field-Induced Suppression of the Heavy-Fermion State in$YbRh_2Si_2$*. Physical Review Letters, **94 (2005), 22**, pp. 226402. 52, 57, 84, 85, 96, 98, 99, 100

[107] Gegenwart, P.; Tokiwa, Y.; Westerkamp, T.; Weickert, F.; Custers, J.; Ferstl, J.; Krellner, C.; Geibel, C.; Kerschl, P.; Muller, K.; and Steglich, F.: *High-field phase diagram of the heavy-fermion metal $YbRh_2Si_2$*. New Journal of Physics, **8 (2006), 9**, p. 171. 52, 55, 56, 57, 83, 84, 88, 96, 98

[108] Pedrero, L.; Brando, M.; Klingner, C.; Krellner, C.; Geibel, C.; and Steglich, F.: *H - T phase diagram of $YbCo_2Si_2$ with H // [100]*. Journal of Physics: Conference Series, **200 (2010), 1**, p. 012157. 52, 61, 81, 108

[109] Pedrero, L.; Klingner, C.; Krellner, C.; Brando, M.; Geibel, C.; and Steglich, F.: *Magnetic phase diagram of $YbCo_2Si_2$ derived from magnetization measurements*. Physical Review B, **84 (2011), 22**, p. 224401. 52, 81

[110] Klingner, C.: *Entwicklung des antiferromagnetischen Zustandes im System $Yb(Rh_{1-x}Co_x)_2Si_2$*. Master's thesis, TU Dresden (**2009**). 52, 53, 59, 61, 62, 65, 74, 79, 114

[111] Klingner, C.; Krellner, C.; Brando, M.; Geibel, C.; and Steglich, F.: *Magnetic behaviour of the intermetallic compound $YbCo_2Si_2$*. New Journal of Physics, **13 (2011), 8**, p. 083024. 52, 53, 59, 60, 61, 79, 83, 114

[112] Klingner, C.; Krellner, C.; Brando, M.; Geibel, C.; Steglich, F.; Vyalikh, D. V.; Kummer, K.; Danzenbächer, S.; Molodtsov, S. L.; Laubschat, C.; Kinoshita, T.; Kato, Y.; and Muro, T.: *Evolution of magnetism in $Yb(Rh_{1-x}Co_x)_2Si_2$*. Physical Review B, **83 (2011), 14**, p. 144405. 52, 53, 59, 61, 62, 63, 64, 65, 74, 75, 76, 77, 78, 79, 80, 82, 102, 107, 108, 110, 113, 116

[113] Rourke, P. M. C.; McCollam, A.; Lapertot, G.; Knebel, G.; Flouquet, J.; and Julian, S. R.: *Magnetic-Field Dependence of the $YbRh_2Si_2$ Fermi Surface*. Physical Review Letters, **101 (2008), 23**, p. 237205. 52, 57, 84, 87

[114] Zwicknagl, G.: *Field-induced suppression of the heavy-fermion state in $YbRh_2Si_2$*. Journal of Physics: Condensed Matter, **23 (2011), 9**, p. 094215. 52, 57, 84, 87

[115] Pfau, H.: *High field thermal and electrical transport studies in $YbRh_2Si_2$*. to be publish, **(2012)**. 52, 57, 84, 87

[116] Pépin, C.: *Fractionalization and Fermi-Surface Volume in Heavy-Fermion Compounds: The Case of $YbRh_2Si_2$*. Phys. Rev. Lett., **94 (2005), 6**, pp. 066402. 52, 56, 57

[117] Friedemann, S.; Westerkamp, T.; Brando, M.; Oeschler, N.; Wirth, S.; Gegenwart, P.; Krellner, C.; Geibel, C.; and Steglich, F.: *Detaching the antiferromagnetic quantum critical point from the Fermi-surface reconstruction in $YbRh_2Si_2$*. Nat Phys, **5 (2009), 7**, pp. 465. 52, 62, 65, 67, 71, 89, 96, 117

[118] Tokiwa, Y.; Radu, T.; Geibel, C.; Steglich, F.; and Gegenwart, P.: *Divergence of the Magnetic Grüneisen Ratio at the Field-Induced Quantum Critical Point in $YbRh_2Si_2$*. Physical Review Letters, **102 (2009), 6**, p. 066401. 52, 58, 90, 100

[119] Hackl, A. and Vojta, M.: *Zeeman-Driven Lifshitz Transition: A Model for the Experimentally Observed Fermi-Surface Reconstruction in $YbRh_2Si_2$*. Physical Review Letters, **106 (2011), 13**, p. 137002. 52

[120] Friedemann, S.; Paschen, S.; Geibel, C.; Wirth, S.; Steglich, F.; Kirchner, S.; Elihu, A.; and Qimiao, S.: *Comment on "Zeeman-Driven Lifshitz Transition: A Model for the Experimentally Observed Fermi-Surface Reconstruction in $YbRh_2Si_2$"*. arXiv:1207.0536, **(2012)**. 52

[121] Hackl, A. and Vojta, M.: *Reply to Comment by S. Friedemann et al. on "Zeeman-Driven Lifshitz Transition: A Model for the Experimentally Observed Fermi-Surface Reconstruction in $YbRh_2Si_2$"*. arXiv:1207.1123, **(2012)**. 52

[122] Sichelschmidt, J.; Ivanshin, V. A.; Ferstl, J.; Geibel, C.; and Steglich, F.: *Low Temperature Electron Spin Resonance of the Kondo Ion in a Heavy Fermion Metal: $YbRh_2Si_2$*. Physical Review Letters, **91 (2003), 15**, p. 156401. 52, 56, 57, 86

[123] Stock, C.; Broholm, C.; Demmel, F.; Van Duijn, J.; Taylor, J. W.; Kang, H. J.; Hu, R.; and Petrovic, C.: *From Incommensurate Correlations to*

Mesoscopic Spin Resonance in $YbRh_2Si_2$. Phys. Rev. Lett., **109 (2012)**, p. 127201. 52, 54, 56, 57, 62

[124] Ishida, K.; MacLaughlin, D. E.; Young, B.; Okamoto, K.; Kawasaki, Y.; Kitaoka, Y.; Nieuwenhuys, G. J.; Heffner, R. H.; Bernal, O. O.; Higemoto, W.; Koda, A.; Kadono, R.; Trovarelli, O.; Geibel, C.; and Steglich, F.: *Low-temperature magnetic order and spin dynamics in* $YbRh_2Si_2$. Physical Review B, **68 (2003), 18**, p. 184401. 53, 54

[125] Westerkamp, T.; Gegenwart, P.; Krellner, C.; Geibel, C.; and Steglich, F.: *Low-temperature magnetic susceptibility of* $Yb(Rh_{1-x}M_x)_2Si_2$ *(M=Ir,Co) single crystals*. Physica B: Condensed Matter, **403 (2008), 5-9**, pp. 1236. 53, 62, 67, 71, 72, 117

[126] Hodges, J. A.: *Magnetic Ordering of Ytterbium in* $YbCo_2Si_2$ *and* $YbFe_2Si_2$. EPL (Europhysics Letters), **4 (1987), 6**, pp. 749. 53, 58, 82, 110, 116

[127] Stockert, O.; Koza, M.; Ferstl, J.; Murani, A.; Geibel, C.; and Steglich, F.: *Crystalline electric field excitations of the non-Fermi-liquid* $YbRh_2Si_2$. Physica B, **378-380 (2006)**, pp. 157. 54, 55, 56, 61

[128] Ernst, S.; Kirchner, S.; Krellner, C.; Geibel, C.; Zwicknagl, G.; Steglich, F.; and Wirth, S.: *Emerging local Kondo screening and spatial coherence in the heavy-fermion metal* $YbRh_2Si_2$. Nature, **474 (2011), 7351**, pp. 362. 54

[129] Trovarelli, O.; Geibel, C.; and Steglich, F.: *Low-temperature properties of* $YbRh_2Si_2$. Physica B: Condensed Matter, **284–288, Part 2 (2000), 0**, pp. 1507. 54

[130] Custers, J.; Gegenwart, P.; Geibel, C.; Steglich, F.; Tayama, T.; Trovarelli, O.; and Harrison, N.: *Low-temperature magnetic and transport properties of the clean NFL system* $YbRh_2(Si_{1-x}Ge_x)_2$. Acta Phys. Pol., **B 32 (2001)**, p. 3211. 54

[131] Köhler, U.; Oeschler, N.; Steglich, F.; Maquilon, S.; and Fisk, Z.: *Energy scales of* $Lu_xYb_{1-x}Rh_2Si_2$ *by means of thermopower investigations*. Phys. Rev. B, **77 (2008)**, p. 104412. 54

[132] Westerkamp, T.: *Quantenphasenübergänge in den Schwere-Fermionen-Systemen* $Yb(Rh_{1-x}M_x)_2Si_2$ *und* $CePd_{1-x}Rh_x$. Ph.D. thesis, Technische Universität Dresden (**2009**). 55, 62, 63, 64, 72, 73, 90

[133] Krellner, C.; Hartmann, S.; Pikul, A.; Oeschler, N.; Donath, J. G.; Geibel, C.; Steglich, F.; and Wosnitza, J.: *Violation of Critical Universality at the*

Antiferromagnetic Phase Transition of $YbRh_2Si_2$. Physical Review Letters, **102 (2009), 19**, p. 196402. 56

[134] Senthil, T.; Vishwanath, A.; Balents, L.; Sachdev, S.; and Fisher, M.: *Deconfined Quantum Critical Points*. Science, **303 (2004), 5663**, pp. 1490. 56, 57

[135] Wykhoff, J.; Sichelschmidt, J.; Lapertot, G.; Knebel, G.; Flouquet, J.; Fazlishanov, I. I.; von Nidda, H. K.; Krellner, C.; Geibel, C.; and Steglich, F.: *On the local and itinerant properties of the ESR in $YbRh_2Si_2$*. Science and Technology of Advanced Materials, **8 (2007), 5**, pp. 389. 56

[136] Rossi, D.; Marazza, R.; and Ferro, R.: *Ternary RMe_2X_2 alloys of the rare earths with the precious metals and silicon (or germanium)*. Journal of the Less Common Metals, **66 (1979), 2**, p. p. 17. 58

[137] Kolenda, M. and Szytula, A.: *The valence state of Yb in $YbCo_2Si_2$ and $YbCo_2Ge_2$ compounds on the basis of magnetic susceptibility measurements*. Journal of Magnetism and Magnetic Materials, **79 (1989), 1**, pp. 57. 58

[138] Goremychkin, E. A. and Osborn, R.: *Crystal field excitations in $Yb(T)_2Si_2$ (T = Fe, Co, Ni)*. J. Appl. Phys, **87 (2000)**, p. 6818. 58, 60

[139] Gruner, T.; Sichelschmidt, J.; Klingner, C.; Krellner, C.; Geibel, C.; and Steglich, F.: *Electron spin resonance of the Yb 4f moment in $Yb(Rh_{1-x}Co_x)_2Si_2$*. Physical Review B, **85 (2012), 3**, p. 035119. 59, 86

[140] Vyalikh, D. V.; Danzenbächer, S.; Kucherenko, Y.; Kummer, K.; Krellner, C.; Geibel, C.; Holder, M. G.; Kim, T. K.; Laubschat, C.; Shi, M.; Patthey, L.; Follath, R.; and Molodtsov, S. L.: *k Dependence of the Crystal-Field Splittings of $4f$ States in Rare-Earth Systems*. Phys. Rev. Lett., **105 (2010), 23**, p. 237601. 61

[141] Mufti, N.; Klingner, C.; Pedrero, L.; Brando, M.; Kaneko, K.; Krellner, C.; Stockert, O.; and Geibel, C.: *Pronounced basal plane anisotropy in the magnetoresistance of $YbCo_2Si_2$*. physica status solidi (b), **247 (2010), 3**, pp. 743. 61, 107, 108, 114

[142] Kaneko, K.; Stockert, O.; Mufti, N.; Kiefer, K.; Klingner, C.; Krellner, C.; Geibel, C.; and Steglich, F.: *Magnetic transitions in $YbCo_2Si_2$*. Journal of Physics: Conference Series, **200 (2010), 3**, p. 032031. 62, 107, 114

[143] Mufti, N.: Unpublished. 62, 107, 110, 114, 116

[144] Mederle, S.; Borth, R.; Geibel, C.; Grosche, F.; Sparn, G.; Trovarelli, O.; and Steglich, F.: *Unconventional metallic state in $YbRh_2Si_2$ – a high-pressure study*. Journal of Magnetism and Magnetic Materials, **226-230 (2001), Part 1**, pp. 254. 62, 63, 64, 104

[145] Knebel, G.; Boursier, R.; Hassinger, E.; Lapertot, G.; Niklowitz, P. G.; Pourret, A.; Salce, B.; Sanchez, J. P.; Sheikin, I.; Bonville, P.; Harima, H.; and Flouquet, J.: *Localization of $4f$ State in $YbRh_2Si_2$ under Magnetic Field and High Pressure: Comparison with $CeRh_2Si_2$*. Journal of the Physical Society of Japan, **75 (2006)**, p. 114709. 62, 63, 64, 65, 75, 77

[146] Krellner, C.: *Ferromagnetische Korrelationen in Kondo-Gittern: YbT_2Si_2 und CeTPO (T=Übergangsmetall)*. Ph.D. thesis, TU Dresden (**2009**). 62, 63

[147] Plessel, J.; Abd-Elmeguid, M. M.; Sanchez, J. P.; Knebel, G.; Geibel, C.; Trovarelli, O.; and Steglich, F.: *Unusual behavior of the low-moment magnetic ground state of $YbRh_2Si_2$ under high pressure*. Physical Review B, **67 (2003), 18**, p. 180403. 62, 63, 64, 75, 79

[148] Hannaske, A.: *private communication* (**2012**). 63, 82

[149] Thompson, J.; Lawrence, J.; and Karl A. Gschneidner, J.: *Chapter 133 High pressure studies - physical properties of anomalous Ce, Yb and U compounds. Lanthanides/Actinides: Physics - II*, vol. Volume 19, Elsevier (**1994**), pp. 383–478. 64

[150] Alami-Yadri, K.; Jaccard, D.; and Andreica, D.: *Thermopower of Yb Heavy Fermion Compounds at High Pressure*. Journal of Low Temperature Physics, **114 (1999)**, pp. 135. 64

[151] Andreica, D.; Amato, A.; Gygax, F.; Pinkpank, M.; and Schenck, A.: *Chemical pressure effects in the $Yb(Cu_{1-x}Ni_x)_2Si_2$ system*. Physica B: Condensed Matter, **289-290 (2000)**, pp. 24. 64

[152] Steglich, F.; Arndt, J.; Friedemann, S.; Krellner, C.; Tokiwa, Y.; Westerkamp, T.; Brando, M.; Gegenwart, P.; Geibel, C.; Wirth, S.; and Stockert, O.: *Superconductivity versus quantum criticality: what can we learn from heavy fermions?* Journal of Physics: Condensed Matter, **22 (2010), 16**, p. 164202. 66, 89

[153] Ishida, K.; Okamoto, K.; Kawasaki, Y.; Kitaoka, Y.; Trovarelli, O.; Geibel, C.; and Steglich, F.: *$YbRh_2Si_2$: Spin Fluctuations in the Vicinity of a*

Quantum Critical Point at Low Magnetic Field. Physical Review Letters, **89 (2002), 10**, p. 107202. 65, 77, 95, 102

[154] Friedemann, S.: *Elektrischer Transport und Quantenkritikalität in reinem und substituiertem $YbRh_2Si_2$*. Ph.D. thesis, Technische Universität Dresden (**2009**). 65, 89, 93

[155] Lausberg, S.: *Unpublished*. Ph.D. thesis, TU Dresden, Max Planck Institute for Chemical Physics of Solids (**2012**). 74

[156] Lausberg, S.: *Magnetic and transport properties of $Yb(Rh_{0.73}Co_{0.27})_2Si_2$*. Unpublished. 76

[157] Steppke, A.: *Unpublished*. Ph.D. thesis, TU Dresden, Max Planck Institute for Chemical Physics of Solids (**2012**). 76, 90, 91, 92, 93, 104, 123, 131

[158] Hannaske, A.: *private communication* (**2012**). 78, 83

[159] Tokiwa, Y.; Gegenwart, P.; Geibel, C.; and Steglich, F.: *Separation of Energy Scales in Undoped $YbRh_2Si_2$ Under Hydrostatic Pressure*. Journal of the Physical Society of Japan, **78 (2009)**, p. 123708. 79, 96, 99, 106

[160] Lifshitz, I.: *Anomalies of electron characteristics of a metal in the high pressure region*. Soviet Physics JETP-USSR, **11 (1960), 5**, pp. 1130. 84

[161] Kusminskiy, S. V.; Beach, K. S. D.; Neto, A. H. C.; and Campbell, D. K.: *Mean-field study of the heavy-fermion metamagnetic transition*. Physical Review B, **77 (2008), 9**, p. 094419. 84

[162] Costi, T. A.: *Kondo Effect in a Magnetic Field and the Magnetoresistivity of Kondo Alloys*. Physical Review Letters, **85 (2000), 7**, pp. 1504. 85

[163] Sichelschmidt, J.; Wykhoff, J.; Gruner, T.; Krellner, C.; Klingner, C.; Geibel, C.; Steglich, F.; Krug von Nidda, H.; Zakharov, D. V.; Loidl, A.; and Fazlizhanov, I.: *Effect of pressure on the electron spin resonance of a heavy-fermion metal*. Physical Review B, **81 (2010), 20**, p. 205116. 86

[164] Mydosh, J. A.: *Spin Glasses: An Experimental Introduction*. CRC Press, 1 ed. (**1993**). 90

[165] Senthil, T.: *Critical Fermi surfaces and non-Fermi liquid metals*. Phys. Rev. B, **78 (2008), 3**, p. 035103. 90, 105

[166] Rosch, A.; Schröder, A.; Stockert, O.; and Löhneysen, H. v.: *Mechanism for the Non-Fermi-Liquid Behavior in $CeCu_{6-x}Ag_x$*. Phys. Rev. Lett., **79 (1997)**, pp. 159. 94

[167] Hake, R. and Mapother, D.: *Effect of pressure on the superconducting transition of lead*. Journal of Physics and Chemistry of Solids, **1 (1956), 3**, pp. 199. 97, 101

[168] Jensen, J. and Rotter, M.: *Magnetic double-q ordering of tetragonal $GdNi_2B_2C$: A way to explain the magnetoelastic paradox*. Phys. Rev. B, **77 (2008), 13**, p. 134408. 116

[169] Tsyrulin, N.: *Neutron Scattering Studies of Low Dimensional Quantum Spin Systems*. Ph.D. thesis, ETH Zurich (**2010**). 122, 123

[170] Wilhelm, H.; Lühmann, T.; Rus, T.; and Steglich, F.: *A compensated heat-pulse calorimeter for low temperatures*. Review of Scientific Instruments, **75 (2004)**, p. 2700. 123

[171] Weickert, F.; Küchler, R.; Steppke, A.; Pedrero, L.; Nicklas, M.; Brando, M.; Steglich, F.; Jaime, M.; Zapf, V. S.; Paduan-Filho, A.; Al-Hassanieh, K. A.; Batista, C. D.; and Sengupta, P.: *Low-temperature thermodynamic properties near the field-induced quantum critical point in $NiCl_2$-4SC$(NH_2)_2$*. Phys. Rev. B, **85 (2012)**, p. 184408. 124, 129, 131

[172] Paduan-Filho, A.; Al-Hassanieh, K. A.; Sengupta, P.; and Jaime, M.: *Critical Properties at the Field-Induced Bose-Einstein Condensation in $NiCl_2$-4SC$(NH_2)_2$*. Physical Review Letters, **102 (2009), 7**, p. 077204. 125, 130

[173] Sebastian, S. E.; Harrison, N.; Batista, C.; Balicas, L.; Jaime, M.; Sharma, P.; Kawashima, N.; and Fisher, I.: *BEC phase boundary in $BaCuSi_2O_6$*. Journal of Magnetism and Magnetic Materials, **310 (2007), 2, Part 2**, pp. e460. 125

[174] Yin, L.; Xia, J. S.; Zapf, V. S.; Sullivan, N. S.; and Paduan-Filho, A.: *Direct Measurement of the Bose-Einstein Condensation Universality Class in $NiCl_2$-4SC$(NH_2)_2$ at Ultralow Temperatures*. Physical Review Letters, **101 (2008), 18**, p. 187205. 127, 131

Acknowledgments

I do thank all the people who were involved directly or indirectly in the development of my PhD. First and foremost, I offer my sincerest gratitude to my *Doktorvater*, Prof. Frank Steglich who gave me the possibility to pursue my research interests in his group over the past five years.
My biggest thanks go to Dr. Manuel Brando, who guided and constantly supervised me through the years. I never hesitated to go directly to his office if questions and ideas came to my mind. I thank him for this very productive work on quantum phase transitions. All my gratitude goes to Dr. Christoph Geibel and Dr. Michael Nicklas who supported me throughout my thesis. I feel obliged to specially thank Dr. Geibel, since it was him who welcomed me to our institute.

I want to thank Dr. Cornelius Krellner and Dipl. Phys. Christoph Klingner for providing $Yb(Rh_{1-x}Co_x)_2Si_2$ single crystals of excellent quality and more importantly for valuable discussions on heavy-fermion physics. I am indebted to Dr. Steffen Wirth for his introductory lessons on low temperature physics and Dr. Burkhard Schmidt for our conversations about low dimensional spin systems and the calculation of the magnetization in DTN. I would like also to acknowledge Dr. Jörg Sichelschmidt for having kindly read and criticized the manuscript.

In the Extreme Conditions group at MPI CPfS Dresden, the scientific discussions with Dr. Robert Küchler, Alexander Steppke, Stefan Lausberg, Heike Pfau, Hugo Vieyra, Dr. Edit Lengyel, Dr. Ramzy Daou, Dr. Thomas Lühmann, Robert Borth, Dr. Jan-Guido Donath, Dr. Tanja Westerkamp, Dr. Lucia Steinke have always been enlightening, helpful and often entertaining.

No scientific challenge can live without discussions and collaborations with scientists from other research institutes. In this context, I deeply acknowledge the inspiring conversations with Prof. Phillip Gegenwart, as well as for Dr. Yoshi Tokiwa. The discussions with Prof. Mathias Vojta, Prof. Julian G. Sereni, as well as Dr. Markus Garst, are also acknowledged. From the Max Planck Institute for Physics of Complex Systems I want to thank Dr. Stefan Kirchner for stimulating discussions. My thanks also go to collaborators at the Los Alamos National Laboratory, Dr. Marcelo Jaime and Dr. Franziska Weickert. It was a pleasure to have worked with such a competent group of neutrons scattering specialists. Thanks to Dr. Oliver Stockert, who was always willing to listen to any problem of physical or technical nature. Dr. Nandgand Mufti and Ariane Haanaske who shared their neutron results in $YbCo_2Si_2$ and $Yb(Rh_{1-x}Co_x)_2Si_2$. Also thanks to Prof. Liu Hao Tjeng who extended my contract to finish this thesis. I would also like to acknowledge Dr. Martin Rotter for reviewing the CEF part in $YbCo_2Si_2$ and carefully read the manuscript. Also for the nice time when we made music together. The same is true for Bürgehan Terlan, for the piano accompaniment in the last three performances. I would like to thank Dr. Maurits Haverkort, who

kindly gave me his *Crystal Field Theory* Mathematica package, that I used to calculate the CEF and magnetization in $YbCo_2Si_2$. It was a very powerful tool to understand crystal fields and magnetism of rare earths. And also to Dr. Thomas Willers for many stimulating discussions, for the input in the $YbCo_2Si_2$ chapter, and for his true friendship.

I have to thank all my good colleagues and friends at the Max Planck Institute for Chemical Physics of Solids who provided a pleasant working atmosphere: Dr. Julia Arndt, Dr. Eva Brüning, Dr. Stefan Ernst, Dr. Tobias Förster, Dr. Hirale Jeevan, Dr. Sven Friedemann, Dr. Anton Jesche, Dr. Stefanie Hartmann, Dr. Ulrike Stockert, Dr. Monica Macovei, Heike Rave, Dr. Sahana Rößler, Dr. Rajib Sakar, Ralf Weise, Dr. Jan Wykhoff, Dr. Micha Deppe, Christoph Bergmann, Dr. Silvia Seiro, Thomas Gruner, Sandra Hamann, Zita Hüsges, Sarah Woitschach, Dr. Ulrich Burkhardt, Dr. Michael Baenitz, Renate Hempel-Weber, Dr. Wilder Carrillo-Cabrera, Dr. Raul Cardoso und Nubia Caroca-Canales.

I greatly appreciate the help provided by the technical staff of the CPfS Dresden during my PhD experiments, specially by Ulrike Ließ, Cristoph Klausnitzer, who helped me in the fabrication and design of the new magnetization cell. Special thanks also go to the people of the electronics workshop, as well as to the head of the Mechanical Workshop, Andreas Schwoboda and his entire team, who provided some parts of the cell and gave me new ideas for its fabrication. I want to thank the *IT* specialists, Thomas Engel and his team for their immediate help in all computer-related concerns, and Jens Schreiber for the reliable supply of liquid helium and liquid nitrogen. I would like to thank the institute administration and library staff, Uta Prautzsch, Petra Laqua, Carmen Kratochwil, Christin Bahr, and Ina Werner for solving all the problems of the daily routine, and in particular to Claudia Strobach for helping me with all my problems concerning my residence in Germany. I appreciate the input to the English correction in some parts of the manuscript from Dr. Ramzy Daou and Ricardo Casarin.

Further thanks go to other friends; For their deep and sincere friendship I thank Melanie, Micha, Katrin und Walter. Also to Frieda Helbig, Samuel Sanchez, Lorena Aquino, Perla Leal, Lena Simons, Federico Fluebert, Vicente Pacheco and Cristina Abello. Also Karolina and Marc Ihle for their truly friendship.

I am indebted to the Max Planck Gesellschaft and to CONACyT for the financial support. It is also a honor be part of the DAAD interchange program from Mexico and Germany, therefore I want to thank Stefanie Büchel for all the support and advice during the first years in Germany.

Furthermore, I would like to thank my wife Cecilia for her unconditional support during the difficult moments, for the continuous encouragement and outstanding help to unify my scientific work and my family. I thank my two daughters Ana and Isabel, who always cheered me up and brought a smile to my face, and of

course my mother-in-law Maria Cecilia Palacios, and my uncle Pedro Giorgana for their moral and economic support. And finally I thank my Parents for constantly reminding me that true humility is the most important virtue in a scientist and for their appreciation and understanding of my work.

Versicherung

Hiermit versichere ich, dass ich die vorliegende Arbeit ohne unzulässige Hilfe Dritter und ohne Benutzung anderer als der angegebenen Hilfsmittel angefertigt habe. Die aus fremden Quellen direkt oder indirekt übernommenen Gedanken sind als solche kenntlich gemacht. Die Arbeit wurde bisher weder im Inland noch im Ausland in gleicher oder ähnlicher Form einer anderen Prüfungsstelle vorgelegt.

Die vorliegende Doktorarbeit wurde am Max-Planck-Institut für chemische Physik fester Stoffe in Dresden unter der wissenschaftlichen Betreuung von Herrn Prof. Frank Steglich, und Herrn Dr. Manuel Brando angefertigt.

Ich erkenne die Promotionsordnung der Technischen Universität Dresden an.

Dresden, den 16. Januar 2013